Rose Koopman

Ageing of the LHCb Outer Tracker & b-hadron production and decay at $\sqrt{s}$ = 7 TeV

Ageing of the LHCb Outer Tracker & b-hadron production and decay at $\sqrt{s}$ = 7 TeV

Rose Koopman

Ageing of the LHCb Outer Tracker
&
b-hadron production and decay at $\sqrt{s} = 7$ TeV

ROSE KOOPMAN

Ageing of the LHCb Outer Tracker & b-hadron production and decay at $\sqrt{s} = 7$ TeV
Thesis, Vrije Universiteit, Amsterdam

Cover design by Buro Brouns
Cover photo “field of sunflowers, Rozsypne, Ukraine”, Reuters/Sergei Karpukhin
Printed by Gildeprint

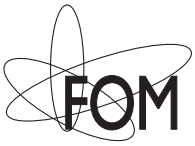

This work is part of the research programme of the Foundation for Fundamental Research on Matter (FOM), which is part of the Netherlands Organisation for Scientific Research (NWO). The work is carried out at the National Institute for Subatomic Physics (Nikhef) in Amsterdam, The Netherlands.

VRIJE UNIVERSITEIT

Ageing of the LHCb Outer Tracker
&
b-hadron production and decay at $\sqrt{s} = 7$ TeV

ACADEMISCH PROEFSCHRIFT

ter verkrijging van de graad Doctor aan
de Vrije Universiteit Amsterdam,
op gezag van de rector magnificus
prof.dr. V. Subramaniam,
in het openbaar te verdedigen
ten overstaan van de promotiecommissie
van de Faculteit der Exacte Wetenschappen
op dinsdag 3 november 2015 om 13.45 uur
in het auditorium van de universiteit,
De Boelelaan 1105

door

Rose Footiní Koopman

geboren te Maastricht

promotor: prof.dr. M.H.M. Merk

copromotor: dr. N. Tuning

Voor Janneke en Peter

Contents

CHAPTER 1

Introduction

The Standard Model (SM) of particle physics, illustrated in Fig. 1.1, has brought order in the zoo of fundamental particles. It successfully describes all known subatomic particles and their interactions. The quarks and leptons are divided in three generations, with increasing mass. The electromagnetic force and weak force are combined in the electroweak theory. Its carriers are the massless photon γ, the massive charged $W^{\pm}$ bosons and the massive neutral Z^0 boson. The $W^{\pm}$ and Z^0 bosons interact with all fundamental particles, while the photons do not couple to the neutrinos ν, as these do not have charge. Electromagnetic interactions dominate atomic physics while weak interactions are responsible for radioactive decay of subatomic particles. The carrier of the strong force is the gluon. The strong force is the inter-quark binding force that keeps together the quarks inside a nucleon. The Higgs mechanism describes a way to generate mass for the otherwise massless bosons and in addition introduces a way to provide mass to the fermions via the Yukawa couplings. The associated particle is the Higgs boson.

The SM allows for very precise predictions [1–3], leading to the discovery of the W [4, 5] and Z bosons [6, 7] in 1983 at CERN and the discovery of the heaviest quark, the top quark, in 1995 at Fermilab [8–10]. With the recent discovery of the Higgs boson [11, 12], the last missing piece of the SM puzzle [13, 14] has been found. The overwhelming success of the SM is best illustrated with the 15 nobel prizes that have been awarded for discoveries closely connected to the development of the SM. Tables 1.1–1.2 give an overview of the important discoveries and theoretical developments that led to the SM in its current form, taking the nobel prizes as a guidance.

While the SM triumphs in explaining phenomena at the smallest scales we can currently probe, there are some long-standing problems for which is does not have a clear answer. For example the dominance of matter over anti-matter is one of the fundamental issues to be addressed. The couplings of the Higgs boson to the quarks, the so-called Yukawa couplings, provide a mechanism to introduce a matter anti-matter asymmetry into the SM. As a result, some $B_{(s)}$ decays are not invariant under the combined operation of charge (C) and parity (P) operators, a process known as CP violation. However, the

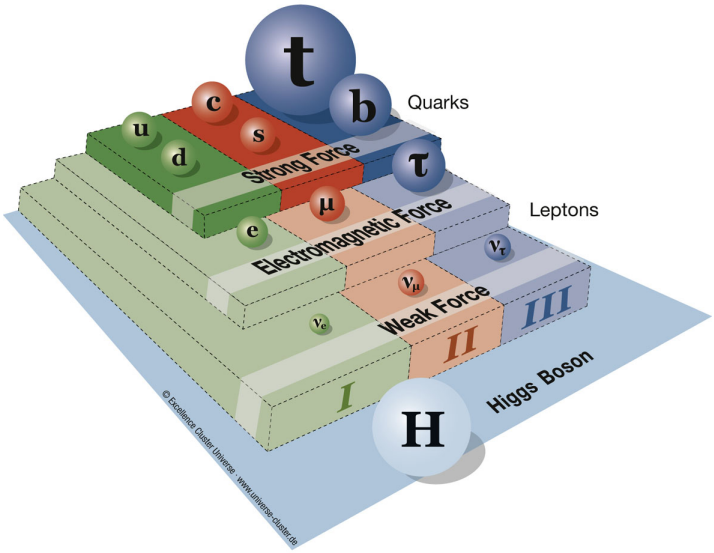

Fig. 1.1 · The particle content of the standard model of particle physics. The size of the spheres is an indication of the relative mass of the particles. The pyramid structure illustrates which forces play a role in the interactions between the different particles. Picture from [15].

size of the observed cosmological asymmetry exceeds what can be explained through this mechanism [16].

Cosmological observations reveal another shortcoming of the SM. The observed rotational speed of most stars in spiral galaxies as a function of the distance to the centre of the galaxy does not meet the expectation [17]. The observations suggest that the gravitational mass in the galaxies is more than the visible mass. This unseen matter is referred to as "dark matter". It has the property that it does not interact electromagnetically, making it invisible to cosmological experiments, while it does interact via gravity. No stable elementary particle has such properties.

The fourth force in nature, gravity, is not incorporated in the SM. Instead, gravity is described by general relativity [18]. No force carrier of the gravitational force has been discovered. At the subatomic scale, gravity is the weakest force of nature by several tens of orders of magnitude, and does not influence any subatomic processes.

New Physics (NP) models have been developed to incorporate the shortcomings of the SM. Beyond the standard model (BSM) scenarios are often an extension to the already existing framework, introducing for instance another Higgs sector (charged Higgs, e.g. [19]), supersymmetric mirror particles of the existing particles ("sparticles", e.g. [20]), or additional bosons (W' or Z', e.g. [21]). Experiments at particle accelerators aim to find signatures of these models.

Several particle accelerator experiments have been operational in the past decades, each adding to the development of the SM to its current form. Of the heavy quarks, the

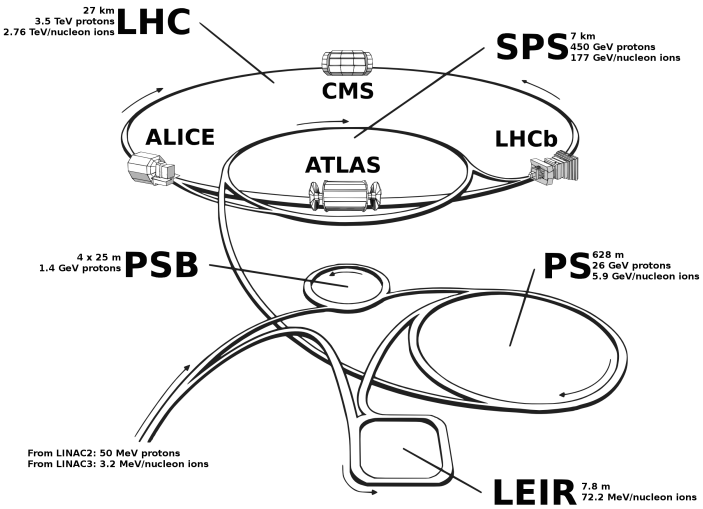

Fig. 1.2 · The accelerator complex of the Large Hadron Collider. The four main LHC experiments are build at the interaction points where the two proton beams collide. The protons are pre-accelerated before they are injected in the LHC. The pre-acceleration takes place at the Proton Synchrotron Booster (PSB), the Proton Synchrotron (PS) and the Super Proton Synchrotron (SPS). The Low Energy Ion Ring (LEIR) is used for the pre-acceleration of heavy ions. Picture from [22].

charm quark was discovered independently at SLAC [23] and Brookhaven National Laboratory [24], in 1974. In 1977, the Fermilab E288 experiment discovered the b quark, when $\Upsilon(1S)$ was produced by protons hitting a fixed target. The Tevatron proton-antiproton accelerator at Fermilab was operational from 1985 to 2011, colliding protons and antiprotons at a centre-of-mass energy of 1.96 TeV during its last decade of operation. The top quark was discovered at the Tevatron experiments CDF and D0 in 1995.

Of the gauge bosons, the gluon was discovered in three-jet events in electron-positron collisions at DESY, 1979 [25–28]. From 1981 to 1984, the SPS accelerator provided proton-antiproton collisions to the UA1 and UA2 experiments at CERN, leading to the discovery of the W and Z bosons. The LEP electron-positron collider at CERN was operational from 1989 until 2000, when it had to make place for the Large Hadron Collider (LHC). The LEP experiments ALEPH, DELPHI, OPAL and L3 contributed to precision measurements of the newly discovered W and Z bosons. In particular, the precise measurement of the Z mass led to the conclusion that there are only three neutrinos in the SM, thereby fixing the number of particle generations to three. In addition, the accuracy of the measurements of the W and Z mass makes them sensitive to the Higgs boson mass through loop corrections, which led to a prediction of the Higgs mass [29, 30].

The B-factory experiments CLEO, Belle and BaBar are served by electron-positron colliders at a centre-of-mass energy corresponding to the $\Upsilon(4S)$ resonance. As the $\Upsilon(4S)$ predominantly decays in pairs of B^0 mesons, this provides a clean environment to study

1

B^0 meson decays. The discovery of CP violation in the B^0 system in 2001 [31, 32], was the experimental evidence for the mechanism proposed by Kobayashi and Maskawa and eventually led to the Nobel Prize in 2008. The Belle and BaBar experiments have stopped taking data, but their data analysis is still ongoing.

The experiments at the LHC are currently in a prime position to either discover or exclude NP theories. The LHC is a proton-proton accelerator that recently started Run II operation and is currently operating at a centre-of-mass energy of 13 TeV. The main LHC experiments are ALICE, ATLAS, CMS and LHCb. The ALICE experiment is designed to study quark-gluon plasma, a state of matter similar to that existing shortly after the Big Bang.

Many beyond the standard model scenarios introduce new heavy particles. The ATLAS and CMS experiments conduct direct searches for these heavy particles. The LHCb experiment takes a different approach and searches for indirect signatures of NP. It measures the parameters in the SM to high precision. New particles, produced virtually in loop processes, can induce small alternations in these parameters. This can result in different branching fractions of certain processes, a change in angular distributions of final state particles, or in different amounts of CP violation. The precision measurements of these observables allow for an indirect observation of NP, similar to the prediction of the Higgs mass based on LEP precision measurements. Moreover, these precision measurements are not experimentally limited by the centre-of-mass energy, as direct searches by ATLAS and CMS are.

The subject of this thesis is twofold and the thesis is divided in two parts accordingly. The first part focusses on the monitoring of radiation damage of the LHCb Outer Tracker. The second part describes the analysis of proton-proton data collected by the LHCb experiment, in particular the measurement of the relative production rates of the different species of b hadrons. The measurements of several branching fractions of b-hadron decays are also included.

Part I: Ageing in the LHCb Outer Tracker

The measurements in this thesis use the dataset collected by the LHCb experiment during Run I. A description of the LHCb experiment and its performance is given in chapter 2.

The LHCb detector operates in the high radiation environment of the LHC. Radiation damage, so-called “ageing”, can impair the working of the detector and thereby the quality of the data taken for physics analysis. The Outer Tracker subdetector system provides information essential for the reconstruction of the trajectory of charged particles. It is a gaseous straw tube detector, a technology known to be sensitive to ageing. Monitoring of the ageing of the Outer Tracker is therefore crucial. Chapter 3 discusses several methods that are used to monitor the ageing of the Outer Tracker. Results of ageing studies performed during Run I are included.

Part II: Fragmentation fractions and branching fractions

The measurements of branching fractions of decays which are heavily suppressed in the SM offer a sensitive probe to NP. Such branching fractions can be enhanced due to virtual NP

particles which enter in loop processes mediating these decays. The prime example of such a decay is $B_s^0 \to \mu^+\mu^-$. A precise measurement of the branching fraction of $B_s^0 \to \mu^+\mu^-$ decays requires precise knowledge about the production of B_s^0 mesons at the LHC. At proton-proton colliders, the production of B_s^0 mesons is expressed relative to the production of B^0 mesons. The B^0 mesons were studied at the B-factories in a low background environment such that absolute branching fractions could be measured. The branching fractions of B^0 decays can therefore act as a normalisation channel at the LHC. The ratio of fragmentation fractions, f_s/f_d, relates the production of B_s^0 and B^0 mesons. Here, the quantity $f_{d,s}$ is the probability that a b quark hadronises to a $B_{d,s}$ meson.

The production of B_s^0 mesons is a process governed by the strong interaction. Quantum Chromo Dynamics (QCD) is the theory of strong interactions that describes the interaction of quarks and gluons. The production of b quarks can be perturbatively calculated within QCD, but the production of b hadrons is a non-perturbative process. The production of B_s^0 mesons is therefore difficult to calculate within QCD. Consequently, the production needs to be measured in experimental data. An overview on the theoretical and experimental knowledge of the production of heavy hadrons is given in chapter 4.

A study on the decay of heavy hadrons can provide information on the relative production fractions of heavy hadrons. This requires a theoretical understanding of the ratios of branching fractions of heavy hadrons. The heavy hadron decays studied in this thesis are governed by the weak interaction. However, as the decays under study have quarks in the final state, also QCD effects need to be taken into account. Chapter 5 introduces the theoretical framework that is needed for the calculation of a branching fraction. In addition, the experimental challenges involved in a measurement of a heavy hadron decay with the LHCb detector are introduced.

A measurement of the relative production of B_s^0 and B^0 mesons is included in chapter 6, as well as a study of the dependence of the relative production on the kinematics of the B meson. This measurement uses the hadronic decays $\overline{B}^0 \to D^+\pi^-$, $\overline{B}^0 \to D^+K^-$ and $\overline{B}_s^0 \to D_s^+\pi^-$. In addition to B_s^0 mesons, also Λ_b^0 baryons offer a channel for investigating CP violation. A study of the relative production of Λ_b^0 baryons and B^0 mesons, using the decays $\Lambda_b^0 \to \Lambda_c^+\pi^-$ and $\overline{B}^0 \to D^+\pi^-$, is included in chapter 7.

The weak interactions between quarks are described within the CKM framework. Using the unitarity of the CKM theory, the relations describing the weak interactions can be represented as triangles in the complex plane. The triangle representing the relation between the first and the third column of the CKM matrix, is referred to as the unitarity triangle. Precise measurements of this triangle provide a test of the SM. The decay $\overline{B}_s^0 \to D_s^\pm K^\mp$ offers a medium to measure the CKM angle γ, which is the angle of the unitarity triangle which is least well known to date. Using knowledge of the relative production of B_s^0 and B^0 mesons, the LHCb collaboration measured the branching fraction of $\overline{B}_s^0 \to D_s^\pm K^\mp$ decays in a subset of the available data. This measurement was however found to be incompatible with a theoretical lower limit. Using the large dataset available from Run I, the measurement has been repeated in chapter 8.

Finally, chapter 9 summarises the measurements presented in this thesis and places them in the context of recent and future measurements.

1957 (1956) T.D. Lee C.N. Yang	*"For their penetrating investigation of the so-called parity laws which has led to important discoveries regarding the elementary particles"*	P violation
1969 (1960s) M. Gell-Mann	*"For his contributions and discoveries concerning the classification of elementary particles and their interactions"*	quarks
1976 (1974) B. Richter S. Ting	*"For their pioneering work in the discovery of a heavy elementary particle of a new kind"*	J/ψ
1979 (1960s) S.L. Glashow A. Salam S. Weinberg	*"For their contributions to the theory of the unified weak and electromagnetic interaction between elementary particles, including, inter alia, the prediction of the weak neutral current"*	$SU(2) \otimes U(1)$
1980 (1964) J.W. Cronin V.L. Fitch	*"For the discovery of violations of fundamental symmetry principles in the decay of neutral K-mesons"*	CP violation
1984 (1983) C. Rubbia S. van der Meer	*"For their decisive contributions to the large project, which led to the discovery of the field particles W and Z, communicators of weak interaction"*	$W^{\pm}$ and Z^0 bosons
1988 (1962) L.M. Lederman M. Schwartz J. Steinberger	*"For the neutrino beam method and the demonstration of the doublet structure of the leptons through the discovery of the muon neutrino"*	ν_μ
1990 (1968) J.I. Friedman H. Kendall R.E. Taylor	*"For their pioneering investigations concerning deep inelastic scattering of electrons on protons and bound neutrons, which have been of essential importance for the development of the quark model in particle physics"*	quarks DIS
1995 (1976) M.L. Perl	*"For pioneering experimental contributions to lepton physics" and "for the discovery of the tau lepton"*	τ
1995 (1956) F. Reines	*"For pioneering experimental contributions to lepton physics" and "for the detection of the neutrino"*	ν_τ
1999 (1971) G. 't Hooft M.J.G. Veltman	*"For elucidating the quantum structure of electroweak interactions in physics"*	Renor-malisation

Table 1.1 · Nobel prizes in physics awarded for discoveries connected to the development of the SM, in chronological order. The year in bold is the year in which the prize was awarded, while the year/period in brackets indicates when the discovery was made. The description is the official reading from [33]. The last column indicates what aspect of the SM the Nobel prize relates to.

2004 (1973) D. Gross H. Politzer F. Wilczek	*"For the discovery of asymptotic freedom in the theory of the strong interaction"*	QCD
2008 (1960) Y. Nambu	*"For the discovery of the mechanism of spontaneous broken symmetry in subatomic physics"*	$V(\phi)$
2008 (1973) M. Kobayashi T. Maskawa	*"For the discovery of the origin of the broken symmetry which predicts the existence of at least three families of quarks in nature"*	*CP* violation
2013 (1964) F. Englert P. Higgs	*"For the theoretical discovery of a mechanism that contributes to our understanding of the origin of mass of subatomic particles, and which recently was confirmed through the discovery of the predicted, fundamental particle by the ATLAS and CMS experiments at CERN's Large Hadron Collider"*	Higgs

Table 1.2 · Continued from Tab. 1.1. Nobel prizes in physics awarded for discoveries connected to the development of the SM, in chronological order. The year in bold is the year in which the prize was awarded, while the year/period in brackets indicates when the discovery was made. The description is the official reading from [33]. The last column indicates what aspect of the SM the Nobel prize relates to.

Part I

Ageing of the LHCb Outer Tracker

CHAPTER 2

The LHCb detector

The LHCb detector [34, 35] is designed to exploit the large number of b hadrons produced at the LHC in order to make precision studies of CP asymmetries and of rare decays in the B meson system. Since $b\bar{b}$ pairs at the LHC are predominantly produced at small angles with respect to the beam axis, the LHCb detector, shown in Fig. 2.1, is designed as single arm forward spectrometer covering the region 10 to 300 (10 to 250) mrad in the $x-z$ ($y-z$) plane. It consists of a vertex locator, a dipole magnet, a tracking system, two ring imaging Cherenkov detectors, a calorimeter system and a muon system.

The Vertex Locator (VELO) provides the required vertex resolution that is needed to study the rapidly oscillating B_s^0 mesons and their CP asymmetries. The vertex resolution is also exploited in the decays studied in this thesis, where it allows to separate the combinatorial background from long-lived b hadrons. To measure the momenta of charged particles a magnet with a bending power of 4 Tm is used. Its vertical polarity can be reversed in order to reduce systematic effects in CP violation studies that can arise from a left-right asymmetry in the efficiency to detect particles.

A sophisticated tracking system is essential for the reconstruction of the multi-body decays described in this thesis. In addition to the VELO, the LHCb tracking system consists of the Trigger Tracker (TT), the Inner Tracker (IT) and the Outer Tracker (OT). The TT is a silicon micro-strip detector located upstream of the magnet. Two technologies are employed in the tracking stations T1–T3, which are located downstream of the magnet. The outer part (OT) consists of straw tube drift chambers, while the inner part (IT), where the particle densities are highest, is covered by silicon micro strip detectors.

Long tracks are formed by combining the reconstructed track segments in the VELO and downstream detectors. Tracks with a mismatch between the VELO and the IT/OT segment are denoted "ghost" tracks. The requirement of the presence of hits on the track in the TT station reduces the number of this type of tracks. Detailed performance studies of the OT are described in the next section.

The subdetectors dedicated to particle identification (PID) are the ring-imaging Cherenkov (RICH) detectors, the calorimeters (ECAL and HCAL) and the muon system (M1–M5). The RICH detectors allow for the identification of different types of charged

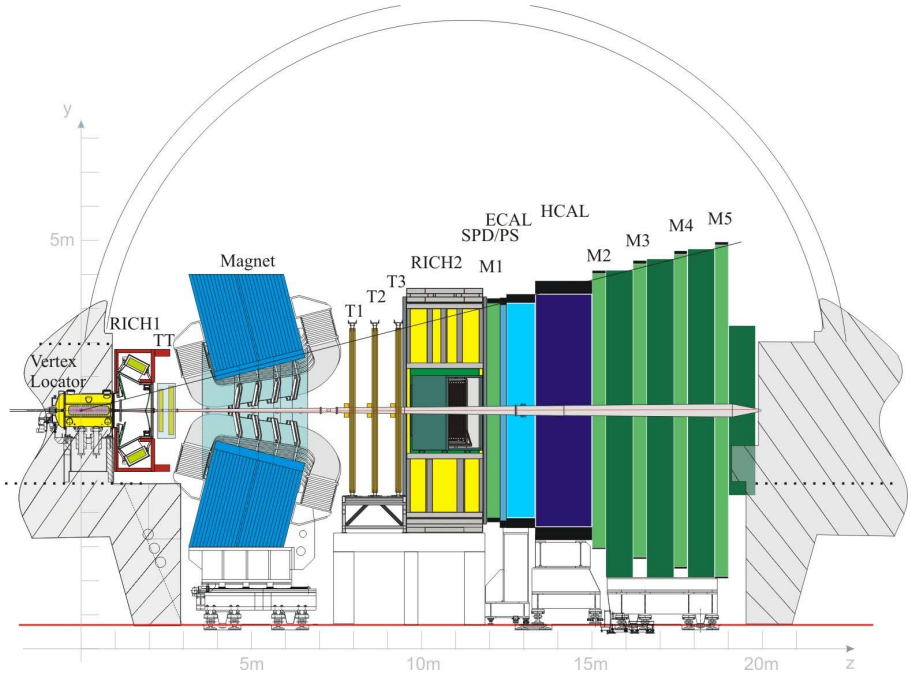

Fig. 2.1 · Schematic overview of the LHCb detector.

hadrons, using the light emitted when charged particles traverse a medium with a velocity greater than the local speed of light. The RICH is crucial to reduce backgrounds with a similar hadronic decay topology but with different particles in the final state, such as the $\overline{B}^0 \to D^+\pi^-$ background to the $\overline{B}^0 \to D^+K^-$ signal decay.

The main purpose of the calorimeters is to provide fast information to the lowest level trigger. In addition the electromagnetic and hdaronic calorimeter enable the reconstructions of photons and neutral pions, respectively. The calorimeter technology consists of a sampling structure of alternating layers of absorber and scintillating material. Information from the muon system is not used for the decays studied in this thesis.

2.1 Performance

The ease with which the LHCb detector can identify b-hadron decays is best illustrated with an example. Figure 2.2a shows the invariant mass distribution of $\overline{B}^0 \to D^+K^-$ candidates with a mass resolution of only 15.3 MeV/c^2, allowing for a clear separation of the signal from peaking background decays.

Without the pion-kaon separation provided by the RICH detector, a study of $\overline{B}^0 \to D^+K^-$ or $\overline{B}^0_s \to D^\pm_s K^\mp$ decays is impossible as the signal drowns in the more abundant background from $\overline{B}^0 \to D^+\pi^-$ and $\overline{B}^0_s \to D^+_s\pi^-$ decays, respectively. For the decays

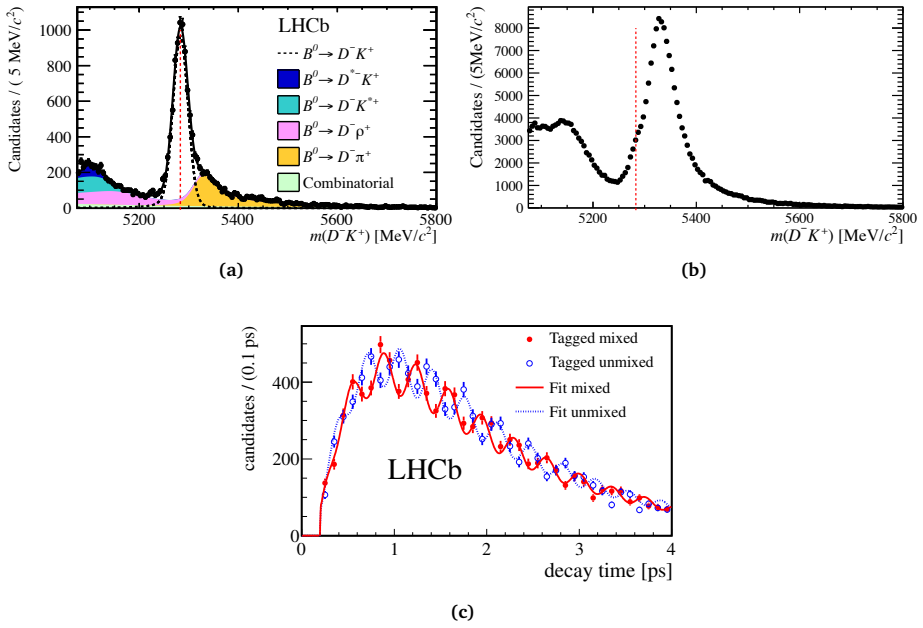

Fig. 2.2 · Invariant mass distribution of $\overline{B}^0 \to D^+K^-$ candidates, with the location of the $\overline{B}^0 \to D^+K^-$ peak indicated with a red dashed line, a) after all selection criteria are applied, and b) after all selection criteria but the PID selection. c) Decay time distribution of $\overline{B}^0_s \to D^+_s\pi^-$ events for events that have a different (same) flavour during production and decay in red (blue) [36].

studied in this thesis, the typical signal efficiency of the PID requirements is approximately 65% with a mis-identification rate of a few percent. Omitting the PID requirement that is applied to the kaon track in the four body decay $\overline{B}^0 \to D^+K^-$ leads to an increase of background decays where a pion is misidentified as a kaon. An apparent shift of the signal peak to higher values due to the presence of misidentified $\overline{B}^0 \to D^+\pi^-$ decays is shown in Fig. 2.2b. Here, also the background in the lower sideband, from the misidentified partially reconstructed $\overline{B}^0 \to D^{*+}\pi^-$ and $\overline{B}^0 \to D^+\rho^-$ decays, is significantly increased.

The use of B and D meson vertex separation in the event selection relies on good vertex resolution. The vertex quality and B meson decay time is already exploited in the trigger selection, and hence the large background at small decay times is not present in the offline data. Therefore, the quality of the vertex resolution is demonstrated in Fig. 2.2c, which shows the fast B^0_s–$\overline{B}^0_s$ oscillations measured using $\overline{B}^0_s \to D^+_s\pi^-$ decays in [36].

The deviation in trajectory of a charged particle downstream of the dipole magnet provides a measure of the momentum of the particle. An accurate momentum determination of the final state particles allows for a good invariant mass resolution of the decaying particle.

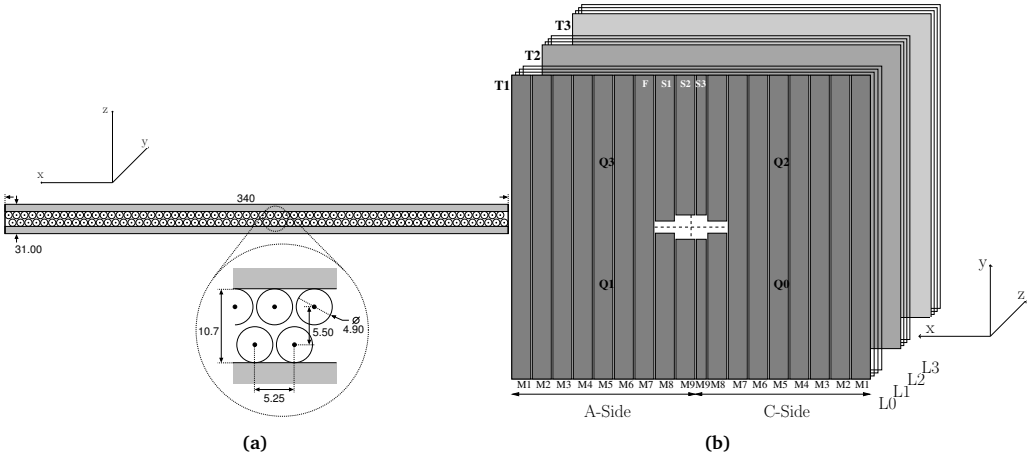

Fig. 2.3 · Outer tracker design: a) OT straws of one module, sandwiched between panels. The units of the dimensions are mm. b) arrangement of OT modules in LHCb. Naming scheme: T = station, L = layer, Q = quadrant, M = module.

This in turn leads to the low background shown in Fig. 2.2a. The IT and OT detectors determine the slope of the trajectory downstream of the magnet.

2.2 The Outer Tracker

The OT is a gaseous straw detector, consisting of 53760 straws with a length of 2.4 m and a diameter of 4.9 mm. The anode wire is made of gold-plated tungsten, while the cathode is made from electrically conducting carbon-doped kapton-XC foil on the inner side of the tubes. A high voltage of 1550 V is applied to the anode wire. Two monolayers of straws are sandwiched between two plates to form a layer, as shown in Fig. 2.3a, and are fixated using araldite AY103-1 glue. The panels are sealed with carbon-fiber sidewalls making an air-tight box, called a module. Each module contains two monolayers of 64 straws. The straw tubes are filled with the gas mixture Ar(70%)-CO_2(28.5%)-O_2(1.5%), which guarantees a fast drift time (below 50 ns) and the high single hit resolution that is needed to obtain a momentum resolution of $\delta p/p \approx 0.4\%$ [37].

The entire Outer Tracker spans an area of approximately 5 $\times$ 6 m^2 and consists of 216 modules. The modules are organised in three stations. Each station contains four layers, indicated as L0−L3. Modules in layers L1 and L2 are tilted with +5° and -5° stereo angles, respectively. The detector geometry is shown in Fig. 2.3b. A layer consists of four quadrants (Q) arranged as nine half-modules (M) each. Two out of nine modules are shorter, as the Inner Tracker occupies the volume closest to the beam pipe. In order to match the dimensions of the Inner Tracker, two of the shorter modules are half the width of a normal module.

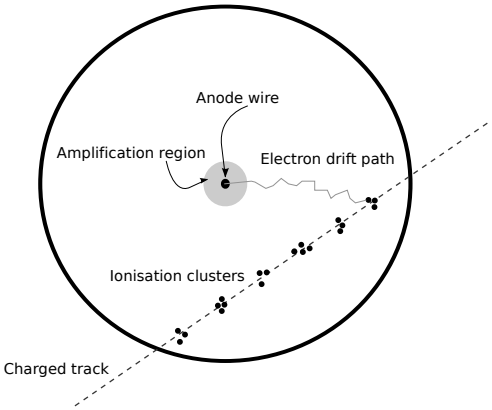

Fig. 2.4 · Schematic diagram of the working principle of an OT straw tube.

When a charged particle traverses an OT straw, as visualised in Fig. 2.4, it ionises the counting gas and pairs of electrons and ions are created. If the electrons have enough energy they can cause further ionisation by producing secondary electron-ion pairs. These ionisations will usually occur close to the primary ionisation resulting in clusters of ionisation. An ionising particle crossing an OT straw tube creates on average 3 ionisation clusters per mm [38]. Under influence of the electric field, the ions slowly drift to the cathode straw surface, while the electrons move towards the anode wire. Doing so, the electrons gain kinetic energy. The nominal gas amplification is 5.5×10^4 [39]. When the ionisation potential of the counting gas is reached, an electromagnetic avalanche is created. As the electrons arrive at the wire, they generate a measurable electrical pulse. The time of occurrence of the pulse with respect to the LHC clock is related to the distance between the wire and the closest ionisation cluster. The OT has a single-hit resolution of approximately 200 μm. As each layer consists of two monolayers, a traversing charged particle can induce at most 24 hits in the OT.

Front-end boxes (FEs) are mounted on each end of the modules. These boxes contain the electronics that digitise the drift-times of ionisation clusters produced by charged particles crossing the straw tubes in one module. Only when the collected charge is larger than approximately 4 fC[1] a hit is recorded. This corresponds to a threshold of 800 mV, after amplification of the cluster's charge[2]. In total 432 FEs are used to read out the data from the OT. For a detailed description of the FE electronics, the reader is referred to Ref. [37].

[1] In a hit approximately 30 primary and secondary electrons are created that induce a measurable pulse. Together they generate a charge of $30 \times 5.5 \cdot 10^4 \times 1.6 \cdot 10^{-19} = 2.6 \cdot 10^2$ fC on the anode wire.

[2] The relation between the amplifier threshold and the collected charge is $Q(\mathrm{fC}) = \mathrm{e}^{-1.25+0.0033 \times V_{\mathrm{th}}(\mathrm{mV})}$, with Q the collected charge and V_{th} the amplifier threshold [40].

CHAPTER 3

Ageing monitoring of the Outer Tracker

Radiation damage of gaseous detectors, so-called "ageing", is a complex phenomenon and poses a potential problem: it could severely impair the use of the Outer Tracker in the unprecedented harsh radiation environment of the LHC. Deterioration of the performance of gaseous detectors under irradiation has been observed since the development of Geiger and proportional counters, and has shown to affect the functioning of gaseous detectors in the high intensity regions at high-energy particle colliders, e.g. [41, 42]. The lifetime of gaseous detectors has been shown to be very sensitive to the nature and purity of the gas mixture, different additives and trace contaminants, materials used in contact with the gas, geometry of electrodes and configuration of electric field [43, 44]. The counting gas and the materials used to construct the OT have been carefully chosen to limit ageing [35, 45, 46]. Radiation damage can manifest itself as a decrease of gas gain and a loss of single hit efficiency, resulting in a reduced track finding efficiency, and a worsening of the momentum resolution. Ageing effects can result from deposits on the anode wire as shown in Fig. 3.1a. In the avalanche region many molecules break up in collisions with electrons. Free radicals are formed as a result of the relatively small energy that is needed for their formation (3–4 eV) compared to the energy of most ionisation processes (10 eV). Free radicals can polymerise to large structures that are highly branched and cross-linked. When adhered to the anode wire they may cause ageing.

The OT modules were designed to survive the harsh conditions of the Outer Tracker during LHC operations. During the 2011 running period the total delivered luminosity was $1.22\,\text{fb}^{-1}$, at an average instantaneous luminosity of $3.5 \times 10^{32}\,\text{cm}^{-2}\text{s}^{-1}$. The current in the straws located closest to the beam pipe was measured to be 650 nA and the intensity in the central region of the Outer Tracker was 13 nA/cm. The delivered dose in this hottest region is 0.045 C/cm for the 2011 running period[1]. During the 2012 running period the delivered luminosity was $2.21\,\text{fb}^{-1}$ at a slightly higher average instantaneous luminosity of

[1] Delivered dose $= \frac{\mathcal{L}^{\text{deliv}}}{\mathcal{L}^{\text{inst}}} \times I_{\text{hot}}$.

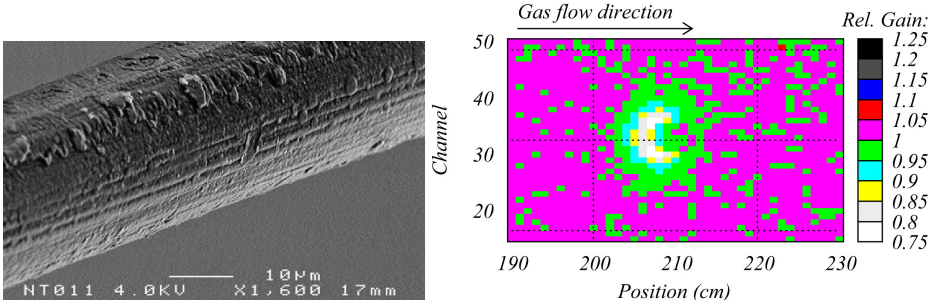

(a) (b)

Fig. 3.1 · a) A structure is observed on the OT wire after irradiation. b) Local gain loss after 20h of irradiation with a collimated ^{90}Sr source with an activity of 74 MBq. The source was located at wire 32, position 208 cm. The counting gas was a mixture of Ar(70%)-CO_2(30%). Figures from [46].

$4 \times 10^{32}\,\mathrm{cm}^{-2}\mathrm{s}^{-1}$. This results in a current of 14 nA/cm in the hottest region. The delivered dose in this region for the 2012 running period is 0.078 C/cm.

Irradiation tests carried out in the lab on a small selection of OT modules revealed that they suffered from gain loss already after moderate irradiation, corresponding to approximately 2 nA/cm [46]. The gain loss was traced back to the outgassing of the glue AY103-1, which uses as plastifier the aromatic hydrocarbon di-isopropyl naphthalene [47]. Carbon deposits were observed on the anode wires at the irradiated area (Fig. 3.1a), forming an insulating layer that was responsible for the loss of gain.

The cause of ageing in the OT was studied in detail [46] and several measures are taken to prevent it. As ageing is caused by outgassing of the glue, harmful vapours are transported away by continuous flushing of the gas. It has been shown that long term flushing decreases the ageing rate significantly. To accelerate the outgassing, all modules were heated in situ for two weeks at 35°C while being flushed at 0.5 volume exchanges per hour. In addition, oxygen has been added to the original counting gas mixture, which is observed to reduce the ageing rate [41] by a factor two [46]. Elevated levels of ozone (O_3) were measured, indicating its production in the avalanche region. The ozone presumably protects the anode wire downstream of the irradiated spot, resulting in the typical half-moon shaped area shown in Fig. 3.1b. Surprisingly, the gain loss is not proportional to the source intensity, as directly under the source the gain loss is found to be less severe. Gain loss is worse at larger gas flow, due to the O_3 being transported away more efficiently.

A wire that suffers of irradiation damage can be "cleaned" by applying a high voltage at elevated values, which induces dark currents of 1–10 μA [46, 47]. A full signal recovery is obtained after 20 hours in most cases. The microscopic mechanism of the cleaning process is unclear. Large currents can also be obtained locally on a wire for cleaning purposes, by irradiating the wire with a radioactive source. The intensity of the source needs to be large

enough to induce the cleaning effect and the irradiation time needs to be short to prevent irradiation damage to occur in the periphery where the intensity is lower.

Although noticeable irradiation damage was expected during LHC running, no gain loss was observed after a delivered luminosity of $1.22\,\mathrm{fb}^{-1}$ [48]. A hypothesis is that the large currents that occur from irradiation by the LHC clean the wires. Nevertheless, a continuous monitoring of the ageing of the Outer Tracker remains crucial. Several methods were developed to this end, which are extensively described in [48, 49]. The salient points of the methods will be illustrated here and the latest results of the monitoring will be included.

3.1 Relative gain determination with amplifier threshold layer scan

Scans were developed which enable the monitoring of ageing of the Outer Tracker during Run I [48, 49].

3.1.1 Method

When a charged particle traverses a straw tube a charge is created on the anode wire. Although the arrival time of the signal is accurately determined by the OT electronics, the signal height is not measured. The ionisation charge of the signal has to pass a digitisation threshold. The hit efficiency as a function of the amplifier threshold is measured to gauge the change in gain due to ageing. This measurement is performed during normal LHC operation. As the threshold of the OT amplifiers is varied during this test, the recorded data cannot be used for physics analysis. It is therefore important that the test be performed as quickly as possible. Typically the test takes about 1.5 hours of data taking, corresponding to approximately 300 000 recorded events per threshold. The method can be summarised with the following steps:

- Data is collected while changing the amplifier threshold value of one layer[1] at a time, and keeping the threshold values for the other layers at the nominal value of 800 mV. Measurements are taken at amplifier threshold values of 800, 1000, 1200, 1250, 1300, 1350, 1400, 1450, 1600 and 1800 mV. This procedure is repeated for each layer. The scan is designed such that the amplifier thresholds for the two monolayers within one layer are changed at the same time.

- For each layer the efficiency to record a hit as a function of the threshold setting is determined. All monolayers are considered individually at first and the results of the two monolayers within one layer are combined in a later step of the analysis. To determine the efficiency, tracks are reconstructed using the hits in all monolayers, except for one monolayer in which the threshold is varied. Using the reconstructed tracks a prediction is made where to find hits in the monolayer under consideration. For this prediction only so-called good tracks are used. These are tracks which have at least 20 hits (out of a maximum of 23 hits) and a χ^2/ndf smaller than 2.

[1] The word layer is consistently used to describe the two monolayers of a module. In other words, a layer consists of two monolayers.

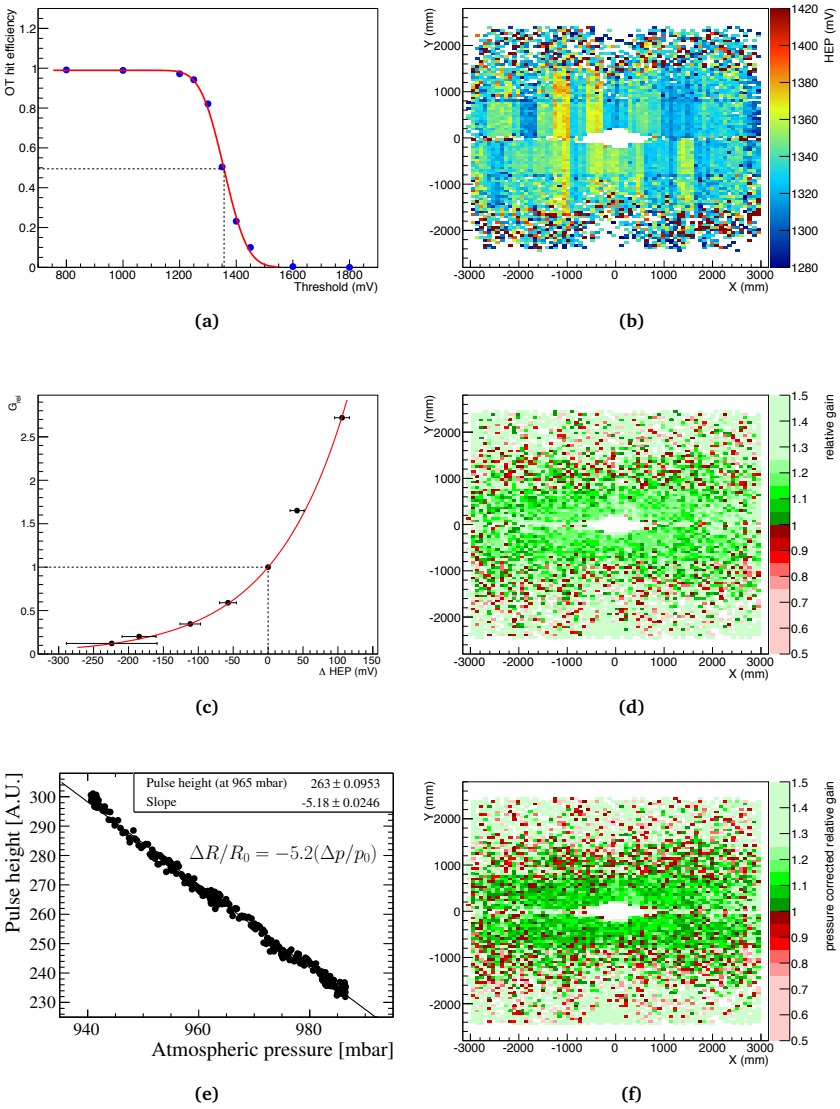

Fig. 3.2 · The various steps in the threshold layer scan are illustrated: a) the experimentally determined S-curve; b) the experimentally determined half-efficiency point distribution; c) the calibration curve relating a shift in H to a relative change in gain [51]; d) the experimentally determined relative gain distribution; e) the pressure correction as determined with an ^{55}Fe source [48]; f) the experimentally determined pressure-corrected relative gain distribution. The data shown in b), d) and f) were recorded for layer T3L3 during the amplifier threshold layer scan in Feb. 2013. The (pressure-corrected) relative gain is measured with respect to the reference scan taken in August 2010.

- Based on the track prediction, the local hit efficiency is measured. This is measured in bins of $85 \times 56\,\text{mm}^2$, where the width in the x direction corresponds to one fourth of one OT module. The measured hit efficiency is combined for the two monolayers within one layer. It is a function of the threshold voltage. The dependence of the hit efficiency on the amplifier threshold can be described with an S-curve, defined as

$$\varepsilon_{\text{hit}}(V_{\text{th}}) = \frac{1}{2}(P+T) - \frac{1}{2}(P-T)\,\text{erf}\left(\frac{V_{\text{th}}-H}{\sqrt{2}\sigma}\right), \tag{3.1}$$

  where V_{th} is the amplifier threshold setting, P is the hit efficiency at the plateau, T is the hit efficiency in the tail (which is typically zero), H is the half-efficiency point where the hit efficiency has dropped to $\frac{1}{2}(P+T)$, and σ accounts for noise. An example of an S-curve is shown in Fig. 3.2a for the last threshold scan taken in Run I. A shift of the half-efficiency point is a probe of gain changes, and a decrease indicates ageing. The half-efficiency point can be determined with a fit of Eq. 3.1 to the data. The shift, ΔH, is determined with respect to a reference scan. The first amplifier threshold scan was taken at the start of the LHC running in August 2010 and is used as the reference. In this scan, no data points were taken at threshold values of 1600 and 1800 mV, and the measurements at these points are therefore not taken into account by the fit for all other amplifier threshold scans. These points are used, however, to confirm that the efficiency in the tail is zero, which allows to set $T = 0$. An example of a measurement of half-efficiency points in one layer is shown in Fig. 3.2b. Typically, the different modules are clearly visible due to differences in the amplifier characteristics between different FEs.

- A shift in half-efficiency point can be translated to a change in gain (G). The relation between high voltage and relative gain was previously measured [50]. The calibration curve was determined by changing the high voltage and measuring the change in H, resulting in the expression

$$G_{\text{rel}} = \text{e}^{\frac{\Delta H\,[\text{mV}]}{105 \pm 10\,[\text{mV}]}}, \tag{3.2}$$

  with the relative gain $G_{\text{rel}} = \frac{G}{G_{\text{ref}}}$, and $\Delta H = H - H_{\text{ref}}$ [51]. The calibration curve is shown in Fig. 3.2c. An example of the distribution of relative gain over one layer is shown in Fig 3.2d. Typically, some fluctuations are visible, which increase in size towards the outer parts of the module. The hit occupancy is lower in this area, leading to a less precise measurement. The $+10\%$ changes, observed in the central region of the OT layer close to the beam pipe, are discussed later.

- A difference in air pressure between the time at which the scan is taken and the time of the reference scan influences the measured relative gain. Using a dedicated module, which was constantly irradiated using a ^{55}Fe source, pulse height variations were measured as a function of the atmospheric pressure (Fig. 3.2e). As gain is proportional to pulse height, this yielded the correction

$$\frac{\Delta G}{G} = \frac{\Delta R}{R_0} = -5.18\frac{\Delta p}{p_0}, \tag{3.3}$$

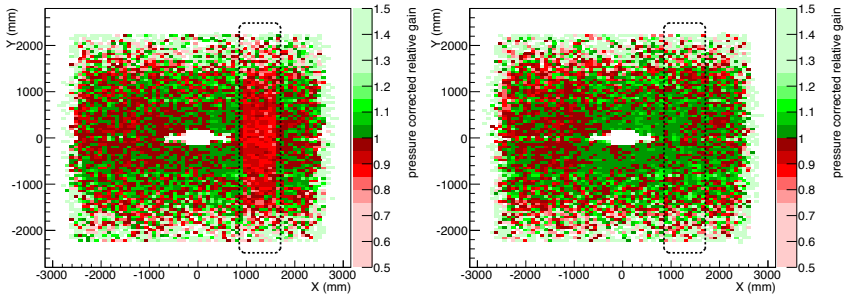

Fig. 3.3 · Pressure-corrected relative gain in layer T2L0 in a) May 2012 and b) July 2012. Instead of using the normal reference scan taken in Aug 2010, the scan taken a month prior to the occurrence of the faulty HV channel, in April 2012, is used as reference. This is done to minimise any secondary effects from ageing, replacement of FEs or variations in the gas mixture. The modules connected to the malfunctioning HV channel are indicated with the dashed box, and are clearly visible in the scan taken in May 2012.

where R is the pulse height and p is the atmospheric pressure. An example of the pressure-corrected relative gain distribution measured in one detector layer is shown in Fig. 3.2f, where an overall shift to lower values is observed compared to Fig. 3.2d due to the correction for the pressure difference.

Systematic uncertainties in the procedure arise from the fit model describing the S-curve, the calibration curve and the pressure correction and amount to a total of 2.2%-points [48, 49]. The uncertainty due to the fit model is estimated by introducing different modifications to the fit model: the tail parameter (T) is left free; the plateau parameter (P) is fixed to 1; the half-efficiency point is changed to 0.5; and finally a different model consisting of two gaussian functions is applied. These uncertainties quadratically add up to a total uncertainty due to the fit model of 2.0%-points.

To estimate the uncertainty from the calibration curve, the constant 105 was varied by $\pm 1\sigma$ and the largest change in gain was taken as a systematic (0.8%-point). The constant in the pressure correction is varied by $\pm 10\%$ yielding an uncertainty of 0.4%-point. If the pressure-corrected relative gain measured for the entire OT surface is considered (rather than the binned values shown in Fig. 3.2f), typically the measurement is dominated by the systematic uncertainty as the statistical uncertainty is two orders of magnitude smaller.

3.1.2 Validation method

The method has been validated exploiting a temporary defect in one of the channels of the high voltage supply, T2L0Q13FE56HV34[1], which provides the high voltage to one monolayer

[1] Naming scheme as indicated in Fig. 2.3b, and in addition FE = Front-End and indicates which module (M) the FE is connected to, and HV = high voltage and indicates which monolayer within the layer the HV channel is connected to.

in the half-modules T2L0Q1M5, T2L0Q1M6, T2L0Q3M5 and T2L0Q3M6. This resulted in a lower measurement of the pressure-corrected relative gain in these modules (Fig. 3.3a). The anomalous behaviour of T2L0Q13FE56HV34 first occurred on May 12th 2012 when the current suddenly dropped to zero. Later instances have been recorded where the current suddenly decreased by a maximum of 50% and then slowly increased to the nominal value[1]. The reason of the lower current was traced to a faulty HV channel supplying a lower voltage to the detector, leading to a reduced gas gain in the monolayers connected to it. An amplifier threshold layer scan was taken on May 30th 2012, when the current was below nominal level. The malfunctioning channel was replaced by a spare HV channel on June 27th 2012, after which the measured current was found to be stable at nominal level, leading to a pressure-corrected relative gain at nominal value (Fig. 3.3b).

The decrease in current due to the malfunctioning HV channel can be directly related to a decrease in gain in the modules connected to it. The pressure-corrected relative gain is measured per layer and thus needs to be converted to a relative gain per *mono*layer. Therefore, the measured inefficiency is multiplied by two. Using the amplifier threshold layer scan taken in April 2012 as a reference, the pressure-corrected relative gain is measured to be 0.80, 0.81, 0.79 and 0.80 in the monolayers in T2L0Q1M5, T2L0Q1M6, T2L0Q3M5 and T2L0Q3M6, respectively. The pressure-corrected relative gain for the entire detector surface is measured to be 1.00. From the measured pressure-corrected relative gain, it thus follows that the current was decreased by $(20.4 \pm 2.2)\%$ during the threshold layer scan taken in May 2012.

A direct measurement of the current in T2L0Q13FE56HV34 yields a decrease of $(18.5 \pm 3.7)\%$ compared to the nominal value, during the scan taken in May 2012. The decrease in current measured using the amplifier threshold layer scan and the direct measurement agree, showing that the amplifier threshold layer scan is sensitive to small gain changes.

3.1.3 Results

To guarantee continuous monitoring of the ageing of the OT, threshold scans are made after approximately every 200 pb^{-1} (400 pb^{-1}) of delivered luminosity in 2011 (2012). In addition, extra scans are made just before and directly after the winter stop and at the end of Run I. The average pressure-corrected relative gain over the entire detector volume is determined for each scan. The scan made in August 2010 is used as a reference. An increase in gain is found for all scans taken between 2010 and 2013, indicating no ageing.

The relative gain variation as a function of time and delivered luminosity is shown in Fig. 3.4. A sudden increase in gain is observed after both the 2010 and 2011 winter stop. While the gain again decreased to the reference level during the 2011 running period, it remained at higher value during the 2012 running period. This is attributed to small changes in the gas mixture, which is determined by mass flow controllers. The accuracy of the flow controllers guarantees a stable Ar fraction within approximately 2.1%-points whereas a change of 1%-point leads to a gain change of 12% [52]. More accurate flow controllers have been installed for Run II.

[1] https://lblogbook.cern.ch/OT/2691.

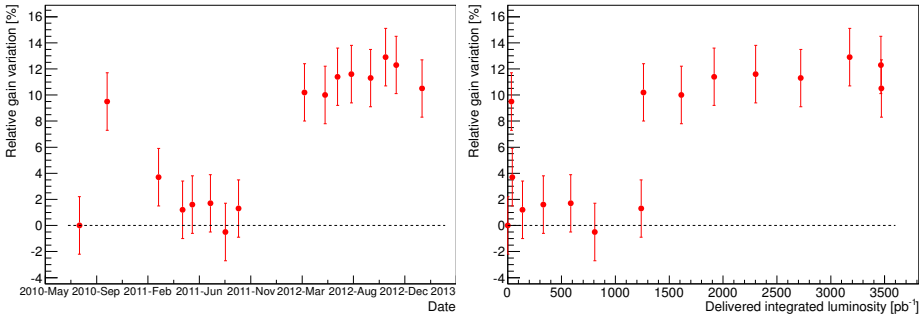

(a) **(b)**

Fig. 3.4 · Pressure-corrected relative gain as a function of a) time and b) delivered luminosity.

In addition, the relative gain variation is studied in specific regions in the OT. The regions are chosen such that they differ in hit occupancy or flow direction with respect to the point of highest occupancy. The different regions are defined in Fig. 3.5. The relative gain variations in these regions are shown in Fig. 3.6 for the scans taken between 2010 and 2013. All regions show a limited increase in gain. The increase is largest in the high occupancy regions and downstream of the region with largest occupancy. This supports the hypothesis mentioned in the introduction, that O_3 provides protection against gain loss. In addition, it is in agreement with the observation in the lab that the gain loss is reduced in the region with the highest current, i.e. directly under the source [46].

The pressure-corrected relative gain measured in the threshold scan taken in Feb. 2013 is shown in Fig. 3.7 for all OT layers separately. The region that can be probed with the amplifier threshold layer scan increases for layers more downstream of the interaction point, due to the stringent requirement on the number of hits on a track. No differences are observed between the different layers. The modules indicated with a black dashed box can all be related to replaced FEs and the difference in pressure-corrected relative gain for these modules compared to the average is understood. These modules are discussed in App. A.1, where also a complete overview of all scans is included.

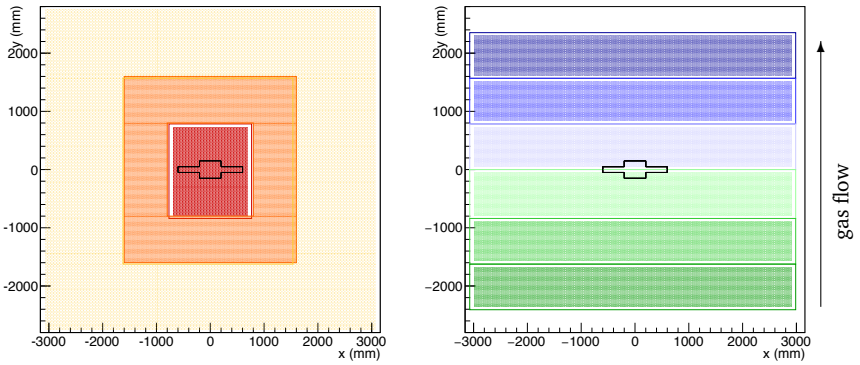

(a) **(b)**

Fig. 3.5 · Different regions in the detector surface for which the pressure-corrected relative gain is determined. a) Regions in order of occupancy: high (red), middle (orange), low (light orange); b) Regions in order of gas flow. Upstream regions (green) and downstream regions (blue). The colour code corresponds to that in Fig. 3.6.

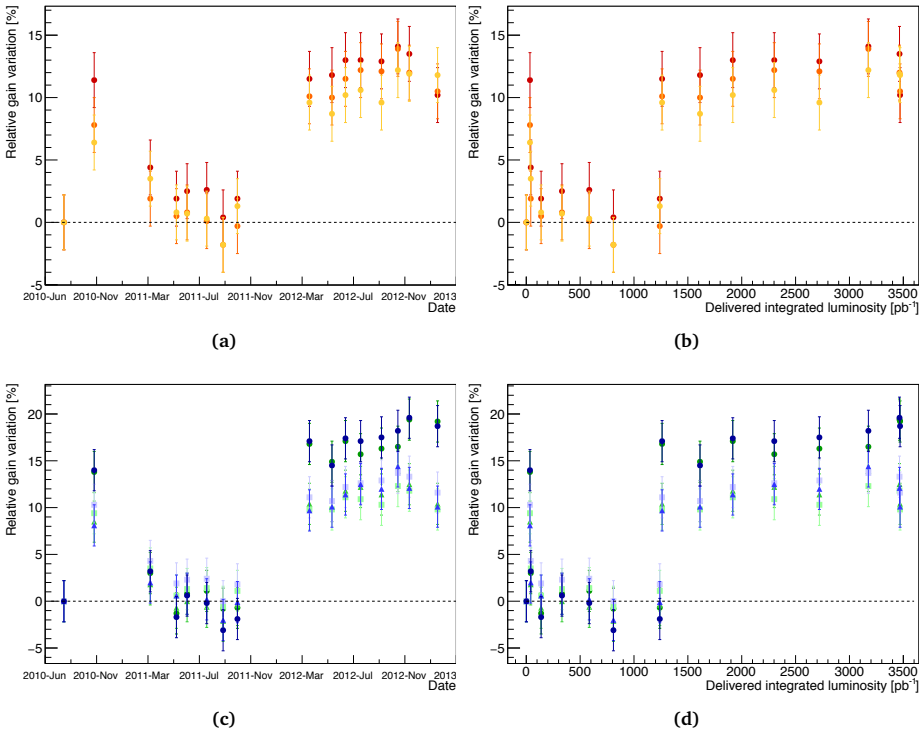

Fig. 3.6 · Pressure-corrected relative gain trend plot for the different regions as defined in Fig. 3.5, as function of time (a,c) and luminosity (b,d).

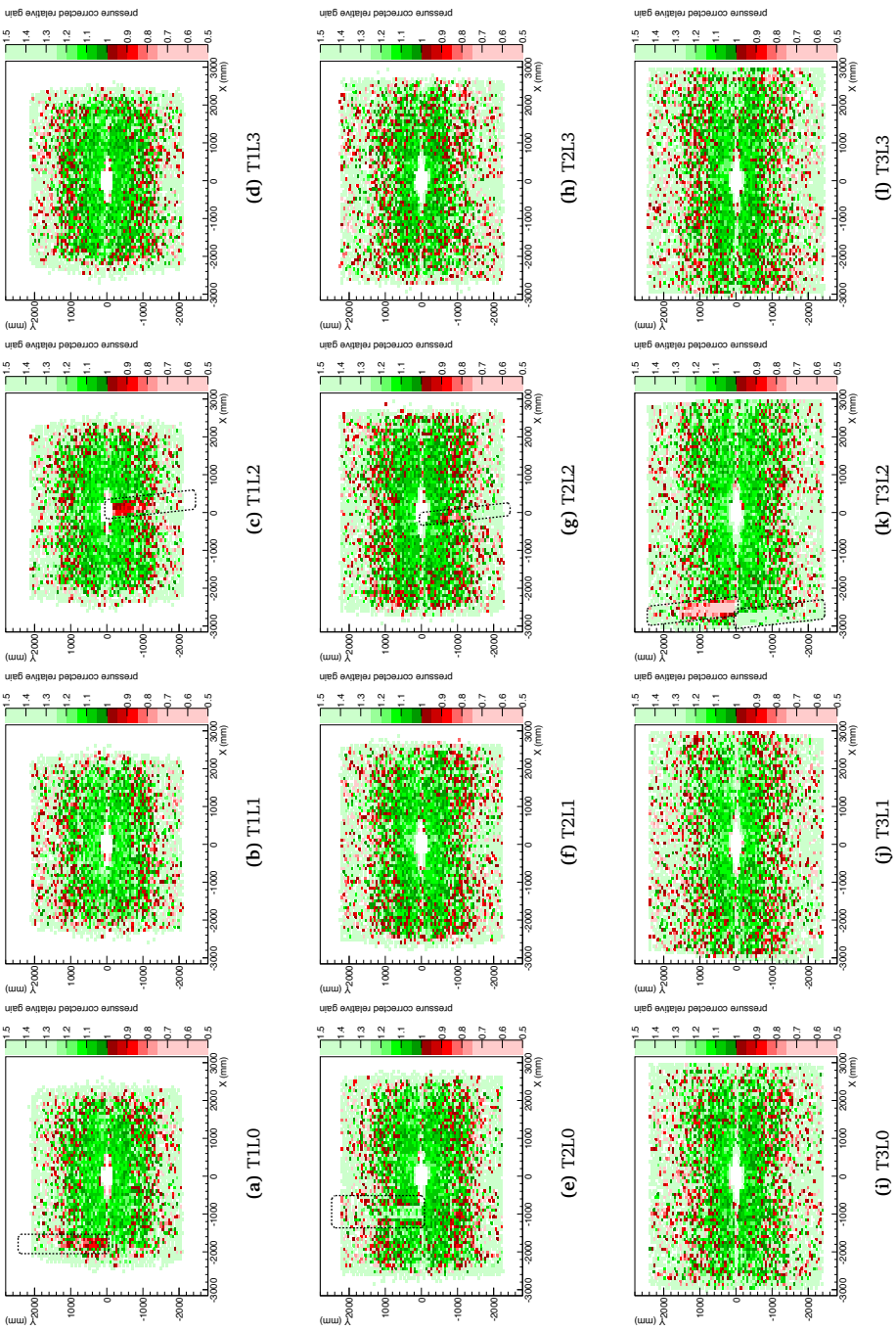

Fig. 3.7 · Pressure-corrected relative gain variation measured in February 2013 with respect to August 2010, for the different layers of the Outer Tracker. Modules that are replaced or otherwise changed are indicated with the black boxes, and are discussed in App. A.1.

3.2 Relative gain determination with a ^{90}Sr source

In addition to the amplifier threshold layer scans which are taken during data-taking (at the expense of valuable data for physics analyses) dedicated scans which can be performed during long periods without beam provide a means to monitor ageing of the OT. These scans, which make use of a radioactive ^{90}Sr source, were initially developed for quality insurance tests during and after module production [39]. Since the installation of the OT, the scanning method is exploited to monitor the ageing of the OT in situ [53].

3.2.1 Method

Using the ^{90}Sr source, the detector surface can be scanned to measure the current. For the ^{90}Sr scan a dedicated movable scanning tool was designed (Fig. 3.8a) which is mounted on the the support frame of the IT detector and gives access to the first layer of station T2. The method can be summarised as follows:

- The entire surface of T2L0Q1 is scanned with two ^{90}Sr sources with an activity of 74 MBq each. This element decays as $^{90}\mathrm{Sr} \rightarrow e^- + \bar{\nu}_e + {}^{90}\mathrm{Y} \rightarrow 2e^- + 2\bar{\nu}_e + {}^{90}\mathrm{Zr}$ with a half-life time of 28.8 years. The electrons have an energy up to 2.28 MeV and induce a measurable current when traversing the OT module. The scan needs to be performed module by module because the two sources together span the width of only one module. The two monolayers within each of the nine modules are scanned separately and therefore the measurement of the relative gain of T2L0Q1 consists of 18 individual scans.

- The current profile as a function of the position along the wire (y) is measured in steps of 1 cm using a custom-made ammeter which is connected to the module at the position of the FE. The current profile versus wire number, shown in Fig 3.8b, reveals a typical sinusoidal shape. This corresponds to irradiation with two sources at wire numbers 14 and 52, with a horizontal separation of about 17 cm (32 wires).

- The measured current profile is compared to a reference scan. Ageing is expected to occur upstream of the area with highest irradiation with respect to the gas flow, as was seen in Fig. 3.1b. This means that the largest irradiation damage is expected at low y values[1]. As a pattern across the module is expected, rather than a simple overall change in current, no correction is made for the difference in atmospheric pressure between the time at which the scan is taken and the time of the reference scan.

This method is sensitive to the source intensity at the detector, which can vary due to the exact position of the sources in their holder. The reproducibility of the source intensity between scans is better than 10%.

[1] Note that a different convention is used in the presentation of the results of the ^{90}Sr scan compared to results of the amplifier threshold scan: the range y = 0–240 cm in Fig. 3.9 corresponds to the range y = -2400–0 mm in Fig. 3.2f. Only the lower half of OT layer T2L0 is accessible to the ^{90}Sr scanning tool.

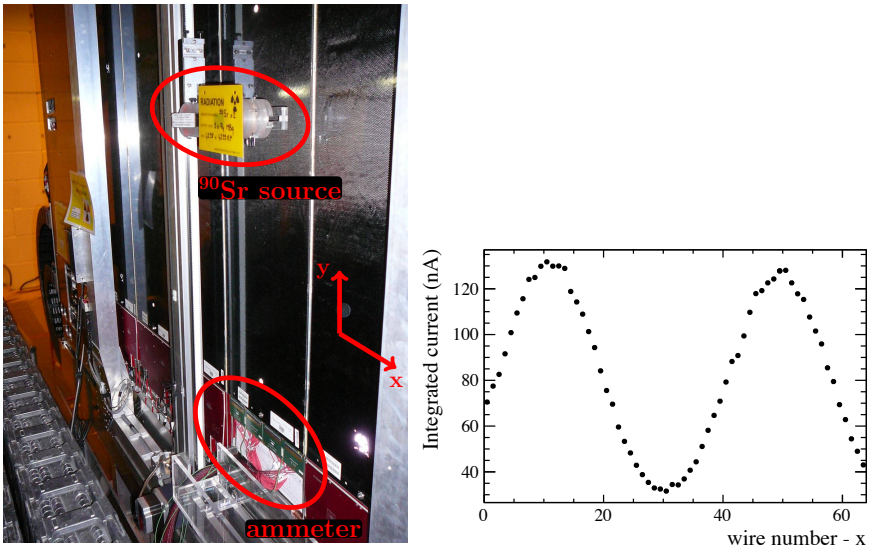

(a) (b)

Fig. 3.8 · a) Scanning tool in front of OT station T2; b) Current profile as induced by two ^{90}Sr sources with a separation of 32 wires.

3.2.2 Validation method

The isotope ^{55}Fe, is often convenient to check gaseous detectors [54]. It offers the advantage that the pulse height is directly proportional to the gas gain, independent of the material traversed by the photon. The measured current in scans using a ^{90}Sr source is affected by the intermediate material. However, the longer time required to perform a scan with a ^{55}Fe source, makes this source unsuitable for the purpose of scanning the large surface of an OT module.

Instead, ^{55}Fe was used to validate the scanning method that uses a ^{90}Sr source [39]. The measured gain variations as function of wire number, as well as along the wire, in a scan using a ^{55}Fe source, were compared to the measured current in a scan using a ^{90}Sr source. An agreement was found to a level of 1.7%.

3.2.3 Results

All modules in T2L0 have been scanned after Run I in the summer of 2013. These scans are compared to scans taken in the winter stop of 2011 between December 20th 2011 and February 1st 2012, with the exception of module M9 for which no scan was taken in winter 2011. For this module a scan from 2008 is used as a reference. The observed gain variation is uniform between $\pm$5% for all modules indicating no ageing, as shown in Fig. 3.9a for module M7A. A complete overview of the results of all modules is given in App. A.2.

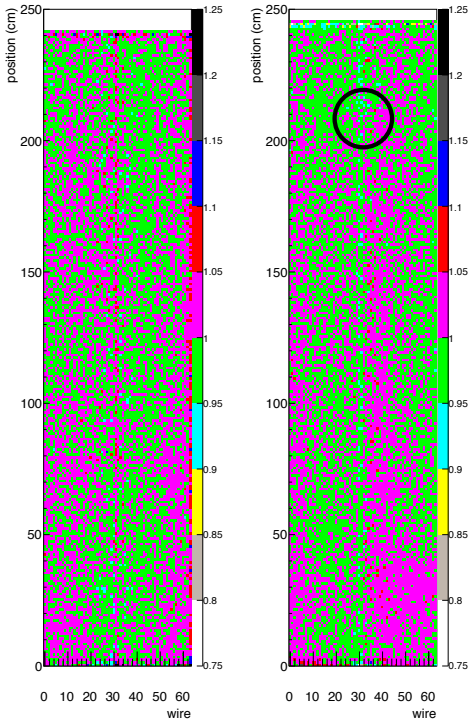

(a) **(b)**

Fig. 3.9 · ^{90}Sr scan results for a) module T2L0Q1M7A between winter 2011 and summer 2013, and for b) module T2L0Q1M1B after irradiation of 475 hours with a source at a localised spot in the middle of the module at a height of 210 cm (indicated with the black circle). The suffix A/B indicates the monolayer, with monolayer A downstream of monolayer B with respect to the LHC bunch crossing point.

3.3 Irradiation test with ^{90}Sr source

Irradiation tests performed on a selection of OT modules in the laboratory showed that the modules suffered from radiation damage already after moderate irradiation [46]. Similar controlled irradiation tests are performed in situ. A laboratory source is used in order to probe the detector's response to irradiation by the LHC. These tests can only be performed in absence of beam and need long availability of the setup to reach an accumulated dose comparable to that received during LHC operation.

3.3.1 Method

A small spot on the OT module is irradiated using a ^{90}Sr source with an activity of 40 MBq. A 6.8 mm collimator is used to focus the irradiation, resulting in an irradiated spot of $4 \times 4\,\text{cm}^2$. After irradiation, the module is scanned in a similar fashion as described in Sec. 3.2, using the setup depicted in Fig. 3.8. The scan is compared to a scan prior to the irradiation and any damage will show as a decrease of gain at the irradiated spot.

3.3.2 Results

Module T2Q1L0M1 has been irradiated for a total of 475 hours in the center of the module (wire 32) at a height $y \approx 210\,\text{cm}$. The current at the hottest region is 50 nA/cm, resulting in a maximum dose of 0.085 C/cm. It is not possible to take a ^{90}Sr scan while the source is present, because the same scanning tool (with a different ^{90}Sr source) is used for scanning and irradiating. The irradiation is therefore interrupted shortly twice to take a scan. A summary of all irradiation periods and the results of the intermediate scans can be found in App. A.3.

The scans taken before and after the total irradiation period are compared in Fig. 3.9b. The observed gain variations are uniform throughout the entire module within $\pm 5\%$. These variations are within the precision of the method, and are therefore considered not significant. No decrease in gain is observed at the irradiated spot, even after a total irradiation time of 475 hours.

3.4 Conclusion

No significant ageing of the OT has been observed after a total delivered luminosity of 3470 pb^{-1}. The amplifier threshold scans instead reveal a small increase in gain. The ^{90}Sr scans in situ also show no sign of irradiation damage upstream of the area of highest irradiation. Moreover, ageing cannot be induced by irradiation with a ^{90}Sr source, even after a total irradiation time of 475 hours, while severe ageing had been observed in the lab already after 20h of irradiation.

Further investigations are needed to understand why no ageing in situ is observed, while the ageing in the lab was significant. A possible explanation is that the large surface irradiation by the LHC leads to a preventive "cleaning": possibly the surface of the wire is microscopically altered, modifying the details of the chemical process on the wire. Also the continuous flushing of the OT modules might have helped to prevent ageing. Moreover,

the addition of O_2 to the OT counting gas allowed for the formation of O_3 in the avalanche region which had been observed to reduce ageing.

Part II

Fragmentation fractions and branching fractions

CHAPTER 4

The production of b hadrons

Measurements of branching fractions are an important ingredient in precision tests of the SM. In order to make a measurement of any B_s^0 or Λ_b^0 decay branching fraction in proton-proton collision experiments, knowledge is needed about the B_s^0 and Λ_b^0 production rate, as the product of the two determines the measured event yields. The production rate of b hadrons is usually expressed as the product of the $b\bar{b}$ production cross section, times the probability of the b quark to form that particular hadron. The probability to hadronise as B^+, B^0, B_s^0 or Λ_b^0 hadron is written as f_u, f_d, f_s and $f_{\Lambda_b^0}$, respectively. These fractions in principle do not need to be universal and can vary depending on the production process of the b quarks. Furthermore, a dependence of the ratio of fragmentation fractions on the kinematics of the decay implies that the ratio measured at LHCb cannot straightforwardly be applied at another LHC experiment where kinematic ranges differ, for example due to different selection criteria or detector geometry.

A key example is the measurement of the branching fraction of the decay $B_s^0 \to \mu^+\mu^-$. This decay is a sensitive probe to new physics, and a study of it is carried out by both the LHCb [55, 56] and the CMS [57] Collaboration. The value of f_s/f_d is a crucial input for this measurement and knowledge about the dependence of f_s/f_d on the B-meson kinematics is of great importance. As the CMS experiment operates in a different pseudorapidity range compared to LHCb, any pseudorapidity dependence of f_s/f_d needs to be taken into account in their calculations. It is challenging to determine f_s/f_d directly at CMS and therefore CMS relies on the determination of f_s/f_d by LHCb.

The hadronisation of a b quark to a b hadron, in which a primary b quark forms either a $b\bar{q}$ meson or a bqq' baryon, is governed by the strong interaction. Quantum Chromodynamics (QCD) is the theory of strong interactions that describes the interactions between quarks and gluons. As the fragmentation process takes place in the non-perturbative regime of QCD, it cannot be predicted reliably. Section 4.1 introduces a theoretical model to describe hadronisation and the concept of fragmentation functions. The relative production rates of different b-hadron species are described by experimentally measurable fragmentation fractions. Section 4.2 gives an overview of current knowledge of fragmentation fractions from measurements of the LEP experiments and the CDF experiment.

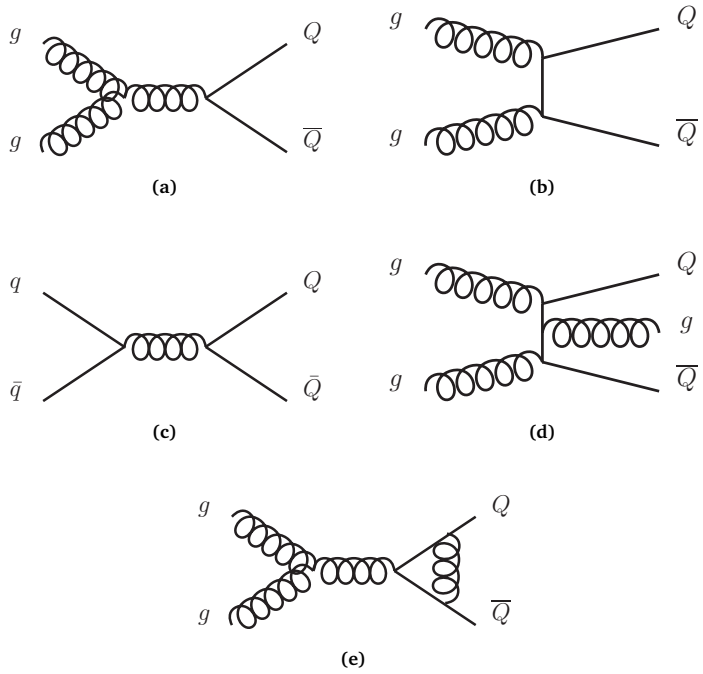

Fig. 4.1 · Leading order $b\bar{b}$ production a)-b) gluon-gluon fusion and c) quark-antiquark annihilation. Examples of higher order contributions from d) gluon bremsstrahlung corrections and e) virtual corrections.

4.1 Heavy quark production and hadronisation

Beauty quarks are predominantly strongly produced in proton-proton collisions and thus emerge in pairs. The leading order (LO) processes, proportional to the coupling constant of the strong interaction squared, α_s^2, are known as gluon-gluon fusion and are shown in Fig.4.1a–4.1b. The LO process quark–antiquark annihilation (Fig. 4.1c) is suppressed, because the gluon density is larger than the (sea-)quark density at LHC energies. Examples of diagrams contributing to the parton cross-section at higher order are shown in Fig. 4.1d for gluon bremsstrahlung corrections, where additional gluons are created alongside the $b\bar{b}$ pair, and in Fig. 4.1e for virtual corrections, where loops are added to the diagrams.

The hadronisation of a heavy quark to a heavy hadron occurs at energy scales $\sim \Lambda_{\rm QCD} \sim 1$ GeV. The coupling constant of the strong interaction, α_s, depends on the energy transfer Q^2 resulting in a large value of the strong coupling constant at these scales. Therefore, hadronisation must be described non-perturbatively. The heavy hadron cross-section can be factored in a perturbative part describing the heavy quark production, and a

non-perturbative part describing the fragmentation of a heavy quark to a heavy hadron [58]:

$$\frac{\mathrm{d}\sigma_H}{\mathrm{d}p_\mathrm{T}}(p_\mathrm{T}) = \int \frac{\mathrm{d}z}{z} \frac{\mathrm{d}\sigma_Q}{\mathrm{d}p_\mathrm{T}} \left(\frac{p_\mathrm{T}}{z}, m\right) f_{Q\to H}(z), \tag{4.1}$$

with m the mass of the heavy quark, σ the cross-section and $f_{Q\to H}(z)$ the non-perturbative fragmentation function accounting for the hadronisation of the heavy quark into the heavy hadron. The fragmentation function is a probability density function $f_{Q\to H}(z)$ which must be normalised: $\int_0^1 f(z)\mathrm{d}z = 1$. It depends on the energy fraction z of the produced hadron with respect to the total available energy[1].

At high energy colliders the produced heavy quarks will be far off-shell. Therefore, the hadronisation of a $b\bar{b}$-quark pair must be viewed as a two-stage process. In the first stage, b quarks radiate hard gluons at scales of $Q^2 \gg \Lambda^2_\mathrm{QCD}$, reducing the heavy quark momentum. The heavy quark cross section can now be factored in a cross section for producing a light parton, σ_i, and a fragmentation function $f_{i\to Q}$ describing the transition of a light parton to a heavy quark [59],

$$\frac{\mathrm{d}\sigma_Q}{\mathrm{d}p_\mathrm{T}}(p_\mathrm{T}, m) = \sum_i \int \frac{\mathrm{d}z}{z} \frac{\mathrm{d}\sigma_i}{\mathrm{d}p_\mathrm{T}} \left(\frac{p_\mathrm{T}}{z}; \mu\right) f_{i\to Q}(z; \mu, m) + \mathcal{O}\left(\frac{m}{p_\mathrm{T}}\right). \tag{4.2}$$

In this description, both the light parton cross-section and the fragmentation $f_{i\to Q}$ can be calculated in perturbative QCD. Note that the two stadia described by σ_i and $f_{i\to Q}$ are not physical themselves and are separated at an artificial factorisation scale μ. DGLAP functions [60–62] are used to evolve σ_i and $f_{i\to Q}$ from the initial scale of the order of m up to the large scale of the order p_T of the produced heavy quark. The heavy quark cross-section determined with Eq. 4.2 can now be used in Eq. 4.1 to determine the heavy hadron cross-section. Different forms of the fragmentation functions are discussed in the next pages.

4.1.1 The Lund model and fragmentation functions

In event generators, the first stage of hadronisation is performed using QCD matrix elements or leading-log parton shower models, and several combinations of these methods have been proposed [63].

Several models are available that describe the second stage of hadron formation, of which the cluster model [64] and the Lund string model [65] are the most commonly used. As the latter is used by the PYTHIA event generator [66, 67], which is used for simulated event generation by the LHCb Collaboration, a short description of this model will be provided below.

The formation of a meson can be described by the Lund string model [65] as follows. When a $b\bar{b}$ pair is created in a hard scattering process in a high energy collision (Fig. 4.1), the two quarks will move apart. Due to colour confinement quarks cannot exist individually. As the two quarks move further away from each other, a confining field emerges between the two colour charges. A potential energy $V(r) = \kappa\, r$ is reached for large distances r.

[1] Instead of $z = \frac{E_H}{E_Q}$ other definitions of z can be used: $z = \frac{p_H}{p_Q}$ or $z = \frac{p_H + E_H}{p_Q + E_Q}$.

This potential describes a string with tension constant $\kappa \sim 1$ GeV/fm [68], meaning that a 5 GeV quark can travel 5 fm before its kinetic energy is transformed into potential energy in the string. When the potential energy is large enough a new quark pair ($q\bar{q}$) will be created from the vacuum. The heavier the quark, the more energy is required to produce it. The production of heavy particles is therefore suppressed and estimated to occur according to the ratio: $u : d : s : c \approx 1 : 1 : 1/3 : 10^{-11}$. Note that no new $b\bar{b}$ pairs are created during this phase, due to the large mass of the b quark. The produced quark $\bar{q}$ can now combine with the original b quark to form a meson, with an energy fraction z of the total available energy. The meson moves apart from the remaining quark q. The remaining quark q now takes over the role of the original b quark and a confining field builds up between this quark and the meson, and the process repeats itself. This process is called fragmentation and is illustrated in Fig. 4.2a.

Baryon production is a more complex process than the production of mesons. Within the Lund string model, a similar mechanism is proposed for the formation of baryons, by allowing strings to break by the production of pairs of diquarks [69, 70]. These are loosely bound states of two quarks, qq or $\bar{q}\bar{q}$, in a colour anti-triplet state[1]. In this model, the resulting baryon and antibaryon in the pair are always nearest neighbour in rank in pseudorapidity. However, data on transverse momentum correlations [72] do not agree with expectations from this conceptually simple model, but indicate that occasionally one or more mesons may be produced in between the baryon and the antibaryon along the string. The so-called popcorn model [73], illustrated in Fig. 4.2b, offers an alternative approach based on the premiss that quantum colour fluctuations can exist in the colour field. Suppose the colour field of the two quarks from the hard scattering is red-antired ($r\bar{r}$), then small regions can occur where the colour field is locally blue–antiblue ($b\bar{b}$) or green-antigreen ($g\bar{g}$). The string-break can now occur in the $r\bar{r}$ part of the colour field, but also in one of the "wrong" parts of the colour field, $b\bar{b}$ or $g\bar{g}$. If in the latter case a $q_2\bar{q}_2$ pair with colour $g\bar{g}$ is created between a $q_1\bar{q}_1$ pair with colour $b\bar{b}$, then q_2 will be dragged towards rb and $\bar{q}_2$ towards $\bar{r}\bar{b}$, forming a colour-neutral baryon and antibaryon. Hence, in this model two $q\bar{q}$ pairs need to be "popped" out the energy field. The density and size of the fluctuations will determine the properties of the baryon production process. If fluctuations are larger, one or more mesons can be produced in between the baryon antibaryon pair.

The energy fraction z of a produced hadron with respect to the total available energy is described by a fragmentation function. This is the probability density function $f_{Q\to H}(z)$, introduced earlier. Different parametrisations are available for the non-perturbative fragmentation functions, a selection of which is highlighted below and shown in Fig. 4.3b.

- **Symmetric Lund function:** Since string-breaks are causally disconnected, they do not have to be considered in a specific time-ordered sequence. As a result the fragmentation process must look the same, irrespective of whether the fragmentation process

[1] Two quark or two antiquark combination, which is anti-symmetric under interchange of the two quarks: $1/\sqrt{2}(rg - gr)$, $1/\sqrt{2}(bg - gb)$ or $1/\sqrt{2}(br - rb)$ [71].

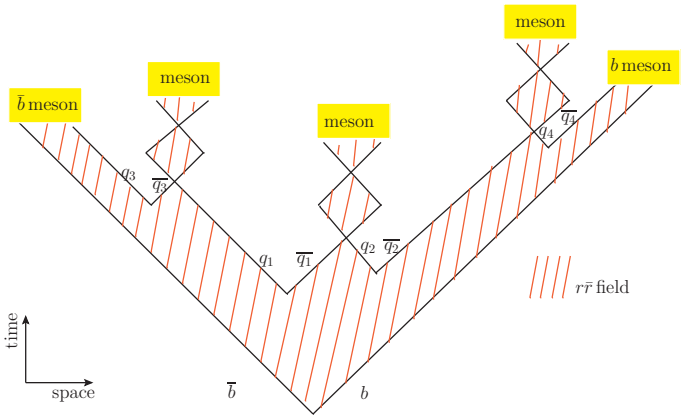

(a)

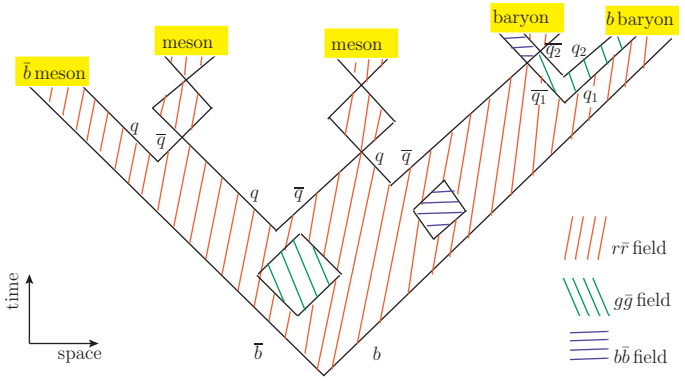

(b)

Fig. 4.2 · Graphical representation of hadron production in the Lund string model. Colour strings between quark and antiquark build up the colour field. The potential energy of the field increases when quarks move apart, until the string breaks through the creation of $q\bar{q}$ pairs. a) Meson production in the $r\bar{r}$ colour field. Figure based on [65]. b) Baryon production in the popcorn model. Figure based on [73].

is viewed from the quark (Q) or the antiquark ($\bar{Q}$), imposing a left-right symmetry along the string. This can be achieved by the fragmentation function [65][1]

$$f_{Q\to H}(z) \sim \frac{1}{z}(1-z)^{a}\mathrm{e}^{-\frac{b\times m_T^2}{z}}, \tag{4.3}$$

where the parameter a depends on the flavour of the initial quark, the parameter b is universal and m_T is the transverse mass of the hadron. Note that the explicit mass dependence in $f_{Q\to H}(z)$ implies a harder spectrum for heavy hadrons. The Bowler modification [74], $f_{Q\to H}(z) \to f_{Q\to H}(z)/z^{b\times m_T^2}$, is introduced for heavy hadrons. It softens the b-hadron spectrum.

- **Peterson function:** The main premiss is that a light quark $\bar{q}$ decelerates the heavy quark Q only slightly in the fragmentation process. The resulting hadron thus carries almost the same energy as the heavy quark. The assumption is that the amplitude of fragmentation is proportional to $1/\Delta E$, with the energy transfer $\Delta E = E_H + E_q - E_Q$, from which the following fragmentation function can be derived [75]:

$$f_{Q\to H}(z) \sim \frac{1}{z\left(1-\frac{1}{z}-\frac{\epsilon_Q}{(1-z)}\right)^2}. \tag{4.4}$$

The parameter ϵ_Q is expected to have a value approximately equal to m_q^2/m_Q^2. The advantage of this functional form of the fragmentation function is that it has only one free parameter that needs to be determined experimentally.

- **Kartevelishvili-Likhoded-Petrov function:** This function was originally designed to describe charm hadron production, but can also be applied to bottom hadron production. The fragmentation function is based on the charm quark distribution function in charmed mesons, and makes use of the Gribov-Lipatov reciprocity relation [61, 76, 77] which connects the wave function of the partons with the wave function of the hadron. The fragmentation function has the form [78]

$$f_{Q\to H}(z) \sim z^{\alpha}(1-z)^{\beta} \tag{4.5}$$

where the parameters α and β depend on the type of hadron.

- **Collins-Spiller:** The fragmentation function is derived from the cross-section $\sigma(e^+e^- \to MX)$, where M denotes a heavy meson (Qq) and X the remaining final state. The mass of the light quark is assumed to be negligible. Furthermore, for heavy mesons, $m_H \approx m_Q \gg k_T$, where k_T is the momentum of the meson transverse to the direction of motion of the heavy quark. The fragmentation function has the form [79]

$$f_{Q\to H}(z) \sim \left(\frac{1-z}{z}+\frac{2-z}{1-z}\epsilon_Q\right)\left(1+z^2\right)\left(1-\frac{1}{z}-\frac{\epsilon_Q}{1-z}\right)^{-2}, \tag{4.6}$$

[1] This function is the most general symmetric form. All other functions listed below do not fulfil the left-right symmetry requirement. They can be used to calculate the energy of the leading hadron, and are therefore sufficient for the purpose in this work, but they cannot be used to generate the complete event.

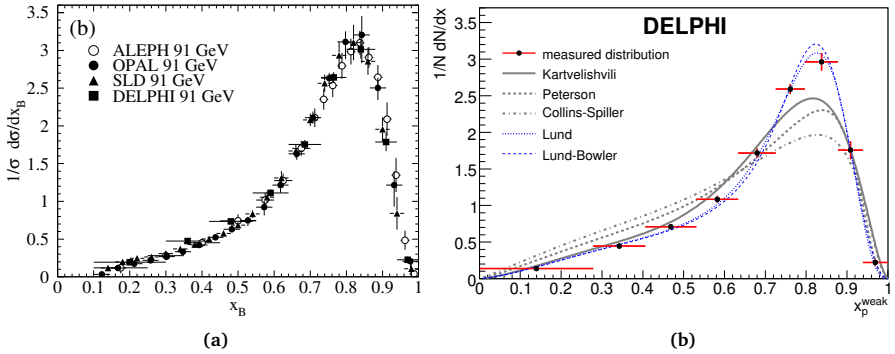

(a) (b)

Fig. 4.3 · a) Fragmentation functions for b quark to b hadron fragmentation, measured in e^+e^- collisions at $\sqrt{s} = 91\,\mathrm{GeV}$. Overview from [84]. b) Comparison of different parametrisations of the non-perturbative fragmentation function with data from the DELHPI detector [83]. The quantity x_B or $x_\mathrm{p}^\mathrm{weak}$ is the fraction of three momentum that is taken by the weakly decaying B hadron, and is closely related to z. The axes labels $1/\sigma\ d\sigma/dx_B$ and $1/N\ dN/dx$ yield the normalised fragmentation functions.

4

where $\epsilon_Q = \langle k_T^2 \rangle / m_Q^2$. In addition, a fragmentation function that takes into account excited mesons, $Q \to M^* \to M$, was proposed. The Collins-Spiller fragmentation function does not exhibit a sharp maximum, which is mainly due to the matching of the fragmentation function to the heavy meson structure function at $z = 1$ resulting in dependence $f_{Q\to H}(z) \sim (1 - z)$ for z close to 1.

Heavy flavour production in electron-positron collisions is the primary source of information on fragmentation effects in heavy-flavour production in hadron-hadron collisions. Figure 4.3a shows the fragmentation function of b quarks into a b hadron measured at $\sqrt{s} = 91\,\mathrm{GeV}$, by the ALEPH [80], OPAL [81], SLD [82] and DELPHI [83] Collaborations. The different parametrisations of the non-perturbative part of the fragmentation function have been compared to the b-quark fragmentation functions measured by these collaborations, an example of which is shown in Fig. 4.3b for the data from the DELPHI Collaboration [83]. The Lund and the Lund-Bowler models are seen to give the best description of the data.

Note that the fragmentation functions $f_{Q\to H}(z)$ can differ for the fragmentation to the different types of hadrons, through their dependence on the mass of the light quark or the hadron. For example, the larger mass of the strange quark with respect to the u and the d quark can affect the fragmentation. In addition, the parameters entering the different fragmentation functions can differ for different types of hadrons, and their values need to be determined from experimental data. The production of baryons involves either an additional diquark pair or two additional quark pairs rather than one quark pair, and might result in yet different dynamics. A theoretical prediction of the p_T dependence of

fragmentation fractions can be obtained by a convolution of the fragmentation function with the $b\bar{b}$ cross-section. This is illustrated in Sec. 9.1.1, where a theoretical description of the $p_{\rm T}$ dependence of f_s/f_d is presented based on the measurement presented in chapter 6. The absolute values of the fragmentation fractions, however, are difficult to obtain from theory as the normalisation of the heavy hadron fragmentation functions cannot easily be calculated. The fragmentation fractions therefore need to be measured in particle collider experiments.

4.2 Experimental knowledge of fragmentation fractions

A b quark hadronises to a B^+, B^0, B_s^0 meson or a b baryon, with the fractions f_u, f_d, f_s, $f_{\rm baryon}$ respectively. The sum of all the fragmentation fractions must be equal to unity, $f_u + f_d + f_s + f_{\rm baryon} = 1$. The production of weakly decaying states consisting of two heavy quarks is very small and is neglected here. Equal production of B^+ and B^0 mesons is assumed, $f_u = f_d$, as the mass difference between the u and the d quark is negligible. The relative amount of B^+ and B^0 mesons is not affected by the electromagnetic decays of excited B^{+*} and B^{0*} mesons, or by the strong decays of B^{+**} and B^{0**} mesons. The production fraction of b baryons can be subdivided as $f_{\rm baryon} = f_{\Lambda_b^0} + f_{\Xi_b^0} + f_{\Xi_b^-} + f_{\Omega_b^-}$. Other b baryons are included through their strong and electromagnetic decay to one of these four baryons.

The fragmentation fractions have been measured by LEP using $Z \to b\bar{b}$ decays from Z production in e^+e^- collisions. The b quarks produced have a $p_{\rm T}$ of approximately 45 GeV/c. The total b-baryon production is estimated from the number of protons found in b-hadron decays [85]. Using partially reconstructed final states including a lepton, the products of the fragmentation fraction and a specific branching fraction are measured, $f_{\Lambda_b^0} \times \mathcal{B}(\Lambda_b^0 \to \Lambda_c^+ l^- \bar{\nu}_l X)$ [86, 87], $f_{\Sigma_b^-} \times \mathcal{B}(\Sigma_b^- \to \Sigma^- l^- \bar{\nu}_l X)$ [88, 89] and $f_s \times \mathcal{B}(B_s^0 \to D_s^+ l^- \bar{\nu}_l X)$ [90–92]. In addition a measurement of f_u is performed by estimating the charge of the weakly decaying b hadrons, after subtraction of the charged b-baryon component [93].

Measurements of the b-hadron fragmentation fraction ratios $f_s/(f_u + f_d)$, $f_{\Lambda_b^0}/(f_u + f_d)$ and f_u/f_d have been performed by CDF [94–96], using semileptonic b-hadron decays from $b\bar{b}$ pairs created in $p\bar{p}$ collisions. The b quarks produced this way have an average $p_{\rm T}$ of approximately 15 GeV/c. In addition, LHCb measured the ratio f_s/f_d using partially reconstructed semileptonic decays [97]. A combined fit to all those measurements, resulted in the following world average values of the fragmentation fractions: $f_u = f_d = 0.401 \pm 0.007$, $f_s = 0.107 \pm 0.005$, $f_{\rm baryon} = 0.091 \pm 0.015$ [98]. An earlier measurement by LHCb using hadronic decays [99] is not included in this average.

The fragmentation fractions can in principle vary as a function of the $p_{\rm T}$ of the produced b hadron and depend on the production process. However, the measurement by LHCb using semileptonic B decays, shown in Fig. 4.4, does not confirm a dependence of $f_s/(f_u + f_d)$ on the $p_{\rm T}$ of the charm + lepton final state [97]. On the other hand, both CDF and LHCb observe a $p_{\rm T}$ dependence of $f_{\Lambda_b^0}/(f_u + f_d)$ [96, 97]. Figure 4.5 shows that this quantity decreases with increasing transverse momentum. The dependence can also explain the much lower value of this quantity computed from the LEP measurements [98]. A $p_{\rm T}$

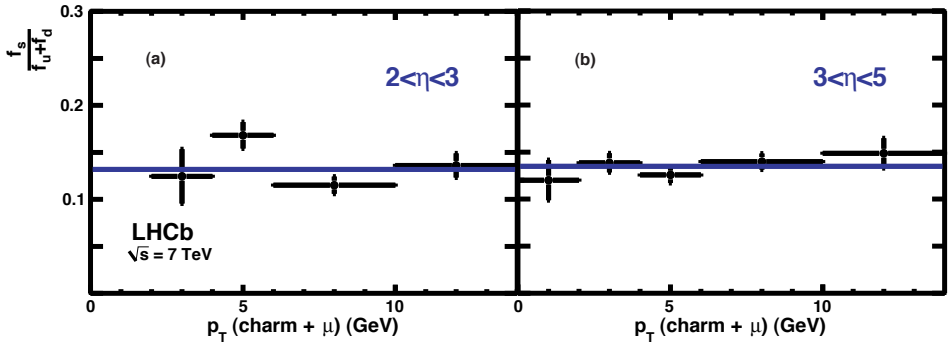

Fig. 4.4 · Ratio of fragmentation fractions $f_s/(f_u + f_d)$ measured using semileptonic decays by LHCb. No dependence on the transverse momentum or pseudorapidity is observed. Figure from [97].

dependence of the ratio $f_{\Lambda_b^0}/f_d$ further motivates the study of other ratios of fragmentation fractions.

Due to its mass resolution, vertex resolution and particle identification, the LHCb detector is particularly well-suited to measure the relative production rates of B^+, B^0, B_s^0 and Λ_b^0 hadrons. This measurement is of value to all LHC experiments. Two different methods have been exploited, semileptonic and fully hadronic, which both rely on the theoretical knowledge of the ratio of branching ratios. The semileptonic measurement uses the assumption that the total semileptonic decay width is equal for all b hadrons, as explained in Sec. 5.1.4. Based on the theoretical understanding of factorisation and $SU(3)$ symmetry, a relation between the hadronic branching fractions of B^0 and B_s^0 decays is introduced in Sec. 5.1.3.

The following two sections present measurements of f_s/f_d and $f_{\Lambda_b^0}/f_d$ and a study of their dependence on the transverse momentum or the pseudorapidity of the b hadron.

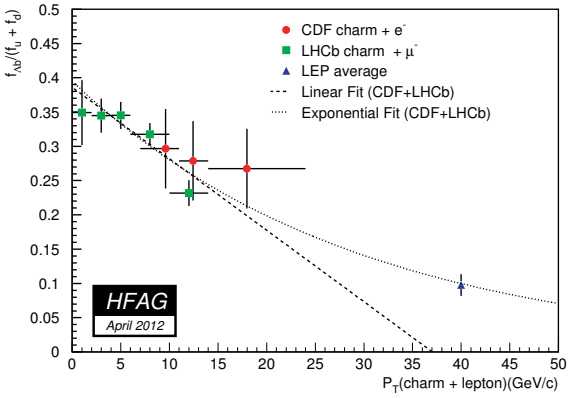

Fig. 4.5 · Ratio of fragmentation fractions $f_{\Lambda_b^0}/(f_u + f_d)$. Measurements of LHCb (green squares), CDF (red circles) and LEP (blue triangle) are included. An overall uncertainty on the scale of 26% due the the $\Lambda_b^0 \to \Lambda_c^+ \pi^-$ branching fraction is not included in this figure. The dashed and dotted lines show a fit to the data (excluding the LEP datapoint) with a linear and exponential function respectively. Figure from [98].

CHAPTER 5

The decay of b hadrons

Charmed two-body B decays, $B \to Dh$, provide a wealth of information and are widely studied at LHCb. Here, the B represents either a charged or a neutral B meson, the D a charged $D_{(s)}$ or a neutral D meson, and the symbol h is used to denote either a pion or a kaon.

The decay time structure of the flavour specific decays $\overline{B}{}^0_s \to D_s^+\pi^-$ and $\overline{B}{}^0 \to D^+\pi^-$ measures the $B^0_{(s)}$–$\overline{B}{}^0_{(s)}$ mixing frequency and thus provides information on the parameters Δm_s and Δm_d, respectively, that describe the mass difference between the mass eigenstates in the $B^0_{(s)} - \overline{B}{}^0_{(s)}$ system [36, 100]. A measurement of $\Delta m_{s,d}$ is essential for all studies of time-dependent CP asymmetries, such as the phase of the $B^0_{(s)}$ mixing diagram ($\phi_{s,d}$). The flavour changing weak interactions are characterised by the CKM matrix. From the unitarity of the theory it follows that there are several relations between the CKM matrix elements. Six of these relations can be represented as triangles in the complex plane. The triangle corresponding to the unitarity relation between the first and the third column of the CKM matrix is referred to as the CKM unitarity triangle. An important objective of the LHCb experiment is to perform precision measurements of the size and angles of this triangle, which describes CP violation within the SM. The ratio $\Delta m_s/\Delta m_d$ is proportional to the CKM elements V_{ts}/V_{td} which enter in the $B^0_{(s)}$–$\overline{B}{}^0_{(s)}$ mixing diagram. A measurement of $\Delta m_s/\Delta m_d$ therefore puts an additional constraint on the apex of the CKM unitarity triangle. Together with other measurements, it provides a test of the SM.

Many efforts have been made to precisely measure the CKM unitarity triangle. The CKM angle γ, however, remains poorly determined [101]. The charmed two-body decay $\overline{B}{}^0_s \to D_s^\pm K^\mp$ is sensitive to this angle through the interference between mixing and decay amplitude. Its value can be obtained from a study of the flavour-tagged decay time distribution of the B^0_s meson [102, 103]. In addition, charged B decays, e.g. $B^\pm \to D^0 h^\pm$, provide an opportunity to measure γ, using asymmetries in the decay time integrated amplitudes [104]. Both neutral $\overline{B}{}^0_s \to D_s^\pm K^\mp$ and charged $B^\pm \to D^0 h^\pm$ decays allow for a determination of the angle γ using colour-allowed tree diagrams. These decays are usually considered robust against new physics, although recently renewed interest appeared in new

physics effects at tree level [105]. A comparison with a determination of γ based on loop diagrams allows to search for different realisations of physics beyond the SM.

The production asymmetry between $B^0_{(s)}$ and $\overline{B}^0_{(s)}$ mesons is an essential ingredient in measurements of time integrated CP violation in B-meson decays, where CP asymmetries must be disentangled from other sources of asymmetry. The production rates of B and $\overline{B}$ mesons in pp collisions are not expected to be identical within the LHCb acceptance, because the colliding protons contain valence quarks and no valence antiquarks. Therefore the production rates of B and $\overline{B}$ mesons need to be measured from data. The production asymmetry is measured using the decay time structure of $\overline{B}^0_s \to D^+_s\pi^-$ and $\overline{B}^0 \to D^+\pi^-$ decays, by fitting an offset in the $B^0_{(s)}-\overline{B}^0_{(s)}$ asymmetry [106].

Other measurements using $B \to Dh$ decays include the measurement of the B-meson lifetimes. For example the measurement of the effective lifetime [107] of B^0_s mesons using the flavour specific decay $\overline{B}^0_s \to D^+_s\pi^-$ [108]. Because the flavour specific final state $D_s\pi$ is not a CP eigenstate, the decay time distribution is a mix of two exponentials corresponding to the different lifetimes of the heavy and light mass eigenstates. A measurement where $\Delta\Gamma$ is neglected and where the decay time distribution is fitted with a single exponential results in an effective lifetime [109].

Branching fraction measurements are usually obtained relative to a decay for which the branching fraction is known; such a measurement does not require knowledge of the production of B mesons. For example, the measurement of $\mathcal{B}(\overline{B}^0_s \to D^\pm_s K^\mp)$ uses $\overline{B}^0_s \to D^+_s\pi^-$ decays as a normalisation channel [110]. When a B^0 decay is used as a normalisation channel of a B^0_s decay [56], knowledge of the relative production of B^0_s and B^0 mesons is required.

The branching fraction of colour-allowed tree decays of the type $B \to Dh$ is theoretically well understood. The decays $B \to Dh$ can therefore be exploited to measure the relative b hadron production rates. Section 5.1 introduces the theoretical framework needed to calculate $\mathcal{B}(B \to Dh)$, and provides a relation between the b-hadron branching fraction to the b-hadron production fraction. In this thesis, the hadronic decays $\overline{B}^0 \to D^+K^-$, $\overline{B}^0 \to D^+\pi^-$ and $\overline{B}^0_s \to D^+_s\pi^-$ are used to probe the production fractions of different B mesons. In addition, the analogue b-baryon decay $\Lambda^0_b \to \Lambda^+_c\pi^-$ is used to study the production of Λ^0_b baryons. Section 5.2 introduces the experimental challenges involved in the measurement of $B \to Dh$ and $\Lambda_b \to \Lambda_c\pi$ decays.

5.1 The branching fraction of charmed two-body B decays

The b and c quarks are considered heavy quarks, for which effective techniques are available to perform numerical calculations. A combination of the b or c quark with a light quark q results in a heavy meson. The decay $B \to Dh$ is labelled as "heavy-light" because it has one heavy and one light meson in the final state. The colour-allowed tree topologies of these decays are expected to factorise to a certain approximation.

5.1.1 Decay topologies

The available Feynman topologies which mediate the decay of a B meson to a heavy-light final state are listed below and shown in Fig. 5.1.

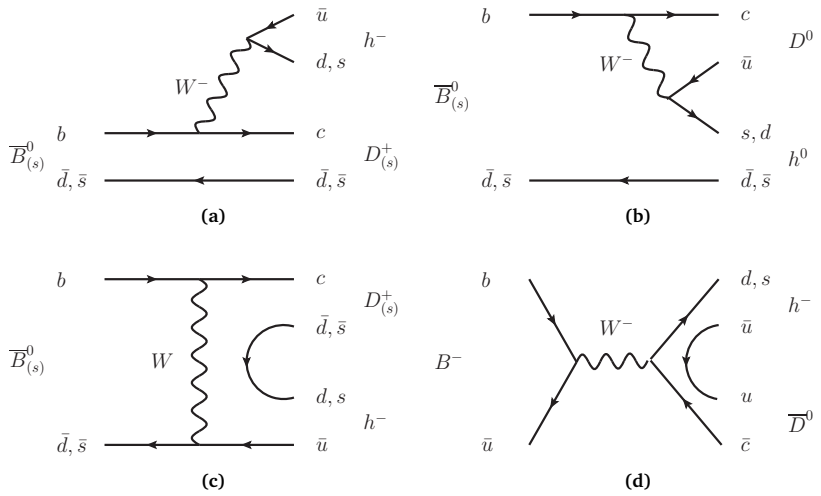

Fig. 5.1 · Decay topologies accessible to the $B \to Dh$ decays: a) colour-allowed tree (T); b) colour-suppressed tree (C); c) Exchange (E); d) Annihilation (A).

- The **Colour-allowed Tree (T)** topology is characterised by a $b \to c\bar{u}q$ transition, with $q \in \{d, s\}$. The $\bar{u}q$ pair originating from the W boson forms the light meson while the heavy meson is formed by a combination of the c quark with the spectator quark.

- The **Colour-suppressed Tree (C)** topology is also characterised by a $b \to c\bar{u}q$ transition, with $q \in \{d, s\}$. However, in this case, the $\bar{u}q$ quarks originating from the W boson hadronise in different mesons. The light meson is formed upon combination of the q quark with the spectator quark, while the heavy meson is formed upon combination of the $\bar{u}$ quark with the c quark.

- The **Exchange (E)** topology is characterised by the exchange of a W boson between the b and $\bar{q}$ quarks forming the B^0_q meson, with $q \in \{d, s\}$. This mediates the transitions $b \to c$ and $\bar{q} \to \bar{u}$. The c and $\bar{u}$ quarks are then combined with a $\bar{q}'q'$ pair from the vacuum to form two mesons. The contribution of these diagrams is usually expected to be small.

- The **Annihilation (A)** topology is only accessible to charged B mesons. The b and $\bar{u}$ quarks forming the B^- meson annihilate to a W boson, from which a $q\bar{c}$ pair ($q \in \{d, s\}$) is created. A $u\bar{u}$ quark pair from the vacuum completes the hadronisation.

The role of the c and u quark can be interchanged in the T and C topologies, i.e. a $b \to u\bar{c}q$ transition with the $\bar{c}q$ pair originating from the W boson. These topologies are often suppressed due to the CKM matrix elements involved in these decays. In the decay $\overline{B}^0_s \to D^\pm_s K^\mp$, however, the contributions of the $b \to c\bar{u}s$ and $b \to u\bar{c}s$ transitions are of

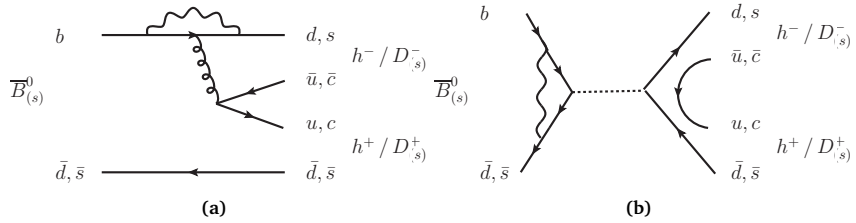

Fig. 5.2 · Decay topologies accessible to B decays to a light-light and heavy-heavy final state: a) penguin (P); b) penguin-annihilation (PA). The dotted line denotes a colour-singlet state.

equal size. Penguin diagrams do not mediate such heavy-light decays. Instead, the final state of a penguin diagram is of the type light-light or heavy-heavy. Two penguin topologies are distinguished. They are listed below for completeness, and shown in Fig. 5.2.

- The **Penguin (P)** topology is characterised by a Flavour Changing Neutral Current interaction $b \to q$ (with $q \in \{d, s\}$) mediated by a W-boson loop. The q quark is combined with a $\bar{q}'$ quark from a $\bar{q}'q'$ pair ($q' \in \{u, c\}$) to form a meson. The q' quark combines with the spectator quark to form the second meson. The flavour of the $\bar{q}'q'$ pair determines whether the light-light or heavy-heavy final state is formed.

- The **Penguin-Annihilation (PA)** topology is only accessible to neutral B meson decays. The b and $\bar{q}$ quark forming the B^0_q meson exchange a W boson to form a $q'\bar{q}'$ pair, which annihilates into a colour singlet state. From the colour singlet state a new $q'\bar{q}'$ pair is created, with $q' \in \{d, s\}$. A second quark pair $q''\bar{q}''$ with $q'' \in \{u, c\}$ completes the hadronisation. The quark pair $q''\bar{q}''$ determines whether the final state is of the type light-light or heavy-heavy. In contrast to the penguin topology, the two final state mesons must be CP conjugates of each other.

5.1.2 The branching fraction of $B \to Dh$ colour-allowed tree decays

The decays $B \to Dh$ offer an opportunity to measure the production fractions of different types of b hadrons at pp-collider experiments [111]. Penguin topologies do not contribute to these decays which makes them robust with respect to new physics. Moreover, factorisation (see below) has been shown to work well for colour-allowed tree decays. Their branching fraction can therefore be theoretically calculated in a solid way. The branching fraction is related to the decay amplitude,

$$\mathcal{B}(B \to Dh) = \Phi\, \tau_B\, |A(B \to Dh)|^2\,, \tag{5.1}$$

with Φ a phase space factor and τ_B the lifetime of the B meson. The calculation of the decay amplitude A, however, is a tedious task as QCD effects play an important role in hadronic B decays.

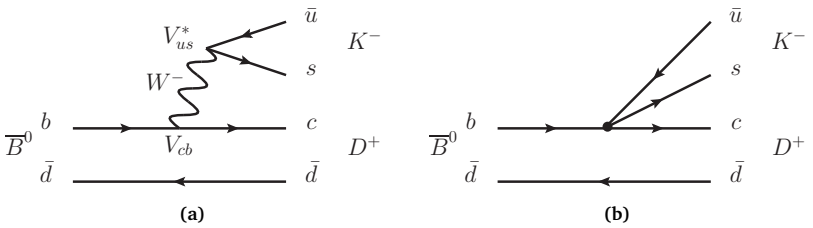

Fig. 5.3 · Feynman diagram describing the decay $\overline{B}^0 \to D^+K^-$ in the a) full theory and b) in the effective theory.

5.1.2.1 4-Fermi effective theory

The colour-allowed tree decay $\overline{B}^0 \to D^+K^-$ will be used as an example, but the formalism applies to all colour-allowed tree decays. Evaluation of the Feynman diagram corresponding to the $\overline{B}^0 \to D^+K^-$ tree decay yields the transition amplitude:

$$T_{fi} = -\frac{g_2^2}{8} V_{us}^* V_{cb} [\bar{s}\gamma^\nu (1-\gamma_5) u] \left[\frac{g_{\mu\nu}}{k^2 - m_W^2}\right] [\bar{c}\gamma^\mu (1-\gamma_5) b] \,, \tag{5.2}$$

with g_2 the weak coupling constant and V_{ij} the appropriate CKM matrix element. The flavour changing processes discussed in this thesis occur at low energies, namely at $E \sim m_B$. Therefore, the W bosons mediating the weak decay must be highly virtual, as $k^2 \approx E^2 << m_W^2$. The weak transition effectively appears as a four-fermion interaction to leading order, as described in the original theory of the Fermi interaction [112]. With the discovery of the W boson in 1983 [4, 5], it was understood that this particle mediates the weak interaction. The heavy mass of the W boson compared to the energy scale is responsible for the "weakness" of the weak interaction, and allows one to "integrate out the W boson":

$$\frac{g_2^2}{8} \frac{1}{k^2 - m_W^2} \quad \longrightarrow \quad \frac{G_F}{\sqrt{2}} \,. \tag{5.3}$$

The effective $\overline{B}^0 \to D^+K^-$ decay is shown in Fig. 5.3b.

In the effective theory, the decay amplitude is obtained from an effective Hamiltonian following

$$A(\overline{B}^0 \to D^+K^-) = \langle DK | H_{\text{eff}} | B \rangle \,. \tag{5.4}$$

5.1.2.2 Operator product expansion

The operator product expansion (OPE) [101, 113, 114] is a general framework that allows the factorisation of perturbative physics from non-perturbative physics. It is particularly useful to describe QCD corrections (Fig. 5.4), which potentially play an important role in hadronic decays. In addition, it provides a framework to include contributions from heavy degrees of freedom.

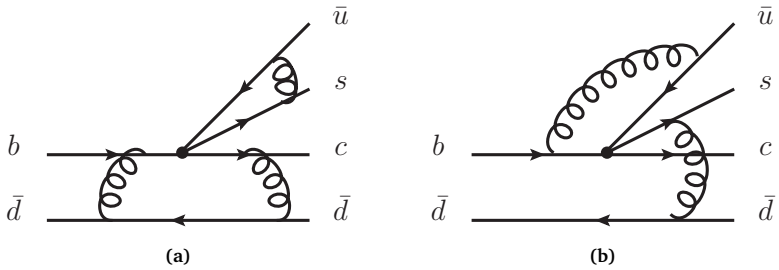

Fig. 5.4 · a) Factorisable and b) non-factorisable QCD corrections contributing to the decay amplitude of the decay $\overline{B}^0 \to D^+K^-$.

The low energy effective Hamiltonian takes the following form

$$H_{\text{eff}} = \frac{G_F}{\sqrt{2}} V_{us}^* V_{cb} \sum_{i=1,2} C_i(\mu)\mathcal{O}_i(\mu)\,, \tag{5.5}$$

with the current−current operators defined as

$$\begin{aligned} \mathcal{O}_1 &= [\bar{s}_\alpha \gamma_\mu (1-\gamma_5) u_\beta] \otimes [\bar{c}_\beta \gamma^\mu (1-\gamma_5) b_\alpha]\,, \\ \mathcal{O}_2 &= [\bar{s}_\alpha \gamma_\mu (1-\gamma_5) u_\alpha] \otimes [\bar{c}_\beta \gamma^\mu (1-\gamma_5) b_\beta]\,. \end{aligned} \tag{5.6}$$

Using the effective theory, the decay amplitude takes the form

$$\langle DK|H_{\text{eff}}|B\rangle = \frac{G_F}{\sqrt{2}} V_{us}^* V_{cb} \sum_{i=1,2} C_i(\mu)\, \langle DK|\mathcal{O}_i(\mu)|B\rangle\ . \tag{5.7}$$

The couplings C_i are the perturbative Wilson coefficients which describe the short-distance physics. The matrix elements of the current−current operators, $\langle DK|\mathcal{O}_i|B\rangle$, describe the long-distance physics and cannot be calculated perturbatively.

A description of the more complex decay amplitudes of QCD penguin and EW penguin diagrams is also possible with OPE, but requires 8 additional operators. The short-distance contributions of the heavy top quark and possible new physics particles in loops are included in the corresponding Wilson coefficients. The penguin topology is not accessible to the $B \to Dh$ decays studied in this thesis, due to the flavour content of the final state. Therefore, a description of the decay amplitude using only the current−current operators $\mathcal{O}_{1,2}$ is sufficient for these decays.

5.1.2.3 Factorisation

In the effective description of the decay $\overline{B}^0 \to D^+K^-$, the b quark decays in a four-fermion point interaction to three quarks. The two light quarks, $u\bar{s}$, move away rapidly due to the kinetic energy that is available. The third quark, c, is heavier and therefore moves less rapidly, which allows it to meet up with the spectator quark. The hadronisation of the

$u\bar{s}$ pair to a kaon is thus well separated from the hadronisation of the $d\bar{c}$ pair to the D meson. It is therefore assumed that the two hadronisations occur independently, without any long-distance gluon interaction. This is referred to as "naive" factorisation [115, 116].

In the factorisation approach, the hadronic matrix element of the four-quark operators are written as the product of two hadronic matrix elements of quark currents,

$$\langle KD|H_{\text{eff}}|B\rangle\,|_{\text{fact}} = \frac{G_F}{\sqrt{2}} V_{us}^* V_{cb}\, a_1\, \langle K|\bar{s}_\alpha \gamma_\mu (1-\gamma_5) u_\alpha|0\rangle\, \langle D|\bar{c}_\beta \gamma^\mu (1-\gamma_5) b_\beta|B\rangle\ , \quad (5.8)$$

with $a_1 = C_2 + C_1/N_C$, where $N_C = 3$ is the number of $SU(N_C)$ quark colours. Calculations of the Wilson coefficients C_1 and C_2, taking into account contributions from hard gluon corrections as shown in Fig. 5.4, result in $a_1 \sim 1$ [117–120]. This means that non-factorisable perturbative QCD corrections play a small role in this decay. Soft gluon corrections, which cannot be calculated perturbatively, are of the order Λ_{QCD}/m_b [114] and therefore small.

The hadronic matrix elements are expressed in terms of the kaon decay constant, f_K, and the $B \to D$ form factors, $F_{0,1}^{(BD)}$ [114, 121]:

$$\begin{aligned} \langle K(q)|\bar{s}_\alpha \gamma_\mu (1-\gamma_5) u_\alpha|0\rangle &= i f_K q_\mu\ , \\ \langle D(k)|\bar{c}_\beta \gamma^\mu (1-\gamma_5) b_\beta|B(p)\rangle &= F_1^{BD}(q^2)\left[(p+k)^\mu - \left(\frac{m_B^2 - m_D^2}{q^2}\right) q^\mu\right] \\ &\quad + F_0^{BD}(q^2)\left(\frac{m_B^2 - m_D^2}{q^2}\right) q^\mu\ , \end{aligned} \quad (5.9)$$

with $q = p - k$ the momentum transfer to the kaon. Upon contraction of the two hadronic matrix elements, the term proportional to F_1 reduces to zero due to momentum conservation and only the term proportional to F_0 remains. The F_1 term however, does play a role in semileptonic decays. The decay constant can be measured experimentally or can be determined using non-perturbative techniques like QCD sum rules [122] or Lattice QCD [123]. Experimentally, the form factor is always measured in combination with the CKM matrix element V_{cb}. Theoretical input is needed to disentangle contributions from the form factor and the CKM element. Recently, a lot of progress in the calculation of the form factor was made using lattice QCD [124, 125].

The expression for the branching fraction is:

$$\mathcal{B}(\overline{B}^0 \to D^+ K^-) = \frac{G_F^2 (m_B^2 - m_D^2)^2 |\vec{q}| \tau_{B^0}}{16\pi m_B^2} |V_{us}^* V_{cb}|^2 |f_K F_0^{(BD)}(m_K^2)|^2 |a_1|^2\ . \quad (5.10)$$

In general, the branching fraction of any hadronic colour-allowed tree decay can be expressed in a similar way using the relevant form factor, decay constant and CKM matrix elements.

Test of factorisation

The expression for the branching fraction of $\overline{B}^0 \to D^+ K^-$ decays given in Eq. 5.10 assumes factorisation between the hadronisation of the kaon and the D meson. The parameter $|a_1|$ describes the deviation from factorisation, with naive factorisation yielding $|a_1| = 1$.

Factorisation has a robust theoretical basis. It has been proven to two-loop order in the heavy quark limit and arguments for factorisation to all orders are provided in [121]. In [126] factorisation of the decay $\overline{B}^0 \to D^+\pi^-$ has been proven to all orders of α_s in the limit where the heavy quark masses approach infinity. Corrections of the order $\Lambda_{\rm QCD}/m_b$ result from the fact that the mass of the b quark is not infinity. In addition, one can show that factorisation of the hadronic matrix element of four-quark operators into matrix elements of quark currents holds in leading order using $1/N_C$ expansion [127].

Factorisation can also be tested experimentally using semileptonic decays [121, 128–131]. Semileptonic tree decays do factorise, as leptons do not carry colour charge and no exchange of gluons between the leptons and quarks is possible. The semileptonic tree decay topology is very similar to that of the decay $\overline{B}^0 \to D^+K^-$, and is obtained by replacing the quark pair forming the kaon by a lepton plus neutrino, as illustrated in Fig. 5.5a. Comparison of the hadronic and semileptonic branching fractions provides a tool to test factorisation. Their ratio is [121]

$$\frac{\mathcal{B}(\overline{B}^0 \to D^{(*)+}h^-)}{d\Gamma(\overline{B}^0 \to D^{(*)+}l^-\bar{\nu}_l)/dq^2|_{q^2=m_h^2}} = 6\pi^2\,\tau_{B^0}\,|V_h|^2\,f_h^2\,|a_1(D^{(*)}h)|^2\,X_h\,, \tag{5.11}$$

where $|V_h|^2$ is the CKM matrix element corresponding to the hadronic decay, f_h is the decay constant of the light h meson and q^2 is the momentum transfer. The term X_h quantifies the difference between the form factor F_1 relevant to semileptonic decays and the form factor F_0 relevant to hadronic decays. It deviates from 1 only by terms of the order m_h^2/m_B^2 which is below the 1% level [121]. Using the differential decay rates for the semileptonic decays $\overline{B}^0 \to D^{(*)}l\bar{\nu}$ [132] and the known values of the $B \to Dh$ branching fractions [133], the deviation from naive factorisation is calculated to be [134]

$$\begin{aligned}
|a_1(\overline{B}^0 \to D^+K^-)| &= 0.88 \pm 0.16\,,\\
|a_1(\overline{B}^0 \to D^{*+}K^-)| &= 0.99 \pm 0.05\,,\\
|a_1(\overline{B}^0 \to D^+\pi^-)| &= 0.88 \pm 0.09\,,\\
|a_1(\overline{B}^0 \to D^{*+}\pi^-)| &= 1.01 \pm 0.04\,.
\end{aligned} \tag{5.12}$$

The hadronic decays $\overline{B}^0 \to D^{(*)+}h^-$ are in agreement with naive factorisation. Other tests of factorisation based on the ratio of hadronic decays [121, 134] and the longitudinal polarisation of vector mesons [135, 136] are consistent with this picture.

5.1.3 The ratio of fragmentation fractions f_s/f_d

The measurement of any B_s^0 branching fraction at pp-collider experiments requires knowledge of the production rate of B_s^0 mesons. The production cross-section of B_s^0 mesons is difficult to calculate within QCD. Knowledge of its value relies on measurements of the $b\bar{b}$ production cross-section [137] and the probability of a b quark to hadronise to a B_s^0 meson [138], resulting in an uncertainty of approximately 18%.

A better precision can be obtained when the branching fraction of B_s^0 mesons is determined relative to that of B^0 mesons. The B^0 decay can be used as a normalisation

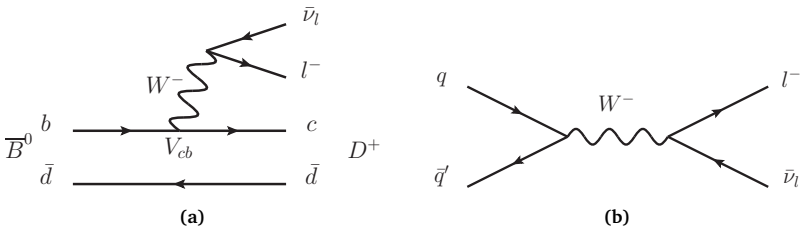

Fig. 5.5 · Non-hadronic decays: a) semileptonic decay $\overline{B}^0$ meson decay, b) leptonic P meson decay, with P a light or heavy meson.

channel, as several branching fractions are precisely measured at the B-factories (for example [139–142]). The $b\bar{b}$ cross-section cancels in such measurement, allowing for a precise $\mathcal{B}(B_s^0)$ measurement. However, it requires knowledge of the relative production of B_s^0 and B^0 mesons.

The ratio of measured yields of $\overline{B}_s^0 \to D_s^+\pi^-$ and $\overline{B}^0 \to D^+K^-$ decays is related to the relative production fractions following

$$\frac{f_s}{f_d} = \frac{N_{D_s\pi}}{N_{DK}} \frac{\epsilon_{DK}}{\epsilon_{D_s\pi}} \frac{\mathcal{B}(\overline{B}^0 \to D^+K^-)}{\mathcal{B}(\overline{B}_s^0 \to D_s^+\pi^-)}, \tag{5.13}$$

with N_X the measured yield and ϵ_X the total efficiency to measure the decay by the LHCb experiment. The values of the branching fractions ($\mathcal{B}$), used here, need to be independent from the measurement of f_s/f_d and thus must be taken from an external input. However, because experimentally no sufficiently precise measurement of these branching fractions is available [143–145], their theoretical calculation is used. Using the expression for the branching fraction of $\overline{B}^0 \to D^+K^-$ decays in Eq. 5.10, and a similar expression for the branching fraction of $\overline{B}_s^0 \to D_s^+\pi^-$ decays with the relevant CKM matrix elements, form factor and decay constant, one arrives at

$$\frac{f_s}{f_d} = \frac{\Phi}{\Phi_s} \frac{\tau_{B^0}}{\tau_{B_s^0}} \left|\frac{V_{us}}{V_{ud}}\right|^2 \left(\frac{f_K}{f_\pi}\right)^2 \left[\frac{F_0^{BD}(m_K^2)}{F_0^{B_sD_s}(m_\pi^2)}\right]^2 \left|\frac{a_1(DK)}{a_1(D_s\pi)}\right|^2 \frac{N_{D_s\pi}}{N_{DK}} \frac{\epsilon_{DK}}{\epsilon_{D_s\pi}} \frac{\mathcal{B}(D^+)}{\mathcal{B}(D_s^+)}, \tag{5.14}$$

using only the charm hadron decays $D_s^+ \to K^-K^+\pi^+$ and $D^+ \to K^-\pi^+\pi^+$. The phase space factor is given by

$$\Phi_{(s)} = \frac{\left(m_{B(s)}^2 - m_{D(s)}^2\right)^2}{16 m_{B(s)}^3} \sqrt{\left(m_{B(s)}^2 - m_{D(s)}^2 - m_h^2\right)^2 - 4m_{D(s)}^2 m_h^2}. \tag{5.15}$$

The kinematic factor $(m_{B(s)}^2 - m_{D(s)}^2)$ originating from the calculation of the hadronic matrix element $\langle D(k)|\bar{c}_\beta\gamma^\mu(1-\gamma_5)b_\beta|B(p)\rangle$ is included here. In order to provide an accurate measurement of f_s/f_d, precise knowledge of the ratio of decay constants, the ratio of form factors and factorisation is needed. The decays $\overline{B}^0 \to D^+K^-$ and $\overline{B}_s^0 \to D_s^+\pi^-$ are related

via $SU(3)$ symmetry. The factorisable $SU(3)$ breaking corrections are included in the form factor ratio

$$\mathcal{N}_F = \left| \frac{F_0^{BD}(m_K^2)}{F_0^{B_s D_s}(m_\pi^2)} \right|^2 , \tag{5.16}$$

while the non-factorisable $SU(3)$ breaking corrections are expressed as

$$\mathcal{N}_a = \left| \frac{a_1(DK)}{a_1(D_s\pi)} \right|^2 . \tag{5.17}$$

The expression for the branching fraction of $B \to Dh$ decays in Eq. 5.10 is the theoretical branching fraction calculated at $t = 0$. However, in Eq. 5.14 the measurement of the yields N_X is time integrated. Therefore the time integrated "experimental" branching fraction needs to be used, which is affected by $B^0_{d,s}$–$\overline{B}^0_{d,s}$ mixing. The theoretical branching fraction is related to the experimental branching fraction as [146],

$$\mathcal{B}(B^0_{d,s} \to f)_{\text{theo}} = \left[\frac{1 - y^2_{d,s}}{1 + \mathcal{A}^f_{\Delta\Gamma}\, y_{d,s}} \right] \mathcal{B}(B^0_{d,s} \to f)_{\text{exp}} , \tag{5.18}$$

with

$$y_{d,s} = \frac{\Delta\Gamma_{d,s}}{2\,\Gamma_{d,s}} , \tag{5.19}$$

and $\mathcal{A}^f_{\Delta\Gamma}$ a CP observable which depends on the specific final state f. In the presence of a sizeable decay width difference $\Delta\Gamma$, this correction is not negligible. In the B^0–$\overline{B}^0$ system, $\Delta\Gamma_d$ is small [84], and the theoretical expression for the branching fraction of $\overline{B}^0 \to D^+K^-$ decays can be used. In the B^0_s–$\overline{B}^0_s$ system, however, $y_s = 0.075 \pm 0.012$ [147], and the difference between the theoretical and experimental branching fractions needs to be taken into account. This yields a small correction of 0.6% for flavour specific final states, like $\overline{B}^0_s \to D^+_s\pi^-$, with $\mathcal{A}^f_{\Delta\Gamma} = 0$.

5.1.3.1 The ratio of decay constants

The kaon and pion decay constants are obtained from measurements using purely leptonic pion and kaon decays (Fig. 5.5b). All QCD effects are included in the decay constant. The decay width of a pseudoscalar P to a leptonic final state $l\nu$ is related to the decay constant following [84]

$$\Gamma(P \to l\nu) = \frac{G_F^2}{8\pi} m_P m_l^2 \left(1 - \frac{m_l^2}{m_P^2}\right) \left|V_{q\bar{q}'}\right| f_P . \tag{5.20}$$

Using the known branching fractions of the decays $\pi \to \mu\nu(\gamma)$ and $K \to \mu\nu(\gamma)$ (where γ represents a radiative photon) and the values of the corresponding CKM matrix elements, the decay constants are extracted [84],

$$\begin{aligned} f_\pi &= 130.41 \pm 0.20\,\text{MeV} , \\ f_K &= 156.2 \pm 0.7\,\text{MeV} . \end{aligned} \tag{5.21}$$

The uncertainty on the ratio of decay constants, $f_K/f_\pi = 1.198 \pm 0.005$, is negligible in the measurement of the fragmentation fractions f_s/f_d.

5.1.3.2 Factorisable $SU(3)$ breaking corrections: the ratio of form factors

The form factors can be determined experimentally using semileptonic decays or calculated using non-perturbative techniques [125]. The product of the form factor $F_1^{BD}(q^2)$ and the absolute value of the CKM matrix element V_{cb} can be probed using the semileptonic decay $\overline{B}^0 \to D^+ l^- \bar{\nu}$, shown in Fig. 5.5a. This allows for a determination of the CKM element V_{cb}, provided that theoretical input on the form factor is used. The differential decay rate of $\overline{B}^0 \to D^+ l^- \bar{\nu}$ decays is [84]

$$\frac{d\Gamma(\overline{B}^0 \to D^+ l^- \bar{\nu})}{d\omega} = \frac{G_F^2 |V_{cb}|^2}{48\pi^3} m_D^3 (m_B + m_D)^2 (\omega^2 - 1)^{3/2} F_1^{BD}(\omega)\,. \tag{5.22}$$

The variable ω denotes the product of the B and D four-velocities and is related to q^2 as $\omega = (m_B^2 + m_D^2 - q^2)/(2 m_B m_D)$. In the heavy quark limit, $F_1^{BD}(\omega)$ coincides with the Isgur-Wise function [148]. This function is normalised to unity at zero recoil, $\omega = 1$. Corrections to this limit are of the order $\Lambda_{\rm QCD}/m_b$ and combined with electroweak corrections, this results in $F_1^{BD}(1) = 1.081 \pm 0.024$ [138]. The decay rate is zero at $\omega = 1$, as can be seen from Eq. 5.22. An extrapolation of the form factor from the measured ω range to $\omega = 1$, allows for an accurate determination of $|V_{cb}|$. This requires knowledge of the shape of the ω dependence of the form factor. The parametrisation in [132], which expresses the non-linear ω dependence of the form factor in terms of a single parameter, is generally used. Results from Belle [149], Babar [150, 151], CLEO [152] and ALEPH [153] are combined [138] to yield $V_{cb} = (39.45 \pm 1.42 \pm 0.88) \times 10^{-3}$.

Lattice QCD calculations are in agreement with the ω dependence of F_1^{BD} measured in experimental data [154, 155]. The form factor F_0^{BD} relevant to hadronic decays differs from the form factor F_1^{BD} relevant to semileptonic decays only below the 1% level at $q^2 = m_{\pi/K}^2$ [121]. The ratio of form factors relevant to the measurement of f_s/f_d using the hadronic decays $\overline{B}^0 \to D^+ K^-$ and $\overline{B}_s^0 \to D_s^+ \pi^-$, is calculated using lattice QCD to be $\mathcal{N}_F = 1.094 \pm 0.088 \pm 0.030$ where the first uncertainty is statistical and the second systematic [154]. This value is in agreement with an alternative determination of $\mathcal{N}_F$ using QCD sum rules [156]. The calculated value of $\mathcal{N}_F$ is close to unity, which means that factorisable $SU(3)$ breaking corrections are small.

5.1.3.3 Test of non-factorisable $SU(3)$ symmetry breaking effects

In the calculation of the branching fraction of a colour-allowed tree decay, the deviation from naive factorisation is accounted for via the parameter $|a_1|$. In the determination of the ratio of fragmentation fractions, this parameter enters both for the $\overline{B}^0 \to D^+ K^-$ and the $\overline{B}_s^0 \to D_s^+ \pi^-$ decay. These decays are related by the exchange of a d and an s quark. In the limit of exact U-spin symmetry[1], factorisation works equally well in both processes, resulting in equal values of $|a_1(DK)|$ and $|a_1(D_s\pi)|$. The deviation of U-spin symmetry, $\mathcal{N}_a$, is an essential input for the determination of f_s/f_d.

An estimate of $SU(3)$ symmetry corrections in B meson decays can be made through a comparison of different decay amplitudes. $SU(3)$ symmetry implies that the branching

[1] $SU(3)$ symmetry refers to the symmetry group interchanging u, d and s quarks. The isospin, U-spin and V-spin subgroups refer to interchanging $u \leftrightarrow d$, $d \leftrightarrow s$ and $s \leftrightarrow u$, respectively.

decay	topology	$\mathcal{B}[10^{-4}]$ [157]	correction [134]	$\frac{\text{\|amplitude\|}_{\text{corr}}}{\|T^*+E^*\|}$ [134]
$\overline{B}^0 \to D^{*+}\pi^-$	$T^* + E^*$	27.6 ± 1.3	–	1
$\overline{B}^0 \to D^{*+}K^-$	$T^{*'}$	2.14 ± 0.16	$\left\|\frac{V_{ud}}{V_{us}}\right\| \frac{f_\pi}{f_K} \frac{F_0^{BD}(m_\pi^2)}{F_0^{BD}(m_K^2)}$	0.983 ± 0.028
$\overline{B}^0 \to D_s^{*+}K^-$	$E^{*'}$	0.219 ± 0.030	$\frac{f_D}{f_{D_s}} \frac{f_\pi}{f_K}$	0.066 ± 0.006

Table 5.1 · The ratio of amplitudes of the colour-allowed tree topology (T) and the exchange topology (E), using the decays $\overline{B}^0 \to D_{(s)}^{*+}h^-$ which are related to each other via $SU(3)$ symmetry [134]. The symbol h denotes either a pion or a kaon.

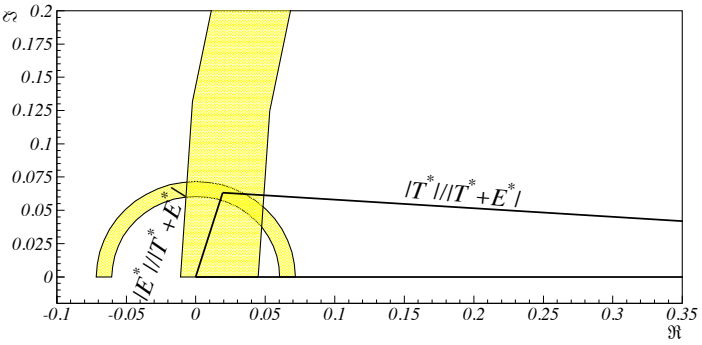

Fig. 5.6 · The amplitudes of the decays $\overline{B}^0 \to D^{*+}\pi^-$, $\overline{B}^0 \to D^{*+}K^-$ and $\overline{B}^0 \to D_s^{*+}K^-$ form a triangle in the complex plane. Here the amplitudes are normalised with respect to $\overline{B}^0 \to D^{*+}\pi^-$. The factorisable $SU(3)$ breaking corrections are accounted for in the amplitudes of the decays $\overline{B}^0 \to D_{(s)}^{*+}K^-$. Figure from [134].

fraction of two decays which are related through the exchange of an s and a d quark is the same, after correcting for factorisable $SU(3)$-breaking factors. Here, an example of a comparison is shown using the decays $\overline{B}^0 \to D^{*+}\pi^-$, $\overline{B}^0 \to D^{*+}K^-$ and $\overline{B}^0 \to D_s^{*+}K^-$ [134].

The decay $\overline{B}^0 \to D^{*+}\pi^-$ proceeds via a colour-allowed tree and an exchange diagram. On exchange of the d quark by an s quark, one finds the colour-allowed tree decay $\overline{B}^0 \to D^{*+}K^-$ and the exchange decay $\overline{B}^0 \to D_s^{*+}K^-$. The amplitude of the $\overline{B}^0 \to D^{*+}\pi^-$ decay, denoted as $T^* + E^*$, can now be compared to the amplitudes of the decays $\overline{B}^0 \to D^{*+}K^-$ and $\overline{B}^0 \to D_s^{*+}K^-$, denoted as $T^{*'}$ and $E^{*'}$, respectively. Here the prime symbol indicates the different particles in the final state, for which a correction factor needs to be applied. This correction factor is composed of the factorisable $SU(3)$-corrections: CKM elements, decay constants and form factors. Using the world average values of the branching fractions, and taking into account the difference in phase space, the amplitudes of the three decays are readily calculated (Table 5.1). The three amplitudes form a triangle in the complex plane, as phases are allowed to exist between the different amplitudes. To illustrate their consistency, they are drawn in the complex plane in Fig. 5.6.

An uncertainty of 2% on $|(a_1(DK))/(a_1(D_s\pi))|^2$ is determined in [134], using $\overline{B}^0 \to D^{*+}_{(s)}h^-$ decays and additional tests using colour-suppressed tree decays. A test of $SU(3)$ symmetry using the colour-allowed tree decays $\overline{B}^0 \to D^+\pi^-$, $\overline{B}^0 \to D^+K^-$ and $\overline{B}^0 \to D_s^+K^-$ will become available when $\mathcal{B}(\overline{B}^0 \to D_s^+K^-)$ is measured to higher precision, and is included in chapter 9.

5.1.3.4 Test of E contribution

The abundant decay $\overline{B}^0 \to D^+\pi^-$ has a branching fraction which is roughly 14 times larger than that of $\overline{B}^0 \to D^+K^-$. A measurement of the ratio of fragmentation fractions using the decay $\overline{B}^0 \to D^+\pi^-$ (in combination with the decay $\overline{B}^0_s \to D_s^+\pi^-$) reduces the statistical uncertainty. However, an additional theoretical uncertainty is introduced as the decay $\overline{B}^0 \to D^+\pi^-$ proceeds via both the colour-allowed tree and the exchange topology. Analogous to Eq. 5.14 one can express f_s/f_d in the theoretical values for the branching fractions of $\overline{B}^0 \to D^+\pi^-$ and $\overline{B}^0_s \to D_s^+\pi^-$ decays, and the number of events measured by the LHCb experiment,

$$\frac{f_s}{f_d} = \frac{\Phi}{\Phi_s}\frac{\tau_{B^0}}{\tau_{B^0_s}}\left[\frac{F_0^{BD}(m_\pi^2)}{F_0^{B_sD_s}(m_\pi^2)}\right]^2 \left|\frac{a_1(D\pi)}{a_1(D_s\pi)}\right|^2 \frac{1}{\mathcal{N}_E}\frac{N_{D_s\pi}}{N_{D\pi}}\frac{\epsilon_{D\pi}}{\epsilon_{D_s\pi}}\frac{\mathcal{B}(D^- \to K^+\pi^-\pi^-)}{\mathcal{B}(D_s^- \to K^+K^-\pi^-)}, \quad (5.23)$$

where $\mathcal{N}_E$ takes into account the contribution of the exchange diagram and is defined as

$$\mathcal{N}_E = \left|\frac{T}{T+E}\right|^2. \quad (5.24)$$

In order to provide an accurate measurement of f_s/f_d using $\overline{B}^0 \to D^+\pi^-$ decays, a precise estimate of the contribution of the exchange diagram needs to be made. Both the test of factorisation and the test of $SU(3)$ symmetry described earlier provide information on the size of the exchange diagram.

The decays described in Eqs. 5.12 with a pion in the final state have access to both the colour-allowed tree and the exchange topology, whereas the decays with a kaon in the final state proceed only via the tree topology. There is no enhancement of $|a_1(D^{(*)}h)|$ for those decays which have an additional exchange topology compared to those decays that have not. This suggests that the contribution of the exchange topology is small compared to the contribution on the tree topology.

In Tab. 5.1 the branching fractions of the decays $\overline{B}^0 \to D^{*+}\pi^-$ and $\overline{B}^0 \to D^{*+}K^-$ are compiled in order to provide a comparison of the size of the amplitudes of the T^* and $T^{*'} + E^{*'}$ diagrams. After correcting for the different particles in the final state, it is found that that $T^* = (0.983 \pm 0.028)\,[T^* + E^*]$. This indicates that the contribution of the exchange topology is small. Adding a 5% additional uncertainty for possible differences between the D and the D^* meson, gives $\mathcal{N}_E = 0.966 \pm 0.056 \pm 0.05$ [134].

Another way to estimate the size of the exchange diagram is by measuring the branching fraction of a decay that only proceeds via the exchange topology. Examples of such decays are $\overline{B}^0 \to D_s^{*+}K^-$ and $\overline{B}^0 \to D_s^+K^-$. Due to their small branching fractions, no precise measurements are available yet. A measurement of $\mathcal{B}(\overline{B}^0 \to D_s^+K^-)$ is included in chapter 8.

5.1.4 Inclusive semileptonic branching fractions

The accurate theoretical prediction of the branching fractions of $\overline{B}^0 \to D^+ K^-$ and $\overline{B}^0_s \to D^+_s \pi^-$ decays allows for the determination of the relative B^0_s and B^0 production fractions using these decays. In a similar fashion, in order to measure the relative production fractions of Λ^0_b and B^0 decays, one would need a theoretical prediction of the branching fraction of $\Lambda^0_b \to \Lambda^+_c \pi^-$ decays. However, the theoretical calculation of $\mathcal{B}(\Lambda^0_b \to \Lambda^+_c \pi^-)$ is not reliable due to uncertainties on the $\Lambda^0_b \to \Lambda^+_c$ form factor [158] and unknown non-factorisable effects in this decay [159].

So far only exclusive b-hadron decays are discussed. The calculation of inclusive decays, where one sums over all possible final states, has smaller theoretical uncertainties. The inclusive decay width of semileptonic b-hadron decays, $\Gamma(H_b \to H_c l^- \bar{\nu}_l X)$, can be calculated in the Heavy Quark Expansion [160–162]. Here, the notation H_b is used to indicate either a B meson or a Λ^0_b baryon, H_c indicates a D meson or Λ_c baryon, and X indicates the remaining final state. The expansion of the decay width in powers of $1/m_b$ results in [160, 163]

$$\Gamma(H_b \to H_c\, l^- \bar{\nu}_l X) = \Gamma(b \to c\, l^- \bar{\nu}_l X) + \mathcal{O}\left(\frac{\Lambda^2_{\rm QCD}}{m^2_b}\right), \tag{5.25}$$

where the b-hadron decay is modelled as the decay of the b quark up to corrections of order $\Lambda^2_{\rm QCD}/m^2_b$.

To leading order, the semileptonic decay width is the same for all b-hadron species. The higher order non-perturbative corrections can be calculated [160–162]. The B^0 and B^0_s mesons are related by $SU(3)$ symmetry and corrections are expected to be of similar size. Small $SU(3)$ violating corrections have been calculated resulting in $\Gamma(B^0_s \to H_c\, l^- \bar{\nu}_l X)/\Gamma(B^0 \to H_c\, l^- \bar{\nu}_l X) - 1 \approx -1\%$ [160]. No symmetry relates the decay rates of b baryons and b mesons. However, the difference of the semileptonic decay widths of Λ^0_b and B^0 decays is still calculated to be small: $\Gamma(\Lambda^0_b \to H_c\, l^- \bar{\nu}_l X)/\Gamma(B^0 \to H_c\, l^- \bar{\nu}_l X) - 1 \approx +3\%$ [160].

Near equality of semileptonic decay widths of Λ^0_b and B^0 hadrons allows for a measurement of the relative production fractions of Λ^0_b baryons and B^0 mesons using inclusive semileptonic decays [97]. The measured value of $f_{\Lambda^0_b}/f_d$ is used in chapter 7 to normalise the $p_{\rm T}$ dependence of $f_{\Lambda^0_b}/f_d$.

5.2 Experimental challenges in measuring fragmentation fractions using hadronic decays

Chapters 6 and 7 are reproductions of the two journal publications in which the studies of the relative production rates f_s/f_d and $f_{\Lambda^0_b}/f_d$ are presented. Both are published in JHEP [164, 165]. Both measurements use the LHCb data taken in 2011, corresponding to a dataset of $1\,\text{fb}^{-1}$. In contrast to most measurements discussed in the section 4.2, these measurements are performed using hadronic decays. Both the semileptonic and the hadronic determination of the fragmentation fractions pose experimental challenges. The semileptonic determination [96, 97] involves a missing neutrino in the final state leading

to larger backgrounds, whereas the hadronic determination [164, 165] relies on kaon-pion separation.

The measurement of f_s/f_d described in chapter 6, is performed using the hadronic decays $\overline{B}^0 \to D^+\pi^-$, $\overline{B}^0 \to D^+K^-$ and $\overline{B}^0_s \to D^+_s\pi^-$, with the $D^+_{(s)}$ meson decaying to the final state $K^-\pi^+\pi^+$ ($K^-K^+\pi^+$). The advantage of the hadronic decays compared to the semileptonic decays, is that the hadronic decays are fully reconstructed, and thus the dependence of the fragmentation fractions can be studied as a function of the momentum and direction of the produced b hadron. An expression for the ratio of the branching fractions of these decays is presented in Sec. 5.1.3, which is used to extract the value of f_s/f_d.

A measurement of the absolute value of the ratio of fragmentation fractions $f_{\Lambda^0_b}/f_d$ cannot be performed using the hadronic decays $\Lambda^0_b \to \Lambda^+_c\pi^-$ ($\Lambda^+_c \to pK^-\pi^+$) and $\overline{B}^0 \to D^+\pi^-$ as the relative branching fractions cannot be calculated reliably due to uncertainties on the $\Lambda^0_b \to \Lambda^+_c$ form factor [158] and unknown non-factorisable effects in this decay [159]. However, a study of these decays does provide insight in the dependency of $f_{\Lambda^0_b}/f_d$ on the b-hadron kinematics. The absolute scale of this measurement is determined using semileptonic decays, for which theoretical knowledge is available on the ratio of branching fractions, as outlined in Sec. 5.1.4.

As the journal publications are concise, the following pages give more detailed information on the most important ingredients of the analysis. Although the final extraction of the dependence of f_x/f_d (where x refers to s or Λ^0_b) on the b-hadron kinematics is different in the two journal publications, the experimental inputs needed for the measurements are in both cases the events yields and efficiencies with which the yields are measured. The following sections will therefore provide more detailed information related to the extraction of the signal yields and efficiencies.

5.2.1 Analysis overview

The selection of signal events can be divided in four steps. A first, coarse selection step is performed online at the trigger level, in order to record only those events that are likely to contain interesting b-hadron decays. The hardware trigger selects events that contain a cluster in the calorimeter with a large transverse energy. The software trigger consists of two stages. In the first stage, tracks are reconstructed and only those events are used in which at least one track is found that has a large (transverse) momentum and that is displaced from the primary vertex (PV). The second stage is a topological trigger that aims to select any b-hadron decay which produces charged tracks. It does so by reconstructing two-, three- or four-track vertices that are displaced from the PV. A multivariate algorithm, which uses information on the properties of this vertex and the properties of the tracks from which the vertex has been reconstructed, is used to select interesting events. The trigger selection is detailed in App. B.

In the second step, the offline reconstruction commences with a full reconstruction of the events: c hadrons are created from combinations of three tracks and are subsequently combined with a bachelor hadron to form a b hadron. Quality requirements are set on each individual track, on the track of the c hadron and on the track of the b hadron, as outlined

Criteria	$\overline{B}^0 \to D^+\pi^-$	$\overline{B}^0 \to D^+K^-$	$\overline{B}^0_s \to D^+_s\pi^-$	$\Lambda^0_b \to \Lambda^+_c\pi^-$
Offline selection				
b-hadron η	2–5	2–5	2–5	2–5
b-hadron p_{T} (GeV/c)	1.5–40.0	1.5–40.0	1.5–40.0	1.5–40.0
bachelor p (GeV/c)	> 150	> 150	> 150	> 150
$D_{(s)}$ FD χ^2	> 2	> 2	> 2	–
$m_{c\,\mathrm{hadron}}$ (MeV/c^2)	1844–1890	1844–1890	1944–1990	2265–2305
$m_{b\,\mathrm{hadron}}$ (MeV/c^2)	5000–5800	5075–5800	5100–5800	5350–6000
BDT	> 0.66	> 0.66	> 0.66	> 0.66
Particle identification to identify pions and kaons (DLL($K-\pi$))				
Bachelor	< 0	< 0	> 5	< 0
π from $D_{(s)}, \Lambda_c$	< 5	< 5	< 5	< 5
K^+ from $D^-_{(s)}, \Lambda_c$	> 0	> 0	> 0	> 0
K^- from D^-_s	–	–	> 5	–
proton from Λ_c	–	–	–	> 0
Particle identification to identify protons from Λ_c (DLL($p-\pi$))				
DLL($p-\pi$)	–	–	–	> 5
DLL($p-\pi$)–DLL($K-\pi$)	–	–	–	> 0

Table 5.2 · Selection criteria to select the decay modes $B \to Dh$, corresponding to step 3 and step 4 as described in the text. The quantity DLL describes the log likelihood difference assigned to two particle ID hypotheses.

in App. B. The requirements are designed to pre-select candidates which are consistent with a multi-body decay with hadronic final state particles and a vertex which is displaced from the PV.

In the third step, the offline selection proceeds to select the specific b-hadron decays described in this thesis: $\overline{B}^0 \to D^+\pi^-$, $\overline{B}^0 \to D^+K^-$, $\overline{B}^0_s \to D^+_s\pi^-$ and $\Lambda^0_b \to \Lambda^+_c\pi^-$. To this end, criteria are placed on the reconstructed mass and flight distance of the c hadron. In addition, a multivariate technique is used to increase signal and background separation. All b-hadron decays used in this study proceed via a b-to-c transition, and all final states consist of four light hadrons. This means that the decay channels used in the analysis are kinematically similar, and the same selection criteria are used so far to select the different modes.

In the fourth step, the different decay channels are finally differentiated, using the particle identification (PID) requirements to identify pions, kaons and protons. The selection criteria corresponding to step three and four, which are exclusively used in the analysis described in this thesis, are summarised in Table 5.2.

For the extraction of the signal yield the invariant mass distribution of reconstructed b-hadron candidates is exploited (Figs. 5.7–5.8). An accurate modelling of the signal shape and the shapes of the different sources of background is essential for a precise yield extraction. The shape of the invariant mass distributions of the signal and the various sources of background are modelled using either simulated data or real data, as described

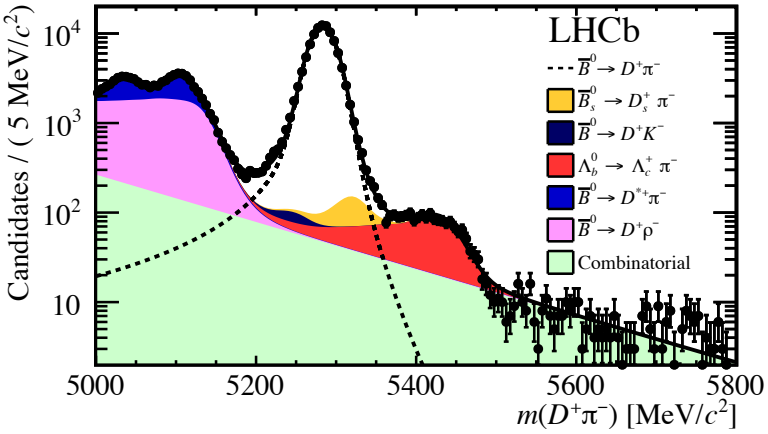

(a)

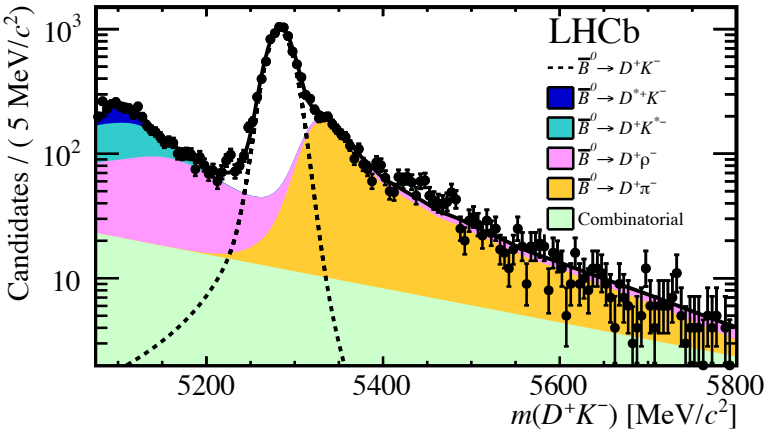

(b)

Fig. 5.7 · Invariant mass distribution for events reconstructed as a) $D^+\pi^-$ and b) D^+K^-. The signal is displayed in white and the various sources of background are coloured.

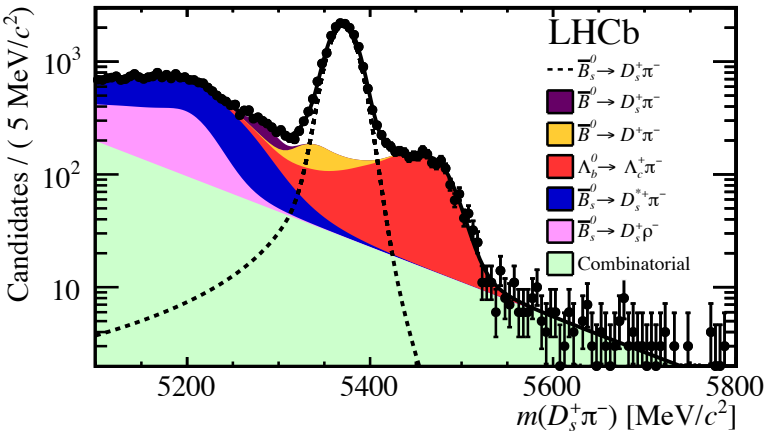

(a)

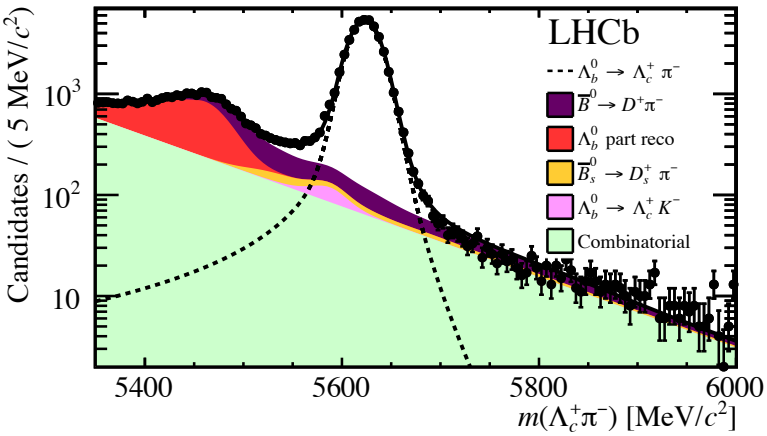

(b)

Fig. 5.8 · Invariant mass distribution for events reconstructed as a) $D_s^+\pi^-$ and b) $\Lambda_c^+\pi^-$. The signal is displayed in white and the various sources of background are coloured.

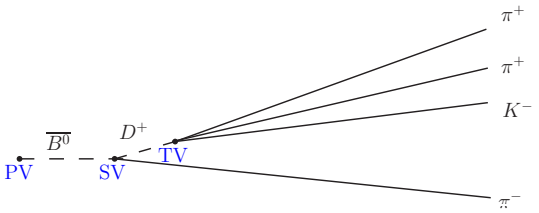

Fig. 5.9 · Schematic representation of the decay $\overline{B}^0 \to D^+\pi^-$ in the lab frame. The B meson is produced in the proton-proton collision at the primary vertex (PV). The secondary vertex (SV) is the B decay vertex, and the tertiary vertex (TV) is the D decay vertex.

in the following pages. The effect of the different selection steps on the shapes need to be taken into account.

The ratio of fragmentation fractions is then readily determined using the efficiency corrected event yields, the theoretical calculation of the branching fractions and their relation in Eq. 5.14. For a measurement of the kinematic dependencies of f_x/f_d a measurement of the efficiency corrected yield ratio of the two different species of b hadrons in bins of the kinematic variable is sufficient.

5.2.2 Decay of beauty hadrons

Due to their long lifetime and large boost, b hadrons typically fly a few mm in the detector before they decay. The b-hadron decays discussed in this work are of the b-to-c type: the b hadron first decays to a bachelor hadron and a charm hadron with finite lifetime, which then further decays into the final state particles. The charm hadron decays under consideration in this work are hadronic three-body decays. The decay chain is shown in Fig. 5.9 using the decay $\overline{B}^0 \to D^+\pi^-$ as an example. There are four tracks in the final state corresponding to the four hadronic decay products. The kinematic distributions of the final state particles are shown in Fig. 5.10. The momentum spectra of the c-hadron daughters are softer than that of the bachelor particle, while all tracks exhibit a very similar pseudorapidity distribution. The different b-hadron decays under consideration in this thesis are kinematically very similar, which allows for the extraction of the different signals with similar selection criteria. The relatively long lifetime of the b hadron and $D_{(s)}$ meson in comparison to the combinatorial background (Fig. 5.12) provides a powerful handle for signal separation.

5.2.3 Offline selection

Multivariate techniques provide a powerful tool to separate signal from combinatorial background, exploiting a combination of small differences in various variables. In the f_x/f_d analyses, a Gradient Boosted Decision Tree (BDT) [166] is used to reject the combinatorial background. The BDT is trained on a subset of the $\overline{B}^0_s \to D^+_s\pi^-$ data sample. Signal events are extracted from data using the *sPlot* technique [167], while events with an invariant mass greater than 5450 MeV/c^2 act as background. The variables used by the BDT are shown

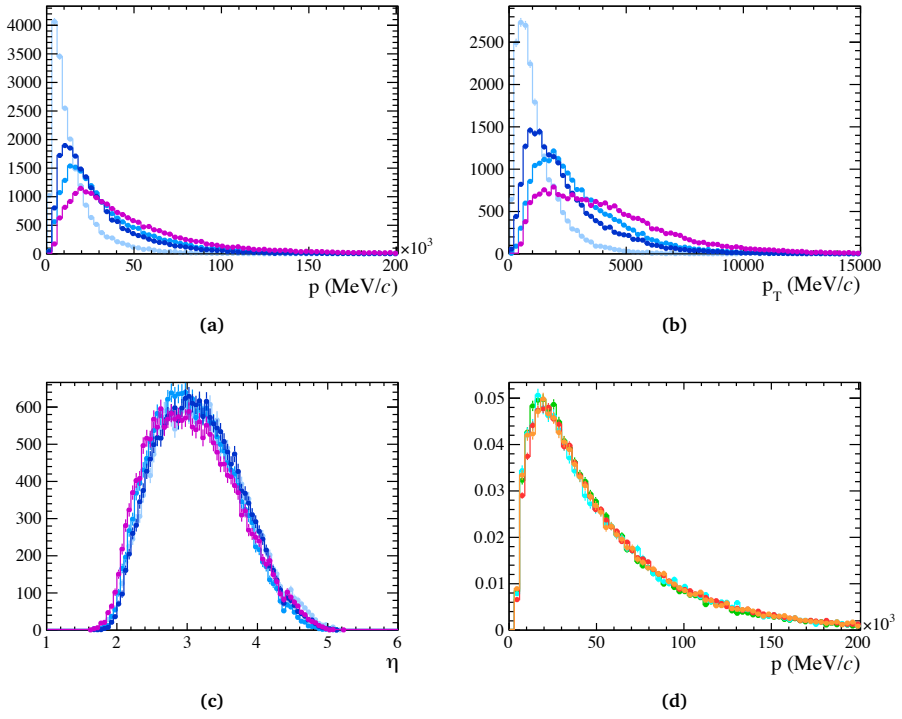

Fig. 5.10 · Kinematic distributions of the four final state particles in simulated $\overline{B}^0 \to D^+\pi^-$ events with all selection criteria applied, with the bachelor track in purple and the D daughter tracks in blue. The darkest blue corresponds to the kaon track, the lightest blue to the low momentum pion and the middle blue to the high momentum pion. The distributions are the a) momentum, b) transverse momentum and c) pseudorapidity. d) The momentum distribution of the bachelor hadron in simulated $\overline{B}^0 \to D^+\pi^-$ (orange), $\overline{B}^0 \to D^+K^-$ (red), $\overline{B}^0_s \to D^+_s\pi^-$ (cyan) and $\Lambda^0_b \to \Lambda^+_c\pi^-$ (green) decays, after the full selection excluding the PID selection criteria. The PID selection criteria are omitted, since they invoke a momentum dependent efficiency.

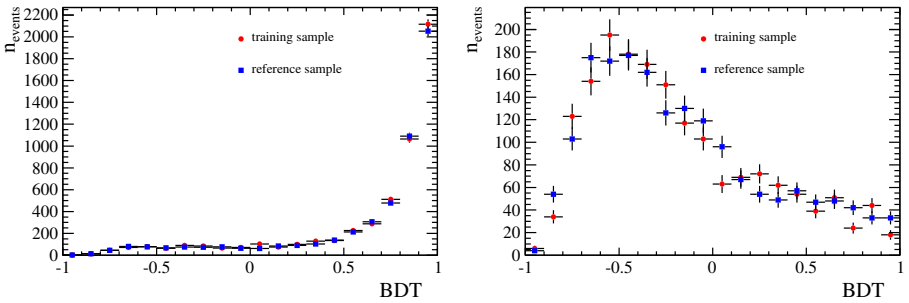

Fig. 5.11 · BDT response in data for the training sample and the reference sample, for a) the signal region and b) the upper sideband defined as $m(D_s^+\pi^-) > 5450\,\mathrm{MeV}/c^2$.

in Fig. 5.12. The most discriminating variables are found to be the impact parameter χ^2 of the B and the pointing angle of the B to the PV (i.e. the cosine of the angle between the momentum of the B and its direction of flight). Despite the difference in D^+, D_s^+ and Λ_c^+ lifetimes, the c-hadron impact parameter and flight distance are used in the optimisation, but they are found to have low importance, such that the BDT efficiency remains very similar for B^0, B_s^0 and Λ_b^0 modes.

Since the BDT is trained on a subset of the data sample used in the analysis described in Sec. 6, there is a danger of introducing a bias due to overtraining. The potential overtraining has been investigated by comparing the BDT response in the training sample to an independent $\overline{B}_s^0 \to D_s^+\pi^-$ sample (checking sample), as shown in Fig. 5.11. Overtraining would show as a difference in BDT response in the training and the reference sample. No indication of overtraining has been observed.

The efficiency of the BDT requirement is evaluated on simulated data and relies on an accurate modelling of the BDT input variables. To check this, a comparison of data and simulated events is made. In simulated events, a reweighting method is exploited to take into account the DLL$(K-\pi)$ requirement, as explained in the next section. In data, signal events are separated from the background using the *sPlot* technique [167]. Good agreement is found between data and simulation for most variables, with the exception of variables related to the track ghost probability and the c-hadron decay vertex χ^2, as shown in Fig. 5.12 for the $\overline{B}^0 \to D^+\pi^-$ sample. As the determination of f_x/f_d involves the ratio of yields, its measurement is not sensitive to the absolute selection efficiency of each decay mode, but only to the ratio of efficiencies. Differences between data and simulation, which can affect the measured selection efficiency, largely cancel in the ratio of different decay modes. Any remaining effect is taken into account in the systematic uncertainty.

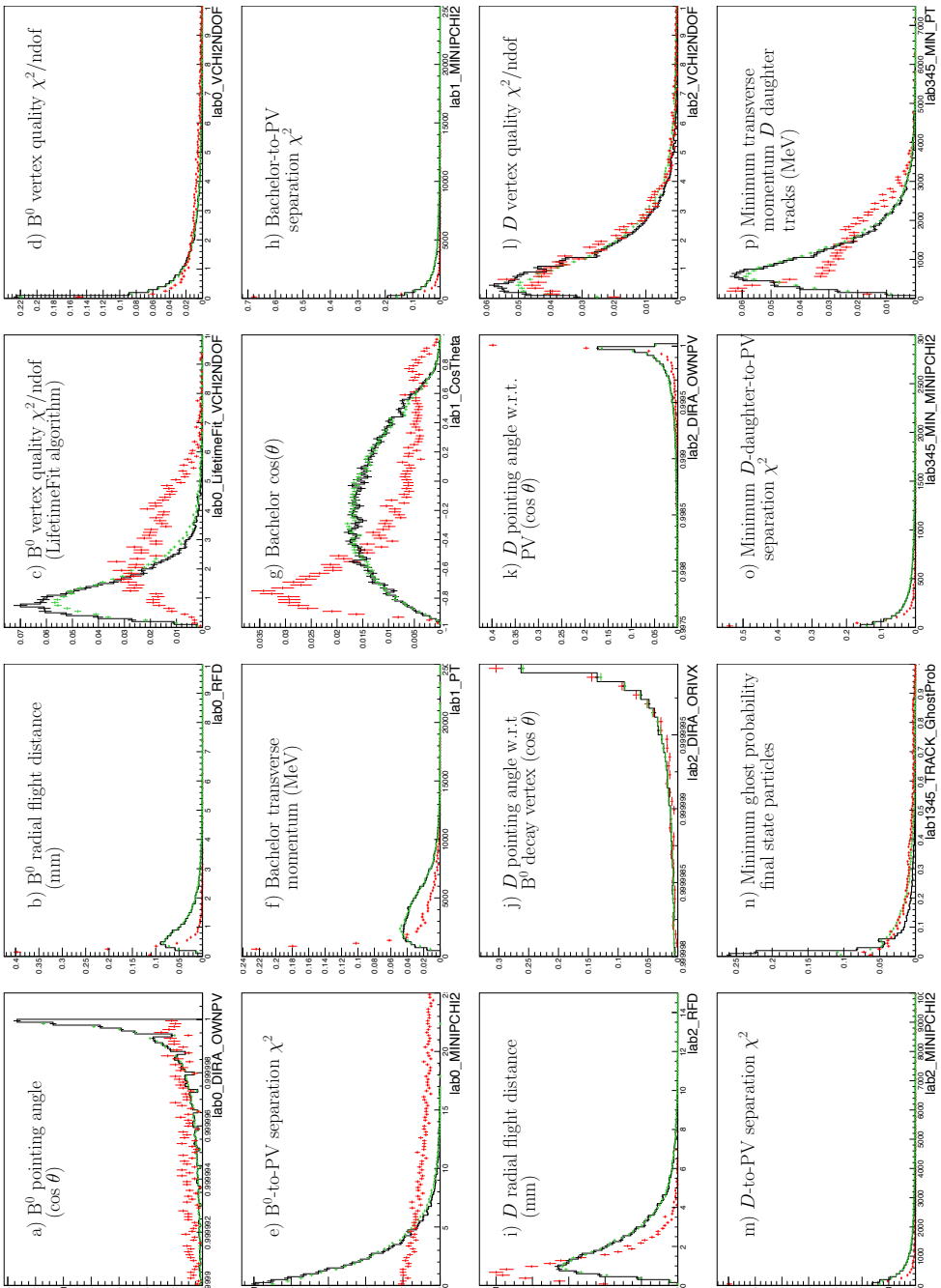

Fig. 5.12 · Variables used by the BDT. Distributions observed in a sWeighted [167] $\overline{B}^0 \to D^+\pi^-$ data sample (green dots), a simulated $\overline{B}^0 \to D^+\pi^-$ data sample (black histogram) and in a background data sample (red dots). The background sample consists of events in the upper sideband, $m(D_s\pi) > 5450\,\mathrm{MeV}/c^2$, of a $\overline{B}^0_s \to D^+_s\pi^-$ data sample. The different variables are annotated inside the figure. The axis labels correspond to the LHCb internal variables.

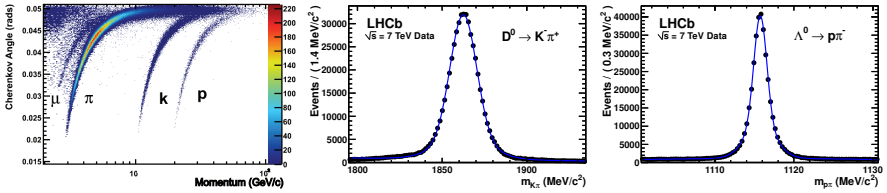

(a) (b) (c)

Fig. 5.13 · a) Cherenkov angle measured with the RICH detector as function of the track momentum measured with the tracking system, for isolated tracks. The backgrounds in the PID calibration samples b) $D^0 \to K^-\pi^+$ and c) $\Lambda \to p\pi^-$ are observed to be very low. Figures from [168].

5.2.4 Particle identification

The particle identification (PID) criteria provided by the RICH detector are used to differentiate between the different kinematically similar final states. The final state particles in the decay channels described in this thesis are light hadrons: pions, kaons and protons. The identification relies on the reconstructed Cherenkov angle and the momentum of isolated tracks (Fig. 5.13a), and is expressed as the difference (D) of the log-likelihood (LL) of the two particle hypotheses. The DLL($K - \pi$) and DLL($p - \pi$) variables are for pion-kaon and pion-proton separation, respectively. Since the performance of the PID requirements is difficult to model accurately in simulated events, the performance of the PID is measured using a control channel in real data.

To obtain the performance of the DLL($K - \pi$) criteria a sample of approximately 27 million $D^{*-} \to \overline{D}^0(K^+\pi^-)\pi^-$ candidates is used. In this low background sample (Fig. 5.13b) pions and kaons are unambiguously selected using the charge of the tracks. The efficiencies and misidentification probabilities for the PID criteria used in the analysis are determined from this sample. They are evaluated in bins of the momentum and transverse momentum of the tracks in the selected events. The efficiency to correctly select a pion (kaon), and the probability of a kaon (pion) to be misidentified as a pion (kaon) are shown in Figs. 5.14a–5.14b (Figs. 5.14c–5.14d), for the PID requirement which is used to select a bachelor pion (kaon). At high momentum the separation power degrades, due to the gradual saturation of the Cherenkov angle.

The (transverse) momentum of the final state tracks differs for events in the calibration sample and events in the signal sample. The total PID efficiency for the different decay channels is therefore determined taking into account the (transverse) momentum distribution of the tracks in samples of signal events. Each event receives a weight that reflects the momentum-dependent efficiency for each of the tracks in that event. The total

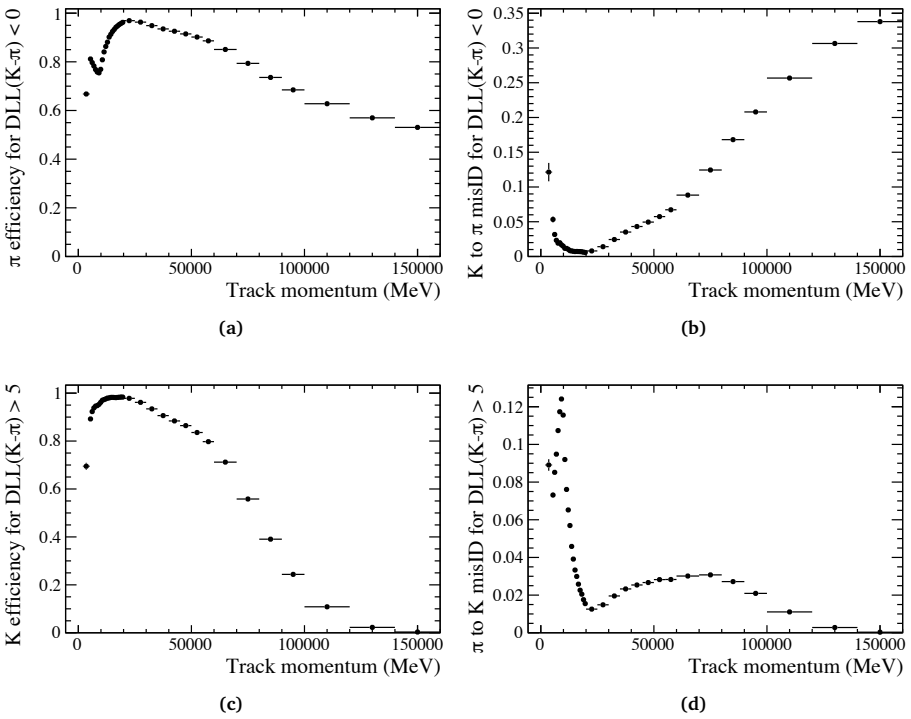

Fig. 5.14 · The momentum dependence of the PID performance. a) Efficiency to select a pion, for the requirement DLL$(K-\pi) < 0$. b) Kaon to pion misidentification, for the requirement DLL$(K-\pi) < 0$. c) Efficiency to select a kaon, for the requirement DLL$(K-\pi) > 5$. b) Pion to kaon misidentification, for the requirement DLL$(K-\pi) > 5$.

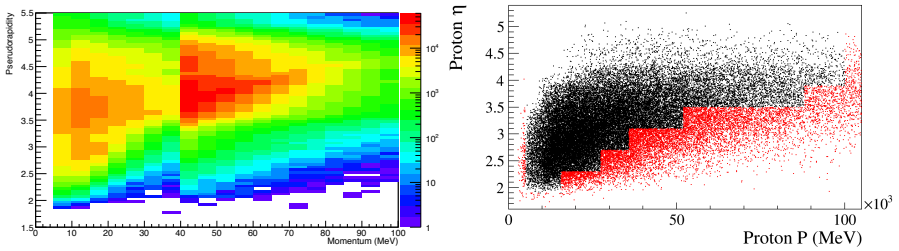

(a) (b)

Fig. 5.15 · a) Proton pseudorapidity–momentum distribution in the $\Lambda \to p\pi^-$ calibration sample. The discontinuity is the result of two different samples, which each have a different selection, that are being used. The colours represent the number of events present in the calibration sample. b) The region in which DLL$(p-\pi)$ criteria are applied is indicated in black. The data points correspond to the $\Lambda_b^0 \to \Lambda_c^+\pi^-$ signal sample.

signal efficiency is then calculated as the sum of all weights divided by the number of events:

$$\epsilon_{tot} = \frac{\sum_{i=0}^{N_s} \epsilon_{\rm cal}(p_i, p_{{\rm T},i})}{N_s}\,, \tag{5.26}$$

with N_s the number of signal events in the signal sample and $\epsilon_{\rm cal}$ the (transverse) momentum dependent efficiency as obtained from the calibration sample.

For the PID criteria on the bachelor particle, the (transverse) momentum distribution in a sample of real $\overline{B}^0 \to D^+\pi^-$ events can be used, as it has only negligible contamination from misidentified $\overline{B}_s^0 \to D_s^+\pi^-$ or $\overline{B}^0 \to D^+K^-$ events. Because the (transverse) momentum distributions of the latter decay channels show negligible differences compared to $\overline{B}^0 \to D^+\pi^-$, as shown in Fig. 5.10d, this sample can also be used to determine the efficiency of the PID criteria on the bachelor in $\overline{B}_s^0 \to D_s^+\pi^-$ and $\overline{B}^0 \to D^+K^-$ events. For the determination of the efficiency and misidentification probability of the PID criteria applied to the daughters of the D meson, the momentum distributions measured in simulated events are used. Because the momentum distributions of the D daughter tracks are different for the different decay channels, already a small amount of contamination from the other type of D can affect the measured performance. The typical efficiency to identify a pion (kaon) for the PID criteria chosen in this work is 85% (73%), while the kaon to pion (pion to kaon) misidentification rate is 9% (3%).

The PID performance also depends on the event occupancy, but since the signal and calibration samples are both hadronically triggered, their occupancy distributions are very similar. Additional reweighting by occupancy is thus not needed.

The efficiency and misidentification rates of the DLL$(p-\pi)$ criteria are obtained in a similar fashion, from a data sample of 13 million $\Lambda \to p\pi^-$ decays (Fig. 5.13c). In this case, the efficiency is also binned in track multiplicity since signal and proton calibration samples

$N^{\text{meas}}_{\overline{B}^0 \to D^+\pi^-}$	$106\,197 \pm 344$
$\epsilon(\pi)_{\text{DLL}(K-\pi)<0}$	$85.6 \pm 0.1\%$
$\epsilon_{\text{misID}}(\pi \to K)_{\text{DLL}(K-\pi)>5}$	$2.77 \pm 0.04\%$
Predicted $N^{\text{ex}}_{\overline{B}^0 \to D^+\pi^-}$	$3\,437 \pm 51$

Table 5.3 · $\overline{B}^0 \to D^+\pi^-$ event yield, efficiency and misidentification rate. All uncertainties are statistical.

have different track multiplicity distributions. To obtain the total signal efficiency simulated data is used. The proton PID calibration sample has poor statistics in the high momentum and high pseudorapidity region, as shown in Fig. 5.15a. As a result, the proton PID efficiency and misidentification cannot be accurately determined in this region. Therefore, the proton PID requirement is only applied to protons in the (p, η) region shown in black in Fig. 5.15b. The typical efficiency to identify a Λ_c baryon is 82%. The misidentification of a $D_{(s)}$ meson as a Λ_c baryon is high due to the limited kinematic region in which the PID criterium to identify a proton can be applied. However, only few events containing a $D_{(s)}$ meson fall within the Λ_c mass window, reducing the misidentification rate to approximately 4%.

5

Using PID for fit validation

The PID can be used as a consistency check between the fitted yields in the different decay channels. A small contribution of $\overline{B}^0 \to D^+\pi^-$ events is found in the $\overline{B}^0 \to D^+K^-$ sample. The number of expected $\overline{B}^0 \to D^+\pi^-$ events in the $\overline{B}^0 \to D^+K^-$ sample can be estimated using the $\overline{B}^0 \to D^+\pi^-$ event yield as obtained from the $\overline{B}^0 \to D^+\pi^-$ data sample, the PID efficiency of the bachelor pion, and the probability for a kaon to be misidentified as a bachelor pion,

$$N^{\text{ex}}_{\overline{B}^0 \to D^+\pi^-} = N^{\text{meas}}_{\overline{B}^0 \to D^+\pi^-} \frac{\epsilon_{\text{misID}}(\pi \to K)_{\text{DLL}(K-\pi)>5}}{\epsilon(\pi)_{\text{DLL}(K-\pi)<0}}. \tag{5.27}$$

Using the numbers obtained in the analysis described in chapter 6, which are summarised in Tab. 5.3 for convenience, one finds that the expected number of misidentified $\overline{B}^0 \to D^+\pi^-$ events in the $\overline{B}^0 \to D^+K^-$ sample is $3\,437 \pm 51$. The number of misidentified $\overline{B}^0 \to D^+\pi^-$ events measured in the $\overline{B}^0 \to D^+K^-$ data sample, using a fit to the invariant mass distribution, is $3\,424 \pm 97$. This yield agrees with the expected yield within one standard deviation. This gives confidence that the data is correctly modelled.

5.2.5 Modelling of the invariant mass distribution

The signal yields are determined from fits to the invariant mass distributions of the different decay channels, as shown in Figs. 5.7–5.8. This requires an accurate modelling of the shape of the invariant mass distribution of the signal and the various sources of background.

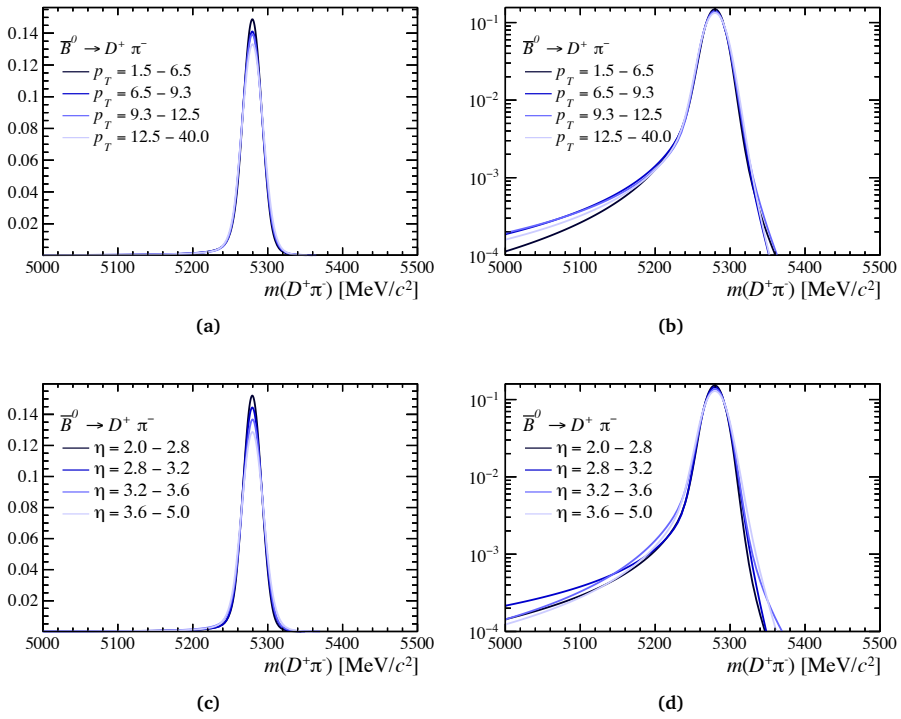

Fig. 5.16 · Signal shape for the $\overline{B}^0 \to D^+\pi^-$ decay channel in a)-b) four bins of p_{T} and c)-d) four bins of η, where the darkest line corresponds to the lowest p_{T} (η) bin and the lightest line to the highest p_{T} (η) bin. a) and c) are on a linear scale, in order to see differences in the width of the distribution, while b) and d) are on a logarithmic scale, in order to see small differences in the tails of the distribution. For clarity only the models are shown, while the data points from which the shapes are obtained are omitted.

5.2.5.1 Signal shape

The invariant mass distributions of the decay channels under study are modelled using a double crystal ball (CB) function [169], whose parameters are obtained from simulated data. The CB function is a Gaussian with a power-low tail,

$$f_{\mathrm{CB}}(m,\mu,\sigma,\alpha,n) = \begin{cases} e^{-\frac{(m-\mu)^2}{2\sigma^2}}, & \text{for } \frac{m-\mu}{\sigma} > -\alpha \\ \left(\frac{n}{|\alpha|}\right)^n \times e^{-|\alpha|^2/2} \times \left(\frac{n}{|\alpha|} - |\alpha| - \frac{m-\mu}{\sigma}\right)^{-n}, & \text{for } \frac{m-\mu}{\sigma} \leq -\alpha \end{cases}, \tag{5.28}$$

with m the invariant mass, μ and σ the mean and width of the signal peak, and the parameters α and n describing the shape of the tail. The double CB signal shape,

$$f_{\mathrm{DCB}}(m,\mu,\sigma,\alpha_1,n_1,\alpha_2,n_2) = f_{\mathrm{CB1}}(m,\mu,\sigma,\alpha_1,n_1) + f_{\mathrm{CB2}}(m,\mu,\sigma,\alpha_2,n_2)\,, \tag{5.29}$$

hence allows for two Gaussian widths and two power-law tails. The Gaussian widths of the two CB functions are chosen to be equal. Variations on this shape are considered, allowing for two different Gaussian widths, and omitting one of the tails. The former introduces an extra degree of freedom, which is not needed to accurately describe the signal shape, and is hence omitted. It is, however, used to estimate the systematic uncertainty resulting from the fit model. The latter is observed not to describe the simulated data well.

In order to measure the dependence of f_x/f_d on the p_{T} or η of the b hadron, the signal yields are determined in kinematic bins of these variables. The dependence of the signal model on the b-hadron kinematics has been studied using simulated data. As an example, the signal shape of the $\overline{B}^0 \to D^+\pi^-$ decay channel is shown in different kinematic bins in Fig. 5.16. An increased width of the signal invariant mass distribution has been observed for increasing p_{T} or η, which can be understood as the momentum resolution worsens for large momenta. The width of the distribution is allowed to float in the fit to data to accommodate for bin to bin variations. The variations seen in the tails of the signal distribution are not significant. The parameters controlling the shape of the tails are therefore fixed to those found in the overall sample. This study is carried out in only four kinematic bins in order to have enough statistics per bin. The bins are chosen to have a similar number of events in each bin.

5

5.2.5.2 Background shape

Two types of background are considered: "peaking" and "non-peaking". The combinatorial background, consisting of random combinations of tracks, is a non-peaking background and the shape of its invariant mass distribution can be determined from the upper side-band region. The sources of peaking background are partially reconstructed decays and misidentified decays. An accurate modelling of these sources of background is essential. The shapes of the invariant mass distributions of these decays are determined from simulated events. An exception is the cross-feed of $\overline{B}^0 \to D^+\pi^-$ decays in the $\overline{B}^0 \to D^+K^-$ and $\overline{B}^0_s \to D^+_s\pi^-$ samples. The shape of this source of background can be determined from data. It is difficult to accurately model the invariant mass distribution of partially reconstructed and misidentified decays based on a physical motivation, taking into account all the effects of the reconstruction and selection. Therefore, most peaking backgrounds are modelled using non-parametric distributions [170].

For partially reconstructed backgrounds typically a photon or a neutral pion is not reconstructed leading to a lower reconstructed invariant mass of the b-hadron candidate. An example of this type of background are $\overline{B}^0 \to D^{*+}\pi^-$ decays, where the D^{*+} meson decays to a D^+ meson and a neutral pion (or photon). The invariant mass distribution of these decays exhibits a very distinct "two hill" shape, as is seen in simulated data (Fig. 5.17a). The reconstructed invariant mass distribution depends on the decay angle θ_D, which is the angle between the D meson originating from the D^* decay (in the rest frame of the D^* meson) and the direction of boost of the D^* meson, as illustrated in Fig. 5.18. Because the D^* meson has a total angular momentum $J = 1$ while it decays to two particles which each have $J = 0$, the D^+-π^0 system must have a relative orbital angular momentum, $L = 1$. This results in a preferred direction of the $D^{*+} \to D^+\pi^0$ decay, following $d\Gamma/d\cos\theta_D = \cos^2\theta_D$, with the

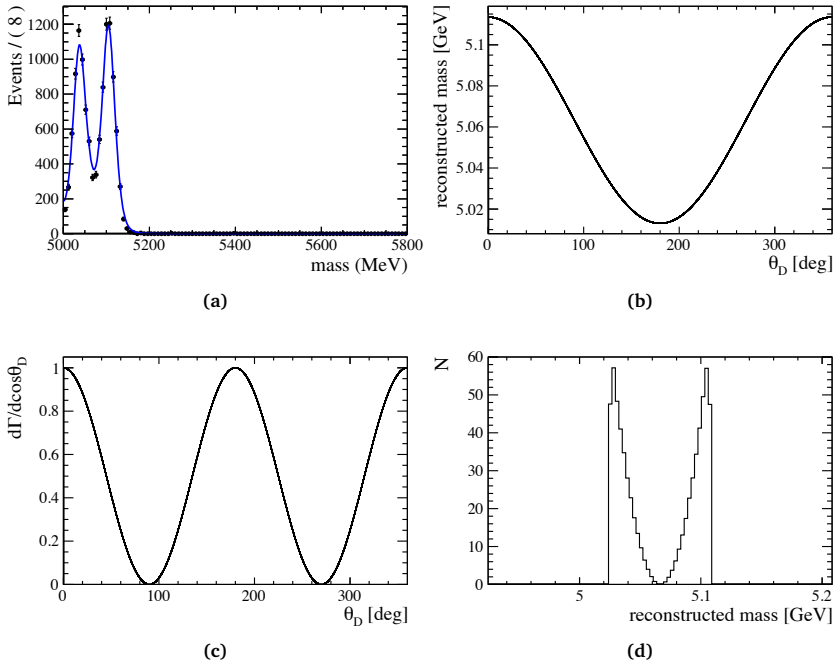

Fig. 5.17 · Shape of the invariant mass distribution of partially reconstructed $\overline{B}^0 \to D^{*+}\pi^-$ decays, where the π^0 from the D^* decay is not reconstructed: a) the invariant mass distribution observed in simulated events; b) the reconstructed mass of the B^0 meson, with the π^0 not reconstructed, depends on the decay angle θ_D; c) the angular distribution of the $D^{*+} \to D^+\pi^0$ decay and d) the invariant mass distribution of $\overline{B}^0 \to D^{*+}\pi^-$ decays determined from b) and c). Resolution, reconstruction, selection and detector effects are not taken into account in b)–d).

π^0 flying preferentially in or against the D^* flight direction. In the decay $\overline{B}^0 \to D^{*+}\pi^-$, both the B meson and the pion have spin zero, which implies that the D^* meson must have the third component of the angular momentum $J_z = m = 0$ and is therefore polarised. This leads to the "two hill" shape, as illustrated in Figs. 5.17b–5.17d.

The decay $\overline{B}^0_s \to D^{*+}_s\pi^-$ is related to the decay $\overline{B}^0 \to D^{*+}\pi^-$ via U-spin symmetry and a similar structure is expected, which is however not observed (see Fig.5.20a). This is understood because the D^{*+}_s decays predominantly via $D^{*+}_s \to D^+_s\gamma$ (because of OZI suppression [171–173] of $D^{*+}_s \to D^+_s\pi^0$) and the photon has spin 1. Hence the D^+_s-γ system has no relative orbital momentum, and there is no preferred direction in this decay.

An example of a source of background where one of the final state particles is misidentified is the decay $\overline{B}^0_s \to D^+_s(\to K^-K^+\pi^+)\pi^-$. It forms a background to both the $\overline{B}^0 \to D^+(\to \pi^+\pi^+K^-)\pi^-$ and the $\Lambda^0_b \to \Lambda^+_c(\to pK^-\pi^+)\pi^-$ decay channels, where a kaon from the D_s decay is misidentified as a pion or a proton, respectively. The shape

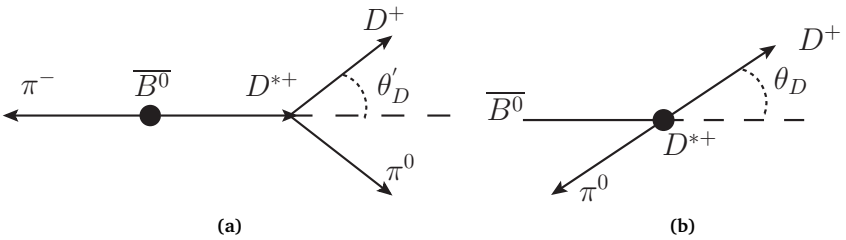

Fig. 5.18 · $\overline{B}^0 \to D^{*+}\pi^-$ decay in a) the B rest frame and b) the D^* rest frame. The angle θ_D is defined in the D^* rest frame as the angle between the D meson and the bachelor pion.

of this background is obtained from simulated events, by applying the pion (proton) mass hypothesis to the positive kaon from the D_s^+ meson. The distribution is reweighted using the momentum dependent misidentification efficiency. Misidentification of a kaon as the lighter pion shifts the mass distribution to lower values, whereas misidentification of a kaon as the heavier proton shifts it to higher values, as illustrated in Fig. 5.19a.

The abundant $\overline{B}^0 \to D^+\pi^-$ decay forms a misidentified background to the other decay channels under consideration in this analysis. In contrast to the other sources of background, the shape of this background can be obtained from real data rather than from simulated events. Due to the low background in the $\overline{B}^0 \to D^+\pi^-$ data sample, a high purity sample of $\overline{B}^0 \to D^+\pi^-$ events can be obtained by selecting events in a narrow mass window 5200–5340 MeV/c^2 around the $\overline{B}^0 \to D^+\pi^-$ peak (Fig. 5.7a).

The shape of the invariant mass distribution of $\overline{B}^0 \to D^+\pi^-$ decays mis-reconstructed as $\overline{B}^0 \to D^+K^-$ decays, is obtained in four steps. The shape of the distribution after each step is shown with a different colour in Fig. 5.19b. In the first step (black), the invariant mass distribution is obtained from the high purity sample. To obtain the high purity sample, the full selection, including the momentum dependent PID selection criteria, is applied. In step 2 (cyan), the events in the high purity sample are reweighted such that the original momentum distribution (before PID selection) of the bachelor pion is restored. The weights used for this reweighting step are obtained from data in the same narrow mass window, from a sample in which no PID criterium is applied to the bachelor hadron and which is thus contaminated with $\overline{B}^0 \to D^+K^-$ decays. However, the momentum distribution of the bachelor particle is very similar for these events, as shown in Fig 5.10d. The reweighting slightly broadens the invariant mass distribution. This can be understood, because the PID criteria to select a bachelor pion are more efficient at low momentum than at high momentum, as shown in Fig. 5.14a. As low momenta tracks are reconstructed with a better resolution, this results in a better mass resolution after the PID selection is applied. In the third step (orange), the reweighted events in the high purity sample are reconstructed using the kaon mass hypothesis for the bachelor particle. The invariant mass distribution now peaks at a higher invariant mass due the larger mass of the kaon compared to the pion, and in addition it broadens. To select $\overline{B}^0 \to D^+K^-$ decays, the momentum dependent PID criterium to

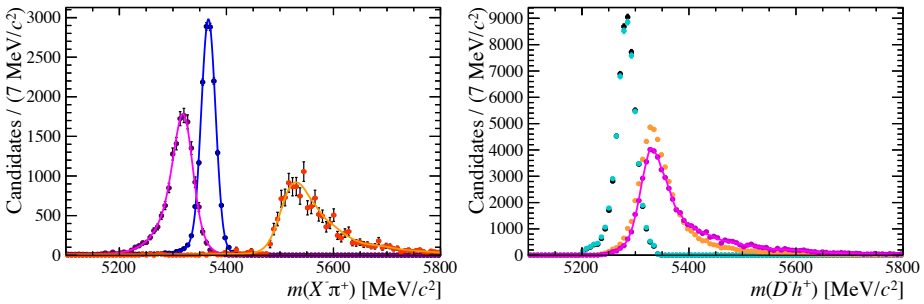

(a) (b)

Fig. 5.19 · Different sources of misidentified background decays. a) Simulated $\overline{B}{}^0_s \to D^+_s\pi^-$ data reconstructed as $\overline{B}{}^0_s \to D^+_s\pi^-$ (blue), $\overline{B}{}^0 \to D^+\pi^-$ (magenta) and $\Lambda^0_b \to \Lambda^+_c\pi^-$ (orange). b) Method to obtain the shape of misidentified $\overline{B}{}^0 \to D^+\pi^-$ decays in the $\overline{B}{}^0 \to D^+K^-$ signal sample. The $\overline{B}{}^0 \to D^+\pi^-$ invariant mass distributions correspond to step 1 (black), step 2 (cyan), step 3 (orange) and step 4 (magenta) described in the text.

select a bachelor kaon is used. In the forth step (magenta), the events are reweighted using the momentum dependent $\pi \to K$ misidentification rate, as obtained from the PID calibration samples (Fig. 5.14d). This broadens the invariant mass distribution and in addition it moves to slightly higher B^0 mass, due to the correlation between momentum and mass.

The dependence of the shape of the invariant mass distribution of all individual background decays on the b-hadron kinematics is studied. This is illustrated in Figs. 5.20a–5.20b for partially reconstructed $\overline{B}{}^0_s \to D^{*+}_s\pi^-$ decays reconstructed as $\overline{B}{}^0_s \to D^+_s\pi^-$ and for misidentified $\overline{B}{}^0 \to D^+\pi^-$ decays reconstructed as $\Lambda^0_b \to \Lambda^+_c\pi^-$. The shape of $\overline{B}{}^0_s \to D^{*+}_s\pi^-$ decays is obtained from simulated events. The dataset is divided in only three kinematic bins due to the limited statistics of the simulated event sample. The shape of the invariant mass distribution is found not to depend on the b-hadron kinematics for all backgrounds, with the only exception the $\overline{B}{}^0 \to D^+\pi^-$ background in the $\Lambda^0_b \to \Lambda^+_c\pi^-$ sample. Due to the limited region in which the proton PID criteria are applied (see Fig. 5.15b), the proton PID criteria are applied to a large fraction of the events in some kinematic bins, while they are applied to only a low fraction of events in others. This causes the invariant mass distribution of misidentified $\overline{B}{}^0 \to D^+\pi^-$ decays, reconstructed as $\Lambda^0_b \to \Lambda^+_c\pi^-$, to differ slightly from bin to bin. Hence, a different shape is used for each kinematic bin for this specific background. For clarity only four bins are shown in Figs. 5.20c–5.20d.

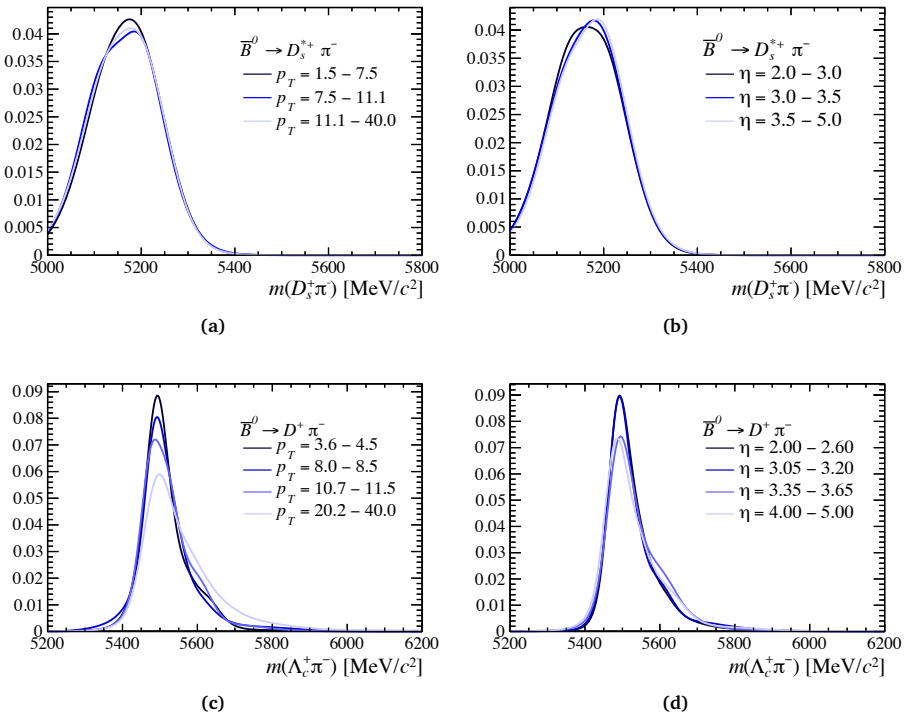

Fig. 5.20 · The shape of the invariant mass distribution can differ for different kinematic regions, as illustrated for a) $\overline{B}_s^0 \to D_s^{*+}\pi^-$, p_{T} binning, b) $\overline{B}_s^0 \to D_s^{*+}\pi^-$, η binning, c) $\overline{B}^0 \to D^+\pi^-$, p_{T} binning and d) $\overline{B}^0 \to D^+\pi^-$, η binning. Dark colours correspond to low p_{T} (η) and light colours to high p_{T} (η). For clarity reasons, only the shapes are shown while the data points are omitted.

5.2.6 Background checks

A detailed understanding of the different sources of potential background is essential for the precise determination of the signal yields. A selection of potential sources of background is discussed in detail.

5.2.6.1 Combinatorial background

The composition of the combinatorial background is studied using the events in the upper sideband of the b-hadron invariant mass distribution. In particular, the contribution of the combination of a real c hadron (D, D_s, Λ_c) with a random track is studied. In addition, a random combination of four tracks forms a source of combinatorial background. The upper sideband is defined as $m > 5500$, $m > 5550$ and $m > 5750$ for $\overline{B}^0 \to D^+\pi^-$, $\overline{B}_s^0 \to D_s^+\pi^-$ and $\Lambda_b^0 \to \Lambda_c^+\pi^-$ decays, respectively, where the first two are chosen to exclude the background from $\Lambda_b^0 \to \Lambda_c^+\pi^-$ decays. The resulting c-hadron mass distribution

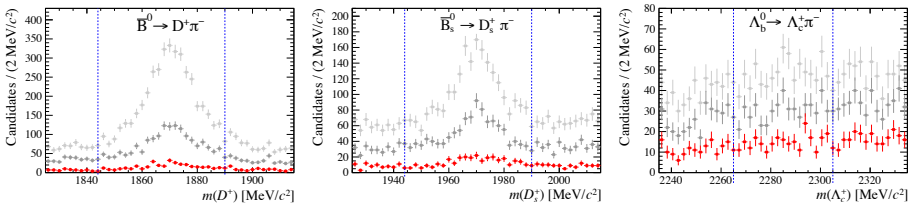

(a) (b) (c)

Fig. 5.21 · Invariant mass distribution of the c hadron, measured in the a) $\overline{B}^0 \to D^+\pi^-$, b) $\overline{B}_s^0 \to D_s^+\pi^-$ and c) $\Lambda_b^0 \to \Lambda_c^+\pi^-$ samples, for events in the upper sideband of the b-hadron invariant mass, for BDT > 0.0 (light grey), BDT > 0.3 (dark grey), and BDT > 0.66 (red), where the latter is the nominal selection criterium used in the analysis. The blue dashed lines indicate the c-hadron mass window used in the analysis.

is shown in Fig. 5.21, for different criteria on the BDT to increase the available statistics. A clear peak at the relevant c-hadron mass can be seen in the $\overline{B}^0 \to D^+\pi^-$ and $\overline{B}_s^0 \to D_s^+\pi^-$ samples for a low criterium on the BDT. The component consisting of four random tracks is larger in the $\overline{B}_s^0 \to D_s^+\pi^-$ sample, which is expected given the lower prompt D_s cross-section [174] and lower D_s branching fraction to the final state used in this analysis [84]. In the $\Lambda_b^0 \to \Lambda_c^+\pi^-$ sample no hint is seen of a contribution of real Λ_c baryons combined with a random track. The BDT is observed to reduce the c-hadron component present in the combinatorial background.

5.2.6.2 Charmonium background

Four-body decays are a potential source of background to the $B \to Dh$ signal modes if (one of) their three-body masses fall into the c-hadron mass window. Decay channels with charmonium, such as $B_s^0 \to J/\psi\,\phi$, $B^0 \to J/\psi\,K^+\pi^-$ or $\Lambda_b^0 \to J/\psi\,pK^-$, can form a background, as J/ψ mesons can decay into two opposite-sign muons which can be misidentified as pions. Moreover, these sources of background will peak in the same region as the signal, due to the small mass difference between the pion and the muon. The PID criteria used to select kaons and protons strongly suppress muons, hence little muon-to-kaon or muon-to-proton misidentification is expected.

The presence of charmonium in the data can be checked by studying the two-body invariant mass distribution of two pions, which are reconstructed with the muon mass assigned. In the $\overline{B}^0 \to D^+\pi^-$ case, this can be either pion from the $D^+ \to K^-\pi^+\pi^+$ decay, combined with the bachelor pion. Note that the two pions used to form the D meson cannot originate from charmonium decay as they carry the same charge. The combination of the low momentum pion from the D with the bachelor, and the combination of the high momentum pion with the bachelor, are considered individually in Fig. 5.22. No clear peak at the J/ψ mass of 3096 MeV/c^2 has been found in the data samples of all signal modes. In the $\Lambda_b^0 \to \Lambda_c^+\pi^-$ data sample a double peaking structure is observed around 1400 MeV/c^2. This structure is caused solely by events occupying the lower sideband of the Λ_b^0 invariant

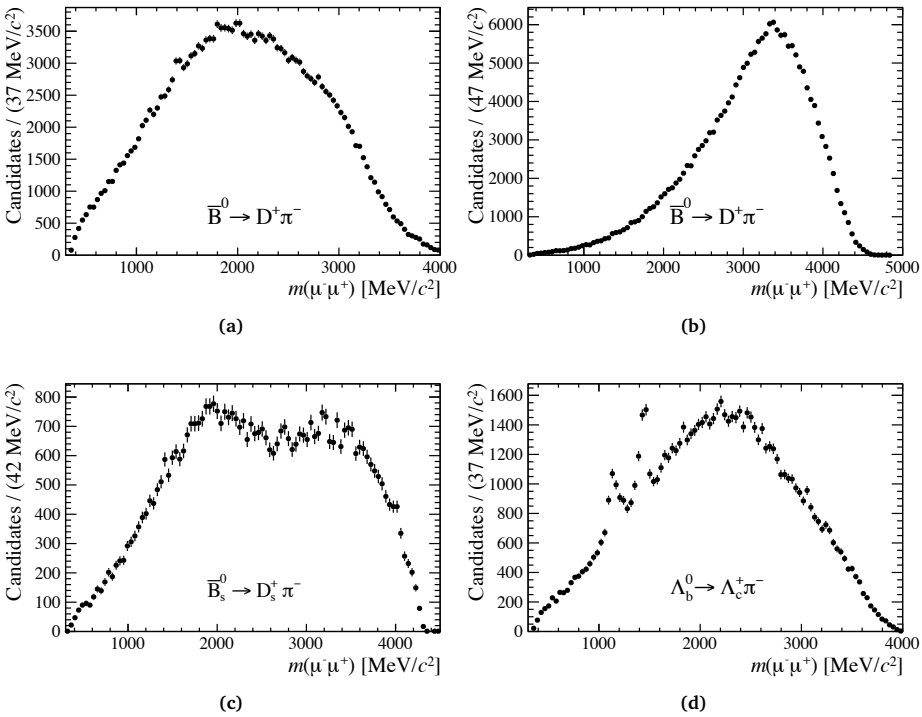

Fig. 5.22 · Invariant mass distribution of two final state pions, reconstructed with the muon mass hypothesis assigned, in data samples of the different signal modes: a) $\overline{B}^0 \to D^+\pi^-$ mode, the low momentum pion from the D meson decay combined with the bachelor; b) $\overline{B}^0 \to D^+\pi^-$ mode, the high momentum pion from the D meson decay combined with the bachelor; c) the $\overline{B}_s^0 \to D_s^+\pi^-$ mode and d) the $\Lambda_b^0 \to \Lambda_c^+\pi^-$ mode.

mass distribution (Fig. 5.23) and is hence not expected to have an effect on the fitted signal yield.

5.2.6.3 Charmless background

Charmless decays, like $B^0 \to K\pi\pi\pi$ or $B_s^0 \to KK\pi\pi$, where the b hadron decays directly to the four final state particles without an intermediate c hadron, can form a background to the studies described in this thesis. Charmless decays are highly suppressed by a requirement on the $D_{(s)}$ flight distance. This requirement is not applied in the $\Lambda_b^0 \to \Lambda_c^+\pi^-$ sample because of the shorter lifetime of the Λ_c baryon. The number of charmless decays surviving the selection can be estimated by analysing the b-hadron invariant mass distribution for events in the c-hadron sidebands.

The presence of cross-feed between the different c hadrons is evaluated on simulated events and illustrated in Fig. 5.24. Misidentified D mesons can inhabit the D_s sideband, and

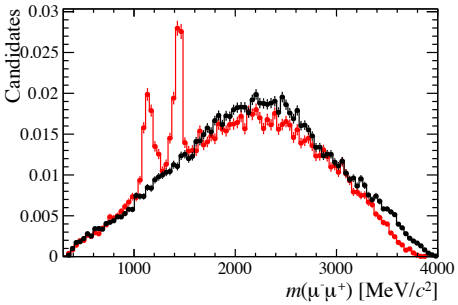

Fig. 5.23 · Normalised invariant mass distribution of two final state pions, reconstructed with the muon mass hypothesis assigned, in a $\Lambda_b^0 \to \Lambda_c^+\pi^-$ data sample in the lower sideband $m(\Lambda_c\pi) < 5575$ (red) and in the signal region $5576 < m(\Lambda_c\pi) < 5670$ corresponding to a 3σ window around the signal peak (black). The peaking structure observed around 1400 MeV/c^2 is entirely attributed to events from the lower sideband.

vice versa. In order to minimise such background, only the upper sideband of the D meson, $1910 < m_D < 1945$ MeV/c^2, and the lower sideband of the D_s meson, $1890 < m_{D_s} < 1925$ MeV/c^2, are used to quantify background from charmless B decays. In addition, misidentified Λ_c baryons inhabit both the lower and the upper sideband of the $D_{(s)}$ meson. Both sidebands of the Λ_c baryon are in turn inhabited with D and D_s mesons, which makes it impossible to select a sideband without a contribution from a misidentified decay. The Λ_c sidebands are chosen as $2205 < m_{\Lambda_c} < 2245$ and $2325 < m_{\Lambda_c} < 2365$ MeV/c^2. All misidentified contributions are suppressed by the PID criteria applied to the daughter tracks of the c hadron.

The resulting b-hadron invariant mass distributions are shown in Fig. 5.25. In the $\overline{B}^0 \to D^+\pi^-$ and $\overline{B}_s^0 \to D_s^+\pi^-$ sample, a peaking contribution around 5450 MeV/c^2 is found from misidentified $\Lambda_b^0 \to \Lambda_c^+\pi^-$ decays, as expected from the presence of misidentified Λ_c baryons in the $D_{(s)}$ sidebands. In the $\Lambda_b^0 \to \Lambda_c^+\pi^-$ sample a large contribution is found from misidentified $\overline{B}^0 \to D^+\pi^-$ decays, which are only partly suppressed due to the limited kinematic region in which the PID criteria can be applied. Furthermore, in the $\overline{B}^0 \to D^+\pi^-$ case, a small peak containing approximately 300 events is seen near the B^0 mass. After scaling to the width of the signal window, this corresponds to 0.4% of the fitted $\overline{B}^0 \to D^+\pi^-$ signal yield. A systematic uncertainty of 0.4% is therefore assigned to the observed $\overline{B}^0 \to D^+\pi^-$ yield to account for backgrounds from charmless B decays. No systematic uncertainty is assigned to the other decay modes.

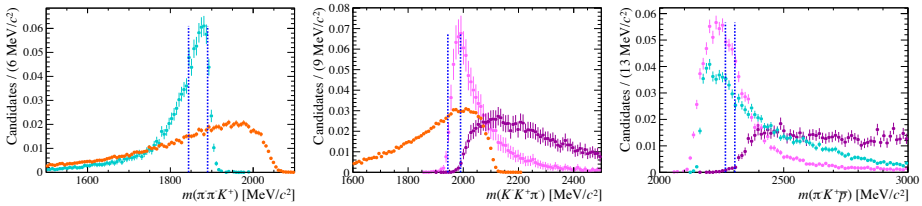

Fig. 5.24 · Normalised invariant mass distribution of c hadrons misidentified as a) the D meson, b) the D_s meson and c) the Λ_c^+ baryon. The magenta distributions correspond to misidentified D mesons, with light magenta if the low momentum pion of the $D^+ \to K^-\pi^+\pi^+$ decay is misidentified and dark magenta if the high momentum pion is misidentified. The cyan distribution corresponds to misidentified D_s mesons and the orange distribution corresponds to misidentified Λ_c baryons. The blue dashed lines indicates the mass windows of the c hadrons used in the analysis.

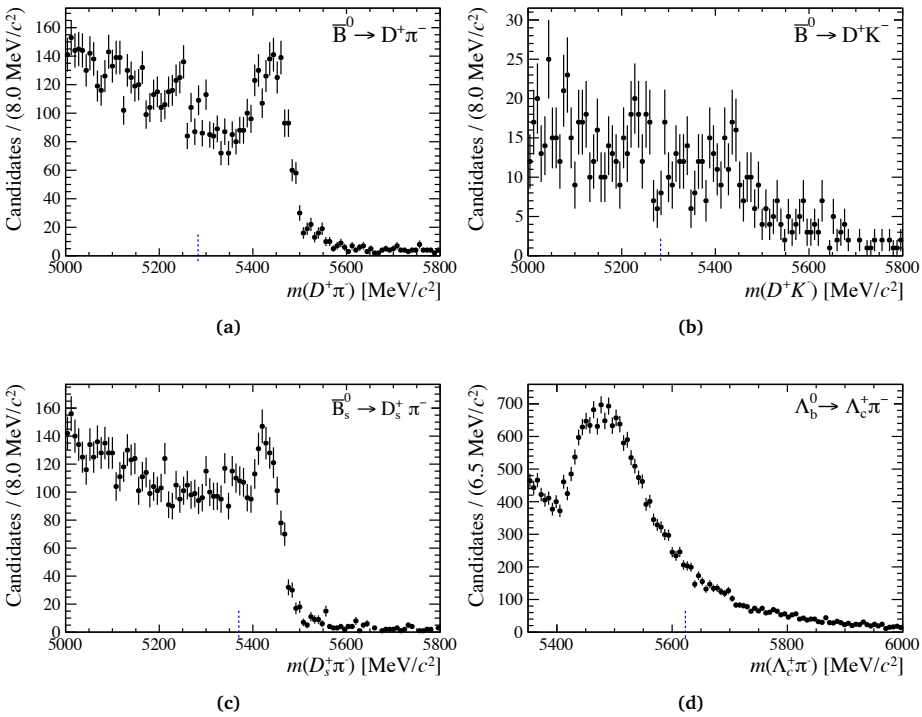

Fig. 5.25 · Invariant mass distribution of the b hadron candidates for events in the c-hadron sideband, for a) $\overline{B}^0 \to D^+\pi^-$, b) $\overline{B}^0 \to D^+K^-$, c) $\overline{B}_s^0 \to D_s^+\pi^-$ and d) $\Lambda_b^0 \to \Lambda_c^+\pi^-$ decays. The blue dashed line indicates the mass of the b hadron.

CHAPTER 6

Measurement of the ratio of B_s^0 and B^0 production: f_s/f_d

A paper describing a measurement of the ratio of fragmentation fractions f_s/f_d using the hadronic decays $\overline{B}^0 \to D^+K^-$ and $\overline{B}^0_s \to D^+_s\pi^-$ is reproduced on the following pages. This measurement uses the full 2011 LHCb dataset taken at $\sqrt{s} = 7\,\text{TeV}$, and supersedes the previous measurement [110] using a subset of this data. The kinematic dependencies of the relative production rates of B^0_s and B^0 mesons are measured for the first time using the hadronic tree decays $\overline{B}^0_s \to D^+_s\pi^-$ and $\overline{B}^0 \to D^+\pi^-$. A dependence of f_s/f_d on the transverse momentum of the B meson is observed. In addition, a measurement of the branching fraction of $\overline{B}^0 \to D^+K^-$ decays is included. The paper titled "Measurement of the fragmentation fraction ratio f_s/f_d and its dependence on the B meson kinematics" is published in JHEP [164].

Published for SISSA by Springer

Received: *January 23, 2013*
Accepted: *March 18, 2013*
Published: *April 2, 2013*

Measurement of the fragmentation fraction ratio f_s/f_d and its dependence on B meson kinematics

The LHCb collaboration

E-mail: Barbara.Storaci@cern.ch

Abstract: The relative production rate of B_s^0 and B^0 mesons is determined with the hadronic decays $B_s^0 \to D_s^- \pi^+$ and $B^0 \to D^- K^+$. The measurement uses data corresponding to $1.0\,\text{fb}^{-1}$ of pp collisions at a centre-of-mass energy of $\sqrt{s} = 7\,\text{TeV}$ recorded in the forward region with the LHCb experiment. The ratio of production rates, f_s/f_d, is measured to be $0.238 \pm 0.004 \pm 0.015 \pm 0.021$, where the first uncertainty is statistical, the second systematic, and the third theoretical. This is combined with a previous LHCb measurement to obtain $f_s/f_d = 0.256 \pm 0.020$. The dependence of f_s/f_d on the transverse momentum and pseudorapidity of the B meson is determined using the decays $B_s^0 \to D_s^- \pi^+$ and $B^0 \to D^- \pi^+$. There is evidence for a decrease with increasing transverse momentum, whereas the ratio remains constant as a function of pseudorapidity. In addition, the ratio of branching fractions of the decays $B^0 \to D^- K^+$ and $B^0 \to D^- \pi^+$ is measured to be $0.0822 \pm 0.0011\,(\text{stat}) \pm 0.0025\,(\text{syst})$.

Keywords: Hadron-Hadron Scattering, Branching fraction, B physics, Flavor physics

ArXiv ePrint: 1301.5286

Contents

1 Introduction

The ratio of fragmentation fractions f_s/f_d quantifies the relative production rate of B_s^0 mesons with respect to B^0 mesons. Knowledge of this quantity is essential when determining any B_s^0 branching fraction at the LHC. The measurement of the branching fraction of the rare decay $B_s^0 \to \mu^+\mu^-$ [1] is the prime example where a precise measurement of f_s/f_d is crucial for reaching the highest sensitivity in the search for physics beyond the Standard Model. The branching fractions of a large number of B^0 and B^+ decays have been measured to high precision at the B factories [2], but no B_s^0 branching fraction is yet known with sufficiently high precision to be used as a normalisation channel.

The relative production rates of b hadrons are determined by the fragmentation fractions f_u, f_d, f_s, f_c and f_Λ, which describe the probability that a b quark will hadronize into a B_q meson (where $q = u, d, s, c$), or a b baryon, respectively[1]. The ratio of fragmentation fractions f_s/f_d has been previously measured at LHCb with hadronic [3] and semileptonic decays [4], and the resulting values were combined [4].

In this paper, the ratio of fragmentation fractions f_s/f_d is determined using $B_s^0 \to D_s^-\pi^+$ and $B^0 \to D^-K^+$ decays collected in pp collisions at a centre-of-mass energy of $\sqrt{s} = 7\,\text{TeV}$, with data corresponding to an integrated luminosity of 1.0 fb^{-1} recorded with the LHCb detector. Since the framework of factorization is well applicable to these decays [5], their ratio of branching fractions is theoretically well understood [6] and their

[1] Charge conjugation is implied throughout this paper.

relative decay rates can be used to determine the ratio of fragmentation fractions for B_s^0 and B^0 mesons through

$$\begin{aligned}\frac{f_s}{f_d} &= \frac{\mathcal{B}(B^0 \to D^- K^+)}{\mathcal{B}(B_s^0 \to D_s^- \pi^+)} \frac{\epsilon_{DK}}{\epsilon_{D_s\pi}} \frac{N_{D_s\pi}}{N_{DK}} \\ &= \Phi_{\rm PS} \left|\frac{V_{us}}{V_{ud}}\right|^2 \left(\frac{f_K}{f_\pi}\right)^2 \frac{\tau_{B^0}}{\tau_{B_s^0}} \frac{1}{\mathcal{N}_a \mathcal{N}_F} \frac{\mathcal{B}(D^- \to K^+\pi^-\pi^-)}{\mathcal{B}(D_s^- \to K^+K^-\pi^-)} \frac{\epsilon_{DK}}{\epsilon_{D_s\pi}} \frac{N_{D_s\pi}}{N_{DK}}, \end{aligned} \tag{1.1}$$

where N corresponds to a signal yield, ϵ corresponds to a total efficiency, $\tau_{B_s^0}/\tau_{B^0} = 0.984 \pm 0.011$ [7] corresponds to the ratio of lifetimes and $\mathcal{B}(D^- \to K^+\pi^-\pi^-) = (9.14 \pm 0.20)\%$ [8] and $\mathcal{B}(D_s^- \to K^+K^-\pi^-) = (5.50 \pm 0.27)\%$ [9] correspond to the $D_{(s)}^-$ meson branching fractions. The factor $\mathcal{N}_a = 1.00 \pm 0.02$ accounts for the ratio of non-factorizable corrections [10], $\mathcal{N}_F = 1.092 \pm 0.093$ for the ratio of $B_{(s)}^0 \to D_{(s)}^-$ form factors [11], and $\Phi_{\rm PS} = 0.971$ for the difference in phase space due to the mass differences of the initial and final state particles. The numerical values used for the CKM matrix elements are $|V_{us}| = 0.2252$, $|V_{ud}| = 0.97425$, and for the decay constants are $f_\pi = 130.41\,\text{MeV}$, $f_K = 156.1\,\text{MeV}$, with negligible uncertainties, below 1% [2]. The measurement is not statistically limited by the size of the $B^0 \to D^- K^+$ sample , and therefore the theoretically less clean $B^0 \to D^-\pi^+$ decays, where exchange diagrams contribute to the total amplitude, do not contribute to the knowledge of f_s/f_d .

The ratio of fragmentation fractions can depend on the centre-of-mass energy, as well as on the kinematics of the $B_{(s)}^0$ meson, as was studied previously at LHCb with partially reconstructed B decays [4]. The dependence of the ratio of fragmentation fractions on the transverse momentum $p_{\rm T}$ and pseudorapidity η of the $B_{(s)}^0$ meson is determined using fully reconstructed $B^0 \to D^-\pi^+$ and $B_s^0 \to D_s^-\pi^+$ decays. Since it is only the dependence that is of interest here, the more abundant $B^0 \to D^-\pi^+$ decay is used rather than the $B^0 \to D^- K^+$ decay. The $B^0 \to D^- K^+$ and $B^0 \to D^-\pi^+$ decays are also used to determine their ratio of branching fractions, which can be used to quantify non-factorizable effects in such heavy-to-light decays [10].

The paper is organised as follows: the detector is described in section 2, followed by the event selection and the relative selection efficiencies in section 3. The fit to the mass distributions and the determination of the signal yields are discussed in section 4. The systematic uncertainties are presented in section 5, and the final results are given in section 6.

2 Detector and software

The LHCb detector [12] is a single-arm forward spectrometer covering the pseudorapidity range $2 < \eta < 5$, designed for the study of particles containing b or c quarks. The detector includes a high precision tracking system consisting of a silicon-strip vertex detector surrounding the pp interaction region, a large-area silicon-strip detector located upstream of a dipole magnet with a bending power of about 4 Tm, and three stations of silicon-strip detectors and straw drift tubes placed downstream. Data are taken with both magnet polarities. The combined tracking system has momentum resolution $\Delta p/p$ that varies from

0.4% at 5 GeV/c to 0.6% at 100 GeV/c, and impact parameter[2] resolution of 20 µm for tracks with high transverse momentum. Charged hadrons are identified using two ring-imaging Cherenkov detectors.

The trigger [13] consists of a hardware stage, based on information from the calorimeter and muon systems, followed by a software stage which applies a full event reconstruction. The events used in this analysis are selected at the hardware stage by requiring a cluster in the calorimeters with transverse energy larger than 3.6 GeV. The software stage requires a two-, three- or four-track secondary vertex with a high sum of the $p_{\rm T}$ of the tracks and a significant displacement from the primary pp interaction vertices (PVs). At least one track should have $p_{\rm T}$ greater than 1.7 GeV/c, track fit χ^2 over the number of degrees of freedom less than two, and IP χ^2 with respect to the associated primary interaction greater than sixteen. The IP χ^2 is defined as the difference between the χ^2 from the vertex fit of the associated PV reconstructed with and without the considered track. A multivariate algorithm is used for the identification of the secondary vertices consistent with the decay of a b hadron.

In the simulation, pp collisions are generated using Pythia 6.4 [14] with a specific LHCb configuration [15]. Decays of hadronic particles are described by EvtGen [16], whilst final state radiation is generated using Photos [17]. The interaction of the generated particles with the detector and its response are implemented using the Geant4 toolkit [18, 19] as described in ref. [20].

3 Event selection

The three decay modes, $B^0 \to D^-\pi^+$, $B^0 \to D^-K^+$ and $B_s^0 \to D_s^-\pi^+$, are topologically very similar and can therefore be selected using the same event selection criteria, thus minimizing efficiency differences between the modes. The $B^0_{(s)}$ candidates are reconstructed from a $D^-_{(s)}$ candidate and an additional pion or kaon (the "bachelor" particle), with the $D^-_{(s)}$ meson decaying to $K^+\pi^-\pi^-$ ($K^+K^-\pi^-$).

After the trigger selection, a loose preselection is made using the $B^0_{(s)}$ and $D^-_{(s)}$ masses, lifetimes and vertex qualities. A boosted decision tree (BDT) [21] is used to further separate signal from background. The BDT is trained on half the $B_s^0 \to D_s^-\pi^+$ data sample. The most discriminating variables are the $B^0_{(s)}$ impact parameter χ^2, the pointing angle of the $B^0_{(s)}$ candidate to the primary vertex and the $p_{\rm T}$ of the tracks. A cut value for the BDT output variable was chosen to optimally reduce the number of combinatorial background events, retaining approximately 84% of the signal events.

The $D^-_{(s)}$ candidates are identified by requiring the invariant mass under the $K^+\pi^-\pi^-$ ($K^+K^-\pi^-$) hypothesis to fall within the selection window 1844–1890 (1944–1990) MeV/c^2. The relative efficiency of the selection procedure is evaluated for all decay modes using simulated events, generated with the appropriate Dalitz plot structures [22, 23]. Since the analysis is only sensitive to relative efficiencies, the impact of any discrepancy between data and simulation is small.

[2]Impact parameter (IP) is defined as the transverse distance of closest approach between the track and a primary interaction.

The final $B_s^0 \to D_s^- \pi^+$, $B^0 \to D^- \pi^+$ and $B^0 \to D^- K^+$ event samples are obtained after particle identification (PID) criteria, based on the difference in log-likelihood between the kaon and pion hypotheses (DLL). The PID performance as a function of $p_{\rm T}$ and η of the track is estimated from data using a calibration sample of approximately 27 million $D^{*-} \to \overline{D}^0 (K^+\pi^-)\pi^-$ decays, which are selected using kinematic criteria only. A cut on the bachelor particle is placed at DLL$(K-\pi)<0$ to select the $B_s^0 \to D_s^- \pi^+$ and $B^0 \to D^- \pi^+$ event samples and at DLL$(K-\pi)>5$ to select the $B^0 \to D^- K^+$ sample. These requirements have an average efficiency of 85.5% and 73.0% respectively with a misidentification probability of 8.81% and 2.77%. The $D_s^- \to K^+K^-\pi^-$ decay is further distinguished from $D^- \to K^+\pi^-\pi^-$ decays by imposing DLL$(K-\pi)>5$ on the kaon candidate with the same charge as the D meson, whilst the DLL criteria for the π^- and K^+ are identical between D^- and D_s^- and are used to discriminate $D_{(s)}^-$ decays from background. The total (PID and invariant mass) efficiency to select the D^- (D_s^-) particle is 84.6% (78.5%) with a misidentification probability of 4.57% (0.77%).

4 Event yields

The relative yields of the three decay modes are determined from unbinned extended maximum likelihood fits to the mass distributions of the reconstructed $B_{(s)}^0$ candidates as shown in figure 1. In order to achieve the highest sensitivity, the sample is separated according to the two magnet polarities, allowing for possible differences in PID performance and in running conditions. A simultaneous fit to the two magnet polarities is performed for each decay mode, with the peak position and width of each signal shared between the two.

The signal mass shape is described by a Gaussian distribution with power-law tails on either side to model the radiative tail and non-Gaussian detector effects. It consists of a Crystal Ball function [24]

$$f_{\rm left}(m,\alpha,n,\mu,\sigma) = N \cdot \begin{cases} e^{-\frac{(m-\mu)^2}{2\sigma^2}}, & \text{for } \frac{m-\mu}{\sigma} > -\alpha \\ \left(\frac{n}{|\alpha|}\right)^n \cdot e^{-|\alpha|^2/2} \cdot \left(\frac{n}{|\alpha|} - |\alpha| - \frac{m-\mu}{\sigma}\right)^{-n}, & \text{for } \frac{m-\mu}{\sigma} \leq -\alpha \end{cases} \tag{4.1}$$

and a second, similar but mirrored, function to describe the right tail, resulting in the signal mass shape $f_{\rm 2CB}(m) = f_{\rm left}(m) + f_{\rm right}(m)$. The parameters of the tails are obtained from simulated events. The mean μ and the width σ of the Gaussian distribution are equal in both Crystal Ball functions, and are allowed to vary in the fit. The parameter N is a normalisation factor.

Three classes of background are considered in the fit: fully reconstructed decays where at least one track is misidentified, partially reconstructed decays with or without misidentified tracks and combinatorial background. The shapes of the invariant mass distributions for the partially reconstructed decays are taken from large samples of simulated events. The main sources are $B^0 \to D^- \rho^+$ and $B^0 \to D^{*-}\pi^+(K^+)$ for the $B^0 \to D^-\pi^+(K^+)$ sample, and $B_s^0 \to D_s^- \rho^+$ and $B_s^0 \to D_s^{*-}\pi^+$ for the $B_s^0 \to D_s^-\pi^+$ sample.

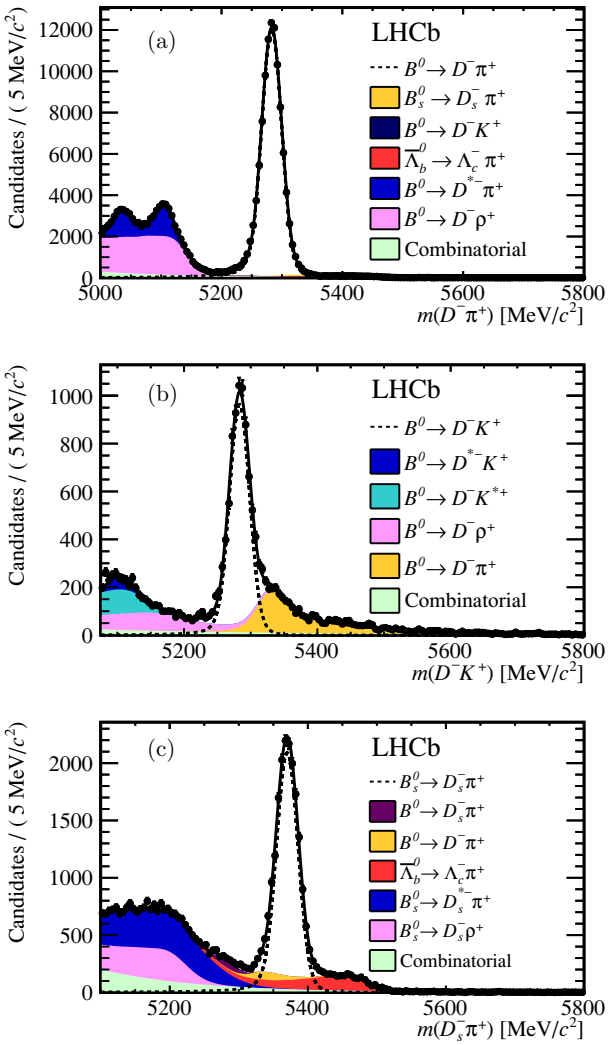

Figure 1. Invariant mass distributions of (a) $B^0 \to D^-\pi^+$ (b) $B^0 \to D^-K^+$ and (c) $B_s^0 \to D_s^-\pi^+$ candidates. The solid line is the result of the fit and the dotted line indicates the signal. The stacked background shapes follow the same top-to-bottom order in the legend and the plot. The B_s^0 and $\overline{\Lambda}_b^0$ backgrounds in the $B^0 \to D^-\pi^+$ mass distribution are invisibly small. The resulting signal yields are listed in table 1. For illustration purposes the figures include events from both magnet polarities, although they are fitted separately as described in the text.

Signal	Yield
$B^0 \to D^-\pi^+$	$106\,197 \pm 344$
$B^0 \to D^-K^+$	$7\,664 \pm 99$
$B_s^0 \to D_s^-\pi^+$	$17\,419 \pm 155$

Table 1. Yields obtained from the fits to the invariant mass distributions.

The invariant mass distributions of the misidentified decays are affected by the PID criteria. The shapes are obtained from simulated events, with the appropriate mass hypothesis applied. The distribution is then reweighted in a data-driven way, according to the particle identification cut efficiency obtained from the calibration sample, which is strongly dependent on the momentum of the particle.

Despite the small $\pi \to K$ misidentification probability of 2.8%, the largest misidentified background in the $B^0 \to D^-K^+$ sample originates from Cabibbo-favoured $B^0 \to D^-\pi^+$ decays where the bachelor pion is misidentified as a kaon. The shape of this particular misidentified decay is determined from data using a high purity sample of $B^0 \to D^-\pi^+$ decays (see figure 1(a)), obtained by selecting events in a narrow mass window 5200–5340 MeV/c^2. The yield of this prominent peaking background is allowed to vary in the fit and is found to be consistent with the expected yield based on the $B^0 \to D^-\pi^+$ signal yield and the misidentification probability. The contamination of $B^0 \to D^-\pi^+$ events in the $B_s^0 \to D_s^-\pi^+$ sample can be caused by the misidentification of either pion from the D^- decay. The misidentification probability is 2.0% (3.2%) for the higher (lower) p_{T} pion. After selecting the D_s^- candidate within the mass window around the nominal D_s^- mass [2], the number of misidentified pions is reduced to 0.75% (0.02%). The yield of this background is constrained in the fit, based on the $B^0 \to D^-\pi^+$ signal yield, the misidentification probability and their associated uncertainties.

The yield of $\overline{\Lambda}_b^0 \to \Lambda_c^-\pi^+$decays is allowed to vary in the fit. The cross-feeds from $B^0 \to D^-K^+$ and $B_s^0 \to D_s^-\pi^+$ events in the $B^0 \to D^-\pi^+$ signal is small, and are constrained to their respective predicted yields. In addition, a contribution from the rare $B^0 \to D_s^-\pi^+$ decay is expected with a yield of 3.3% compared to the $B_s^0 \to D_s^-\pi^+$ signal, and is accounted for accordingly.

The combinatorial background consists of events with random pions and kaons, forming a fake D^- or D_s^- candidate, as well as real D^- or D_s^- mesons, that combine with a random pion or kaon. The combinatorial background is modelled with an exponential shape.

The results of the fits are presented in figure 1, and the corresponding signal yields are listed in table 1. The total yields of the decays $B^0 \to D^-\pi^+$ and $B^0 \to D^-K^+$ are used to determine the ratio of their branching fractions, while the event yields of the decays $B_s^0 \to D_s^-\pi^+$ and $B^0 \to D^-K^+$ are used to measure the average ratio of fragmentation fractions.

The dependence of the relative b-hadron production fractions as a function of the transverse momentum and pseudorapidity of the $B_{(s)}^0$ meson is studied in the ranges $2.0 < \eta < 5.0$ and $1.5 < p_{\mathrm{T}} < 40$ GeV/c, using $B^0 \to D^-\pi^+$ and $B_s^0 \to D_s^-\pi^+$ decays. The

Source	$\frac{B^0\to D^-\pi^+}{B^0\to D^-K^+}$ (%)	$\frac{B_s^0\to D_s^-\pi^+}{B^0\to D^-K^+}$ (%)	$\frac{B_s^0\to D_s^-\pi^+}{B^0\to D^-\pi^+}$ (%)
Detector acceptance and reconstruction	0.7	0.7	$2.0-2.9$
Hardware trigger efficiency	2.0	2.0	0.8
Offline selection	1.2	1.1	1.2
BDT cut	1.0	1.0	1.5
PID selection	1.0	1.5	1.1
Comb. background	0.7	1.0	0.8
Signal shape (tails)	0.5	0.6	[correl.]
Signal shape (core)	0.8	1.0	[correl.]
Charmless background	0.4	—	[correl.]
Total	3.1	3.4	$3.2-3.8$

Table 2. Systematic uncertainties for the measurement of the corrected ratio of event yields used for the measurements of f_s/f_d and the relative branching fraction of $B^0\to D^-K^+$. The systematic uncertainty in $p_{\rm T}$ and η bins is shown as a range in the last column, and the total systematic uncertainty is the quadratic sum of the uncorrelated uncertainties. The systematic uncertainties on the ratio of $B^0\to D^-\pi^+$ and $B_s^0\to D_s^-\pi^+$ yields that are correlated among the bins do not affect the dependence on $p_{\rm T}$ or η, and are not accounted for in the total systematic uncertainty.

event sample is subdivided in 20 bins in $p_{\rm T}$ and 10 bins in η, with the bin sizes chosen to obtain approximately equal number of events per bin. The fitting model for each bin is the same as that for the integrated samples, apart from the treatment of the exponent of the combinatorial background distribution, which is fixed to the value obtained from the fits to the integrated sample.

5 Systematic uncertainties

The systematic uncertainties on the measurement of the relative event yields of the $B^0\to D^-\pi^+$, $B^0\to D^-K^+$ and $B_s^0\to D_s^-\pi^+$ decay modes are related to trigger and offline selection efficiency corrections, particle identification calibration and the fit model.

The response to charged pions and kaons of the hadronic calorimeter used at the hardware trigger level has been investigated. As the hardware trigger mostly triggers on the high-$p_{\rm T}$ bachelor, a systematic uncertainty of 2% is assigned to the ratio of trigger efficiencies for the decays $B^0\to D^-K^+$ and $B^0\to D^-\pi^+$, estimated from dedicated studies with $D^{*-}\to\overline{D}^0(K^+\pi^-)\pi^-$ decays. This uncertainty is assumed to be uncorrelated between the individual bins in the binned analysis.

The relative selection efficiencies from simulation are studied by varying the BDT criterion, changing the signal yields by about $\pm25\%$. The variation of the relative efficiency is 1.0% which is assigned as systematic uncertainty.

The uncertainty on the PID efficiencies is estimated by comparing, in simulated events, the results obtained using the D^{*-} calibration sample to the true simulated PID perfor-

mance on the signal decays. The corresponding uncertainty ranges from 1.0% to 1.5% for the different measurements.

The exponent of the combinatorial background distribution is allowed to vary in the fits to the $B^0 \to D^-\pi^+$ and $B_s^0 \to D_s^-\pi^+$ mass distributions. By studying $D^-\pi^-$ and D^-K^- combinations, it is suggested that the value of the exponent is smaller for the $B^0 \to D^-K^+$ decays than for the $B^0 \to D^-\pi^+$ decays, and therefore in the fit to the $B^0 \to D^-K^+$ candidates the exponent is fixed to half the value found in the fit to the $B^0 \to D^-\pi^+$ sample. The uncertainty on the signal yields due to the shape of the combinatorial background is estimated by reducing the exponent to half its value in the fits to the $B^0 \to D^-\pi^+$ and $B_s^0 \to D_s^-\pi^+$ mass distributions, and by taking a flat background for the fit to the $B^0 \to D^-K^+$ mass distribution. An uncertainty of 1.0% (0.7%) is assigned to the relative $B^0 \to D^-K^+$ and $B_s^0 \to D_s^-\pi^+$ ($B^0 \to D^-\pi^+$) yields.

The tails of the signal distributions are fixed from simulation due to the presence of large amounts of partially reconstructed decays in the lower sidebands. The uncertainty on the signal yield is estimated by varying the parameters that describe the tails by 10%. The uncertainty from the shape of the central peak is taken from a fit allowing for two different widths for the Crystal Ball functions in eq. 4.1, leading to a 1.0% (0.8%) uncertainty on the relative $B^0 \to D^-K^+$ and $B_s^0 \to D_s^-\pi^+$ ($B^0 \to D^-\pi^+$) yields.

The contribution of *charmless* B decays without an intermediate D meson is ignored in the fit. To evaluate the systematic uncertainty due to these decays, the B mass spectra for candidates in the sidebands of the D mass distribution are examined. A contribution of 0.4% relative to the signal yield is found in the $B^0 \to D^-\pi^+$ decay mode, and no contribution is seen in the other modes. For the $B^0 \to D^-\pi^+$ decay mode no correction is applied and the full size is taken as an uncertainty. No systematic uncertainty is assigned for the other decay modes.

The various sources of the systematic uncertainty that contribute to the uncertainties on the ratios of signal yields are listed in table 2. No uncertainty is associated to the $\overline{\Lambda}_b^0 \to \Lambda_c^-\pi^+$background, as the yield is allowed to vary in the fit. Other cross checks, like varying the $B^0 \to D_s^-\pi^+$yield in the $B_s^0 \to D_s^-\pi^+$ fit or including $\overline{\Lambda}_b^0 \to \Lambda_c^-K^+$in the $B^0 \to D^-K^+$ fit, show a negligible effect on the signal yields.

All systematic variations are also performed in bins, and the corresponding relative changes in the ratio of yields have been quantified. Variations showing correlated behaviour do not affect the slope and are therefore not considered further.

6 Results

The relative signal yields of the decays $B^0 \to D^-\pi^+$, $B^0 \to D^-K^+$ and $B_s^0 \to D_s^-\pi^+$ are used to determine the branching fraction of the decay $B^0 \to D^-K^+$, and the ratio of fragmentation fractions f_s/f_d .

The efficiency corrected ratio of $B^0 \to D^-K^+$ and $B^0 \to D^-\pi^+$ signal yields results in the ratio of branching fractions

$$\frac{\mathcal{B}\left(B^0 \to D^-K^+\right)}{\mathcal{B}\left(B^0 \to D^-\pi^+\right)} = 0.0822 \pm 0.0011\,(\text{stat}) \pm 0.0025\,(\text{syst}).$$

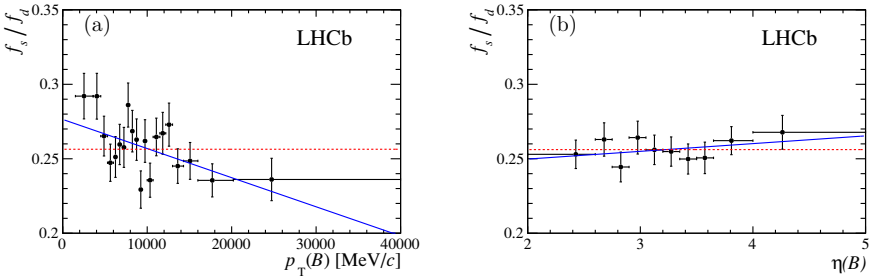

Figure 2. Ratio of fragmentation fractions f_s/f_d as functions of (a) $p_{\rm T}$ and (b) η. The errors on the data points are the statistical and uncorrelated systematic uncertainties added in quadrature. The solid line is the result of a linear fit, and the dashed line corresponds to the fit for the no-dependence hypothesis. The average value of $p_{\rm T}$ or η is determined for each bin and used as the center of the bin. The horizontal error bars indicate the bin size. Note that the scale is zero suppressed.

This is combined with the world average branching fraction $\mathcal{B}\left(B^0 \to D^-\pi^+\right) = (26.8 \pm 1.3) \times 10^{-4}$ [2], to give

$$\mathcal{B}\left(B^0 \to D^- K^+\right) = (2.20 \pm 0.03 \pm 0.07 \pm 0.11) \times 10^{-4},$$

where the first uncertainty is statistical, the second is systematic and the last is due to the uncertainty on the $B^0 \to D^-\pi^+$ branching fraction.

The ratio of fragmentation fractions is determined from the efficiency corrected event yields. The ratio of efficiencies is 0.913 ± 0.027. This results in

$$\begin{aligned}\frac{f_s}{f_d} &= (0.261 \pm 0.004 \pm 0.017) \times \frac{1}{\mathcal{N}_a \mathcal{N}_F} \\ &= 0.238 \pm 0.004 \pm 0.015 \pm 0.021\,,\end{aligned}$$

where the first uncertainty is statistical, the second is systematic containing the sources listed in table 2 as well as errors from external measurements, and the third is theoretical, due to the knowledge of $\mathcal{N}_a$ and $\mathcal{N}_F$. The last source is dominated by the uncertainty on the form factor ratio.

This measurement supersedes and is in agreement with the previous determination with hadronic decays [3]. It also agrees with the previous measurement based on semileptonic decays [4]. The two independent results are combined taking into account the various sources of correlated systematic uncertainties, notably the $D^-_{(s)}$ branching fractions and $B^0_{(s)}$ lifetimes, to give

$$\frac{f_s}{f_d} = 0.256 \pm 0.020, \tag{6.1}$$

which supersedes the previous measurement from LHCb.

The value of f_s/f_d in bins of $p_{\rm T}$ or η is determined using the $B_s^0 \to D_s^- \pi^+$ and $B^0 \to D^- \pi^+$ decay modes and is presented in figure 2. A linear χ^2 fit gives

$$f_s/f_d\,(p_{\rm T}) = (0.256 \pm 0.020) + (-2.0 \pm 0.6) \times 10^{-3}/\,{\rm GeV}/c \times (p_{\rm T} - \langle p_{\rm T}\rangle)$$
$$f_s/f_d\,(\eta) = (0.256 \pm 0.020) + (0.005 \pm 0.006) \times (\eta - \langle\eta\rangle),$$

with $\langle p_{\rm T}\rangle = 10.4\,{\rm GeV}/c$ and $\langle\eta\rangle = 3.28$. The data points are normalised with a scale factor to match the average value of 0.256. The uncertainty associated to this parameter is taken from eq. 6.1, whilst the error from the fit is 0.003 for both $p_{\rm T}$ and η.

The p-value for this linear fit is found to be 0.16 (0.87) for $p_{\rm T}$ (η). The observed slope for the dependence on the transverse momentum of the $B_{(s)}^0$ meson deviates from zero with a significance of three standard deviations. No indication of a dependence on $\eta(B)$ is found.

7 Conclusions

The relative production rate of B_s^0 and B^0 mesons is determined using the hadronic decays $B_s^0 \to D_s^- \pi^+$ and $B^0 \to D^- K^+$ resulting in $f_s/f_d = 0.238 \pm 0.004({\rm stat}) \pm 0.015({\rm syst}) \pm 0.021({\rm theo})$. This value is consistent with a previous LHCb measurement based on semileptonic decays, with which it is averaged to obtain $f_s/f_d = 0.256 \pm 0.020$. The ratio of fragmentation fractions f_s/f_d is determined as a function of the transverse momentum and pseudorapidity of the $B_{(s)}^0$ meson, and a variation consistent with a linear dependence on the transverse momentum of the the $B_{(s)}^0$ meson is observed, with a significance of three standard deviations. In addition, the ratio of branching fractions of the decays $B^0 \to D^- K^+$ and $B^0 \to D^- \pi^+$ is measured to be $0.0822 \pm 0.0011\,({\rm stat}) \pm 0.0025\,({\rm syst})$.

6

Acknowledgments

We express our gratitude to our colleagues in the CERN accelerator departments for the excellent performance of the LHC. We thank the technical and administrative staff at the LHCb institutes. We acknowledge support from CERN and from the national agencies: CAPES, CNPq, FAPERJ and FINEP (Brazil); NSFC (China); CNRS/IN2P3 and Region Auvergne (France); BMBF, DFG, HGF and MPG (Germany); SFI (Ireland); INFN (Italy); FOM and NWO (The Netherlands); SCSR (Poland); ANCS/IFA (Romania); MinES, Rosatom, RFBR and NRC "Kurchatov Institute" (Russia); MinECo, XuntaGal and GENCAT (Spain); SNSF and SER (Switzerland); NAS Ukraine (Ukraine); STFC (United Kingdom); NSF (USA). We also acknowledge the support received from the ERC under FP7. The Tier1 computing centres are supported by IN2P3 (France), KIT and BMBF (Germany), INFN (Italy), NWO and SURF (The Netherlands), PIC (Spain), GridPP (United Kingdom). We are thankful for the computing resources put at our disposal by Yandex LLC (Russia), as well as to the communities behind the multiple open source software packages that we depend on.

References

[1] LHCb collaboration, *First evidence for the decay $B_s \to \mu^+\mu^-$*, *Phys. Rev. Lett.* **110** (2013) 021801 [arXiv:1211.2674] [INSPIRE].

[2] Particle Data Group collaboration, J. Beringer et al., *Review of particle physics*, *Phys. Rev.* **D 86** (2012) 010001 [INSPIRE].

[3] LHCb collaboration, *Determination of f_s/f_d for 7 TeV pp collisions and a measurement of the branching fraction of the decay $B_d \to D^- K^+$"*, *Phys. Rev. Lett.* **107** (2011) 211801 [arXiv:1106.4435] [INSPIRE].

[4] LHCb collaboration, *Measurement of b-hadron production fractions in* 7 TeVpp *collisions*, *Phys. Rev.* **D 85** (2012) 032008 [arXiv:1111.2357] [INSPIRE].

[5] M. Beneke, G. Buchalla, M. Neubert and C.T. Sachrajda, *QCD factorization for exclusive, nonleptonic B meson decays: General arguments and the case of heavy light final states*, *Nucl. Phys.* **B 591** (2000) 313 [hep-ph/0006124] [INSPIRE].

[6] R. Fleischer, N. Serra and N. Tuning, *A new strategy for B_s branching ratio measurements and the search for new physics in $B_s^0 \to \mu^+\mu^-$*, *Phys. Rev.* **D 82** (2010) 034038 [arXiv:1004.3982] [INSPIRE].

[7] Heavy Flavor Averaging Group collaboration, Y. Amhis et al., *Averages of b-hadron, c-hadron and τ-lepton properties as of early 2012*, arXiv:1207.1158 [INSPIRE].

[8] CLEO collaboration, S. Dobbs et al., *Measurement of absolute hadronic branching fractions of D mesons and $e^+e^- \to D\bar{D}$ cross-sections at the $\psi(3770)$*, *Phys. Rev.* **D 76** (2007) 112001 [arXiv:0709.3783] [INSPIRE].

[9] CLEO collaboration, J. Alexander et al., *Absolute measurement of hadronic branching fractions of the D_s^+ meson*, *Phys. Rev. Lett.* **100** (2008) 161804 [arXiv:0801.0680] [INSPIRE].

[10] R. Fleischer, N. Serra and N. Tuning, *Tests of Factorization and* SU(3) *Relations in B Decays into Heavy-Light Final States*, *Phys. Rev.* **D 83** (2011) 014017 [arXiv:1012.2784] [INSPIRE].

[11] J.A. Bailey et al., *$B_s \to D_s/B \to D$ semileptonic form-factor ratios and their application to $BR(B_s^0 \to \mu^+\mu^-)$*, *Phys. Rev.* **D 85** (2012) 114502 [*Erratum ibid.* **D 86** (2012) 039904] [arXiv:1202.6346] [INSPIRE].

[12] LHCb collaboration, *The LHCb detector at the LHC*, 2008 *JINST* **3** S08005 [INSPIRE].

[13] R. Aaij et al., *The LHCb trigger and its performance*, arXiv:1211.3055 [INSPIRE].

[14] T. Sjöstrand, S. Mrenna and P.Z. Skands, *PYTHIA 6.4 physics and manual*, *JHEP* **05** (2006) 026 [hep-ph/0603175] [INSPIRE].

[15] I. Belyaev et al., *Handling of the generation of primary events in* Gauss*, the LHCb simulation framework*, *IEEE Nucl. Sci. Symp. Conf. Rec.* (2010) 1155.

[16] D. Lange, *The EvtGen particle decay simulation package*, *Nucl. Instrum. Meth.* **A 462** (2001) 152 [INSPIRE].

[17] P. Golonka and Z. Was, *PHOTOS Monte Carlo: a precision tool for QED corrections in Z and W decays*, *Eur. Phys. J.* **C 45** (2006) 97 [hep-ph/0506026] [INSPIRE].

[18] GEANT4 collaboration, J. Allison et al., *GEANT4 developments and applications*, *IEEE Trans. Nucl. Sci.* **53** (2006) 270.

[19] GEANT4 collaboration, S. Agostinelli et al., *GEANT4: a simulation toolkit*, *Nucl. Instrum. Meth.* **A 506** (2003) 250 [INSPIRE].

[20] M. Clemencic et al., *The LHCb simulation application,* GAUSS*: design, evolution and experience*, *J. Phys. Conf. Ser.* **331** (2011) 032023.

[21] L. Breiman, J.H. Friedman, R.A. Olshen and C.J. Stone, *Classification and regression trees*, Wadsworth international group, Belmont U.S.A. (1984).

[22] BABAR collaboration, P. del Amo Sanchez et al., *Dalitz plot analysis of* $D_s^+ \to K^+K^-\pi^+$, *Phys. Rev.* **D 83** (2011) 052001 [arXiv:1011.4190] [INSPIRE].

[23] CLEO collaboration, G. Bonvicini et al., *Dalitz plot analysis of the* $D^+ \to K^-\pi^+\pi^+$ *decay*, *Phys. Rev.* **D 78** (2008) 052001 [arXiv:0802.4214] [INSPIRE].

[24] T. Skwarnicki, *A study of the radiative cascade transitions between the* Υ' *and* Υ *resonances*, Ph.D. thesis, Institute of Nuclear Physics, Krakow, Poland (1986) [INSPIRE].

CHAPTER 7

Measurement of the ratio of Λ_b^0 and B^0 production: $f_{\Lambda_b^0}/f_d$

A paper describing the study of the kinematic dependencies of the relative production rates of Λ_b^0 baryons and B^0 mesons is reproduced on the following pages. This measurement uses the full 2011 LHCb dataset taken at $\sqrt{s} = 7\,\text{TeV}$. The measurement of the efficiency corrected events yields of $\Lambda_b^0 \to \Lambda_c^+\pi^-$ and $\overline{B}^0 \to D^+\pi^-$ decays reveals a dependence of $f_{\Lambda_b^0}/f_d$ on both the transverse momentum and the pseudorapidity of the b hadron. In addition, the branching fraction of $\Lambda_b^0 \to \Lambda_c^+\pi^-$ decays is determined, using external input from a previous measurement of $f_{\Lambda_b^0}/f_d$ using semileptonic decays [97]. This is the most precise Λ_b^0 branching fraction known to date. The paper titled "Study of the kinematic dependencies of Λ_b^0 production in pp collisions and a measurement of the $\Lambda_b^0 \to \Lambda_c^+\pi^-$ branching fraction" is published in JHEP [165].

Published for SISSA by Springer

Received: *May 28, 2014*
Accepted: *July 15, 2014*
Published: *August 26, 2014*

Study of the kinematic dependences of Λ_b^0 production in pp collisions and a measurement of the $\Lambda_b^0 \to \Lambda_c^+\pi^-$ branching fraction

The LHCb collaboration

E-mail: l.carson@ed.ac.uk

Abstract: The kinematic dependences of the relative production rates, $f_{\Lambda_b^0}/f_d$, of Λ_b^0 baryons and B^0 mesons are measured using $\Lambda_b^0 \to \Lambda_c^+\pi^-$ and $\overline{B}^0 \to D^+\pi^-$ decays. The measurements use proton-proton collision data, corresponding to an integrated luminosity of $1\,\text{fb}^{-1}$ at a centre-of-mass energy of 7 TeV, recorded in the forward region with the LHCb experiment. The relative production rates are observed to depend on the transverse momentum, p_T, and pseudorapidity, η, of the beauty hadron, in the studied kinematic region $1.5 < p_\text{T} < 40\,\text{GeV}/c$ and $2 < \eta < 5$. Using a previous LHCb measurement of $f_{\Lambda_b^0}/f_d$ in semileptonic decays, the branching fraction $\mathcal{B}\left(\Lambda_b^0 \to \Lambda_c^+\pi^-\right) = \Big(4.30 \pm 0.03\,^{+0.12}_{-0.11} \pm 0.26 \pm 0.21\Big) \times 10^{-3}$ is obtained, where the first uncertainty is statistical, the second is systematic, the third is from the previous LHCb measurement of $f_{\Lambda_b^0}/f_d$ and the fourth is due to the $\overline{B}^0 \to D^+\pi^-$ branching fraction. This is the most precise measurement of a Λ_b^0 branching fraction to date.

Keywords: Hadron-Hadron Scattering, B physics, Heavy quark production, Branching fraction, Particle and resonance production

ArXiv ePrint: 1405.6842

Contents

1 Introduction

Measurements of beauty hadron production in high-energy proton-proton (pp) collisions provide valuable information on fragmentation and hadronisation within the framework of quantum chromodynamics [1]. The study of beauty baryon decays also provides an additional channel for investigating CP violation [2]. While significant progress has been made in the understanding of the production and decay properties of beauty mesons, knowledge of beauty baryons is limited.

The relative production rates of beauty hadrons are described by the fragmentation fractions f_u, f_d, f_s, f_c and $f_{\Lambda_b^0}$, which describe the probability that a b quark fragments into a B_q meson (where $q = u, d, s, c$) or a Λ_b^0 baryon, respectively, and depend on the kinematic properties of the b quark. Strange b baryons are less abundantly produced [3] and are neglected here. Measurements of ground state b hadrons produced at the pp interaction point also include decay products of excited b hadrons. In the case of B mesons, such excited states include B^* and B^{**} mesons, while Λ_b^0 baryons can be produced via decays of Λ_b^{*0} or $\Sigma_b^{(*)}$ baryons.

Knowledge of the relative production rate of Λ_b^0 baryons is necessary to measure absolute Λ_b^0 branching fractions. The measurement of the branching fraction of the $\Lambda_b^0 \to \Lambda_c^+\pi^-$ decay reported in this paper improves the determination of any Λ_b^0 branching fraction measured relative to the $\Lambda_b^0 \to \Lambda_c^+\pi^-$ decay. The inclusion of charge conjugate processes is implied throughout this paper. The average branching fraction and production ratios are measured.

Previous measurements of $f_{\Lambda_b^0}/f_d$ have been made in e^+e^- collisions at LEP [4], $p\overline{p}$ collisions at CDF [5, 6] and pp collisions at LHCb [7]. The value of $f_{\Lambda_b^0}/f_d$ measured at LEP differs significantly from the values measured at the hadron colliders, indicating a strong dependence of $f_{\Lambda_b^0}/f_d$ on the kinematic properties of the b quark.

The LHCb analysis [7] was based on semileptonic $\Lambda_b^0 \to \Lambda_c^+ \mu^- \bar{\nu} X$ and $\overline{B} \to D\mu^- \bar{\nu} X$ decays, where the B meson is charged or neutral, and X represents possible additional decay products of the b hadron that are not included in the candidate reconstruction. Near equality of the inclusive semileptonic decay width of all b hadrons was assumed. The analysis measured $f_{\Lambda_b^0}/(f_u + f_d)$, which can be converted into $f_{\Lambda_b^0}/f_d$ under the assumption of isospin symmetry, i.e. $f_u = f_d$. A clear dependence of $f_{\Lambda_b^0}/f_d$ on the transverse momentum $p_{\rm T}$ of the $\Lambda_c^+\mu^-$ and $D\mu^-$ pairs was observed. A CMS analysis [8] using $\Lambda_b^0 \to J/\Psi\Lambda$ decays also found that the cross-section for Λ_b^0 baryons fell faster with $p_{\rm T}$ than the b-meson cross-sections.

The present paper uses a data sample, corresponding to an integrated luminosity of $1\,{\rm fb}^{-1}$ of pp collision data at a centre-of-mass energy of 7 TeV, collected with the LHCb detector. This is a substantially increased data sample compared to that in ref. [7]. The analysis aims to clarify the extent and characteristics of the $p_{\rm T}$ dependence of $f_{\Lambda_b^0}/f_d$. Moreover, the dependence of $f_{\Lambda_b^0}/f_d$ on the pseudorapidity η, defined in terms of the polar angle θ with respect to the beam direction as $-\ln(\tan\theta/2)$, is studied for the first time. The analysis covers the fiducial region $1.5 < p_{\rm T} < 40\,{\rm GeV}/c$ and $2 < \eta < 5$.

The hadronic decays $\Lambda_b^0 \to \Lambda_c^+\pi^-$ and $\overline{B}^0 \to D^+\pi^-$ are used, with the charm hadrons reconstructed using the decay modes $\Lambda_c^+ \to pK^-\pi^+$ and $D^+ \to K^-\pi^+\pi^+$, respectively. The data sample and the selection of $\overline{B}^0 \to D^+\pi^-$ decays are identical to those used in ref. [9]. Although a precise measurement of the absolute value of $f_{\Lambda_b^0}/f_d$ is not possible with these decays, since the $\Lambda_b^0 \to \Lambda_c^+\pi^-$ branching fraction is poorly known [10], they can be used to measure the dependence of $f_{\Lambda_b^0}/f_d$ on the b-hadron kinematic properties to high precision. This is achieved by measuring the efficiency-corrected yield ratio $\mathcal{R}$ in bins of $p_{\rm T}$ or η of the beauty hadron

$$\mathcal{R}(x) \equiv \frac{N_{\Lambda_b^0 \to \Lambda_c^+\pi^-}(x)}{N_{\overline{B}^0 \to D^+\pi^-}(x)} \times \frac{\varepsilon_{\overline{B}^0 \to D^+\pi^-}(x)}{\varepsilon_{\Lambda_b^0 \to \Lambda_c^+\pi^-}(x)}, \tag{1.1}$$

where N is the event yield, ϵ is the total reconstruction and selection efficiency, and x denotes $p_{\rm T}$ or η. The quantity $\mathcal{R}$ is related to $f_{\Lambda_b^0}/f_d$ through

$$\begin{aligned} \frac{f_{\Lambda_b^0}}{f_d}(x) &= \frac{\mathcal{B}\left(\overline{B}^0 \to D^+\pi^-\right)}{\mathcal{B}(\Lambda_b^0 \to \Lambda_c^+\pi^-)} \times \frac{\mathcal{B}(D^+ \to K^-\pi^+\pi^+)}{\mathcal{B}(\Lambda_c^+ \to pK^-\pi^+)} \times \mathcal{R}(x) \\ &\equiv \mathcal{S} \times \mathcal{R}(x), \end{aligned} \tag{1.2}$$

where $\mathcal{S}$ is a constant scale factor.

Since the value of $f_{\Lambda_b^0}/f_d$ in a given bin of $p_{\rm T}$ or η is independent of the decay mode of the b hadron, the values of $f_{\Lambda_b^0}/f_d(p_{\rm T})$ from the semileptonic analysis [7] can be compared to the measurement of $\mathcal{R}(p_{\rm T})$, which allows for the extraction of the value of $\mathcal{S}$. The branching fraction $\mathcal{B}\left(\Lambda_b^0 \to \Lambda_c^+\pi^-\right)$ can then be readily obtained using eq. (1.2). Notably, the dependence on $\mathcal{B}\left(\Lambda_c^+ \to pK^-\pi^+\right)$ cancels when extracting $\mathcal{B}\left(\Lambda_b^0 \to \Lambda_c^+\pi^-\right)$ in this way, because this branching fraction also enters in the semileptonic measurement of $f_{\Lambda_b^0}/f_d$. Furthermore, the branching fractions $\mathcal{B}\left(\overline{B}^0 \to D^+\pi^-\right)$ [10] and $\mathcal{B}\left(D^+ \to K^-\pi^+\pi^+\right)$ [11] are well known, leading to a precise determination of $\mathcal{B}\left(\Lambda_b^0 \to \Lambda_c^+\pi^-\right)$.

The dependence of the semileptonic $f_{\Lambda_b^0}/f_d$ measurement on $\mathcal{B}\left(\Lambda_b^0 \to \Lambda_c^+ \mu^- \bar{\nu} X\right)$, and the assumption of near equality of the inclusive semileptonic decay width of all b hadrons, implies that the measurement of $\mathcal{B}\left(\Lambda_b^0 \to \Lambda_c^+ \pi^-\right)$ from the current paper cannot be used to normalise existing measurements of $\mathcal{B}\left(\Lambda_b^0 \to \Lambda_c^+ \mu^- \bar{\nu} X\right)$ [10].

2 Detector and simulation

The LHCb detector [12] is a single-arm forward spectrometer covering the pseudorapidity range $2 < \eta < 5$, designed for the study of particles containing b or c quarks. The detector includes a high-precision tracking system consisting of a silicon-strip vertex detector surrounding the pp interaction region, a large-area silicon-strip detector located upstream of a dipole magnet with a bending power of about 4 Tm, and three stations of silicon-strip detectors and straw drift tubes placed downstream. The combined tracking system provides a momentum measurement with relative uncertainty that varies from 0.4% at 5 GeV/c to 0.6% at 100 GeV/c, and impact parameter resolution of 20 µm for tracks with large $p_{\rm T}$. Different types of charged hadrons are distinguished by information from two ring-imaging Cherenkov detectors. Photon, electron and hadron candidates are identified by a calorimeter system consisting of scintillating-pad and preshower detectors, an electromagnetic calorimeter and a hadronic calorimeter. Muons are identified by a system composed of alternating layers of iron and multiwire proportional chambers.

The trigger consists of a hardware stage, based on information from the calorimeter and muon systems, followed by a software stage, which applies a full event reconstruction. The events used in this analysis are selected at the hardware stage by requiring a cluster in the calorimeters with transverse energy greater than 3.6 GeV. The software trigger requires a two-, three- or four-track secondary vertex (SV) with a large sum of the $p_{\rm T}$ of the particles and a significant displacement from the primary pp interaction vertices (PVs). At least one charged particle should have $p_{\rm T} > 1.7\,\text{GeV}/c$ and $\chi^2_{\rm IP}$ with respect to any PV greater than 16, where $\chi^2_{\rm IP}$ is defined as the difference in fit χ^2 of a given PV reconstructed with and without the considered track. A multivariate algorithm is used for the identification of SVs consistent with the decay of a b hadron.

Simulated collision events are used to estimate the efficiency of the reconstruction and selection steps for signal as well as background b-hadron decay modes. In the simulation, pp collisions are generated using Pythia [13] with a specific LHCb configuration [14]. Decays of hadronic particles are described by EvtGen [15], in which final-state radiation is generated using Photos [16]. The interaction of the generated particles with the detector and its response are implemented using the Geant4 toolkit [17, 18] as described in ref. [19].

3 Event selection

Since the $\Lambda_b^0 \to \Lambda_c^+(\to pK^-\pi^+)\pi^-$ and $\overline{B}^0 \to D^+(\to K^-\pi^+\pi^+)\pi^-$ decays have the same topology, the criteria used to select them are chosen to be similar. This minimises the systematic uncertainty on the ratio of the selection efficiencies. Following the trigger selection, a preselection is applied using the reconstructed masses, decay times and vertex qualities of the b-hadron and c-hadron candidates. Further separation between signal and background

is achieved using a boosted decision tree (BDT) [20]. The BDT is trained and tested on a sample of $\overline{B}{}_s^0 \to D_s^+\pi^-$ events from the same data set as the signal events. This sample of events is not used elsewhere in the analysis. For the signal, a weighted data sample based on the *sPlot* technique [21] is used. A training sample representative of combinatorial background is selected from B_s^0 candidates with mass greater than 5445 MeV/c^2. The variables with the most discriminating power are found to be the $\chi^2_{\rm IP}$ of the b-hadron candidate with respect to the PV, the $p_{\rm T}$ of the final-state particles, and the angle between the b-hadron momentum vector and the vector connecting its production and decay vertices. In events with multiple PVs, the b hadron is associated to the PV giving the smallest $\chi^2_{\rm IP}$.

The BDT requirement is chosen to maximise the signal yield divided by the square root of the sum of the signal and background yields. It rejects approximately 84% of the combinatorial background events while retaining approximately 84% of the signal events. The D^+ (Λ_c^+) candidates are identified by requiring the invariant mass under the $K^-\pi^+\pi^+$ ($pK^-\pi^+$) hypothesis to fall within the range 1844–1890 (2265–2305) MeV/c^2. The mass resolution of the charm hadrons is approximately 6 MeV/c^2.

The ratio of selection efficiencies is evaluated using simulated events. The $D^+ \to K^-\pi^+\pi^+$ decay is generated using the known Dalitz structure [22], while the $\Lambda_c^+ \to pK^-\pi^+$ decay is generated using a combination of non-resonant and resonant decay modes with proportions according to ref. [23]. Interference effects in the Λ_c^+ decay are not taken into account. Consistency checks, using a phase-space only model for the $\Lambda_c^+ \to pK^-\pi^+$ decay, show negligible differences in the relative efficiencies. The distributions of the input variables to the BDT are compared in data and simulation. Good agreement is observed for most variables. The largest deviation is seen for quantities related to the track quality. The simulated events are reweighted so that the distributions of these quantities reproduce the distributions in data.

The final stage of the event selection applies particle identification (PID) criteria on all tracks, based on the differences in the natural logarithm of the likelihood between the pion, kaon and proton hypotheses [24]. The PID performance as a function of the $p_{\rm T}$ and η of the charged particle is estimated from data. This is performed using calibration samples, selected using only kinematic criteria, and consisting of approximately 27 million $D^{*-} \to \overline{D}{}^0(K^+\pi^-)\pi^-$ decays for kaons and pions, and 13 million $\Lambda \to p\pi^-$ decays for protons. The size of the proton calibration sample is small at high $p_{\rm T}$ of the proton and does not allow a reliable estimate of the efficiency of the proton PID requirement in this kinematic region. Hence, proton PID criteria are only applied to candidates restricted to a kinematic region in proton momentum and pseudorapidity corresponding to low-$p_{\rm T}$ protons. Outside of this region, no PID criteria are imposed on the proton.

The ratio of total selection efficiencies, $\varepsilon_{\overline{B}{}^0\to D^+\pi^-}/\varepsilon_{\Lambda_b^0\to\Lambda_c^+\pi^-}$, is shown in figure 1. Fluctuations are included in the calculation of the efficiency-corrected yield ratio.

4 Event yields

The dependences of $f_{\Lambda_b^0}/f_d$ on the $p_{\rm T}$ and η of the b hadron are studied in the ranges $1.5 < p_{\rm T} < 40\,{\rm GeV}/c$ and $2 < \eta < 5$. The event sample is sub-divided in 20 bins in $p_{\rm T}$ and 10 bins in η, with bin boundaries chosen to obtain approximately equal numbers

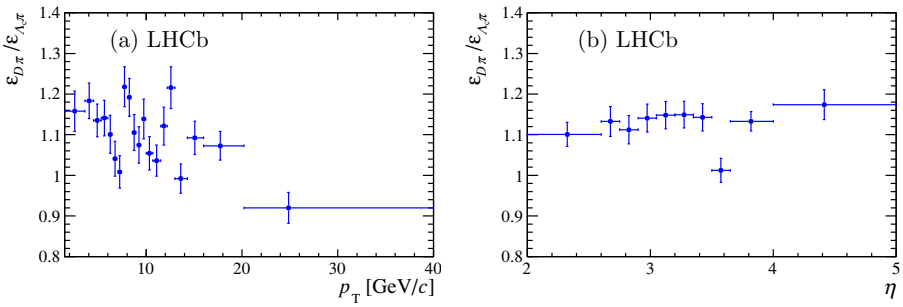

Figure 1. Ratio of total selection efficiencies in bins of the (a) p_{T} and (b) η of the b hadron. The horizontal error bars indicate the range of each bin in p_{T} or η respectively.

of $\overline{B}^0 \to D^+\pi^-$ candidates per bin. The bin centres are obtained from simulated events without any selection applied, and are defined as the mean of the average p_{T} or η of the $\Lambda_b^0 \to \Lambda_c^+\pi^-$ and $\overline{B}^0 \to D^+\pi^-$ samples in each bin.

The yields of the two decay modes are determined from extended maximum likelihood fits to the unbinned mass distributions of the reconstructed b-hadron candidates, in each bin of p_{T} or η. To improve the mass resolution, the value of the beauty hadron mass is refit with the invariant mass of the charm hadron constrained to its known value [10]. Example fits in the p_{T} bin with the lowest fitted signal yield and in an arbitrarily chosen η bin are shown in figure 2 for $\Lambda_c^+\pi^-$ and $D^+\pi^-$ candidates. The total signal yields, obtained from fits to the total event samples, are $44\,859 \pm 229$ for the $\Lambda_b^0 \to \Lambda_c^+\pi^-$ sample and $106\,197 \pm 344$ for the $\overline{B}^0 \to D^+\pi^-$ sample.

The signal mass shape is described by a modified Gaussian distribution with power-law tails on either side to model the radiative tail and non-Gaussian detector effects. The parameters of the tails are obtained from simulated events and fixed in the fit. The mean and the width of the Gaussian distribution are allowed to vary.

Three classes of background are considered: partially reconstructed decays with or without misidentified tracks, fully reconstructed decays where at least one track is misidentified, and combinatorial background. The shapes of the invariant mass distributions for the partially reconstructed decays are obtained using large samples of simulated events. For the $\overline{B}^0 \to D^+\pi^-$ sample, the decays $\overline{B}^0 \to D^+\rho^-$ and $\overline{B}^0 \to D^{*+}\pi^-$ are modelled with non-parametric distributions [25]. The main sources for the $\Lambda_b^0 \to \Lambda_c^+\pi^-$ sample are $\Lambda_b^0 \to \Lambda_c^+\rho^-$ and $\Lambda_b^0 \to \Sigma_c^+\pi^-$ decays, which are modelled with a bifurcated Gaussian function. All these processes involve a neutral pion that is not included in the candidate's reconstruction.

The invariant mass distributions of the misidentified decays are affected by the PID criteria. The shapes are obtained from simulated events, reweighted according to the momentum-dependent particle identification efficiency, with the mass hypothesis of the signal applied. The $\overline{B}^0 \to D^+\pi^-$ background in the $\Lambda_b^0 \to \Lambda_c^+\pi^-$ sample is most abundant in the highest p_{T} bins, since the proton PID criteria are least effective in this kinematic region.

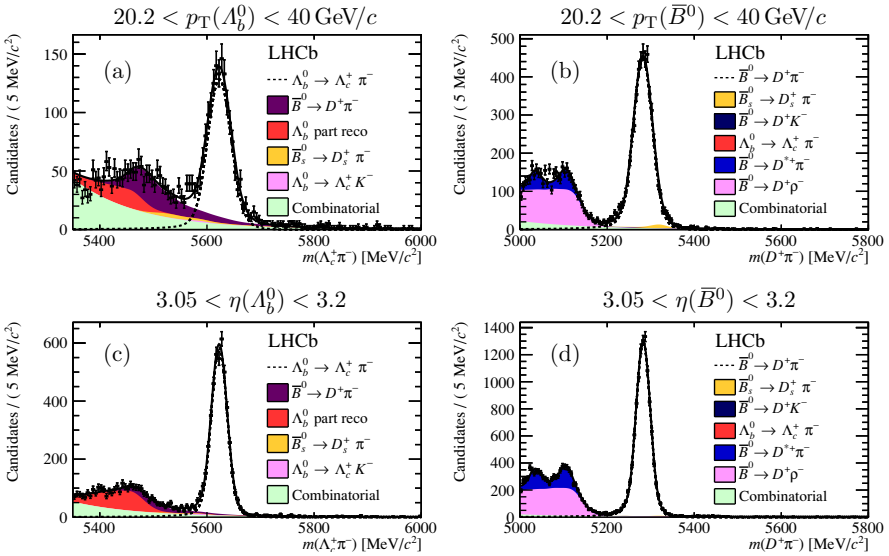

Figure 2. Invariant mass distributions of (a,c) $\Lambda_c^+\pi^-$ candidates and (b,d) $D^+\pi^-$ candidates for specific ranges in p_T and η of the b hadron, with fit projections overlaid. The different components are defined in the legend, where "part reco" refers to the sum of partially reconstructed decays.

The Cabibbo-suppressed decays $\Lambda_b^0 \to \Lambda_c^+ K^-$ and $\overline{B}^0 \to D^+ K^-$ contribute to the background in the $\Lambda_b^0 \to \Lambda_c^+ \pi^-$ and $\overline{B}^0 \to D^+\pi^-$ fits, respectively, when the kaon of the b-hadron decay is misidentified as a pion. The yields of these backgrounds relative to the signal yield are constrained in the fits, using LHCb measurements of the relevant ratios of branching fractions [9, 26] and the misidentification probabilities with their associated uncertainties.

The combinatorial background consists of events with random pions, kaons and protons forming a mis-reconstructed D^+ or Λ_c^+ candidate, as well as genuine D^+ or Λ_c^+ hadrons, that combine with a random pion. The combinatorial background is modelled with an exponential shape. The slope is fixed in the fit in each kinematic bin to the value found from a fit to the total sample.

5 Results

The study of the dependences of $f_{\Lambda_b^0}/f_d$ on the p_T and η of the b hadron and the measurement of the branching fraction of $\Lambda_b^0 \to \Lambda_c^+\pi^-$ decays are performed using candidates restricted to the fiducial region $1.5 < p_T < 40\,\text{GeV}/c$ and $2 < \eta < 5$. A discussion on the systematic uncertainties related to these measurements can be found in the next section.

The ratio of efficiency-corrected event yields as a function of p_T is shown in figure 3(a), and is fitted with an exponential function,

$$\mathcal{R}(p_T) = a + \exp\left(b + c \times p_T[\text{GeV}/c]\right), \tag{5.1}$$

with

$$
\begin{aligned}
a &= +0.181 \pm 0.018 \pm 0.026\,, \\
b &= -0.391 \pm 0.023\,{}^{+0.069}_{-0.067}\,, \\
c &= -0.095 \pm 0.007 \pm 0.014\,[\mathrm{GeV}/c]^{-1}\,,
\end{aligned}
$$

where the first uncertainties are statistical and the second systematic. The correlation matrix of the parameters is

$$
\rho(a,b,c) = \begin{pmatrix} 1 & -0.22 & -0.94 \\ -0.22 & 1 & -0.10 \\ -0.94 & -0.10 & 1 \end{pmatrix}.
$$

The correlation between the parameters leads to a relatively large apparent uncertainty on the individual parameters. Systematic uncertainties are not included in this matrix. The χ^2/ndf value of the fit is 23.3/17, which corresponds to a p-value of 0.14.

The η dependence is described by a linear function,

$$
\mathcal{R}(\eta) = a + b \times (\eta - \overline{\eta})\,, \tag{5.2}
$$

with

$$
\begin{aligned}
a &= 0.464 \pm 0.003\,{}^{+0.008}_{-0.010}\,, \\
b &= 0.081 \pm 0.005\,{}^{+0.013}_{-0.009}\,, \\
\overline{\eta} &= 3.198\,,
\end{aligned}
$$

where the first uncertainties are statistical and the second systematic. The offset $\overline{\eta}$ is fixed to the average value of the measured η distribution. The correlation between the two fit parameters is negligible for this choice of $\overline{\eta}$. The χ^2/ndf value of the fit is 13.1/8, corresponding to a p-value of 0.11.

To extract the scale factor $\mathcal{S}$ given in eq. (1.2), the normalisation of $\mathcal{R}(x)$, with fixed parameters a, b and c, is allowed to vary in a fit to the published $f_{\Lambda_b^0}/f_d$ data [7], as shown in figure 3(b). The result quoted in ref. [7] was measured as a function of the p_{T} of the $\Lambda_c^+\mu^-$ system. A shift, estimated from simulation, is applied to the p_{T} values to obtain the corresponding average p_{T} of the b hadron for each bin. Furthermore, the semileptonic results are updated using recent determinations of $\mathcal{B}(\Lambda_c^+ \to pK^-\pi^+) = \big(6.84 \pm 0.24\,{}^{+0.21}_{-0.27}\big)\%$ [27] and the ratio of lifetimes $(\tau_{B^+} + \tau_{B^0})/2\tau_{\Lambda_b^0} = 1.071 \pm 0.008$ [28, 29].

The following value of the scale factor $\mathcal{S}$ is determined,

$$
\mathcal{S} = 0.834 \overbrace{\pm 0.006\,(\mathrm{stat})\,{}^{+0.023}_{-0.021}\,(\mathrm{syst})}^{\text{hadronic}} \overbrace{\pm 0.027\,(\mathrm{stat})\,{}^{+0.058}_{-0.062}\,(\mathrm{syst})}^{\text{semileptonic}}\,,
$$

where the statistical and systematic uncertainties associated with the hadronic and semileptonic measurement are shown separately. The χ^2/ndf value of the fit is 8.68/3, which corresponds to a p-value of 0.03.

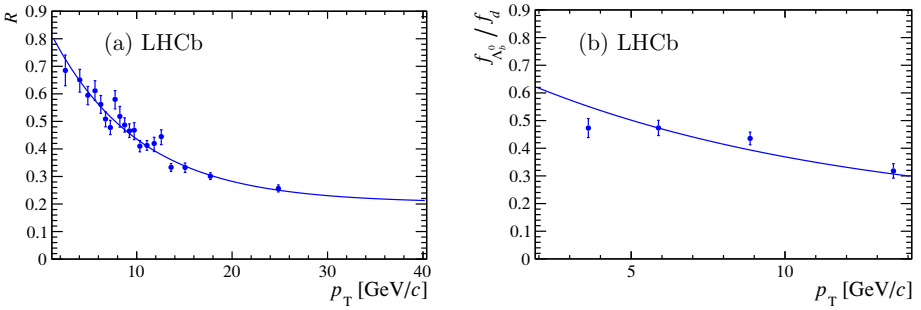

Figure 3. (a) Dependence of the efficiency-corrected ratio of yields, $\mathcal{R}$, between $\Lambda_b^0 \to \Lambda_c^+\pi^-$ and $\overline{B}^0 \to D^+\pi^-$ decays on the p_T of the beauty hadron, fitted with an exponential function. The error bars on the data show the statistical and systematic uncertainties added in quadrature. (b) The resulting parametrisation is then fitted to the rescaled $f_{\Lambda_b^0}/f_d$ measurements from the semileptonic analysis [7], to obtain the scale factor $\mathcal{S}$. The error bars include only the statistical uncertainty.

By multiplying the ratio of the efficiency-corrected yields $\mathcal{R}$ with the scale factor $\mathcal{S}$, the dependences of $f_{\Lambda_b^0}/f_d$ on p_T and η are obtained. The p_T dependence is described with the exponential function

$$f_{\Lambda_b^0}/f_d(p_T) = a' + \exp(b' + c' \times p_T\,[\text{GeV}/c])\,, \tag{5.3}$$

with

$$\begin{aligned} a' &= +0.151 \pm 0.016\,^{+0.024}_{-0.025}\,, \\ b' &= -0.573 \pm 0.040\,^{+0.101}_{-0.097}\,, \\ c' &= -0.095 \pm 0.007 \pm 0.014\,[\text{GeV}/c]^{-1}\,, \end{aligned}$$

where the first uncertainty is the combined statistical and the second is the combined systematic from the hadronic and semileptonic measurements. The correlations between the three fit parameters change due to the uncertainty on the scale factor $\mathcal{S}$. The correlation matrix of the parameters is

$$\rho(a', b', c') = \begin{pmatrix} 1 & 0.55 & -0.73 \\ 0.55 & 1 & -0.03 \\ -0.73 & -0.03 & 1 \end{pmatrix}.$$

The η dependence is described by the linear function

$$f_{\Lambda_b^0}/f_d(\eta) = a' + b' \times (\eta - \overline{\eta})\,, \tag{5.4}$$

with

$$\begin{aligned} a' &= 0.387 \pm 0.013\,^{+0.028}_{-0.030}\,, \\ b' &= 0.067 \pm 0.005\,^{+0.012}_{-0.009}\,, \end{aligned}$$

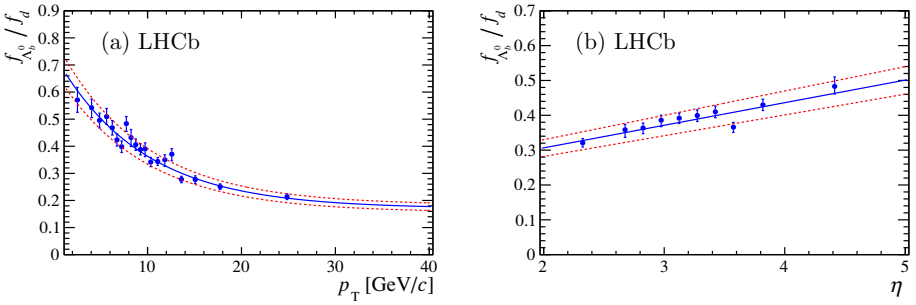

Figure 4. Dependence of $f_{\Lambda_b^0}/f_d$ on the (a) $p_{\rm T}$ and (b) η of the beauty hadron. To obtain this figure, the ratio of efficiency-corrected event yields is scaled to the absolute value of $f_{\Lambda_b^0}/f_d$ from the semileptonic analysis [7]. The error bars include the statistical and systematic uncertainties associated with the hadronic measurement. The dashed red lines indicate the uncertainty on the scale of $f_{\Lambda_b^0}/f_d$ from the semileptonic analysis.

where the first uncertainty is the combined statistical and the second is the combined systematic from the hadronic and semileptonic measurements. The dependences of $f_{\Lambda_b^0}/f_d$ on the $p_{\rm T}$ and η of the b hadron are shown in figure 4.

The absolute value for $\mathcal{B}\left(\Lambda_b^0 \to \Lambda_c^+\pi^-\right)$ is obtained by substituting the results for $\mathcal{S}$ and $\mathcal{B}(\overline{B}^0 \to D^+\pi^-) = (2.68 \pm 0.13) \times 10^{-3}$ [10] into eq. (1.2). The value for $\mathcal{B}\left(\Lambda_c^+ \to pK^-\pi^+\right)$ is also used in the determination of $f_{\Lambda_b^0}/f_d$ using semileptonic decays and therefore cancels in the final result. The branching fraction for $\Lambda_b^0 \to \Lambda_c^+\pi^-$ is measured to be

$$\mathcal{B}\left(\Lambda_b^0 \to \Lambda_c^+\pi^-\right) = \left(4.30 \pm 0.03\ ^{+0.12}_{-0.11} \pm 0.26 \pm 0.21\right) \times 10^{-3},$$

where the first uncertainty is statistical, the second is systematic, the third is from the previous LHCb measurement of $f_{\Lambda_b^0}/f_d$, and the fourth is due to the knowledge of $\mathcal{B}(\overline{B}^0 \to D^+\pi^-)$. This value is in agreement with the current world average [10]. It also agrees within 2.4 standard deviations with the recent LHCb measurement using $\Lambda_b^0 \to \Lambda_c^+(\to pK_{\rm S}^0)\pi^-$ decays [30], taking into account the correlated uncertainty from the semileptonic value for $f_{\Lambda_b^0}/f_d$ (6.1%). Combining the two LHCb measurements, and using a consistent value for the lifetime ratio of $(\tau_{B^+} + \tau_{B^0})/2\tau_{\Lambda_b^0} = 1.071 \pm 0.008$, we obtain $\mathcal{B}\left(\Lambda_b^0 \to \Lambda_c^+\pi^-\right) = (4.46 \pm 0.36) \times 10^{-3}$, where the uncertainty is the combined statistical and systematic uncertainty of both measurements.

6 Systematic uncertainties

Systematic uncertainties on the measurement of the relative efficiency-corrected event yields of the $\Lambda_b^0 \to \Lambda_c^+\pi^-$ and $\overline{B}^0 \to D^+\pi^-$ decay modes relate to the fit models and to the efficiencies of the PID, BDT and trigger selections. The effect of each systematic uncertainty on the efficiency-corrected yield ratio is calculated separately for each bin of $p_{\rm T}$ or η. The systematic uncertainties are considered to be correlated across the bins, unless mentioned otherwise. The effect of the systematic uncertainties on the model of the $\mathcal{R}(x)$ dependence

	$p_{\rm T}$ bins $\mathcal{R} = a + \exp(b + c \times p_{\rm T})$			η bins $\mathcal{R} = a + b \times (\eta - \overline{\eta})$		$\mathcal{B}(\Lambda_b^0 \to \Lambda_c^+\pi^-)$
	a	b	c	a	b	
Fit model						
Signal	$^{+0.7}_{-0.4}\%$	$^{+0.5}_{-0.2}\%$	$^{+0.2}_{-0.3}\%$	$^{+0.3}_{-0.1}\%$	$^{+1.1}_{-1.8}\%$	$^{+0.2}_{-0.1}\%$
Background	$^{+5.5}_{-1.7}\%$	$^{+2.8}_{-2.1}\%$	$^{+2.6}_{-1.1}\%$	$^{+0.6}_{-0.1}\%$	$^{+2.4}_{-4.7}\%$	$^{+0.6}_{-0.0}\%$
Efficiencies						
PID	0.0%	0.5%	2.5%	−1.3%	12.7%	−1.1%
BDT	$^{+5.8}_{-7.6}\%$	$^{-15.1}_{+14.2}\%$	$^{+9.6}_{-10.2}\%$	$^{+1.3}_{-1.3}\%$	$^{+4.7}_{-4.8}\%$	$^{+2.3}_{-2.2}\%$
Sample size	±12.1%	±9.0%	±10.8%	±0.9%	±9.3%	±1.2%
Trigger	0.9%	1.0%	1.0%	−0.3%	−0.1%	−0.3%
Other						
Bin centre	±0.3%	±0.3%	±0.1%	±0.1%	±1.3%	0.0%
Total	$^{+14.6}_{-14.5}\%$	$^{+17.1}_{-17.7}\%$	$^{+14.9}_{-14.9}\%$	$^{+1.8}_{-2.1}\%$	$^{+16.6}_{-11.6}\%$	$^{+2.6}_{-2.8}\%$

Table 1. Relative systematic uncertainties for the measurements of $\mathcal{R}(x)$ (first five columns) and $\mathcal{B}(\Lambda_b^0 \to \Lambda_c^+\pi^-)$ (last column). The uncertainties from the various sources are uncorrelated and added in quadrature to obtain the total uncertainty. Sample size refers to the size of the simulated events sample.

and the measurement of $\mathcal{B}\left(\Lambda_b^0 \to \Lambda_c^+\pi^-\right)$ are determined by refitting the data points when the $\mathcal{R}$ value in each bin is varied by its associated uncertainty. The various sources of systematic uncertainty are discussed below and summarised in table 1.

The uncertainty due to the modelling of the signal shape is estimated by replacing the modified Gaussian with two modified Gaussians, which share the same mean but are allowed to have different widths. In addition, the parameters that describe the tails are varied by ±10% relative to their nominal values, which is the maximum variation found for these parameters when leaving them free in the fit. This affects the ratio of yields by a maximum of 0.3%.

A possible variation of the slope of the combinatorial background shape across the bins is observed in a data sample of $\Lambda_c^+\pi^+$ candidates. To account for this, the slope is varied from ±50% in the lowest $p_{\rm T}$ or η bin to ∓50% in the highest $p_{\rm T}$ or η bin. The signal yield ratio varies by less than 1%, with the exception of one $p_{\rm T}$ bin which shows a variation of approximately 2%.

The uncertainty on the shapes of partially reconstructed backgrounds is estimated by modelling them with a non-parametric distribution [25] for $\Lambda_b^0 \to \Sigma_c^+\pi^-$ and $\Lambda_b^0 \to \Lambda_c^+\rho^-$ decays and with two modified Gaussian distributions with tails on either side for the $\overline{B}^0 \to D^{*+}\pi^-$ shape. The effect on the signal yield ratio is below 0.5% in most bins, increasing to about 2% for the highest $p_{\rm T}$ bin.

The contribution of b-hadron decays without an intermediate c hadron is ignored in the fit. To evaluate the systematic uncertainty due to these decays, the b-hadron mass

spectra for candidates in the sidebands of the c-hadron mass distribution are examined. A contribution of 0.4% relative to the signal yield is found in the $\overline{B}^0 \to D^+\pi^-$ decay mode, and its full size is taken as systematic uncertainty. No contribution is seen in the $\Lambda_b^0 \to \Lambda_c^+\pi^-$ decay mode and no systematic uncertainty is assigned.

The uncertainty on the PID efficiency and misidentification rate is estimated by comparing the PID performance measured using simulated D^* and Λ calibration samples with that observed in simulated signal events. The efficiency ratio varies by between 1% and 4% across the bins.

As discussed in section 3, the simulated events are reweighted so that the distributions of quantities related to the track quality match the distributions observed in data. The systematic uncertainty on the selection efficiency is obtained by recalculating the efficiency without this reweighting. The yield ratio varies by between 0.2% and 6%. In addition, there is a 5% statistical uncertainty per bin due to the simulated sample size, which is uncorrelated across bins.

The uncertainty due to the trigger efficiency, caused by possible differences in the response to a proton compared to a charged pion in the calorimeter, is estimated to be about 0.4%, taking into account that at most 10% of the events containing $\Lambda_b^0 \to \Lambda_c^+\pi^-$ candidates are triggered by the proton. The systematic uncertainty due to the choice of bin centre is evaluated by redefining the bin centres using the average $p_{\rm T}$ or η of the Λ_b^0 or B^0 sample only, instead of the mean of the Λ_b^0 and B^0 samples.

7 Conclusions

The dependences of the production rate of Λ_b^0 baryons with respect to B^0 mesons are measured as functions of the transverse momentum $p_{\rm T}$ and of the pseudorapidity η of the b hadron. The $p_{\rm T}$ dependence is accurately described by an exponential function. The ratio of fragmentation fractions $f_{\Lambda_b^0}/f_d$ decreases by a factor of three in the range $1.5 < p_{\rm T} < 40\,{\rm GeV}/c$. The ratio of fragmentation fractions $f_{\Lambda_b^0}/f_d$ versus η is described by a linear dependence in the range $2 < \eta < 5$.

The absolute scale of $f_{\Lambda_b^0}/f_d$ is fixed using the measurement of $f_{\Lambda_b^0}/f_d$ from semileptonic b-hadron decays [7]. The branching fraction of the decay $\Lambda_b^0 \to \Lambda_c^+\pi^-$ is determined with a total precision of 8%,

$$\mathcal{B}\left(\Lambda_b^0 \to \Lambda_c^+\pi^-\right) = \left(4.30 \pm 0.03\,^{+0.12}_{-0.11} \pm 0.26 \pm 0.21\right) \times 10^{-3},$$

which is the most precise determination of a branching fraction of a beauty baryon to date.

Acknowledgments

We express our gratitude to our colleagues in the CERN accelerator departments for the excellent performance of the LHC. We thank the technical and administrative staff at the LHCb institutes. We acknowledge support from CERN and from the national agencies: CAPES, CNPq, FAPERJ and FINEP (Brazil); NSFC (China); CNRS/IN2P3 and Region Auvergne (France); BMBF, DFG, HGF and MPG (Germany); SFI (Ireland);

INFN (Italy); FOM and NWO (The Netherlands); SCSR (Poland); MEN/IFA (Romania); MinES, Rosatom, RFBR and NRC "Kurchatov Institute" (Russia); MinECo, XuntaGal and GENCAT (Spain); SNSF and SER (Switzerland); NASU (Ukraine); STFC and the Royal Society (United Kingdom); NSF (U.S.A.). We also acknowledge the support received from EPLANET, Marie Curie Actions and the ERC under FP7. The Tier1 computing centres are supported by IN2P3 (France), KIT and BMBF (Germany), INFN (Italy), NWO and SURF (The Netherlands), PIC (Spain), GridPP (United Kingdom). We are indebted to the communities behind the multiple open source software packages on which we depend. We are also thankful for the computing resources and the access to software R&D tools provided by Yandex LLC (Russia).

References

[1] A.V. Berezhnoy and A.K. Likhoded, *The relative yields of heavy hadrons as function of transverse momentum at LHC experiments*, arXiv:1309.1979 [INSPIRE].

[2] I. Dunietz, *CP violation with beautiful baryons*, *Z. Phys.* **C 56** (1992) 129 [INSPIRE].

[3] LHCb collaboration, *Measurement of the Ξ_b^- and Ω_b^- baryon lifetimes*, *Phys. Lett.* **B 736** (2014) 154 [arXiv:1405.1543] [INSPIRE].

[4] Heavy Flavor Averaging Group collaboration, Y. Amhis et al., *Averages of B-Hadron, C-Hadron and tau-lepton properties as of early 2012*, arXiv:1207.1158 [INSPIRE].

[5] CDF collaboration, T. Aaltonen et al., *Measurement of Ratios of Fragmentation Fractions for Bottom Hadrons in $p\bar{p}$ Collisions at $\sqrt{s} = 1.96$ TeV*, *Phys. Rev.* **D 77** (2008) 072003 [arXiv:0801.4375] [INSPIRE].

[6] CDF collaboration, T. Aaltonen et al., *First Measurement of the Ratio of Branching Fractions $B(\Lambda_b^0 \to \Lambda_c^+ \mu^- \bar{\nu}_\mu)/B(\Lambda_b^0 \to \Lambda_c^+ \pi^-)$*, *Phys. Rev.* **D 79** (2009) 032001 [arXiv:0810.3213] [INSPIRE].

[7] LHCb collaboration, *Measurement of b-hadron production fractions in 7 TeV pp collisions*, *Phys. Rev.* **D 85** (2012) 032008 [arXiv:1111.2357] [INSPIRE].

[8] CMS collaboration, *Measurement of the Λ_b cross section and the $\bar{\Lambda}_b$ to Λ_b ratio with $J/\Psi\Lambda$ decays in pp collisions at $\sqrt{s} = 7$ TeV*, *Phys. Lett.* **B 714** (2012) 136 [arXiv:1205.0594] [INSPIRE].

[9] LHCb collaboration, *Measurement of the fragmentation fraction ratio f_s/f_d and its dependence on B meson kinematics*, *JHEP* **04** (2013) 001 [arXiv:1301.5286] [INSPIRE].

[10] Particle Data Group collaboration, J. Beringer et al., *Review of Particle Physics (RPP)*, *Phys. Rev.* **D 86** (2012) 010001 [INSPIRE].

[11] CLEO collaboration, S. Dobbs et al., *Measurement of absolute hadronic branching fractions of D mesons and $e^+e^- \to D\overline{D}$ cross-sections at the $\Psi(3770)$*, *Phys. Rev.* **D 76** (2007) 112001 [arXiv:0709.3783] [INSPIRE].

[12] LHCb collaboration, *The LHCb Detector at the LHC*, 2008 *JINST* **3** S08005 [INSPIRE].

[13] T. Sjöstrand, S. Mrenna and P.Z. Skands, *PYTHIA 6.4 Physics and Manual*, *JHEP* **05** (2006) 026 [hep-ph/0603175] [INSPIRE].

[14] I. Belyaev et al., *Handling of the generation of primary events in* GAUSS*, the LHCb simulation framework*, *IEEE Nucl. Sci. Symp. Conf. Rec.* (2010) 1155.

[15] D.J. Lange, *The EvtGen particle decay simulation package*, *Nucl. Instrum. Meth.* **A 462** (2001) 152 [INSPIRE].

[16] P. Golonka and Z. Was, *PHOTOS Monte Carlo: A precision tool for QED corrections in Z and W decays*, *Eur. Phys. J.* **C 45** (2006) 97 [hep-ph/0506026] [INSPIRE].

[17] GEANT4 collaboration, J. Allison et al., *Geant4 developments and applications*, *IEEE Trans. Nucl. Sci.* **53** (2006) 270.

[18] GEANT4 collaboration, S. Agostinelli et al., *GEANT4: A simulation toolkit*, *Nucl. Instrum. Meth.* **A 506** (2003) 250 [INSPIRE].

[19] M. Clemencic et al., *The LHCb simulation application, Gauss: Design, evolution and experience*, *J. Phys. Conf. Ser.* **331** (2011) 032023 [INSPIRE].

[20] L. Breiman, J.H. Friedman, R.A. Olshen and C.J. Stone, *Classification and regression trees*, Wadsworth international group, Belmont, California, U.S.A. (1984).

[21] M. Pivk and F.R. Le Diberder, *SPlot: A statistical tool to unfold data distributions*, *Nucl. Instrum. Meth.* **A 555** (2005) 356 [physics/0402083] [INSPIRE].

[22] CLEO collaboration, G. Bonvicini et al., *Dalitz plot analysis of the $D^+ \to K^-\pi^+\pi^+$ decay*, *Phys. Rev.* **D 78** (2008) 052001 [arXiv:0802.4214] [INSPIRE].

[23] E791 collaboration, E.M. Aitala et al., *Multidimensional resonance analysis of $\Lambda_c^+ \to pK^-\pi^+$*, *Phys. Lett.* **B 471** (2000) 449 [hep-ex/9912003] [INSPIRE].

[24] LHCb RICH GROUP collaboration, *Performance of the LHCb RICH detector at the LHC*, *Eur. Phys. J.* **C 73** (2013) 2431 [arXiv:1211.6759] [INSPIRE].

[25] K.S. Cranmer, *Kernel estimation in high-energy physics*, *Comput. Phys. Commun.* **136** (2001) 198 [hep-ex/0011057] [INSPIRE].

[26] LHCb collaboration, *Studies of beauty baryon decays to D^0ph^- and $\Lambda_c^+h^-$ final states*, *Phys. Rev.* **D 89** (2014) 032001 [arXiv:1311.4823] [INSPIRE].

[27] BELLE collaboration, A. Zupanc et al., *Measurement of the Branching Fraction $Br(\Lambda_c^+ \to pK^-\pi^+)$*, *Phys. Rev. Lett.* **113** (2014) 042002 [arXiv:1312.7826] [INSPIRE].

[28] LHCb collaboration, *Measurements of the B^+, B^0, B_s^0 meson and Λ_b^0 baryon lifetimes*, *JHEP* **04** (2014) 114 [arXiv:1402.2554] [INSPIRE].

[29] LHCb collaboration, *Precision measurement of the ratio of the Λ_b^0 to $\overline{B}^0$ lifetimes*, *Phys. Lett.* **B 734** (2014) 122 [arXiv:1402.6242] [INSPIRE].

[30] LHCb collaboration, *Searches for Λ_b^0 and Ξ_b^0 decays to $K_S^0p\pi^-$ and $K_S^0pK^-$ final states with first observation of the $\Lambda_b^0 \to K_S^0p\pi^-$ decay*, *JHEP* **04** (2014) 087 [arXiv:1402.0770] [INSPIRE].

CHAPTER 8

Measurement of the branching fraction of $\overline{B}{}^0_s \to D^\pm_s K^\mp$ decays

The decay $\overline{B}{}^0_s \to D^\pm_s K^\mp$ can proceed through two different tree level diagrams, as shown in Fig. 8.1. The $\overline{B}{}^0_s$ can decay to a $D^+_s K^-$ pair via a $b \to c$ transition, or it can decay to a $D^-_s K^+$ pair via a $b \to u$ transition. In the latter decay, the decay amplitude is proportional to the CKM matrix element V_{ub} which carries a complex phase γ relative to V_{cb}. Similarly, the B^0_s meson can also decay to these two different final states. Taking B^0_s–$\overline{B}{}^0_s$ mixing into account allows an initially produced B^0_s or $\overline{B}{}^0_s$ meson to end up in both final states. The interference between mixing and decay makes $\overline{B}{}^0_s \to D^\pm_s K^\mp$ decays sensitive to the CKM angle γ. Moreover, the amplitudes of the two diagrams are comparable in size, leading to a large interference term and hence large CP violation is expected.

A theoretical lower bound for the branching fraction of $\overline{B}{}^0_s \to D^\pm_s K^\mp$ decays exists in the presence of a sizeable decay width difference $\Delta\Gamma_s$ [175]. Using $SU(3)$ symmetry relations, the decay $\overline{B}{}^0_s \to D^+_s \pi^-$ can be used to quantify the $b \to c$ topology of the $\overline{B}{}^0_s \to$

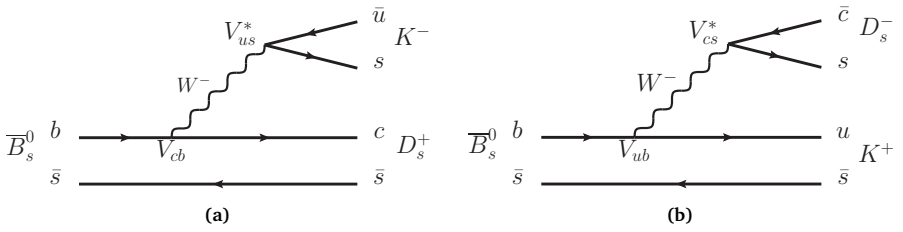

Fig. 8.1 · Decay topologies of the decay $\overline{B}{}^0_s \to D^\pm_s K^\mp$: colour-allowed tree diagrams with a) a $b \to c$ transition and b) a $b \to u$ transition.

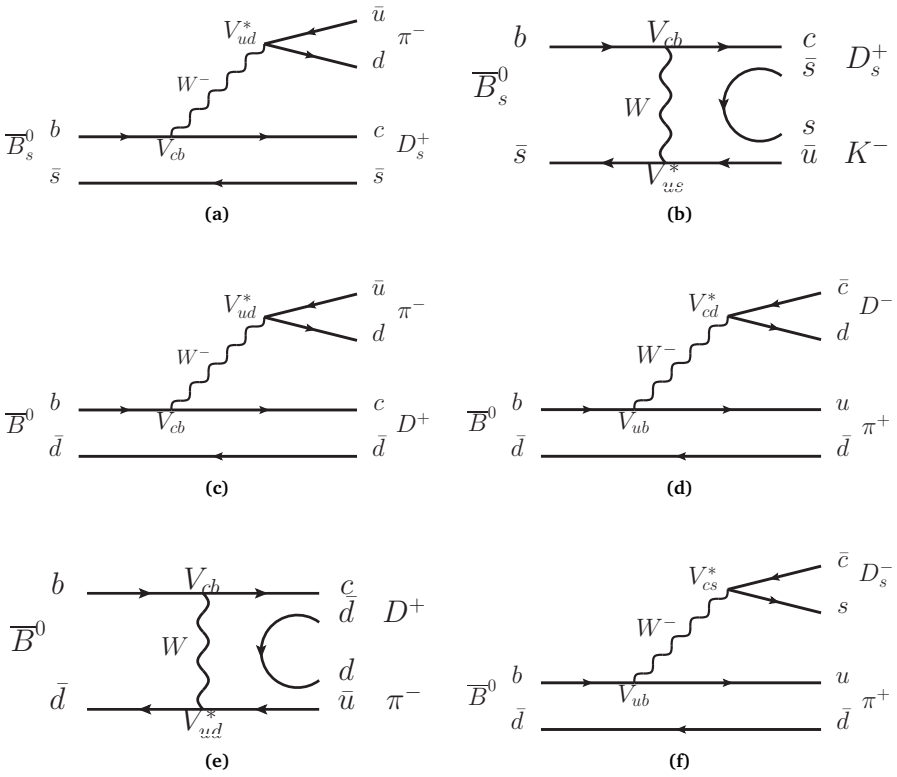

Fig. 8.2 · Decay topologies of $B \to Dh$ decays that are used for the calculation of the lower limit on and theoretical prediction of $\mathcal{B}(\overline{B}{}^0_s \to D^\pm_s K^\mp)$: a) $\overline{B}{}^0_s \to D^+_s \pi^-$ ($b \to c$ transition); b) $\overline{B}{}^0_s \to D^\pm_s K^\mp$ (exchange); c) $\overline{B}{}^0 \to D^+ \pi^-$ ($b \to c$ transition); d) $\overline{B}{}^0 \to D^+ \pi^-$ ($b \to u$ transition); e) $\overline{B}{}^0 \to D^+ \pi^-$ (exchange); and f) $\overline{B}{}^0 \to D^-_s \pi^+$ ($b \to u$ transition).

$D^\pm_s K^\mp$ decay. The hadronic quantity $x_s = \left| A(B^0_s \to D^+_s K^-)/A(\overline{B}{}^0_s \to D^+_s K^-) \right|$ [103] can then be written as[1]:

$$x_s = y_s \cos(\delta_s) \cos(\phi_s + \gamma) \pm \sqrt{\left[\frac{\mathcal{C}(1-\lambda^2)}{\lambda^2}\right]\left[\frac{\mathrm{BR}(B_s \to D^\pm_s K^\mp)_{\mathrm{exp}}}{\mathrm{BR}(B_s \to D^\pm_s \pi^\mp)_{\mathrm{exp}}}\right] - 1 + y_s^2 \cos^2(\delta_s) \cos^2(\phi_s + \gamma)}\,, \tag{8.1}$$

where y_s is related to the decay width following $\frac{1}{2}\Delta\Gamma_s/\Gamma_s$, the Wolfenstein parameter $\lambda \equiv |V_{us}| = 0.2252 \pm 0.0009$, ϕ_s is the $B^0_s - \overline{B}{}^0_s$ mixing phase, γ is the CKM angle, δ_s is the

[1] The subscript "exp" indicates that the experimental value of the branching fraction is used here. The experimental value differs slightly form the theoretical branching fraction, as explained in Sec. 5.1, due to a difference in lifetime of the heavy and light mass eigenstates of the B^0_s meson. From here onwards, all branching fractions refer to the experimental time-integrated value.

CP-conserving phase difference between the two diagrams of Fig. 8.1. The coefficient $\mathcal{C}$ is needed to account for differences between $\overline{B}{}^0_s \to D^+_s \pi^-$ and $\overline{B}{}^0_s \to D^+_s K^-$ decays and is defined as

$$\mathcal{C} = \frac{\Phi_{D_s\pi}}{\Phi_{D_sK}} \frac{f_\pi}{f_K} \mathcal{N}_F \mathcal{N}_a \mathcal{N}_E \tag{8.2}$$

with $\mathcal{N}_F$, $\mathcal{N}_a$ and $\mathcal{N}_E$, the ratio of form factors, the deviation from $SU(3)$ symmetry and the contribution of the colour suppressed W-exchange diagram, respectively, as defined in Sec. 5.1. The quantity $\mathcal{N}_E$, is estimated to be 0.97 ± 0.08 for the decay $\overline{B}{}^0_s \to D^\pm_s K^\mp$. The fact that it is close to unity demonstrates that the exchange topology is heavily suppressed compared to the colour-allowed tree topology. The requirement that x_s should be real is transformed into a lower bound on the ratio of branching fractions [175],

$$\frac{\mathcal{B}(B_s \to D^\pm_s K^\mp)}{\mathcal{B}(B_s \to D^\pm_s \pi^\mp)} \geq \frac{\lambda^2}{\mathcal{C}(1-\lambda^2)} \left[1 - y_s^2 \cos^2(\delta_s) \cos^2(\phi_s + \gamma)\right] = 0.080 \pm 0.007\,, \tag{8.3}$$

using knowledge of the phases [98, 176], of the factorisable and non-factorisable $SU(3)$ breaking effects [132, 134, 157], of the contribution of the exchange diagram [134] and the calculable phase space factors. No precise measurement of δ_s is available, and its value was chosen such to minimise the lower bound.

In addition, Ref. [175] utilises Eq. 8.1 to make a theoretical prediction for the ratio of branching fractions. This prediction relies on U-spin flavour symmetry of strong interactions, which is used to relate the parameters x_d and δ_d in the B^0 system to the corresponding parameters x_s and δ_s in the B^0_s system [103]:

$$x_s = -\frac{1-\lambda^2}{\lambda^2} x_d\,, \qquad \delta_s = \delta_d\,. \tag{8.4}$$

Measurements of $\overline{B}{}^0 \to D^+\pi^-$ decays at B-factories [177, 178] were used to extract the parameters x_d and δ_d. Additional input on $x_d = \left|A(\overline{B}{}^0 \to D^-\pi^+)/A(\overline{B}{}^0 \to D^+\pi^-)\right|$ is obtained using the constraint

$$|x_d| = \sqrt{\frac{\lambda^2}{C'(1-\lambda^2)} \left[\frac{\mathcal{B}(\overline{B}{}^0 \to D^-_s \pi^+)}{\mathcal{B}(\overline{B}{}^0 \to D^+\pi^-)}\right]} = 0.0163 \pm 0.0011|_{\mathcal{B}} \pm 0.0026|_{SU(3)}\,, \tag{8.5}$$

with $C' = \frac{\Phi_{D_s\pi}}{\Phi_{D\pi}} \mathcal{N}'_F \mathcal{N}'_a \mathcal{N}'_E$. The size of non-factorisable effects and the contribution of the exchange diagram to the $\overline{B}{}^0 \to D^+\pi^-$ decay are assumed to have an effect of at most 20%. Here, the decay $\overline{B}{}^0 \to D^-_s\pi^+$ is used to quantify the $b \to u$ topology of the $\overline{B}{}^0 \to D^-\pi^+$ decay. Combining the measured values of the hadronic quantities x_d and δ_d, and Eq. 8.4, results in the prediction for the ratio of branching fractions

$$\frac{\mathrm{BR}(B_s \to D^\pm_s K^\mp)}{\mathrm{BR}(B_s \to D^\pm_s \pi^\mp)} = 0.0864\,^{+0.0087}_{-0.0072}\,. \tag{8.6}$$

The decay $\overline{B}{}^0_s \to D^\pm_s K^\mp$ was first observed in $p\bar{p}$ collisions by the CDF Collaboration [179] who measured its branching fraction relative to that of $\overline{B}{}^0_s \to D^+_s \pi^-$ decays, followed by an observation by the Belle Collaboration [143] who measured the

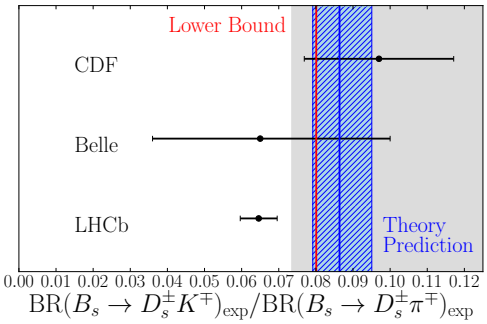

Fig. 8.3 · Status of the measurement of the ratio of branching fractions $\frac{\mathcal{B}(B_s \to D_s^\pm K^\mp)}{\mathcal{B}(B_s \to D_s^\pm \pi^\mp)}$ by CDF, Belle and LHCb in 2012. The lower bound on this ratio is indicated with the red line, and its predicted value with the blue shaded area. Figure from [175].

absolute branching fraction of $\overline{B}{}^0_s \to D^\pm_s K^\mp$ and $\overline{B}{}^0_s \to D^+_s \pi^-$ decays using knowledge of f_s. The LHCb Collaboration measured $\mathcal{B}(\overline{B}{}^0_s \to D^\pm_s K^\mp)$ in a 0.37 fb^{-1} dataset collected in pp collisions at $\sqrt{s} = 7\,\text{TeV}$ [110], using knowledge of the ratio of fragmentation fractions f_s/f_d. In addition, LHCb measured the ratio of branching fractions $\mathcal{B}(\overline{B}{}^0_s \to D^\pm_s K^\mp)/\mathcal{B}(\overline{B}{}^0_s \to D^+_s \pi^-)$. The different experiments measured the values

$$\frac{\mathcal{B}(B_s \to D_s^\pm K^\mp)}{\mathcal{B}(B_s \to D_s^\pm \pi^\mp)} = \begin{cases} 0.097 \pm 0.018\,(\text{stat.}) \pm 0.009\,(\text{syst.})\,, & [\text{CDF}] \\ 0.065^{+0.035}_{-0.029}\,(\text{stat.})\,, & [\text{Belle}] \\ 0.0646 \pm 0.0043\,(\text{stat.}) \pm 0.0025\,(\text{syst.})\,, & [\text{LHCb}, 0.37\,\text{fb}^{-1}] \end{cases} \tag{8.7}$$

which are summarised in Fig. 8.3, where also the lower bound on and the theoretical prediction of the ratio of branching fractions is illustrated. The measurements by the Belle and LHCb Collaborations are found to have a central value which is below the theoretical bound. Moreover, the LHCb value is found to have an approximately 2σ tension with the theoretical lower bound.

To either resolve or strengthen the tension, the measurement of $\mathcal{B}(\overline{B}{}^0_s \to D^\pm_s K^\mp)$ is repeated using the full Run I LHCb dataset, consisting of 1 fb^{-1} pp collisions at $\sqrt{s} = 7\,\text{TeV}$ and 2 fb^{-1} at $\sqrt{s} = 8\,\text{TeV}$ collected in 2011 and 2012, respectively. The hadronic modes $\overline{B}{}^0_s \to D^\pm_s K^\mp$, $\overline{B}{}^0_s \to D^+_s \pi^-$ are measured, with the D_s meson reconstructed as $D^-_s \to K^- K^+ \pi^-$. The branching fraction of $\overline{B}{}^0_s \to D^\pm_s K^\mp$ decays is determined relative to the branching fraction of $\overline{B}{}^0_s \to D^+_s \pi^-$ decays,

$$\frac{\mathcal{B}(\overline{B}{}^0_s \to D^\pm_s K^\mp)}{\mathcal{B}(\overline{B}{}^0_s \to D^+_s \pi^-)} = \frac{N_{\overline{B}{}^0_s \to D^\pm_s K^\mp}}{N_{\overline{B}{}^0_s \to D^+_s \pi^-}} \frac{\epsilon_{\overline{B}{}^0_s \to D^+_s \pi^-}}{\epsilon_{\overline{B}{}^0_s \to D^\pm_s K^\mp}}\,, \tag{8.8}$$

where N_X is the measured event yield and ϵ_X is the total selection and reconstruction efficiency.

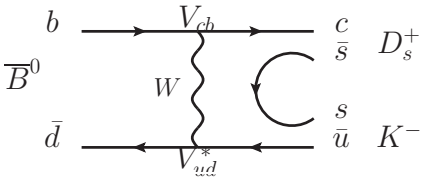

Fig. 8.4 · $\overline{B}^0 \to D_s^+ K^-$ exchange topology.

In addition to $\mathcal{B}(\overline{B}_s^0 \to D_s^\pm K^\mp)$, the branching fraction of the decay $\overline{B}^0 \to D_s^+ K^-$ is extracted relative to the branching fraction of $\overline{B}^0 \to D^+\pi^-$ decays, with the D meson reconstructed as $D^- \to K^+\pi^-\pi^-$,

$$\frac{\mathcal{B}(\overline{B}^0 \to D_s^+ K^-)}{\mathcal{B}(\overline{B}^0 \to D^+\pi^-)} = \frac{N_{\overline{B}^0 \to D_s^+ K^-}}{N_{\overline{B}^0 \to D^+\pi^-}} \frac{\epsilon_{\overline{B}^0 \to D^+\pi^-}}{\epsilon_{\overline{B}^0 \to D_s^+ K^-}} \frac{\mathcal{B}(D^- \to K^+\pi^-\pi^-)}{\mathcal{B}(D_s^- \to K^-K^+\pi^-)}\,, \tag{8.9}$$

with $\mathcal{B}(D^- \to K^+\pi^-\pi^-) = (9.13 \pm 0.19) \times 10^{-2}$ and $\mathcal{B}(D_s^- \to K^-K^+\pi^-) = (5.39 \pm 0.21) \times 10^{-2}$ [84]. As the decay $\overline{B}^0 \to D_s^+ K^-$ can only proceed via the colour suppressed W-exchange topology (Fig. 8.2b), this measurement gives us insight in the magnitude of this type of topology and therefore provides an estimate of $\mathcal{N}_E$. This can be used to estimate the size of the exchange distribution in $\overline{B}^0 \to D^+\pi^-$ decays, as is needed for the measurement of fragmentation fractions using the hadronic decays $\overline{B}^0 \to D^+\pi^-$ and $\overline{B}_s^0 \to D_s^+\pi^-$, as described in Sec. 5.1.3.4.

The branching fraction of $\overline{B}_s^0 \to D_s^+\pi^-$ decays can be determined from the same dataset, using the known branching fraction of $\overline{B}^0 \to D^+\pi^-$ decays,

$$\mathcal{B}(\overline{B}_s^0 \to D_s^+\pi^-) = \frac{N_{\overline{B}_s^0 \to D_s^+\pi^-}}{N_{\overline{B}^0 \to D^+\pi^-}} \frac{\epsilon_{\overline{B}^0 \to D^+\pi^-}}{\epsilon_{\overline{B}_s^0 \to D_s^+\pi^-}} \frac{f_d}{f_s} \frac{\mathcal{B}(D^- \to K^+\pi^-\pi^-)}{\mathcal{B}(D_s^- \to K^-K^+\pi^-)}\, \mathcal{B}(\overline{B}^0 \to D^+\pi^-)\,, \tag{8.10}$$

with $\mathcal{B}(\overline{B}^0 \to D^+\pi^-) = (2.68 \pm 0.13) \times 10^{-3}$ [84]. The branching fractions of the $D_{(s)}$ meson, $\mathcal{B}(D^+ \to K^-\pi^+\pi^+)$ and $\mathcal{B}(D_s^+ \to K^+K^-\pi^+)$, are also used in the determination of f_s/f_d [97], and hence cancel in the determination of $\mathcal{B}(\overline{B}_s^0 \to D_s^+\pi^-)$. The hadronic determination of the ratio of fragmentation fractions f_s/f_d presented in chapter 6 cannot be used here, as the decay $\overline{B}_s^0 \to D_s^+\pi^-$ is also used in this determination. The two measurements are therefore not independent. Instead, the semileptonic determination of f_s/f_d [97] is used, which was updated in Sec. 9.1.2. Taking into account the cancellation of the uncertainties from the $D_{(s)}$ branching fractions, its value becomes $f_s/f_d = 0.265\,^{+0.019}_{-0.016}$.

The measurement of the branching fractions of $\overline{B}_s^0 \to D_s^\pm K^\mp$, $\overline{B}^0 \to D_s^+ K^-$ and $\overline{B}_s^0 \to D_s^+\pi^-$ decays is described in the remainder of this chapter and published in [180].

8.1 Event yields

The selection of the decay modes $\overline{B}_s^0 \to D_s^+\pi^-$ and $\overline{B}^0 \to D^+\pi^-$, described in Sec. 5.2 and chapter 6, remains unchanged apart from small changes in the offline pre-selection

Decay mode	Signal yield	Efficiency
$\overline{B}{}^0_s \to D^\pm_s K^\mp$	5 101 ± 100	1.15 ± 0.01%
$\overline{B}{}^0 \to D^+_s K^-$	2 452 ± 98	0.99 ± 0.02%
$\overline{B}{}^0_s \to D^+_s \pi^-$	75 566 ± 342	1.28 ± 0.01%
$\overline{B}{}^0 \to D^+ \pi^-$	458 940 ± 959	1.40 ± 0.01%

Table 8.1 · Signal yields obtained from the fit to the invariant mass distribution and total efficiency to select the decay mode. Uncertainties are statistical only.

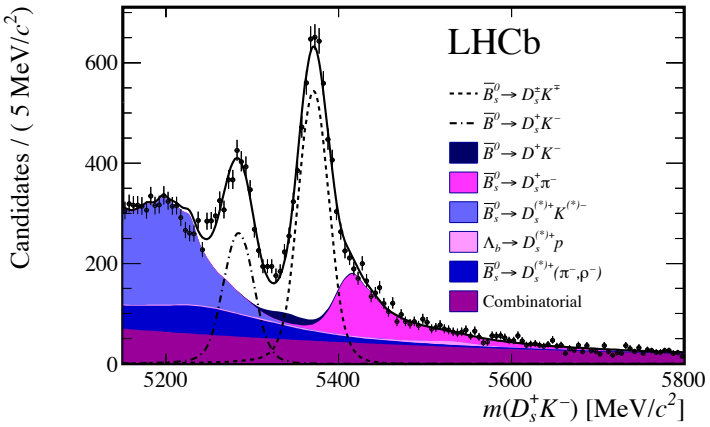

(a)

Fig. 8.5 · Invariant mass distribution of candidates reconstructed as $D^+_s K^-$. Two signal peaks can be identified, corresponding to the $\overline{B}{}^0 \to D^+_s K^-$ signal at lower mass and the $\overline{B}{}^0_s \to D^\pm_s K^\mp$ signal at higher mass.

described in Table B.2 in App. B. The decay modes $\overline{B}{}^0_s \to D^\pm_s K^\mp$ and $\overline{B}{}^0 \to D^+_s K^-$ are topologically very similar and the same selection criteria are used. In addition to the selection described in Table 5.2 in Sec. 5.2, a veto is applied to reject background from $\Lambda^0_b \to \Lambda^+_c \pi^-$ decays with $\Lambda^+_c \to p K^- \pi^+$, where the proton is mis-identified as a kaon. This veto is also applied to the $\overline{B}{}^0_s \to D^+_s \pi^-$ data sample. The PID selection criteria to select the D_s meson are unchanged, and the requirement $DLLK > 5$ is placed on the bachelor particle to separate the decay modes $\overline{B}{}^0_{(s)} \to D^\pm_s K^\mp$ from the more abundant $\overline{B}{}^0_s \to D^+_s \pi^-$ decay mode.

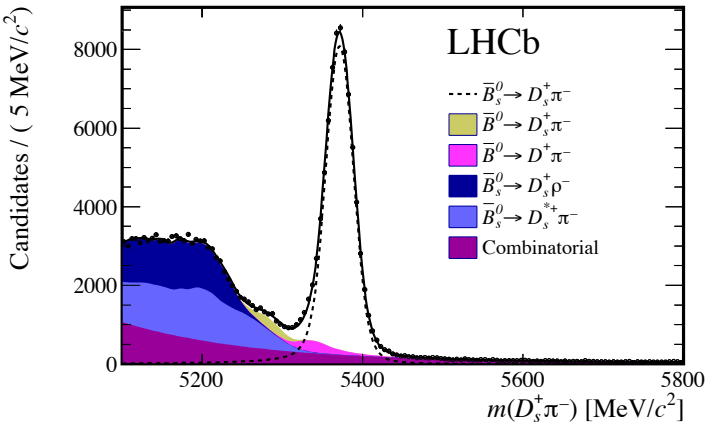

(a)

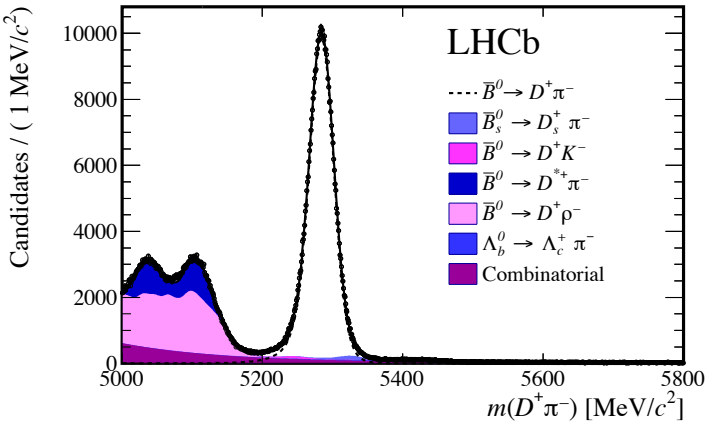

(b)

Fig. 8.6 · Invariant mass distribution of candidates reconstructed as a) $D^+_s\pi^-$ and b) $D^+\pi^-$, using the 3 fb^{-1} dataset collected at LHCb.

The event yields of the different signal modes are obtained using an unbinned maximum likelihood fit to the invariant mass distribution of reconstructed B meson candidates (Figs. 8.5–8.6). The fitting procedure is unchanged compared to that described in Section 5.2 and chapter 6. The $\overline{B}{}^0_{(s)} \to D_s^\pm K^\mp$ data sample, however, suffers from contamination of a large number of different sources of peaking background. The data does not have enough discriminating power to successfully separate between all these different sources of background. Therefore, the yields of some sources of background are constrained to their expected yield. The use of a gaussian constraint allows the uncertainty on the expected yield to be taken into account. The expected yield is determined based on the b-hadron production, the branching fraction of the decay and its total selection efficiency. The yields obtained from the fit to the invariant mass distribution are summarised in Table 8.1 together with the selection efficiencies of the different decay modes.

8.2 Systematic uncertainties

As ratios of branching fractions are measured and the different decay modes are selected with similar selection criteria, the systematic uncertainties largely cancel. Small uncertainties resulting from the selection efficiency and the use of the fit model are still present. The selection consists of three different steps: the online selection performed by the trigger, the offline kinematic selection and the PID selection. A systematic uncertainty is associated to each step.

The L0 trigger has a different selection efficiency for kaons and pions of approximately 2% [181], which is not reproduced in simulation. This average uncertainty is reduced by the fraction of events that are actually triggered by a kaon or pion from the B decay, which is approximately 50% for the bachelor particle and 10% for the K/π from the $D_{(s)}$ meson decay. In the ratio of branching fractions, only those particles that are different in the two decays need to be considered.

The offline kinematic selection efficiencies are determined separately for the 2011 dataset taken at $\sqrt{s} = 7\,\text{TeV}$ and the 2012 dataset at $\sqrt{s} = 8\,\text{TeV}$. Small efficiency differences are found between the 2011 and 2012 simulated datasets, for decays with a bachelor pion. For decays with a bachelor kaon, the differences were found to be negligible compared to the statistical uncertainty. The total selection efficiency is therefore calculated as the weighted average, with weights representing the sizes of the 2011 and 2012 datasets. The origin of the difference is not fully understood and an uncertainty is added to take this into account. This introduces a 2% uncertainty on the ratio of branching fractions. In addition, small differences between data and simulated events introduce an uncertainty on the kinematic selection efficiency. To gauge this uncertainty, the input parameters of the BDT are compared in simulation and in a background-subtracted data sample. Small differences have been observed for quantities describing the track ghost probability. The simulated events are reweighed such that the distribution of this quantity matches the one in data. The efficiency is recalculated using this reweighed data sample, and the corresponding 1% change provides an estimate of the uncertainty. The differences between simulation and data are assumed to be the same for all decay modes.

The uncertainty due to the PID selection is estimated to be 1–1.5%, using a simulated D^* calibration sample (Sec. 5.2.4). The performance of the PID calibration method obtained from this sample is compared to the true PID performance obtained from a simulated signal sample. For the measurement of the ratio of branching fractions, only the uncertainty due to final state particles which are different between the two decay modes need to be considered, as others cancel in the ratio.

The uncertainty related to the fit model for the invariant mass distribution (Figs. 8.5–8.6) has been evaluated with a set of checks. The shape of the combinatorial background has been changed from the default shape (exponential plus constant) to exponential only, resulting in a negligible change in all decay modes other than $\overline{B}^0 \to D^+\pi^-$ where a change of 0.6% was observed. A different set of shapes for the partially reconstructed and misidentified background is used, based on simulated collisions at $\sqrt{s} = 7\,\text{TeV}$ corresponding to the 2011 conditions, rather than the default based on simulated collisions at $\sqrt{s} = 8\,\text{TeV}$ which corresponds to the majority of the data sample. As a result of the different centre of mass energy in 2011 and 2012 data taking, small differences in the shape of the invariant mass distributions are found, which induce changes in the fitted signal yields. This effect is most prominent for the $\overline{B}^0 \to D_s^+K^-$ decay mode (1.8%) which suffers most from partially reconstructed and misidentified sources of background, while it is approximately 0.3% in the other decay modes. The signal is described by a Double Crystal Ball function. The parameters describing the tails of this shape are obtained from simulation and are fixed in the fit to the data, with the exception of the fit to the $\overline{B}^0 \to D^+\pi^-$ candidates where the background is sufficiently low to allow for a correct estimation of these parameters in the data. The uncertainty arising from fixing the values of the tail parameters to those found in simulation, can only be measured using the $\overline{B}^0 \to D^+\pi^-$ decay mode. Fixing the signal tail parameters in this data sample results in a 2.4% change in signal yield. Data versus simulation differences are assumed to be the same for each decay mode, which allows us to assign the 2.4% uncertainty to each decay mode where the tail parameters are fixed from simulation. An uncertainty specific to the $\overline{B}_s^0 \to D_s^\pm K^\mp$ and $\overline{B}^0 \to D_s^+K^-$ decay modes originates from the $\Lambda_b^0 \to D_s^{(*)-}p$ background. The contribution of this background is fixed based on calculations using the upper limit of the branching fraction [182]. Omitting this background changes the signal yield by 1.0% (2.0%) for $\overline{B}_s^0 \to D_s^\pm K^\mp$ ($\overline{B}^0 \to D_s^+K^-$) decays. An uncertainty specific to the $\overline{B}^0 \to D^+\pi^-$ decay is motivated by a small discrepancy between fit and data observed in the lower B^0 sideband. The fit is redone in the range 5100–5800 MeV/c^2, showing that the effect of this discrepancy can not be larger than 0.1%.

A possible contribution of charmless background decays, such as $B_s^0 \to KK\pi\pi$ or $B^0 \to K\pi\pi\pi$, is ignored in the fit. A study of the $D_{(s)}$ sidebands reveals a small contribution of charmless B^0 decays in the $D_s^\pm K^\mp$ event sample. An additional systematic uncertainty of 1.0% is added to $\mathcal{B}(\overline{B}^0 \to D_s^+K^-)$, to take this into account.

The uncertainties from the different sources described above are added in quadrature. The resulting uncertainties are 2.5% on $\mathcal{B}(\overline{B}_s^0 \to D_s^\pm K^\mp)$, 4.9% on $\mathcal{B}(\overline{B}^0 \to D_s^+K^-)$ and 3.8% on $\mathcal{B}(\overline{B}_s^0 \to D_s^+\pi^-)$.

8.3 Results

The measured relative yields of the decay modes $\overline{B}{}^0_s \to D^\pm_s K^\mp$, $\overline{B}{}^0 \to D^+_s K^-$, $\overline{B}{}^0_s \to D^+_s \pi^-$ and $\overline{B}{}^0 \to D^+ \pi^-$ are used to determine the branching fractions of the first three decay modes.

The efficiency corrected ratio of $\overline{B}{}^0_s \to D^\pm_s K^\mp$ and $\overline{B}{}^0_s \to D^+_s \pi^-$ signal yields results in the ratio of branching fractions

$$\frac{\mathcal{B}(\overline{B}{}^0_s \to D^\pm_s K^\mp)}{\mathcal{B}(\overline{B}{}^0_s \to D^+_s \pi^-)} = 0.0752 \pm 0.0015 \pm 0.0019\,, \tag{8.11}$$

where the first uncertainty is statistical and the second is systematic. This is combined with the world average value of the $\overline{B}{}^0_s \to D^+_s \pi^-$ branching fraction [84], to give

$$\mathcal{B}(\overline{B}{}^0_s \to D^\pm_s K^\mp) = (2.29 \pm 0.05 \pm 0.06 \pm 0.17) \times 10^{-4}\,, \tag{8.12}$$

where the first uncertainty is statistical, the second systematic and the third is from the uncertainty on $\mathcal{B}(\overline{B}{}^0_s \to D^+_s \pi^-)$.

The relative yields of $\overline{B}{}^0 \to D^+_s K^-$ and $\overline{B}{}^0 \to D^+ \pi^-$ decays are measured and the ratio of branching fractions is extracted,

$$\frac{\mathcal{B}(\overline{B}{}^0 \to D^+_s K^-)}{\mathcal{B}(\overline{B}{}^0 \to D^+ \pi^-)} = 0.0129 \pm 0.0005 \pm 0.0007 \pm 0.0004\,, \tag{8.13}$$

with the first uncertainty statistical, the second systematic and the third from the $D_{(s)}$ branching fractions. Using the world average value of the $\overline{B}{}^0 \to D^+ \pi^-$ branching fraction [84], the branching fraction of $\overline{B}{}^0 \to D^+_s K^-$ is

$$\mathcal{B}(\overline{B}{}^0 \to D^+_s K^-) = (3.45 \pm 0.14 \pm 0.20 \pm 0.20) \times 10^{-5}\,, \tag{8.14}$$

where the first uncertainty is statistical, the second systematic and the third originates from the B^0 and $D_{(s)}$ branching ratios.

Finally, the branching fraction of $\overline{B}{}^0_s \to D^+_s \pi^-$ decays is determined from the relative yields of $\overline{B}{}^0_s \to D^+_s \pi^-$ and $\overline{B}{}^0 \to D^+ \pi^-$ decays and using the world average value of the $\overline{B}{}^0 \to D^+ \pi^-$ branching fraction [84], to be [1]

$$\mathcal{B}(\overline{B}{}^0_s \to D^+_s \pi^-) = \left(3.08 \pm 0.02 \pm 0.12\,^{+0.23}_{-0.26}\right) \times 10^{-3}\,, \tag{8.15}$$

where the first uncertainty is statistical, the second systematic and the third is from the uncertainties on f_s/f_d and $\mathcal{B}(B^0)$.

[1] The $\mathcal{B}(\overline{B}{}^0_s \to D^+_s \pi^-)$ presented here differs from [180] using the value of f_s/f_d calculated in chapter 9, taking into account the latest values of the B meson lifetimes and $\mathcal{B}(D_s)$, and the difference between the theoretical and experimental branching fraction of B^0_s decays.

8.4 Conclusion

The measurement of $\mathcal{B}(\overline{B}{}^0_s \to D^\pm_s K^\mp) = (2.29 \pm 0.19) \times 10^{-4}$ supersedes the previous LHCb measurement [110]. Its value relative to the $\overline{B}{}^0_s \to D^+_s \pi^-$ branching ratio is measured to be 0.0752 ± 0.0025. This ratio is compatible with the lower theoretical bound of 0.080 ± 0.007 [175] that is shown in Fig. 8.3. The branching fraction of the decay $\overline{B}{}^0 \to D^+_s K^-$ is measured to be $(3.45 \pm 0.30) \times 10^{-5}$ which is world's most precise measurement of this quantity. As expected, this decay, which proceeds through the W-exchange topology, is suppressed compared to $\mathcal{B}(\overline{B}{}^0 \to D^+\pi^-) = (2.68 \pm 0.13) \times 10^{-3}$, which proceeds predominantly through colour-allowed tree diagrams. The measurement of $\mathcal{B}(\overline{B}{}^0_s \to D^+_s \pi^-) = \left(3.08\,^{+0.26}_{-0.29}\right) \times 10^{-3}$ is found to be consistent with the previous LHCb measurement [110]. It is limited by the uncertainty on the semileptonic determination of f_s/f_d and the $\mathcal{B}(\overline{B}{}^0 \to D^+\pi^-)$, resulting in an uncertainty which is as large as the previous measurement despite the larger dataset available. The branching fraction of $\overline{B}{}^0_s \to D^+_s \pi^-$ decays is the most precise B^0_s branching ratio known to date.

CHAPTER 9

Conclusions

The ratios of b-hadron production fractions and their kinematic dependencies, as presented in the previous chapters, are indispensable ingredients for B^0_s and Λ^0_b branching fraction measurements at the LHC. In addition, these measurements help to improve the theoretical understanding of the fragmentation process. Sections 9.1–9.2 illustrate the application of the results on the ratio of fragmentation fractions in various domains. The impact of the measurement of f_s/f_d on the recent measurement of the branching fraction $\mathcal{B}(B^0_s \to \mu^+\mu^-)$ as reported by LHCb and CMS will be discussed .

Measurements of branching fractions of $B \to Dh$ tree decays are presented in chapters 6–8. The impact of these results on future measurements is discussed in Sec 9.3. A test of $SU(3)$ symmetry, as was introduced in Sec. 5.1 using $\overline{B}^0 \to D^{*+}_{(s)}h^-$ decays, is included using $\overline{B}^0 \to D^+_{(s)}h^-$ decays .

9.1 On the ratio of B^0_s and B^0 production fractions

The ratio of fragmentation fractions f_s/f_d is measured using hadronic tree decays in chapter 6. The main results are repeated here for convenience. The measurement is combined with an independent measurement of the same quantity using semileptonic decays, to yield

$$f_s/f_d = 0.256 \pm 0.020\,. \tag{9.1}$$

A dependence of the relative production fractions of B^0_s and B^0 mesons on the B meson transverse momentum is observed (Fig. 9.1), which is best described with

$$f_s/f_d(p_{\rm T}) = (0.256 \pm 0.020) + (-2.0 \pm 0.6) \times 10^{-3}/\,{\rm GeV}/c \times \left(p_{\rm T} - \langle p_{\rm T}\rangle\right), \tag{9.2}$$

with $\langle p_{\rm T}\rangle = 10.4\,{\rm GeV}/c$. No significant dependence on the B meson pseudorapidity was seen.

9.1.1 Theoretical modelling of the $p_{\rm T}$ dependence of f_s/f_d

The measurements described in chapters 6 and 7 provide valuable input for the improvement of fragmentation function models. It has been shown that the shape of the $p_{\rm T}$ dependence

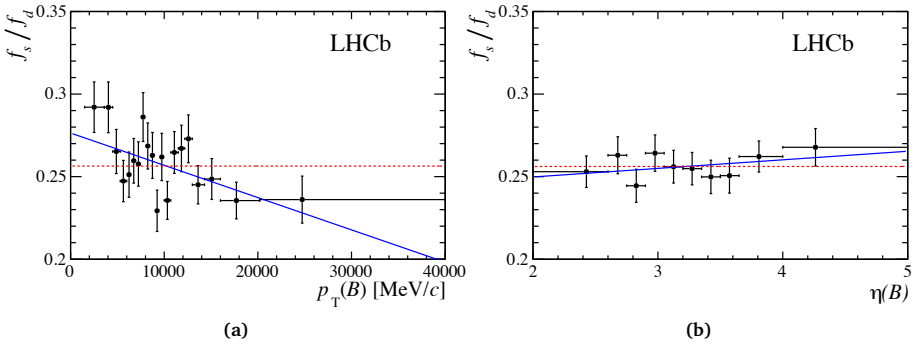

(a) (b)

Fig. 9.1 · Ratio of fragmentation fractions f_s/f_d and its dependence on a) transverse momentum, b) pseudorapidity of the B meson, as presented in chapter 6.

of f_s/f_d measured by LHCb can be understood by the fragmentation approach [183], as will be outlined below.

Perturbative QCD can predict both the shape and normalisation of fragmentation functions for *doubly heavy* mesons. For instance, the fragmentation function for the formation of B_c^+ mesons has the form [183]

$$f_{\bar{b}\to B_c}(z) = \frac{2\alpha_s^2|R_S(0)|^2}{27\pi m_c^3}\frac{rz(1-z)^2}{\big(1-(1-r)z\big)^6}\Big(2-2(3-2r)z+3(3-2r+4r^2)z^2 \\ -2(1-r)(4-r+2r^2)z^3+(1-r)^2(3-2r+2r^2)z^4\Big), \quad (9.3)$$

where $R_S(0)$ is the value of the non-relativistic B_c^+ wave function at the origin, and $r = \frac{m_c}{m_c+m_b}$. This fragmentation function can also be applied to the formation of *heavy-light* mesons, in which case the quantity r is a phenomenological parameter to be obtained from data. In this case, the normalisation cannot be determined from perturbative QCD.

The p_T dependence of the ratio of fragmentation fractions f_s/f_d, as presented in chapter 6, can be obtained assuming fragmentation functions for the B_s^0 and B^0 meson of the form shown in Eq. 9.3. Figure 9.2a shows these functions with $r = 0.057$ (using $m_b = 5.0\,\text{GeV}, m_d = 0.3\,\text{GeV}$) and $r = 0.074$ (using $m_b = 5.0\,\text{GeV}, m_s = 0.4\,\text{GeV}$) for the B^0 and the B_s^0 meson, respectively. The parameters r are not derived from experimental data, but empirically chosen such to arrive at a ratio of fragmentation fractions which describes the observed p_T dependence. The p_T dependence of the ratio of fragmentation fractions is calculated from the fragmentation functions, by a convolution of these functions with the $b\bar{b}$ cross-section.

9.1.2 Update of f_s/f_d measurement by LHCb

The ratio of fragmentation fractions f_s/f_d is measured at LHCb using hadronic decays in chapter 6 and published in [164], and using semileptonic decays [97], to be, respec-

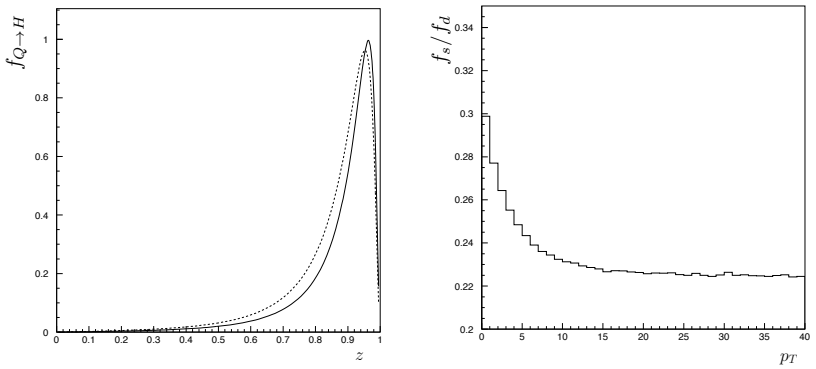

(a) (b)

Fig. 9.2 · a) Fragmentation functions of B^0 (solid) and B_s^0 (dashed) mesons, derived from perturbative QCD and described by Eq. 9.3. b) Convolution with the $b\bar{b}$ cross section within QCD allows the extraction of the ratio of fragmentation fractions f_s/f_d. Figures from [183].

tively, $f_s/f_d = 0.238 \pm 0.004\,(\text{stat}) \pm 0.015\,(\text{syst}) \pm 0.021\,(\text{theo})$ and $f_s/f_d = 0.268 \pm 0.008\,(\text{stat})\ ^{+0.022}_{-0.020}\,(\text{syst})$. Both measurements use data from pp collisions at $\sqrt{s} = 7\,\text{TeV}$. The sizes of the datasets are 1 fb^{-1} for the hadronic determination and 3 pb^{-1} for the semileptonic determination. A combination of the two measurements was included in chapter 6. A new combination is presented here, taking into account the latest world average values of the branching fraction of $D_s^+ \to K^-K^+\pi^+$ decays, and the B meson lifetimes. Both analyses use samples of B decays produced in LHCb with the same transverse momentum distribution. The event selection has a negligible systematic effect on the average value of f_s/f_d compared to its uncertainty. Using the values summarised in Table 9.1, the updated value of the hadronic measurement becomes

$$(f_s/f_d)_{\text{hadr}} = 0.239 \pm 0.004 \pm 0.013 \pm 0.021\,, \tag{9.4}$$

where the first uncertainty is statistical, the second systematic and the third due to the uncertainty on theoretical input. The central value of the measurement increases, while the systematic uncertainty decreases due to better known lifetimes and D_s branching ratio. The semileptonic measurement becomes

$$(f_s/f_d)_{\text{semilep}} = 0.265 \pm 0.008\ ^{+0.021}_{-0.018}\,. \tag{9.5}$$

where the first uncertainty is statistical and the second is systematic. The central value of the measurement decreases, as does the systematic uncertainty due to better known lifetimes and D_s branching ratio. The difference between the experimental and theoretical branching fractions of B_s^0 decays of 0.6% (Eq. 5.18 in Sec. 5.1, with $\mathcal{A}^f_{\Delta\Gamma} = 0$ for flavour specific B_s^0 decays) is taken into account in the calculation of both the hadronic and semileptonic f_s/f_d.

	Previous value used in		Value used for
	hadronic [164]	semileptonic [97]	update
$\mathcal{B}(D_s^+ \to K^-K^+\pi^+)$	$(5.50 \pm 0.27)\%$	$(5.50 \pm 0.27)\%$	$(5.39 \pm 0.21)\%$
τ_{B^0}		1.525 ± 0.009 ps	1.520 ± 0.004 ps
$\tau_{B_s^0}$		1.472 ± 0.025 ps	1.509 ± 0.004 ps
τ_{B^+}		1.638 ± 0.011 ps	1.638 ± 0.004 ps
$\tau_{B_s^0}/\tau_{B^0}$	0.984 ± 0.011		0.993 ± 0.004
$(\tau_{B^0} + \tau_{B^+})/\tau_{B_s^0}$		2.149 ± 0.038	2.093 ± 0.007

Table 9.1 · Values for the lifetimes and branching fractions as used in the hadronic and semileptonic measurements, and the updated values used in this combination. The updated lifetime values are from [187] and the updated $\mathcal{B}(D_s^+ \to K^-K^+\pi^+)$ is from [84]. The ratio of lifetimes reported in the last row is calculated from the lifetimes.

The averaging procedure takes into account the correlated and uncorrelated uncertainties, as summarised in Table 9.2. The average value is determined using one million pseudo experiments. The hadronic measurement is modelled using a Gaussian distribution with a width which represents the uncorrelated uncertainty. The semileptonic measurement is modelled using a bifurcated Gaussian function to take into account the asymmetric uncertainties [184, 185], convolved with a Gaussian that represents the symmetric uncertainties. The average value is then calculated as

$$f_s/f_d = \alpha \times (f_s/f_d)_{\text{hadr}} + (1-\alpha) \times (f_s/f_d)_{\text{semilep}} \,. \tag{9.6}$$

where $\alpha = 0.35$ is chosen such to minimise the 68% CL interval. The correlated uncertainty is added in quadrature, giving the combined value

$$f_s/f_d = 0.260 \pm 0.018 \,. \tag{9.7}$$

The most probable value differs slightly from a simple weighted average of the two measurements because of the asymmetric uncertainty of the semileptonic measurement. This combination supersedes all previous combinations [97, 164, 186].

9.1.3 Measurement of $\mathcal{B}(B_s^0 \to \mu^+\mu^-)$

Flavour Changing Neutral Current processes are heavily suppressed in the SM and can occur only through higher order diagrams. The decay $B_s^0 \to \mu^+\mu^-$ is the prime example of this type of decays. Its branching fraction in the SM is predicted to be [188, 189]

$$\mathcal{B}(B_s^0 \to \mu^+\mu^-) = (3.66 \pm 0.23) \times 10^{-9}, \tag{9.8}$$

taking into account the average B_s^0 meson lifetime difference [190]. The decay proceeds predominantly via box and penguin topologies, as shown in Fig. 9.3a–9.3b. Several NP models predict heavy particles which can enter the loops of these diagrams as indicated in Fig. 9.3c–9.3d, altering the predicted branching fraction. A measurement of the branching fraction of $B_s^0 \to \mu^+\mu^-$ decays is thus a sensitive probe to physics beyond the standard model.

Source	Hadronic (%)	Semileptonic (%)
Uncorrelated gaussian uncertainties		
Statistical	1.7	3.0
Theoretical	8.8	
Binning		1.0
Fit model	1.5	3.0
Backgrounds		2.0
Tracking efficiency		2.0
Selection efficiency	2.6	
PID efficiency	1.5	1.5
$\mathcal{B}((B^-/B^0) \to D_s^+ K X \mu \bar{\nu}_\mu)$		2.0
Total	9.6	5.8
Uncorrelated asymmetric uncertainties		
$\overline{B}_s^0 \to D^0 K^+ X \mu \bar{\nu}_\mu$		$^{+4.1}_{-1.1}$
Correlated gaussian uncertainties		
$\mathcal{B}(D^+ \to K^- \pi^+ \pi^+)$	2.2	
$\mathcal{B}(D_s^+ \to K^- K^+ \pi^+)$	3.9	
Lifetimes	0.4	
Total	4.5	

Table 9.2 · Sources of uncertainty for the hadronic and semileptonic measurements of f_s/f_d. The uncertainties are categorised according to correlated/uncorrelated between the two measurements, and symmetric/asymmetric uncertainties.

The branching fraction of $B_s^0 \to \mu^+\mu^-$ decays could in principle be measured at LHCb as

$$\mathcal{B}(B_s^0 \to \mu^+\mu^-) = \frac{N_{B_s^0 \to \mu^+\mu^-} / \epsilon_{B_s^0 \to \mu^+\mu^-}}{N_{B_s^0}}, \tag{9.9}$$

where $N_{B_s^0 \to \mu^+\mu^-}$ is the measured yield, $\epsilon_{B_s^0 \to \mu^+\mu^-}$ is the total selection and reconstruction efficiency, and $N_{B_s^0}$ is the number of produced B_s^0 mesons. The number of B_s^0 mesons can be determined as

$$N_{B_s^0} = \sigma(pp \to b\bar{b})\, f_s\, \mathcal{L}, \tag{9.10}$$

with $\sigma(pp \to b\bar{b})$ the $b\bar{b}$ production cross-section, f_s the fraction of b quarks that fragment into a B_s^0 meson and $\mathcal{L}$ the luminosity.

The LHCb Collaboration measured the total $b\bar{b}$ cross-section using $b \to J/\psi X$ decays to be $\sigma_{\text{tot}}(pp \to b\bar{b}) = 288 \pm 4\,(\text{stat}) \pm 48\,(\text{syst})\,\mu\text{b}$ [137]. The cross-section within LHCb is readily obtained as $\sigma_{2<\eta<6}(pp \to b\bar{b}) = \sigma_{\text{tot}}(pp \to b\bar{b})/3.77 = 76 \pm 1\,(\text{stat}) \pm 13\,(\text{syst})$, where the factor 3.77 is determined using PYTHIA 6.4 [191]. The luminosity is measured with a precision of 1.16% for the total 2011 plus 2012 dataset, which is the most precise luminosity determination achieved so far at a bunched-beam hadron collider. The determination was performed by LHCb using a combination of two independent luminosity

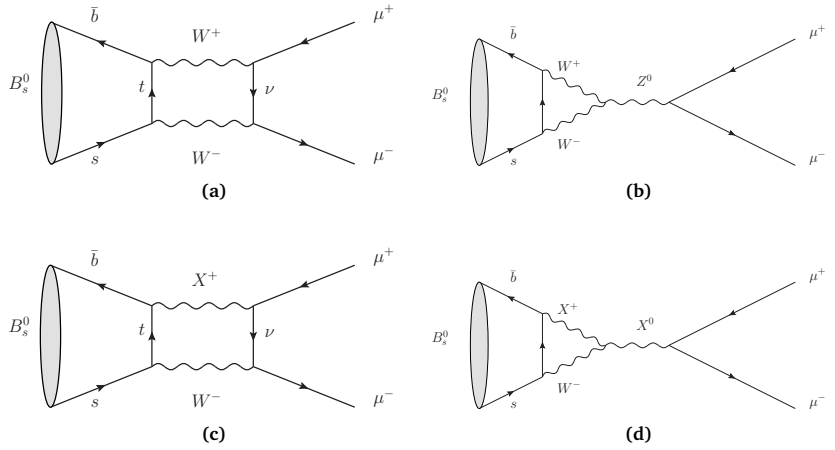

Fig. 9.3 · Box (a-c) and penguin (b-d) decay topologies for the decay $B_s^0 \to \mu^+\mu^-$. Several new physics models predict heavy particles which can enter in the loops (c-d).

calibration methods: van der Meer scans and beam-gas imaging [192]. Measurements of the fragmentation fraction f_s are performed at LEP [90–92] and Tevatron [94, 95, 193] and a global fit using information on all measured fragmentation fractions f_x results in $f_s = 0.105 \pm 0.005$ [187]. The measurement of f_s/f_d shown in chapter 6 and published in [164] is also included in this average. The resulting uncertainty on $N_{B_s^0}$ from a direct measurement as described in Eq. 9.10 is 18%, dominated by the uncertainty of σ_{tot}. In addition, the selection efficiency $\epsilon_{B_s^0 \to \mu^+\mu^-}$, carries a sizeable uncertainty due to data and simulation differences. Together this would result in a large uncertainty on the measured branching fraction of $B_s^0 \to \mu^+\mu^-$ decays.

Alternatively, the branching fraction can be measured relative to that of a decay for which the branching fraction is measured to high precision, and where uncertainties on the event selection largely cancel. No branching fraction measurement of B_s^0 meson decays exists with a sufficient precision. However, branching fractions of B^0 and B^+ decays have been measured to a precision of a few percent and are therefore suitable to use as normalisation channels. This requires the use of the ratio of fragmentation fractions f_s/f_d, which is measured with a precision of 7%, as outlined in Sec. 9.1.2.

9.1.3.1 LHCb measurement using the 3 fb^{-1} dataset

The LHCb Collaboration reported a measurement of the branching fraction of $B_s^0 \to \mu^+\mu^-$ decays using the combined 2011 and 2012 datasets, obtained at $\sqrt{s} = 7\,\text{TeV}$ and $\sqrt{s} = 8\,\text{TeV}$, respectively, resulting in [56]

$$\mathcal{B}(B_s^0 \to \mu^+\mu^-) = \left(2.9\,^{+1.1}_{-1.0}\right) \times 10^{-9}\,. \tag{9.11}$$

Two complementary decays, $B^+ \to J/\psi(\to \mu^+\mu^-)K^+$ and $B^0 \to K^+\pi^-$, are used as normalisation channels. The first decay has similar trigger and muon identification effi-

ciencies as the signal but a different number of particles in the final state, while the second channel has a similar decay topology but a different trigger selection. Their branching fractions are $(6.025 \pm 0.205) \times 10^{-5}$ and $(1.94 \pm 0.06) \times 10^{-5}$ [157], respectively. The small uncertainty on the branching fraction, and the similarity of these decays to the signal decay, make them suitable as normalisation channels. The branching fraction of $B_s^0 \to \mu^+\mu^-$ decays is measured using

$$\mathcal{B}(B_s^0 \to \mu^+\mu^-) = \frac{N_{B_s^0\to\mu^+\mu^-}}{\epsilon_{B_s^0\to\mu^+\mu^-}} \frac{f_d}{f_s} \frac{\epsilon_{\text{norm}}}{N_{\text{norm}}} \mathcal{B}(\text{norm}) \,, \tag{9.12}$$

with N the yields of the signal and normalisation channel, ϵ their total selection and reconstruction efficiencies, and $\mathcal{B}(\text{norm})$ the branching fraction of the normalisation channel. Also for the B^+ normalisation channel the ratio of fragmentation fractions f_s/f_d is used, assuming U-spin symmetry to be valid: $f_u = f_d$.

The dependence of f_s/f_d on the centre-of-mass energy is evaluated using $B^+ \to J/\psi K^+$ and $B_s^0 \to J/\psi \phi$ decays. The ratio of yields measured separately in the 2011 and 2012 datasets, is a probe for a variation of f_s/f_d. The ratio of fragmentation fractions was found to be stable.

A dependence of f_s/f_d on the transverse momentum of the B meson is presented in chapter 6 and published in [164]. The central value of f_s/f_d, measured using hadronic decays, is reported at an average p_{T} of the B_s^0 meson of 10.4 GeV. The measurement of $\mathcal{B}(B_s^0 \to \mu^+\mu^-)$ is performed in bins in which the average p_{T} of the B_s^0 meson varies from 3 GeV to 9 GeV. As a cross-check, the value of f_s/f_d was evaluated at 3 GeV and found to differ from the reported central value by 0.02, which corresponds to one standard deviation of the f_s/f_d measurement. The measurement of $\mathcal{B}(B_s^0 \to \mu^+\mu^-)$ is statistically limited. Therefore, the effect of the p_{T} dependence of f_s/f_d is assumed to be negligible. The dominating systematic uncertainty, however, is due to the uncertainty on f_s/f_d.

The yield of $B_s^0 \to \mu^+\mu^-$ decays is extracted from a fit to the $m(\mu^+\mu^-)$ invariant mass distribution, as shown in Fig. 9.4a for the most significant BDT bin of the analysis.

9.1.3.2 CMS measurement

The CMS collaboration reported a measurement of the $B_s^0 \to \mu^+\mu^-$ branching fraction using the 5 fb^{-1} dataset taken at $\sqrt{s} = 7$ TeV and the 20 fb^{-1} dataset taken at $\sqrt{s} = 8$ TeV [57],

$$\mathcal{B}(B_s^0 \to \mu^+\mu^-) = \left(3.0\,^{+1.0}_{-0.9}\right) \times 10^{-9} \,. \tag{9.13}$$

The collected CMS dataset is much larger than that collected by the LHCb collaboration, but CMS has a lower efficiency for triggering and reconstructing low-mass particles, resulting in a similar sensitivity for both experiments.

The decay $B^+ \to J/\psi(\to \mu^+\mu^-)K^+$ is used as a normalisation channel and the $B_s^0 \to \mu^+\mu^-$ branching fraction is determined following Eq. 9.12. The ratio of fragmentation fractions f_s/f_u is not measured by the CMS experiment, and they rely on its determination by LHCb [164]. As the CMS experiment probes a different kinematic region ($|\eta| < 2.4$) compared to the LHCb experiment, and selects B_s^0 candidates with typically a higher transverse momentum compared to those reconstructed by LHCb, an additional

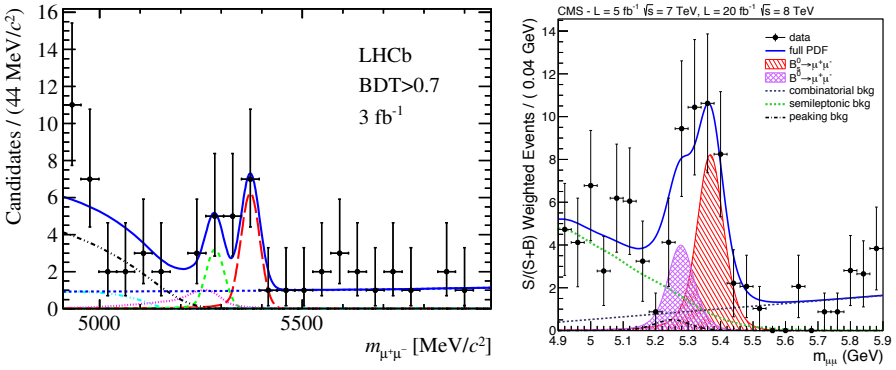

(a) (b)

Fig. 9.4 · Fit to the di-muon invariant mass distribution for a) the LHCb measurement and b) the CMS measurement with both muons reconstructed in the barrel.

systematic uncertainty of 5% is assigned for a possible pseudorapidity and p_{T} dependence of the ratio of fragmentation fractions. A possible η or p_{T} dependence of f_s/f_u within the kinematic region used in the analysis is evaluated using the ratio of yields measured for $B^+ \to J/\psi K^+$ and $B_s^0 \to J/\psi \phi$ decays, and is found to be negligible.

The yield of $B_s^0 \to \mu^+\mu^-$ decays is extracted from a fit to the $m(\mu^+\mu^-)$ invariant mass distribution, as shown in Fig. 9.4b.

9.1.3.3 Combination of LHCb and CMS measurements

The two experiments follow similar data analysis strategies and their results are combined to increase the precision of the $B_s^0 \to \mu^+\mu^-$ branching fraction measurement [189]. In this combination systematic uncertainties and their correlations are accounted for. An unbinned extended maximum likelihood fit to the di-muon invariant mass distribution is performed simultaneously to the LHCb and CMS datasets, resulting in Fig. 9.5a. In addition to $\mathcal{B}(B_s^0 \to \mu^+\mu^-)$, also $\mathcal{B}(B^0 \to \mu^+\mu^-)$ is measured, which is related to the former by the exchange of the s quark for a d quark (Fig. 9.3). This decay is further suppressed by a factor 35 with respect to $B_s^0 \to \mu^+\mu^-$ [188], mainly because the CKM matrix element V_{td} involved is smaller than the corresponding element V_{ts} in $B_s^0 \to \mu^+\mu^-$ decays.

The reported combined measurement is

$$\begin{aligned} \mathcal{B}(B_s^0 \to \mu^+\mu^-) &= \left(2.8\,^{+0.7}_{-0.6}\right) \times 10^{-9}\,, \\ \mathcal{B}(B^0 \to \mu^+\mu^-) &= \left(3.9\,^{+1.6}_{-1.4}\right) \times 10^{-10}\,, \end{aligned} \tag{9.14}$$

and is statistically limited. The statistical significance is computed to be 6.2σ for $B_s^0 \to \mu^+\mu^-$ decays and 3.2σ for $B^0 \to \mu^+\mu^-$ decays. The expected significances assuming SM branching fractions are 7.4σ and 0.8σ, respectively. The measured branching fractions are compared to their SM predictions in Fig. 9.5b.

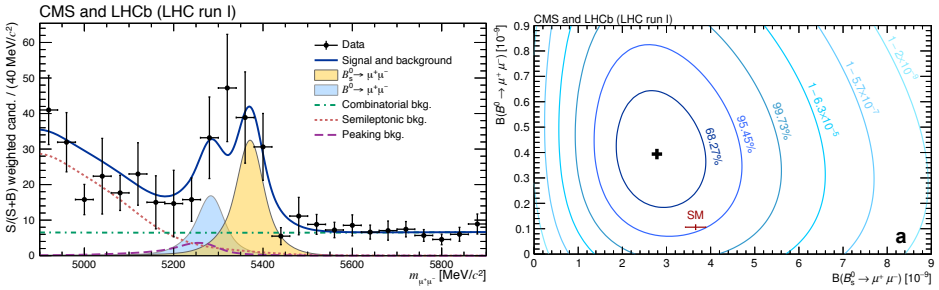

Fig. 9.5 · a) Fit to the di-muon invariant mass distribution for the combined LHCb and CMS datasets. b) Likelihood contours in the $\mathcal{B}(B_s^0 \to \mu^+\mu^-)$-$\mathcal{B}(B^0 \to \mu^+\mu^-)$ plane. Figures from [189].

9.1.3.4 Outlook

The measurement of $\mathcal{B}(B_s^0 \to \mu^+\mu^-)$ is currently statistically limited. However, the large datasets that will become available to LHCb during Run II ($5\,\text{fb}^{-1}$) and in particular during the Upgrade phase ($50\,\text{fb}^{-1}$) [194] will demand a more precise measurement of f_s/f_d in order to avoid a systematic limitation.

The measurement $\mathcal{B}(B_s^0 \to \mu^+\mu^-) = \left(2.8\,^{+0.7}_{-0.6}\right) \times 10^{-9}$ [189] is in agreement with the SM prediction, indicating no hint of NP. The ratio of branching fractions $\mathcal{B}(B^0 \to \mu^+\mu^-)/\mathcal{B}(B_s^0 \to \mu^+\mu^-)$ is a robust observable that is also sensitive to NP scenarios [195]. Figure 9.6 shows the 5σ discovery potential for new physics using the ratio of these branching fractions. When large data samples of $B_{d,s}^0 \to \mu^+\mu^-$ decays will have been collected, the accuracy of the extracted ratio of branching fractions $\mathcal{B}(B^0 \to \mu^+\mu^-)/\mathcal{B}(B_s^0 \to \mu^+\mu^-)$ will be limited by the accuracy on f_s/f_d. Figure 9.6 illustrates that a new physics scenario which predicts an increased ratio of branching fractions compared to the SM prediction which is smaller than 0.039 cannot be distinguished from SM with 5σ, even when an infinitely large dataset has been collected (assuming $\delta(f_s/f_d) = 6.9\%$, as calculated in Sec. 9.1.2).

The hadronic measurement of f_s/f_d using the decays $\overline{B}_s^0 \to D_s^+\pi^-$ and $\overline{B}^0 \to D^+K^-$ depends on theoretical input on the ratio of form factors, $\mathcal{N}_F$, and on the deviation from naive factorisation for the two decays modes, $\mathcal{N}_a$, as defined in Sec. 5.1.3. Both factors reduce to 1 in the limit of U-spin symmetry. The dominating uncertainty originates from the ratio of form factors. Different calculations of $\mathcal{N}_F$ using non-perturbative techniques are available, using QCD sum rules, $\mathcal{N}_F = 1.24 \pm 0.08$ [156], or using Lattice QCD [154], $\mathcal{N}_F = 1.094 \pm 0.093$. The latter measurement, showing no large effects from U-spin breaking, is considered to be more robust. Despite its larger uncertainty it is used in the measurement of f_s/f_d, as this choice is more conservative.

The semileptonic measurement of f_s/f_d is based on the equality of inclusive semileptonic branching fractions of all the B-meson species, and does not suffer from large theoretical uncertainties. The largest systematic uncertainties on this measurement are related to the contribution of $\overline{B}_s^0 \to D^0K^+X\mu\bar{\nu}_\mu$ decays and the fit model (Table 9.2). Only a subset

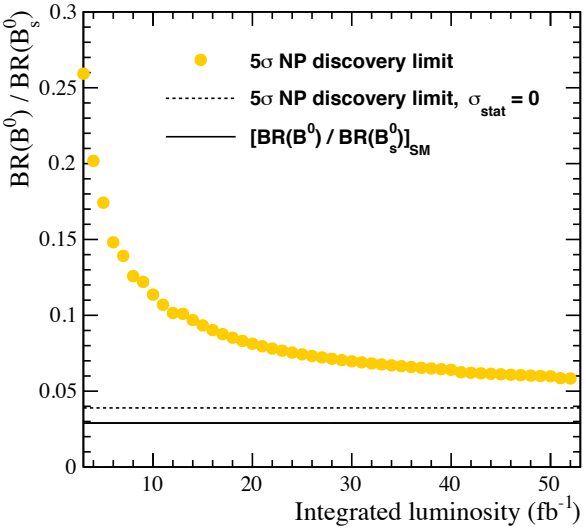

Fig. 9.6 · New physics discovery potential using the ratio of $B^0_{d,s} \to \mu^+\mu^-$ decays. The SM prediction is indicated with the solid line. The minimum ratio of branching fractions as predicted in a NP scenario which can be measured with 5σ, assuming an uncertainty on f_s/f_d of 6.9% (Sec. 9.1.2) and no statistical uncertainty is indicated with the horizontal dashed line. An infinitely large data sample is assumed. The orange points corresponds to the minimum ratio of branching fractions for which a 5σ NP signal can be discovered, taking into account the statistical uncertainty resulting from the limited size of the available data sample. The statistical uncertainty as a function of integrated luminosity is estimated using an extrapolation of the number of $B^0 \to \mu^+\mu^-$ signal events measured in the LHCb 3 fb^{-1} dataset [196], corrected for the difference between the standard model prediction of $\mathcal{B}(B^0 \to \mu^+\mu^-)$ and its measured value. The measurement of the ratio of branching fractions is expected to remain statistically limited, also during the upgrade phase of the LHCb experiment. Figure from [197].

of the available data is used for the semileptonic measurement. The size of this subset results in a limiting uncertainty, which could be improved using the larger datasets recorded in 2011 and 2012.

9.1.4 Measurement of f_s/f_d at $\sqrt{s} = 8$ TeV

The value of f_s/f_d at $\sqrt{s} = 8\,\text{TeV}$ can be determined relative to the value of f_s/f_d at $\sqrt{s} = 7\,\text{TeV}$ using any ratio of B^0_s and B^0 decays measured at $\sqrt{s} = 8\,\text{TeV}$ and $\sqrt{s} = 7\,\text{TeV}$. A measurement using $B^+ \to J/\psi K^+$ and $B^0_s \to J/\psi\phi$ decays resulted in the conclusion that f_s/f_d is independent of the centre-of-mass energy [56].

The dependence of f_s/f_d on the centre-of-mass energy is also studied using the decays $\overline{B}^0_s \to D^+_s\pi^-$ and $\overline{B}^0 \to D^+\pi^-$ in chapter 8 of this thesis. The measured yield ratios and efficiency ratios are shown in Table 9.3 for the 2011 dataset at $\sqrt{s} = 7\,\text{TeV}$ and the

	2011	2012
$N_{B_s^0}/N_{B^0}$	16.95 ± 0.45	16.34 ± 0.42
$\epsilon_{B^0}/\epsilon_{B_s^0}$	1.04 ± 0.02	1.08 ± 0.02

Table 9.3 · Ratio of signal yields and efficiencies for the decays $\overline{B}_s^0 \to D_s^+\pi^-$ and $\overline{B}^0 \to D^+\pi^-$, as obtained in the measurement described in chapter 8 of this thesis. The uncertainties are statistical only and are related to the limited size of the different datasets.

2012 dataset at $\sqrt{s} = 8\,\text{TeV}$ separately. The efficiency corrected yield ratio is determined to be $N_{B^0}/N_{B_s^0} = 17.63 \pm 0.58$ and $N_{B^0}/N_{B_s^0} = 17.65 \pm 0.56$ for the 2011 and 2012 datasets, respectively, leading to $(f_s/f_d)_{8\ \text{TeV}}/(f_s/f_d)_{7\ \text{TeV}} = 1.00 \pm 0.05$. No dependence of the ratio of fragmentation fractions f_s/f_d on the centre-of-mass energy is observed.

9.2 On the ratio of Λ_b^0 and B^0 production fractions

The kinematic dependencies of Λ_b^0 and B^0 production are measured in chapter 7. The main results are repeated here for convenience. The ratio of fragmentation fractions $f_{\Lambda_b^0}/f_d$ is observed to be dependent on the b-hadron transverse momentum and pseudorapidity, as shown in Fig. 9.7. The p_T dependence is best described by

$$f_{\Lambda_b^0}/f_d(p_\text{T}) = a' + \exp(b' + c' \times p_\text{T}[\,\text{GeV}/c]), \tag{9.15}$$

with

$$\begin{aligned} a' &= +0.151 \pm 0.016\ ^{+0.024}_{-0.025}, \\ b' &= -0.573 \pm 0.040\ ^{+0.101}_{-0.097}, \\ c' &= -0.095 \pm 0.007 \pm 0.014\ \ [\,\text{GeV}/c]^{-1}, \end{aligned}$$

where the first uncertainty is statistical and the second systematic. The correlations between the three parameters are given by the correlation matrix

$$\rho(a', b', c') = \begin{pmatrix} 1 & 0.55 & -0.73 \\ 0.55 & 1 & -0.03 \\ -0.73 & -0.03 & 1 \end{pmatrix}.$$

The η dependence is described by the linear function

$$f_{\Lambda_b^0}/f_d(\eta) = a' + b' \times (\eta - \overline{\eta})\,, \tag{9.16}$$

with

$$\begin{aligned} a' &= 0.387 \pm 0.013\ ^{+0.028}_{-0.030}, \\ b' &= 0.067 \pm 0.005\ ^{+0.012}_{-0.009}, \end{aligned}$$

where the first uncertainty is statistical and the second systematic.

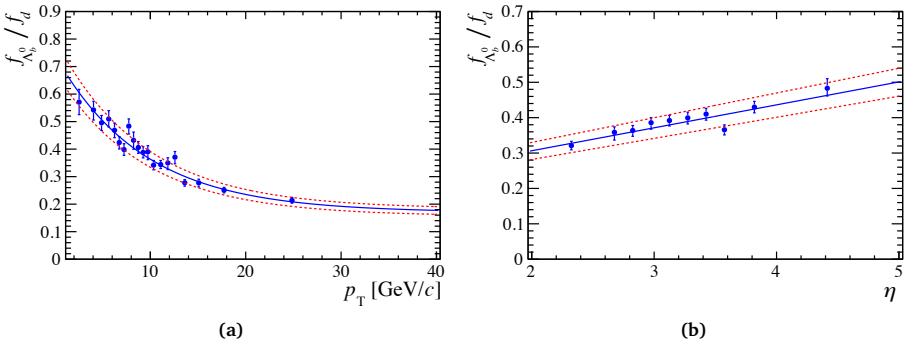

Fig. 9.7 · Ratio of fragmentation fractions $f_{\Lambda_b^0}/f_d$ and its dependence on a) transverse momentum, b) pseudorapidity of the b hadron, as presented in chapter 7.

9.2.1 Universality of fragmentation fraction ratio $f_{\Lambda_b^0}/f_d$

A summary of measurements of the p_T dependence of $f_{\Lambda_b^0}/f_d$ was shown in Fig. 4.5 in Sec. 4.2. The Heavy Flavour Averaging Group recently published [187] an update of this summary (Fig. 9.8), now including the measurement reported in chapter 7 and published in [165]. Excellent agreement of the p_T dependence is found between the two measurements performed by LHCb using hadronic [165] and semileptonic decays [97]. Moreover, a measurement performed by the CDF collaboration using $p\bar{p}$ collision data, which is not included in Fig. 9.8, is consistent with the LHCb measurements as can be seen in Fig. 4.5 in Sec. 4.2. The calculation of the LEP value at $p_T = 40\,\text{GeV}/c$ further supports the exponential functional form that is used to parametrize the p_T dependence. The remarkable agreement between the measurements performed on data from pp, $p\bar{p}$ and e^+e^- collisions, where each dataset is obtained at a different centre-of-mass energy, supports the notion that the ratio of fragmentation fractions is universal.

9.2.2 Branching fraction measurement exploiting the $f_{\Lambda_b^0}/f_d$ dependence

The p_T dependence of $f_{\Lambda_b^0}/f_d$ measured using the decays $\Lambda_b^0 \to \Lambda_c^+\pi^-$ and $\overline{B}^0 \to D^+\pi^-$ does not depend on the specific Λ_b^0 and B^0 decay channel and its functional form can therefore be used to fit any other ratio of Λ_b^0 and B^0 decays. A new strategy to measure a branching fraction was introduced in chapter 7 and published in [165], which exploits the p_T dependence of $f_{\Lambda_b^0}/f_d$. This strategy is also applied in a LHCb publication [198] to measure the double ratio of branching fractions

$$\left[\frac{\mathcal{B}(\Lambda_b^0 \to \Lambda_c^+ D_s^-)}{\mathcal{B}(\overline{B}^0 \to D^+ D_s^-)}\right] \Big/ \left[\frac{\mathcal{B}(\Lambda_b^0 \to \Lambda_c^+ \pi^-)}{\mathcal{B}(\overline{B}^0 \to D^+ \pi^-)}\right] = 0.96 \pm 0.02\,(\text{stat}) \pm 0.06\,(\text{syst})\,, \quad (9.17)$$

in a production cross-section independent manner. Figure 9.9 shows the p_T dependence of the efficiency corrected yield ratio of $\Lambda_b^0 \to \Lambda_c^+ D_s^-$ to $\overline{B}^0 \to D^+ D_s^-$ decays. The p_T

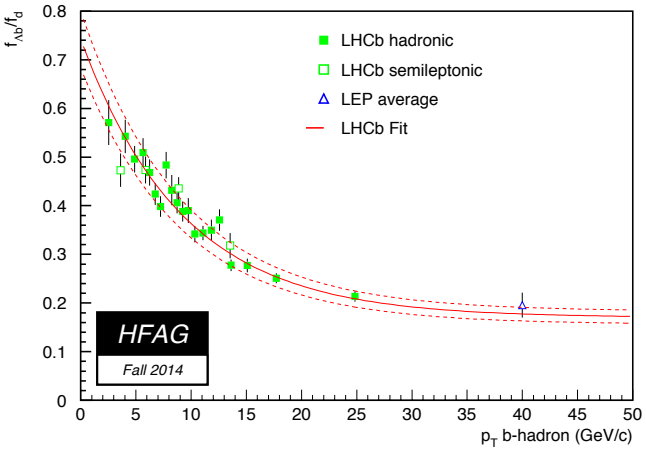

Fig. 9.8 · The p_{T} dependence of the ratio of fragmentation fractions $f_{\Lambda_b^0}/f_d$ measured using hadronic (closed green) [165] and semileptonic (open green) [97] decays by LHCb. The b hadron transverse momentum of the semileptonic data is determined in chapter 7. The curve is the fit to the hadronic data, as presented in chapter 7. The calculated LEP value (open blue) [187] is in agreement with the curve. Figure from [187].

dependence of $f_{\Lambda_b^0}/f_d$ from chapter 7 is overlaid, and the overall normalisation is fitted to obtain the result of Eq. 9.17. A remarkable agreement is observed between the functional form of the p_{T} dependence measured in chapter 7 and the data measured in [198].

The measurement of $\mathcal{B}(\Lambda_b^0 \to \Lambda_c^+\pi^-)$ presented in chapter 7 combined with Eq. 9.17 allow for the determination of the branching fraction of $\Lambda_b^0 \to \Lambda_c^+ D_s^-$ decays. Using the known branching fractions of $\overline{B}^0 \to D^+\pi^-$ and $\overline{B}^0 \to D^+ D_s^-$ decays [84], one finds

$$\mathcal{B}(\Lambda_b^0 \to \Lambda_c^+ D_s^-) = (11.1 \pm 1.3) \times 10^{-3}\,. \tag{9.18}$$

9.2.3 Production of Λ_b^0 baryons at low transverse momenta

The Λ_b^0 double differential production cross-section times the branching fraction of $\Lambda_b^0 \to J/\psi p K^-$ decays is being measured as a function of the b hadron transverse momentum and rapidity by LHCb [199]. The decay $\overline{B}^0 \to J/\psi \overline{K}^*$ is used as a normalisation channel. The ratio

$$R_{\Lambda_b^0/\overline{B}^0} = \frac{\sigma_{\Lambda_b^0}}{\sigma_{\overline{B}^0}} \frac{\mathcal{B}(\Lambda_b^0 \to J/\psi p K^-)}{\mathcal{B}(\overline{B}^0 \to J/\psi \overline{K}^*)} \tag{9.19}$$

is extracted in the rapidity region $2.0 < y < 4.5$ for b hadrons with a transverse momentum $p_{\mathrm{T}} < 20$ GeV/c. The high trigger selection efficiency of muons, even at low momenta, allows for an extension of the existing measurement of the p_{T} dependence of $f_{\Lambda_b^0}/f_d$ in the

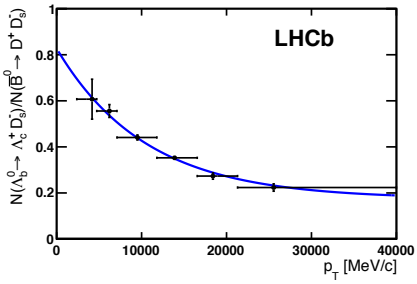

Fig. 9.9 · Efficiency corrected yield ratio of $\Lambda_b^0 \to \Lambda_c^+ D_s^-$ and $\overline{B}^0 \to D^+ D_s^-$ decays, overlaid with the functional form of the p_{T} dependence of $f_{\Lambda_b^0}/f_d$ as determined using the efficiency corrected yield ratio of $\Lambda_b^0 \to \Lambda_c^+ \pi^-$ and $\overline{B}^0 \to D^+ \pi^-$ decays (presented in Sec. 7). The normalisation of the curve is fitted to the data points. Figure from [198].

region $1.5 < p_{\mathrm{T}} < 40$ GeV/c to even lower values of the transverse momentum. A falling p_{T} dependence of $f_{\Lambda_b^0}/f_d$ is observed, which is in agreement with that observed in chapter 7 and published in [165], with a plateau at low transverse momenta (Fig. 9.10c). The rapidity dependence (Fig. 9.10d) cannot straightforwardly be compared to the previous measurement as the current measurement probes a different region in transverse momentum. The measurements are performed separately for the $1\,\mathrm{fb}^{-1}$ dataset taken at $\sqrt{s} = 7\,\mathrm{TeV}$ and the $2\,\mathrm{fb}^{-1}$ dataset taken at $\sqrt{s} = 8\,\mathrm{TeV}$. The measurements are in agreement within their uncertainty, and no indication of a dependence of $f_{\Lambda_b^0}/f_d$ on the centre-of-mass energy has been observed. In addition, a small production asymmetry is suggested as a function of rapidity, with more Λ_b^0 baryons produced close to the beam and less at central rapidity (Fig. 9.10f).

The decay $\Lambda_b^0 \to J/\psi p K^-$ was also used for the discovery of the pentaquark P_c^+, in the decay $\Lambda_b^0 \to P_c^+(\to J/\psi p) K^-$ [200].

9.2.4 Λ_b^0 production and the measurement of $|V_{ub}|$

The magnitude of the CKM element V_{ub} can be measured via the transition $b \to u l^- \bar{\nu}_l$. Measurements using the exclusive decay $\overline{B} \to \pi l^- \bar{\nu}_l$ [201–204] differ by approximately three standard deviations from inclusive measurements [84], posing a puzzle to flavour physics. LHCb uses for the first time baryon decays to probe $|V_{ub}|$ [205]. The exclusive measurement using $\Lambda_b^0 \to p\mu^- \bar{\nu}_\mu$ decays, results in $|V_{ub}| = 3.27 \pm 0.23$ and is in agreement with previous exclusive measurements.

The ratio of CKM elements $|V_{ub}|/|V_{cb}|$ is determined by LHCb following

$$\frac{|V_{ub}|^2}{|V_{cb}|^2} = \frac{\mathcal{B}(\Lambda_b^0 \to p\mu^- \bar{\nu}_\mu)}{\mathcal{B}(\Lambda_b^0 \to \Lambda_c^+ \mu^- \bar{\nu}_\mu)} R_{\mathrm{FF}}\,, \tag{9.20}$$

where R_{FF} is the ratio of the relevant form factors. As a result of the selection criteria applied to select signal candidates and candidates for the normalisation channel, the Λ_b^0 candidate of the normalisation channel $\Lambda_b^0 \to \Lambda_c^+ \mu^- \bar{\nu}_\mu$ has on average a much harder p_{T}

spectrum. As shown in chapter 7, the Λ_b^0 production cross-section depends strongly on the transverse momentum. This leads to a different cross-section in the kinematic region of the signal and in the kinematic region of the normalisation channel.

The dependence of the Λ_b^0 production on the transverse momentum is difficult to calculate and is not emulated correctly in simulation, resulting in different (transverse) momentum distributions in data and simulations. As the kinematic selection efficiency is obtained from simulated events, a bias is introduced in the measurement. This is corrected for using $\Lambda_b^0 \to J/\psi p K^-$ decays, for which differences between data and simulated data can be determined. Using simulated samples of $\Lambda_b^0 \to p\mu^-\bar{\nu}_\mu$ and $\Lambda_b^0 \to \Lambda_c^+\mu^-\bar{\nu}_\mu$ decays, the distribution of "production corrections" is determined. Due to the kinematic selection criteria which result in a harder Λ_b^0 spectrum in the normalisation channel, the distribution of production corrections corresponding to the normalisation channel differs from that corresponding to the signal channel. The production corrections are found to introduce a 7% correction to the relative efficiency.

Alternatively, the measurement of $f_{\Lambda_b^0}/f_d\ (p_{\mathrm{T}})$ presented in chapter 7 can be used to quantify the effect of the p_{T} dependence of the Λ_b^0 production on the measurement of V_{ub}. The p_{T} dependence of $\sigma(pp \to \Lambda_b^0 X)$ can be obtained from the measured yields and efficiencies of $\Lambda_b^0 \to \Lambda_c^+\pi^-$ decays, in the 20 p_{T} bins in which the measurement of $f_{\Lambda_b^0}/f_d\ (p_{\mathrm{T}})$ is performed. The p_{T} dependence in data is compared to the p_{T} dependence observed in simulated $\Lambda_b^0 \to \Lambda_c^+\pi^-$ decays in Fig. 9.11. The advantage of using $\Lambda_b^0 \to \Lambda_c^+\pi^-$ decays is that this allows for an efficiency corrected comparison, i.e. before any selection of detector effects.

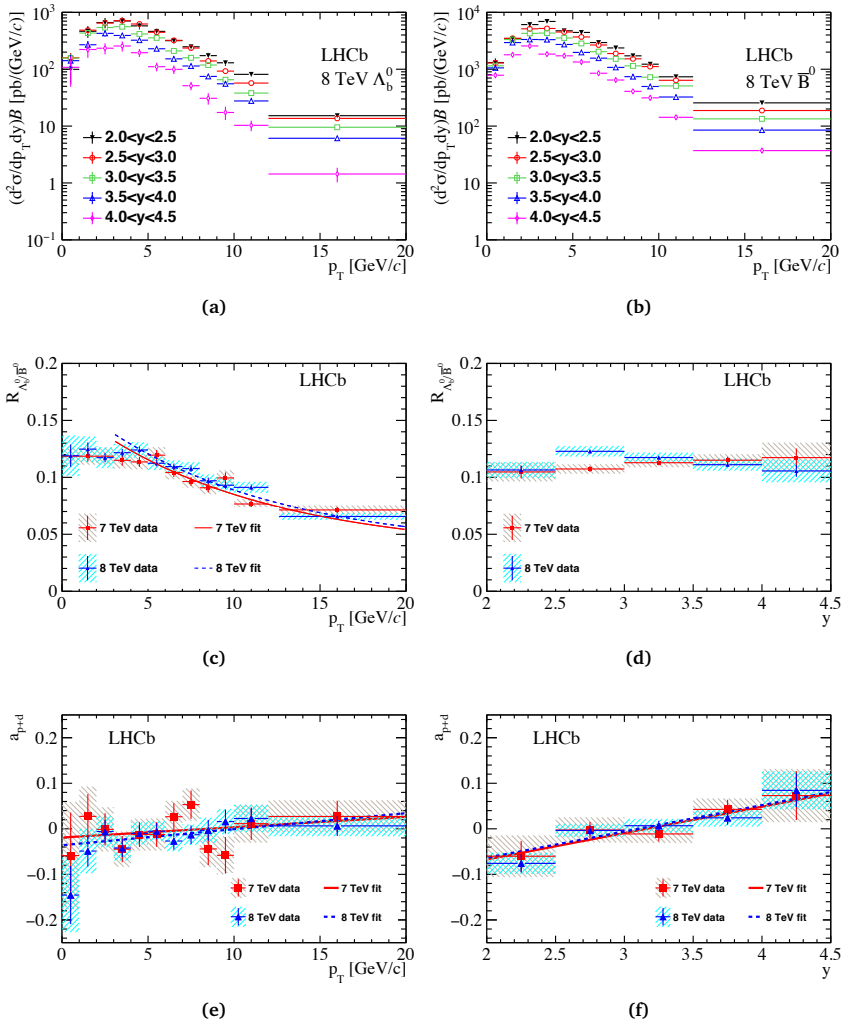

Fig. 9.10 · Double differential production cross section for a) Λ_b^0 baryons and b) B^0 meson, measured in 2012 data. The ratio $R_{\Lambda_b^0/B^0} = \sigma_{\Lambda_b^0}/\sigma_{\overline{B}^0} \times \mathcal{B}(\Lambda_b^0 \to J/\psi p K^-)/\mathcal{B}(\overline{B}^0 \to J/\psi \overline{K}^*)$ in bins of c) transverse momentum and d) rapidity. The transverse momentum dependence is fit with the functional form of $f_{\Lambda_b^0}/f_d\,(p_{\rm T})$ measured in chapter 7. Production and decay asymmetry, a_{p+d}, of Λ_b^0 and $\overline{\Lambda}_b^0$ as function of d) $p_{\rm T}$ and f) rapidity. Results are shown for the 2011 (red) and 2012 (blue) datasets separately. Figures from [199].

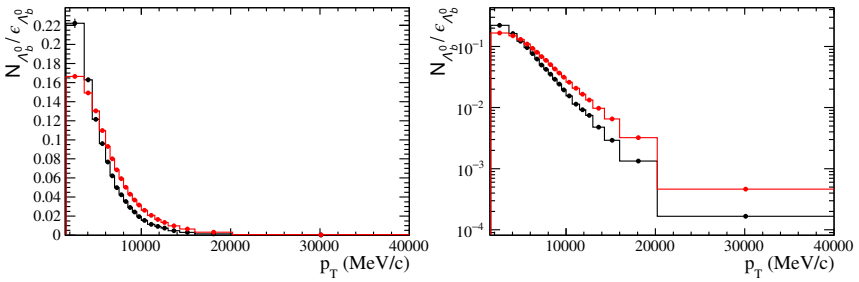

(a) (b)

Fig. 9.11 · p_{T} dependence of Λ_b^0 production cross-section in data (black) and simulation (red), as measured in chapter 7 using $\Lambda_b^0 \to \Lambda_c^+ \pi^-$ decays, on a a) linear and b) logarithmic scale. Only statistical uncertainties are included.

9.3 On the measurement of the absolute branching fractions

Several measurements of b-hadron branching fractions are described throughout chapters 6–8. Their measured values are collected here for convenience:

$$\begin{aligned}
\mathcal{B}(\overline{B}^0 \to D^+ K^-) &= (2.20 \pm 0.13) \times 10^{-4}, && \text{[chapter 6]} \\
\mathcal{B}(\Lambda_b^0 \to \Lambda_c^+ \pi^-) &= \left(4.30\,^{+0.36}_{-0.35}\right) \times 10^{-3}, && \text{[chapter 7]} \\
\mathcal{B}(\overline{B}_s^0 \to D_s^\pm K^\mp) &= (2.29 \pm 0.19) \times 10^{-4}, && \text{[chapter 8]} \\
\mathcal{B}(\overline{B}^0 \to D_s^+ K^-) &= (3.45 \pm 0.30) \times 10^{-5}, && \text{[chapter 8]} \\
\mathcal{B}(\overline{B}_s^0 \to D_s^+ \pi^-) &= \left(3.08\,^{+0.26}_{-0.29}\right) \times 10^{-3}. && \text{[chapter 8]}
\end{aligned} \tag{9.21}$$

9.3.1 $\Lambda_b^0 \to \Lambda_c^+ \pi^-$ decays as normalisation channel

The measurement of $\mathcal{B}(\Lambda_b^0 \to \Lambda_c^+ \pi^-) = (4.30 \pm 0.36) \times 10^{-3}$ in chapter 7 is the most precise Λ_b^0 branching fraction measurement to date, with an uncertainty of 8.3%. In contrast to the measurement of the ratio of fragmentation fractions $f_{\Lambda_b^0}/f_d$ [97], the $\Lambda_b^0 \to \Lambda_c^+ \pi^-$ measurement does not suffer from the large uncertainty (26% [84]) from the branching fraction of $\Lambda_c^+ \to p K^- \pi^+$ decays as it cancels in the branching fraction determination. This results in a smaller uncertainty on $\mathcal{B}(\Lambda_b^0 \to \Lambda_c^+ \pi^-)$ than on $f_{\Lambda_b^0}/f_d$. The decay $\Lambda_b^0 \to \Lambda_c^+ \pi^-$ therefore provides a valuable normalisation channel for other Λ_b^0 branching fraction measurements.

9.3.2 $\mathcal{B}(B_s^0)$ measurements at the $\Upsilon(5S)$ resonance

The measurement of $\mathcal{B}(\overline{B}_s^0 \to D_s^+ \pi^-)$ presented in chapter 8, and published in [110, 180], is the most precise B_s^0 branching fraction measurement and is the dominating contribution to the world average value $\mathcal{B}(\overline{B}_s^0 \to D_s^+ \pi^-) = (3.04 \pm 0.23) \times 10^{-3}$. Its uncertainty is still larger than that of f_s/f_d and since many B^0 branching fractions are known to high precision, they can provide suitable normalisation channels for B_s^0 branching fraction measurements at the LHC. However, the decay $\overline{B}_s^0 \to D_s^+ \pi^-$ might become an important normalisation channel at future colliders, for instance at SuperKEKB which is designed to also operate at the $\Upsilon(5S)$ resonance. As the ratio of fragmentation fractions f_s/f_d depends on the kinematic region and on the centre-of-mass energy (clearly $f_{\Lambda_b^0} = 0$ at the $\Upsilon(5S)$ resonance), its value measured by LHCb [97, 164] cannot straightforwardly be used at SuperKEKB. Instead, any B_s^0 branching fraction at SuperKEKB relies on the knowledge of $f_s = \mathcal{B}(\Upsilon(5S) \to B_s^{(*)} \overline{B}_s^{(*)})$.

The B_s^0 production fraction f_s is measured by the Belle Collaboration using the 121.4 fb^{-1} dataset collected at the $\Upsilon(5S)$ resonance [206, 207]. It is determined from a measurement of the $\Upsilon(5S) \to D_s X$ branching fraction using $D_s^+ \to \phi \pi^+$ decays, which is related to f_s via

$$\mathcal{B}(\Upsilon(5S) \to D_s X)/2 = f_s \times \mathcal{B}(B_s \to D_s X) + (1 - f_s) \times \mathcal{B}(B \to D_s X)\,, \tag{9.22}$$

where the fraction of final states without a B meson is assumed to be zero. The large uncertainties associated to the branching fraction $\mathcal{B}(B_{(s)} \to D_s X)$, result in a precision of

17% on f_s. The uncertainty on f_s remains large, taking into account the latest values of these branching fractions [84].

The CLEO Collaboration used the 0.423 fb^{-1} dataset collected at the $\Upsilon(5S)$ resonance to measure the production fraction f_s in a similar fashion using D_s meson yields [208]. In addition, CLEO measured f_s using ϕ meson yields which are related to B_s^0 production via

$$\mathcal{B}(\Upsilon(5S) \to \phi X)/2 = f_s \times \mathcal{B}(B_s \to \phi X) + \frac{1-f_s}{2} \times \mathcal{B}(\Upsilon(4S) \to \phi X)\,. \tag{9.23}$$

Finally, a measurement of the total $e^+e^- \to \Upsilon(5S)$ cross-section is used to determine the inclusive $\Upsilon(5S) \to B\overline{B}X$ branching fraction [208]. Assuming that the $\Upsilon(5S)$ decay is dominated by $b\bar{b}$ decays, this branching fraction is equal to $1 - f_s$. Also the CLEO measurement suffers from the large uncertainties associated to the different branching fractions involved in the calculations, and its reported values carry an uncertainty of at least 17%.

The world average value of $\mathcal{B}(\Upsilon(5S) \to B_s^{(*)}\overline{B}_s^{(*)}) = 0.201 \pm 0.031$ [84] has an uncertainty of 14%. As a result, the decay $\overline{B}_s^0 \to D_s^+\pi^-$, which can be used as a normalisation channel and which branching fraction is known to a precision better than 8%, provides a competitive alternative for any B_s^0 branching fraction measurement at the $\Upsilon(5S)$ resonance at SuperKEKB.

9.3.3 Test of $SU(3)$ symmetry using $\overline{B}^0 \to D^+K^-$ and $\overline{B}^0 \to D_s^+K^-$ decays

The test of $SU(3)$ symmetry described in Sec. 5.1.3.3 is performed using the decays $\overline{B}^0 \to D^{*+}\pi^-$, $\overline{B}^0 \to D^{*+}K^-$ and $\overline{B}^0 \to D_s^{*+}K^-$. The same test can be performed using the decays measured in this thesis: $\overline{B}^0 \to D^+\pi^-$, $\overline{B}^0 \to D^+K^-$ and $\overline{B}^0 \to D_s^+K^-$. The amplitude of $\overline{B}^0 \to D^+\pi^-$ decays is of the $T+E$ topology, as shown in Fig. 9.12. Upon the replacement of the d for an s quark, one finds the decays $\overline{B}^0 \to D^+K^-$ and $\overline{B}^0 \to D_s^+K^-$ which are denoted by the $T^{'}$ and $E^{'}$ topologies, respectively. The amplitudes of the decays $\overline{B}^0 \to D^+\pi^-$, $\overline{B}^0 \to D^+K^-$ and $\overline{B}^0 \to D_s^+K^-$ span a triangle, in analogy to Fig. 5.6 in Sec. 5.1.3.3.

The measurements of the different branching fractions described in this thesis are used to estimate the magnitude of the various topologies, and test whether a picture consistent with $SU(3)$ symmetry arises. The branching faction of $\overline{B}^0 \to D^+K^-$ decays relative to that of $\overline{B}^0 \to D^+\pi^-$ decays is measured in chapter 6 and published in [164],

$$\frac{\mathcal{B}(\overline{B}^0 \to D^+K^-)}{\mathcal{B}(\overline{B}^0 \to D^+\pi^-)} = 0.0822 \pm 0.0027\,. \tag{9.24}$$

The branching fraction of $\overline{B}^0 \to D_s^+K^-$ decays relative to $\mathcal{B}(\overline{B}^0 \to D^+\pi^-)$ is measured in chapter 8 and published in [180]

$$\frac{\mathcal{B}(\overline{B}^0 \to D_s^+K^-)}{\mathcal{B}(\overline{B}^0 \to D^+\pi^-)} = 0.0129 \pm 0.0009\,. \tag{9.25}$$

The decay amplitude is related to the branching fraction as

$$\mathcal{B}(B \to Dh) = \Phi_{Dh}^{B}\,\tau_B\,|A(B^0 \to Dh)|^2\,, \tag{9.26}$$

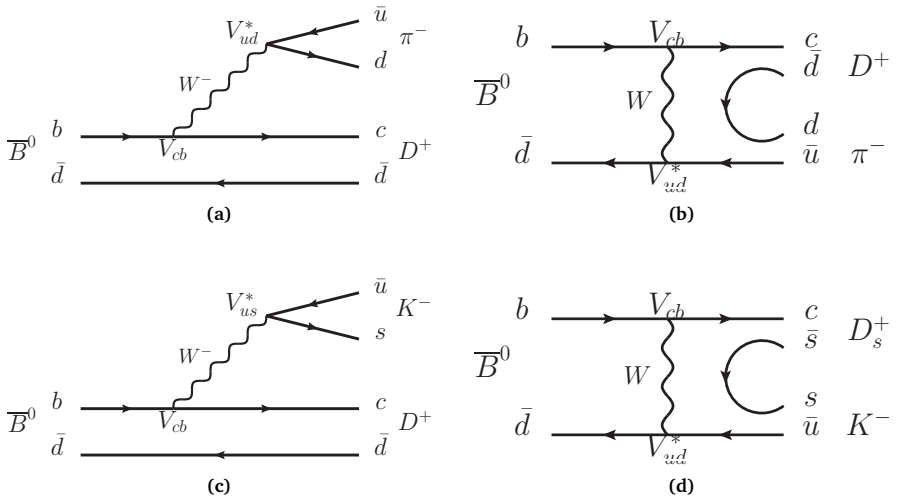

Fig. 9.12 · Feynman diagrams describing the decays a) $\overline{B}^0 \to D^+\pi^-$ (T), b) $\overline{B}^0 \to D^+\pi^-$ (E), c) $\overline{B}^0 \to D^+K^-$ (T') and d) $\overline{B}^0 \to D_s^+K^-$ (E').

where τ_B is the B meson lifetime and the phase space factor is given by[1]

$$\Phi_{Dh}^B = \frac{\sqrt{(m^2_{B_{(s)}} - m^2_{D_{(s)}} - m_h^2)^2 - 4m^2_{D_{(s)}} m_h^2}}{16\pi m^3_{B_{(s)}}} \,. \tag{9.27}$$

Following the approach in [134], the amplitudes of $\overline{B}^0 \to D^+K^-$ and $\overline{B}^0 \to D_s^+K^-$ decays are corrected for the different particles in the final state (compared to the $\overline{B}^0 \to D^+\pi^-$ decay). These factorisable $SU(3)$-breaking corrections were summarised in chapter 5.1 to be

$$\left|\frac{T}{T'}\right| = \left|\frac{V_{ud}}{V_{us}}\right| \frac{f_\pi}{f_K} \frac{F_0^{BD}(m_\pi^2)}{F_0^{BD}(m_K^2)} \qquad \text{and} \qquad \left|\frac{E}{E'}\right| = \frac{f_D}{f_{D_s}} \frac{f_\pi}{f_K} \tag{9.28}$$

for $\overline{B}^0 \to D^+K^-$ and $\overline{B}^0 \to D_s^+K^-$ decays, respectively. Using the variables collected in Table 9.4, and the ratios of branching fractions in Eqs 9.24–9.25, the ratio of amplitudes are measured to be

$$\frac{\overline{B}^0 \to D^+K^-}{\overline{B}^0 \to D^+\pi^-} \;:\; \frac{|T|}{|T+E|} = 1.03 \pm 0.07 \tag{9.29}$$

[1] The equation for the phase space factor given here differs from that in chapter 5.1 by a factor $\left(m^2_{B_{(s)}} - m^2_{D_{(s)}}\right)^2$. This factor originates from the evaluation of the hadronic matrix element describing the hadronisation of the D meson in a colour-allowed tree decay and was incorporated in the phase space factor in chapter 5.1. As this factor does not play a role in the exchange topology and cancels in the calculation of $|T/(T+E)|$, it is omitted here.

Amplitude calculation			Correction factor calculation		
m_{B^0}	=	5279.17 MeV/c^2	$\lvert V_{ud}\rvert$	=	0.97425
m_D	=	1869.6 MeV/c^2	$\lvert V_{us}\rvert$	=	0.2252
m_{D_s}	=	1968.47 MeV/c^2	f_π	=	130.41 MeV/c^2
m_π	=	139.57 MeV/c^2	f_K	=	156.1 MeV/c^2
m_K	=	497.61 MeV/c^2	$F_0^{BD}(m_\pi^2)/F_0^{BD}(m_K^2)$	=	0.992 ± 0.064
τ_{B^0}	=	1.519×10^{-12}s	f_D	=	206.7 ± 8.9 MeV/c^2
			f_{D_s}	=	257.5 ± 6.1 MeV/c^2

Table 9.4 · Parameters for the calculation of the amplitude and the correction for the different particles in the final states. All values are taken from [157], except for the form factor ratio which is obtained from [154].

and

$$\frac{\overline{B}^0 \to D_s^+ K^-}{\overline{B}^0 \to D^+ \pi^-} \quad : \qquad \frac{|E|}{|T+E|} = 0.077 \pm 0.005\,, \tag{9.30}$$

where the uncertainty is associated to the uncertainty on the branching fractions and the factorisable $SU(3)$-breaking corrections. Interestingly, the amplitude $|T+E|$ is smaller than the amplitude $|T|$, which could be a result of a destructive interference between the $|T|$ and $|E|$ decay topologies in $\overline{B}^0 \to D^+\pi^-$ decays. The uncertainty on $|T|/|T+E|$ can almost entirely be attributed to the ratio of form factors which enters through the factorisable $SU(3)$ corrections. In the calculation of $|E|/|T+E|$ the uncertainties from the branching fraction and the factorisable $SU(3)$ corrections are approximately of equal size. The triangle relation between the T, E and $T+E$ amplitudes is illustrated in Fig. 9.13. Unfortunately, a measurement of the relative strong phase between the T and E amplitude is not possible until the theoretical uncertainties are reduced.

Estimating the size of the exchange amplitude

The ratio $|T|/|T+E|$ is measured to be close to unity. From this measurement it follows that both the non-factorisable $SU(3)$-breaking effects and the size of the exchange amplitude are small. This is consistent with the measurement of $\mathcal{B}(\overline{B}^0 \to D_s^+ K^-)$ from which the size of the exchange amplitude, E, is inferred.

LHCb recently reported a measurement of CP asymmetries with $\overline{B}_s^0 \to D_s^\pm K^\mp$ decays [102]. These decays are sensitive to the CKM angle γ via CP violation in the interference between mixing and decay. The measured value is $\gamma = \left(115\,^{+28}_{-43}\right)^\circ$. Also the strong phase difference between the two diagrams in Fig. 8.1 was measured and its value is $\delta_s = \left(3\,^{+19}_{-20}\right)^\circ$. In addition to the two favoured tree decay topologies of Fig. 8.1, the $\overline{B}_s^0 \to D_s^\pm K^\mp$ decay can also proceed via the suppressed W-exchange topology in Fig. 8.2b. This topology does not influence the measurement of the weak phase γ, it does however contribute to the measurement of the strong phase δ_s. The measured small value of the strong phase difference, indicates that either the strong phase difference between the exchange topology and the tree topology (δ_E) is small, or that the amplitude of the

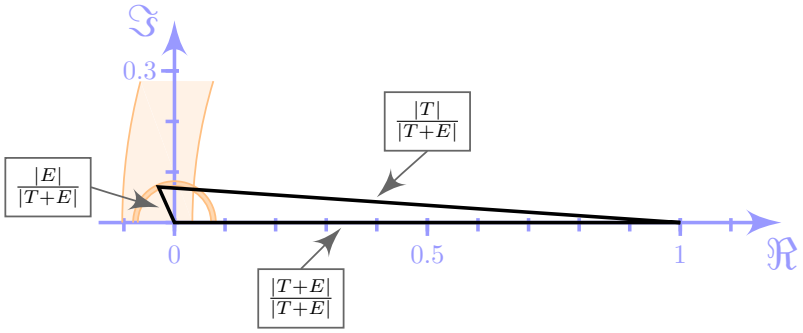

Fig. 9.13 · $SU(3)$ symmetry demands that the amplitudes of $\overline{B}^0 \to D^+\pi^-$ (T+E), $\overline{B}^0 \to D^+K^-$ (T') and $\overline{B}^0 \to D_s^+K^-$ (E') decays form a triangle in the complex plane.

exchange topology (E) is small. As can be seen from Fig. 9.13 and Fig. 5.6 in chapter 5.1, δ_E is not constrained to be small. The size of the exchange amplitude is likely to be small, which is in agreement with the measurement of $\mathcal{B}(\overline{B}^0 \to D_s^+K^-)$.

APPENDIX A

Results of ageing tests of the Outer Tracker

A.1 Results of amplifier threshold scans

All threshold scans taken between 2010 and 2013 are summarised in Table A.1 and the relative gain variation of the entire OT is given.

A number of modules have been identified in Fig. 3.7 in chapter 2, which show a deviant gain change that is reoccurring in every scan since the first occurrence of the phenomena. These modules can all be related to FEs that are replaced since the time of the reference scan, indicating that there exist small differences in the amplifier characteristics of the FEs. The different modules showing odd behaviour in the threshold scans are briefly discussed below.

- **T1L0Q2M4**[1]: Replaced on 11 May 2011 because of frequent errors (DLL). However, errors from this FE are still observed and it has therefore been masked on the alarm screen of the monitoring system.
- **T1L2Q1M9**[2]: On 23 April 2012 this FE was not responding. Replaced on 24 April 2012.
- **T2L0Q2M7**[3]: On 16 February 2012, FE T2L0Q2M6 was swapped with this FE because it showed some problems.
- **T2L2Q0M9**[4]: Frequent errors starting from 3 July 2012. Replaced on 17 September 2012.

[1] http://lblogbook.cern.ch/OT/1624.
[2] http://lblogbook.cern.ch/OT/2567, http://lblogbook.cern.ch/OT/2561.
[3] http://lblogbook.cern.ch/OT/2344, http://lblogbook.cern.ch/OT/2343.
[4] http://lblogbook.cern.ch/OT/2825, http://lblogbook.cern.ch/OT/2842, http://lblogbook.cern.ch/OT/3039.

date	total delivered lumi [pb^{-1}]	atmospheric pressure	pres. corr. G_{rel}
Jul. 4 2010	0.6	981.0	
Aug. 14 2010	1.2	975.0	
Oct. 27 2010	34.4	971.5	9.5%
Mar. 13 2011	41.8	971.0	3.7%
May 16 2011	137.8	987.8	1.2%
Jun. 11 2011	331.4	978.0	1.6%
Jul. 29 2011	584.8	977.2	1.7%
Sep. 7 2011	809.2	979.0	0.5%
Oct. 12 2011	1239.5	985.3	1.3%
Apr. 4 2012	1260.8	969.0	10.2%
May 30 2012	1612.7	979.0	10.0%
Jul. 2 2012	1917.0	976.5	11.4%
Aug. 8 2012	2302.1	983.2	11.6%
Sep. 27 2012	2721.0	974.7	11.3%
Sep. 28 2012	2721.0	980.2	11.3%
Nov. 7 2012	3175.7	989.3	12.9%
Dec. 5 2012	3464.7	968.3	12.3%
Feb. 12 2013	3469.8	961.3	10.5%

Table A.1 · All threshold scans taken thus far. The total delivered luminosity is taken from `https://lbrundb.cern.ch/rundb/fill`. The pressure-corrected relative gain is given for the entire OT surface, and corresponds to the values shown in Fig. 3.4 in chapter 2. The scan taken in August 2010 is used as the reference. The scan of Sep 27th 2012 was interrupted and was continued on Sep 28th 2012.

- **T3L2Q2M2**[1]: Frequent errors (DLL) starting from 24 October 2010. Replaced on 6 July 2011.
- **T3L2Q0M1**[2]: FE replaced on 17 December 2010.

The effect of the replaced FEs on the measurement of the pressure-corrected relative gain, as summarised in Table A.1, has been studied for the scan taken in December 2012. It was found that the change in relative gain is at most 0.1 percentage point, which is negligible compared to the systematic uncertainty. This can be understood as the replaced FE affects one layer, whereas the averages are calculated over all 12 layers.

[1] `http://lblogbook.cern.ch/OT/1760`, `https://lbproblems.cern.ch/problems/2225/`.
[2] `http://lblogbook.cern.ch/OT/1412`.

A.2 Results of the ^{90}Sr scan

All ^{90}Sr scans are summarised in Table A.2. The results are shown in Figs. A.1-A.2 for all modules, and are discussed below. Gain variations of $\pm 5\%$ are observed, indicating no sign of ageing.

An area with slightly increased gain levels has been observed at $y \approx 20$ cm for modules M2, M3, M4 in the monolayer closest to the interaction point, while for the monolayer furthest from the interaction point a decrease of gain was found in the same area. The feature of changing gain at the ends of the modules was already observed directly after production at the testing facility, and was also present in previous scans. Although this feature is not understood, these are indications that this is not a sign of ageing, because the gain also varied without any irradiation.

For most modules a change of gain is observed at wires 32−33. This is due to the lay-out of the ammeter, which consists of two parts. The edge of the two parts is at wires 32−33, which makes this place more prone to having contamination on the connectors, even after careful cleaning. Also the band at wire 25 in module M2A is attributed to a dirty connector at the time of scanning in 2013. For module M8A, wire 29 was malfunctioning during the 2011 scan, which shows as a white band. The alternating pattern between increased and decreased gain as observed in modules M9A and M9B can be explained by a small horizontal shift of the sources between the two scans. Because the profile of the sources is not uniform but sinusoidal as shown in Fig. 3.8b such a behaviour is expected. The horizontal structure in module M9B is attributed to the scan taken in 2008, presumably due to a glitch of the HV power supply.

Note that all the effects discussed above are largely understood. Any remaining effects are within the $\pm 5\%$ level and are therefore considered not significant.

A.3 Results of the irradiation test with a ^{90}Sr source

A summary of all irradiation periods can be found in Table A.3. Table A.4 summarises all scans and the results are shown in Fig. A.3. Each scan is compared to the previous scan. The first scan is compared to a scan taken in October 2012. The observed gain variations are uniform throughout the entire module within $\pm 5\%$. No decrease in gain is observed at the irradiated spot in the middle of the module at a height of 210 cm.

module	name	scan date	reference scan
T2L0Q1M1A	90A	2 July 2013	13 January 2012
T2L0Q1M1B	90B	2 July 2013	1 February 2012
T2L0Q1M2A	91A	2 July 2013	11 January 2012
T2L0Q1M2B	91B	2 July 2013	11 January 2012
T2L0Q1M3A	92A	2 July 2013	11 January 2012
T2L0Q1M3B	92B	2 July 2013	11 January 2012
T2L0Q1M4A	93A	2 July 2013	10 January 2012
T2L0Q1M4B	93B	2 July 2013	10 January 2012
T2L0Q1M5A	94A	3 July 2013	10 January 2012
T2L0Q1M5B	94B	3 July 2013	10 January 2012
T2L0Q1M6A	194A	3 July 2013	20 December 2011
T2L0Q1M6B	194B	3 July 2013	20 December 2011
T2L0Q1M7A	204A	3 July 2013	10 January 2012
T2L0Q1M7B	204B	3 July 2013	10 January 2012
T2L0Q1M8A	122A	3 July 2013	20 December 2011
T2L0Q1M8B	122B	3 July 2013	20 December 2011
T2L0Q1M9A	73A	3 July 2013	20 August 2008
T2L0Q1M9B	73B	3 July 2013	20 August 2008

Table A.2 · ^{90}Sr scans.

start date	end date	hours	hours (cum)
06-05-2013 16.30	08-05-2013 14.30	46.0	46.0
08-05-2013 15.00	11-05-2013 15.30	72.5	118.5
13-05-2013 14.00	28-05-2013 10.30	356.5	475.0

Table A.3 · Irradiation of module 90B.

scan	reference scan	figure
06-05-2013	01-10-2012	A.3a
08-05-2013	06-05-2012	A.3b
13-05-2013	08-05-2013	A.3c
28-05-2013	13-03-2013	A.3d

Table A.4 · Scans of module 90B.

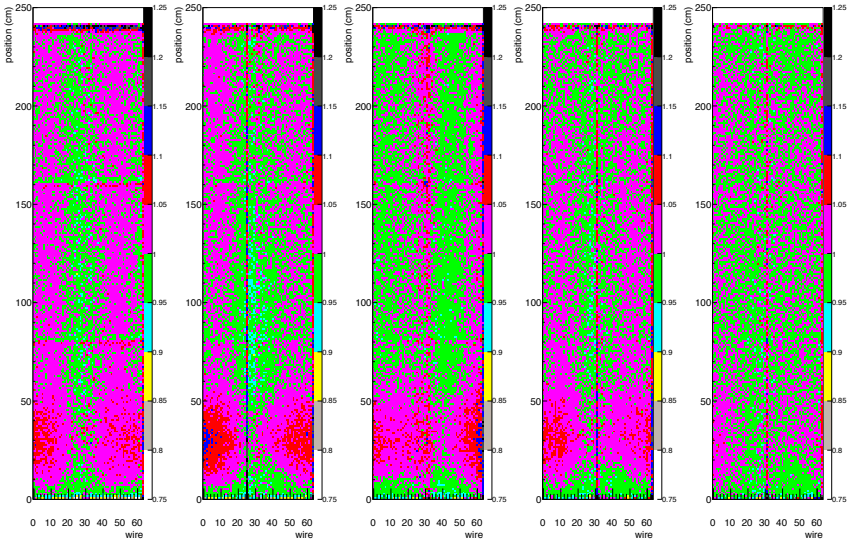

(a) T2L0Q1M1A **(b)** T2L0Q1M2A **(c)** T2L0Q1M3A **(d)** T2L0Q1M4A **(e)** T2L0Q1M5A

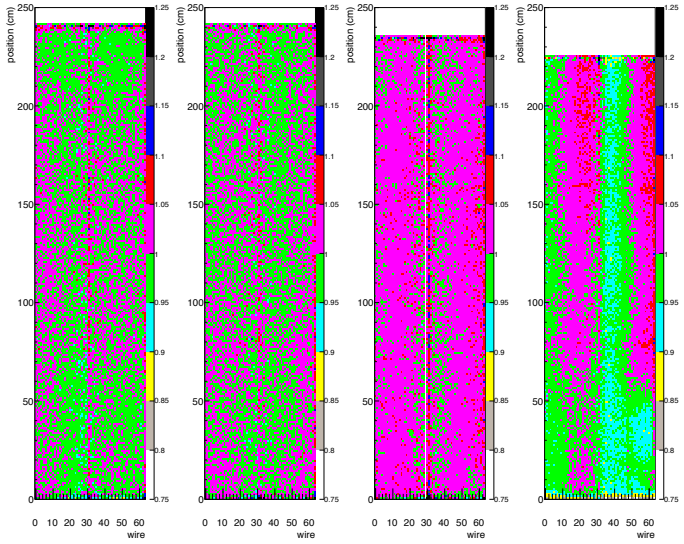

(f) T2L0Q1M6A **(g)** T2L0Q1M7A **(h)** T2L0Q1M8A **(i)** T2L0Q1M9A

Fig. A.1 · ^{90}Sr scan results for all modules in T2L0Q1 for the monolayer furthest from the interaction point. Modules 8 and 9 are shorter due to the presence of the inner tracking system.

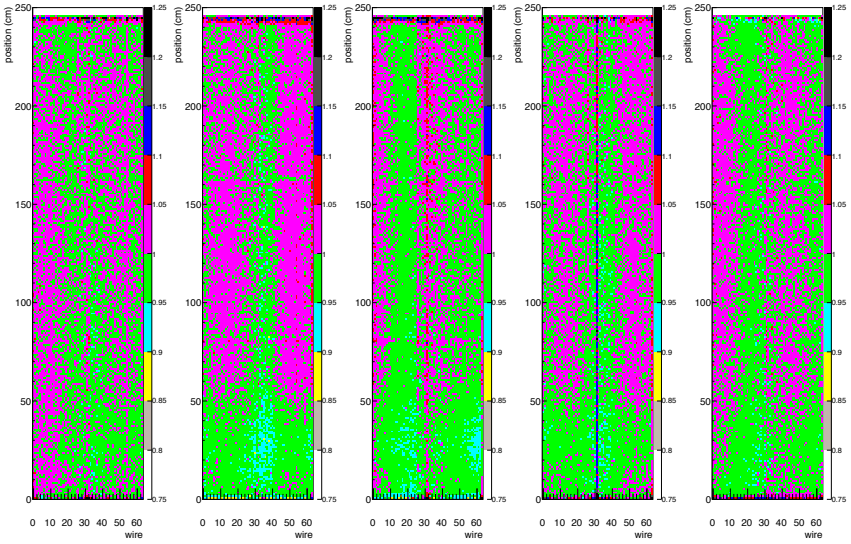

(a) T2L0Q1M1B **(b)** T2L0Q1M2B **(c)** T2L0Q1M3B **(d)** T2L0Q1M4B **(e)** T2L0Q1M5B

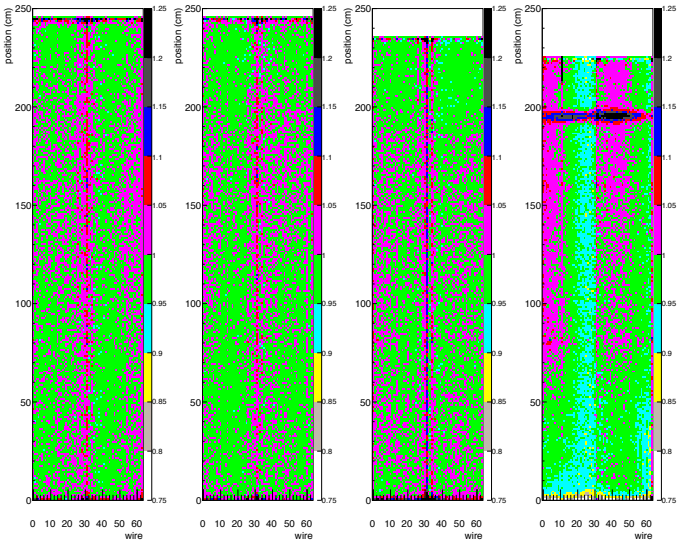

(f) T2L0Q1M6B **(g)** T2L0Q1M7B **(h)** T2L0Q1M8B **(i)** T2L0Q1M9B

Fig. A.2 · ^{90}Sr scan results for all modules in T2L0Q1 for the monolayer closest to the interaction point. Modules 8 and 9 are shorter due to the presence of the inner tracking system.

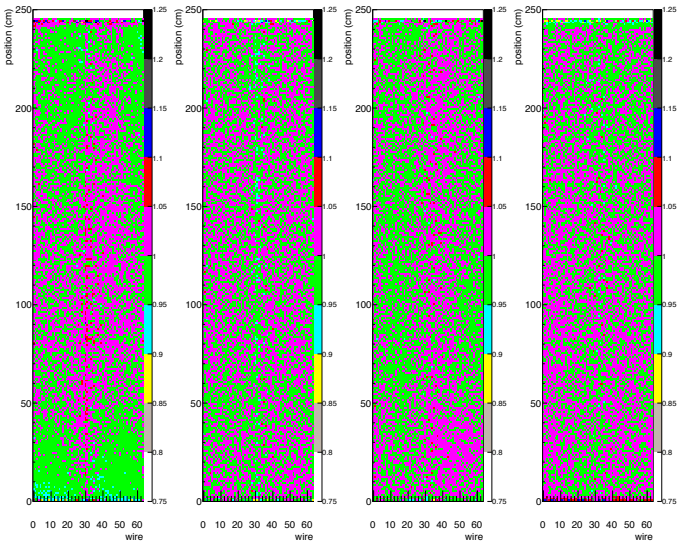

Fig. A.3 · Results of ^{90}Sr irradiation test scans of module 90B.

APPENDIX B

Selection criteria of the trigger and the pre-selection

Given the high rate of beam crossings that result in at least one visible interaction in the LHCb detector, 11MHz [209], and the limited time available to read out the detector, a fast first selection is needed to decide whether an event is likely to contain interesting b-hadron decays. This is provided by the trigger [210], which reduces the output rate, in three steps, to 3kHz. Different trigger lines are designed to select different classes of events, depending on the types of particles in the final state [211]. The event can either be triggered on one of the tracks of the signal event (TOS), or independently of the signal on one of the other tracks in the event (TIS) [212].

The events used for the measurements described in chapters 6–8 are recorded using the trigger lines listed in Table B.1. These lines inclusively select b-hadron decays with hadrons in the final state. The selection criteria corresponding to these lines are summarised in Table B.2. The hardware trigger, L0, rejects busy events that contain more than 600 hits in the SPD, as these events would saturate HLT1. Furthermore, it selects events which have a cluster with large transverse momentum, $E_T = E \sin\theta$. The first stage of the software trigger, HLT1, employs a cut-based selection, to select events with at least one high (transverse) momentum track which is displaced from the PV. Quality requirements are set on this track by requiring a minimum number of hits in the VELO and the downstream tracking stations, and a maximum number of missed hits in the VELO. The second stage of the software trigger, HLT2, aims to select events with two-, three- or four-body vertices. It employs a multivariate algorithm, Bonsai Boosted Decision Tree (BBDT) [213], which uses information on the sum of transverse momenta of the tracks of the n-body vertex, the minimum p_{T} of the tracks, the reconstructed mass, the corrected mass, the DOCA of the $n-1$ particle combination and the additional particle, and the IP χ^2 and the FD χ^2 of the n-body combination [209]. The corrected mass is defined as $m_{\mathrm{corr}} = \sqrt{m^2 + |p'_{\mathrm{T\,miss}}|^2} + |p'_{\mathrm{T\,miss}}|$, with $p'_{\mathrm{T\,miss}}$ the missing momentum transverse to the direction of flight.

L0	L0Hadron TOS or any L0 line TIS
HLT1	HLT1TrackAllL0 TOS
HLT2	HLT2TopoNBodyBBDTDecision TOS

Table B.1 · Triggers lines used for the measurements described in chapters 6 and 7.

Trigger			
L0	E_{T}	$>$	3500 MeV/c
	N_{SPD}	$<$	600
HLT1	N_{velo}	$>$	9
	$N_{\mathrm{velo,miss}}$	$<$	3
	IP	$>$	100 µm
	$N_{\mathrm{IT,OT}}$	$>$	16
	p_{T}	$>$	1700 MeV/c
	p	$>$	10000 MeV/c
	track χ^2/ndf	$<$	2.5
	IP χ^2	$>$	16
HLT2	2-body BBDT	$>$	0.4
	3-body BBDT	$>$	0.4
	4-body BBDT	$>$	0.3

Table B.2 · Trigger selection requirements [181, 209].

The offline pre-selection criteria, summarised in Table B.3[1], are designed to select candidates which are consistent with a $B \to Dh$ decay with a three-body D decay. It assumes hadronic particles in the final state and B and D decay vertices which are displaced from the PV. Quality requirements are placed on the tracks, on the B and D vertices, on the cosine of the angle between the momentum of the particle and the direction of flight from the PV to the decay vertex (DIRA) and the distance of closest approach (DOCA) of track combinations. Small differences in the offline pre-selection requirements used in the analyses described in chapters 6 and 7 and in chapter 8 are summarised in Table B.4.

[1] http://lhcb-release-area.web.cern.ch/LHCb-release-area/DOC/stripping/config/stripping17/bhadron/
strippingb02dpid2hhhbeauty2charmline,
strippingb02dkd2hhhbeauty2charmline,
strippinglb2lcpilc2pkpibeauty2charmline.

	Pre-selection		
Global event cut	Number of long tracks in the event	$<$	500
	TOPO TOS or TIS		1
	BBDT	$>$	0.05
D meson	m_D		1769.62–2068.49 MeV/c^2
	vertex fit χ^2/ndf	$<$	10
	χ^2-separation from related PV	$>$	36
	DIRA	$>$	0
	$\sum_{\text{daughters}} p_{\mathrm{T}}$	$>$	1800 MeV/c
all daughter tracks	track χ^2/ndf	$<$	4
	p_{T}	$>$	100 MeV/c
	p	$>$	1000 MeV/c
	IP χ^2 w.r.t. PV	$>$	4
	DOCA between 2 tracks	$<$	0.5 mm
min 1 track	track χ^2/ndf	$<$	3
	p_{T}	$>$	500 MeV/c
	p	$>$	5000 MeV/c
Bachelor	track χ^2/ndf	$<$	3
	p_{T}	$>$	500 MeV/c
	p	$>$	5000 MeV/c
	IP χ^2 track w.r.t. PV	$>$	4
B meson	m_B		4750–7000 MeV/c^2
	vertex fit χ^2/ndf	$<$	10
	IP χ^2 on related PV	$<$	25
	proper time	$>$	0.2 ps
	DIRA	$>$	0.999
	$\sum_{\text{all tracks}} p_{\mathrm{T}}$	$>$	5000 MeV/c
min 1 track with	p_{T}	$>$	1700 MeV/c
	p	$>$	10000 MeV/c
	track χ^2/ndf	$<$	2.5
	IP χ^2 daughter tracks w.r.t. PV	$>$	16
	IP	$>$	0.1 mm
min 2 tracks with	p_{T}	$>$	500 MeV/c
	p	$>$	5000 MeV/c
	track χ^2/ndf	$<$	3

Table B.3 · Pre-selection requirements used to select the decays modes described in chapters 6 and 7. The decay $\Lambda_b^0 \to \Lambda_c^+ \pi^-$ is selected using the mass windows 2276.46–2396.46 MeV/c^2 and 5200–7000 MeV/c^2 for the Λ_c^+ and Λ_b^0 baryon, respectively.

B

		chapter 6-7 2011 data	chapter 8 2011 data	chapter 8 2012 data
Global event cut	Number of long tracks	< 500	< 250	< 250
Individual particles	Track χ^2_{IP}	> 4	> 3	> 3
	Track ghost probability		< 0.3	< 0.4
D meson	Daughter track χ^2/ndf	< 4	< 2.5	< 2.5
Bachelor particle	Track χ^2/ndf	< 3	< 2.5	< 2.5

Table B.4 · Small differences in pre-selection between the analyses described in chapters 6-7 and chapter 8.

Bibliography

[1] S. L. Glashow, *Partial Symmetries of Weak Interactions*, Nucl. Phys. **22** (1961) 579.

[2] S. Weinberg, *A Model of Leptons*, Phys. Rev. Lett. **19** (1967) 1264.

[3] A. Salam, *Weak and Electromagnetic Interactions*, Conf. Proc. **C680519** (1968) 367.

[4] UA1 Collaboration, G. Arnison *et al.*, *Experimental Observation of Isolated Large Transverse Energy Electrons with Associated Missing Energy at* $\sqrt{s} = 540\ GeV$, Phys. Lett. **B122** (1983) 103.

[5] UA2 Collaboration, M. Banner *et al.*, *Observation of Single Isolated Electrons of High Transverse Momentum in Events with Missing Transverse Energy at the CERN* $\bar{p}p$ *Collider*, Phys. Lett. **B122** (1983) 476.

[6] UA1 Collaboration, G. Arnison *et al.*, *Experimental Observation of Lepton Pairs of Invariant Mass Around 95 GeV/*c^2 *at the CERN SPS Collider*, Phys. Lett. **B126** (1983) 398.

[7] UA2 Collaboration, P. Bagnaia *et al.*, *Evidence for* $Z^0 \to e^+e^-$ *at the CERN* $\bar{p}p$ *Collider*, Phys. Lett. **B129** (1983) 130.

[8] M. Kobayashi and T. Maskawa, *CP Violation in the Renormalizable Theory of Weak Interaction*, Prog. Theor. Phys. **49** (1973) 652.

[9] CDF Collaboration, F. Abe *et al.*, *Observation of top quark production in* $\bar{p}p$ *collisions*, Phys. Rev. Lett. **74** (1995) 2626, arXiv:hep-ex/9503002.

[10] D0 Collaboration, S. Abachi *et al.*, *Observation of the top quark*, Phys. Rev. Lett. **74** (1995) 2632, arXiv:hep-ex/9503003.

[11] ATLAS Collaboration, G. Aad *et al.*, *Observation of a new particle in the search for the Standard Model Higgs boson with the ATLAS detector at the LHC*, Phys. Lett. **B716** (2012) 1, arXiv:1207.7214.

[12] CMS Collaboration, S. Chatrchyan *et al.*, *Observation of a new boson at a mass of 125 GeV with the CMS experiment at the LHC*, Phys. Lett. **B716** (2012) 30, arXiv:1207.7235.

[13] P. W. Higgs, *Broken Symmetries and the Masses of Gauge Bosons*, Phys. Rev. Lett. **13** (1964) 508.

[14] F. Englert and R. Brout, *Broken Symmetry and the Mass of Gauge Vector Mesons*, Phys. Rev. Lett. **13** (1964) 321.

[15] www.universe-cluster.de/.

[16] A. Sakharov, *Violation of CP Invariance, C Asymmetry, and Baryon Asymmetry of the Universe*, Pis'ma Zh. Eksp. Teor. Fiz. **5** (1967) 32.

[17] V. C. Rubin, N. Thonnard, and W. K. Ford, Jr., *Rotational properties of 21 SC galaxies with a large range of luminosities and radii, from NGC 4605 (R = 4kpc) to UGC 2885 (R = 122 kpc)*, Astrophys. J. **238** (1980) 471.

[18] A. Einstein, *The Foundation of the General Theory of Relativity*, Ann. Phys. **49** (1916) 769, [Ann. Phys. **14** (2005) 517].

[19] O. Buchmueller *et al.*, *The CMSSM and NUHM1 in Light of 7 TeV LHC, $B_s \to \mu^+\mu^-$ and XENON100 Data*, Eur. Phys. J. **C72** (2012) 2243, arXiv:1207.7315.

[20] S. P. Martin, *A Supersymmetry primer*, arXiv:hep-ph/9709356, [Adv. Ser. Direct. High Energy Phys.18,1(1998)].

[21] G. Altarelli, B. Mele, and M. Ruiz-Altaba, *Searching for New Heavy Vector Bosons in $p\bar{p}$ Colliders*, Z. Phys. **C45** (1989) 109, [Erratum: Z. Phys. **C47** (1990) 676].

[22] J. J. Goodson, *Search for Supersymmetry in States with Large Missing Transverse Momentum and Three Leptons including a Z-Boson*, PhD thesis, SUNY, Stony Brook, 2012, CERN-THESIS-2012-053.

[23] SLAC-SP-017 Collaboration, J. E. Augustin *et al.*, *Discovery of a Narrow Resonance in e^+e^- Annihilation*, Phys. Rev. Lett. **33** (1974) 1406, [Adv. Exp. Phys. **5** (1976) 141].

[24] E598 Collaboration, J. J. Aubert *et al.*, *Experimental Observation of a Heavy Particle J*, Phys. Rev. Lett. **33** (1974) 1404.

[25] TASSO Collaboration, R. Brandelik *et al.*, *Evidence for Planar Events in e^+e^- Annihilation at High-Energies*, Phys. Lett. **B86** (1979) 243.

[26] D. P. Barber *et al.*, *Discovery of Three Jet Events and a Test of Quantum Chromodynamics at PETRA Energies*, Phys. Rev. Lett. **43** (1979) 830.

[27] C. Berger *et al.*, *Evidence for gluon bremsstrahlung in e^+e^- annihilations at high energies*, Phys. Lett. **B86** (1979) 418.

[28] JADE Collaboration, W. Bartel *et al.*, *Observation of Planar Three Jet Events in e^+e^- Annihilation and Evidence for Gluon Bremsstrahlung*, Phys. Lett. **B91** (1980) 142.

[29] SLD Heavy Flavor Group, DELPHI, ALEPH, OPAL, LEP Electroweak Working Group, L3, *A Combination of preliminary electroweak measurements and constraints on the standard model*, arXiv:hep-ex/0212036.

[30] OPAL, DELPHI, LEP Working Group for Higgs boson searches, ALEPH, L3, R. Barate *et al.*, *Search for the standard model Higgs boson at LEP*, Phys. Lett. **B565** (2003) 61, arXiv:hep-ex/0306033.

[31] BaBar Collaboration, B. Aubert *et al.*, *Observation of CP violation in the B^0 meson system*, Phys. Rev. Lett. **87** (2001) 091801, arXiv:hep-ex/0107013.

[32] Belle Collaboration, K. Abe *et al.*, *Observation of large CP violation in the neutral B meson system*, Phys. Rev. Lett. **87** (2001) 091802, arXiv:hep-ex/0107061.

[33] www.nobelprize.org/.

[34] LHCb Collaboration, A. A. Alves *et al.*, *The LHCb Detector at the LHC*, JINST **3** (2008) S08005.

[35] LHCb Collaboration, R. Antunes-Nobrega *et al.*, *LHCb reoptimized detector design and performance: Technical Design Report*, LHCb-TDR-9.

[36] LHCb collaboration, R. Aaij *et al.*, *Precision measurement of the B_s^0–$\overline{B}_s^0$ oscillation frequency in the decay $B_s^0 \to D_s^- \pi^+$*, New J. Phys. **15** (2013) 053021, arXiv:1304.4741.

[37] B. Hommels, *The Tracker in the Trigger of LHCb*, PhD thesis, Vrije Universiteit, Amsterdam, 2006, CERN-THESIS-2006-058.

[38] F. Sauli, *Gaseous radiation detectors - Fundamentals and applications*, Cambridge University Press, 2014.

[39] G. van Apeldoorn *et al.*, *Outer Tracker module production at Nikhef - Quality Assurance*, LHCb-2004-078.

[40] G. van Apeldoorn *et al.*, *Beam tests of final modules and electronics of the LHCb Outer Tracker in 2005*, LHCb-2005-076.

[41] CDF Collaboration, D. Allspach *et al.*, *Aging in the large CDF axial drift chamber*, IEEE Trans. Nucl. Sci. **52** (2005) 2956.

[42] C. Niebuhr, *Aging in the Central Jet Chamber of the H1 experiment*, Nucl. Instrum. Meth. **A515** (2003) 43.

[43] M. Capeans, *Aging and materials: lessons for detectors and gas systems*, Nucl. Instrum. Meth. **A515** (2003) 73, Proceedings of the International Workshop on Aging Phenomena in Gaseous Detectors.

[44] M. Titov, *Radiation damage and long-term ageing in gas detectors*, World Scientific, 2004. Proceedings of the 42nd Workshop of the INFN ELOISATRON Project, doi: 10.1142/9789812702951_0014.

[45] S. Bachmann *et al.*, *The straw tube technology for the LHCb outer tracking system*, Nucl. Instrum. Meth. **A535** (2004) 171, Proceedings of the 10th International Vienna Conference on Instrumentation.

[46] S. Bachmann *et al.*, *Ageing in the LHCb outer tracker: Phenomenon, culprit and effect of oxygen*, Nucl. Instrum. Meth. **A617** (2010) 202, Proceedings of the 11th Pisa Meeting on Advanced Detectors.

[47] N. Tuning *et al.*, *Ageing in the LHCb outer tracker: Aromatic hydrocarbons and wire cleaning*, Nucl. Instrum. Meth. **A656** (2011) 45.

[48] D. van Eijk *et al.*, *Radiation hardness of the LHCb Outer Tracker*, Nucl. Instrum. Meth. **A685** (2012) 62.

[49] D. van Eijk, *Ageing and the Decay of Beauty: Radiation Hardness of the LHCb Outer Tracker and Time-Dependent CP Violation using $B_s^0 \to J/\psi\phi$*, PhD thesis, Vrije Universiteit, Amsterdam, 2012, CERN-THESIS-2012-137.

[50] V. Suvorov, G. van Apeldoorn, I. Gouz, and T. Sluijk, *Avalanche and streamer production in Ar/CO_2 mixtures*, CERN-LHCb-2005-038.

[51] E. Visser, *Preventing, monitoring and curing the ageing in the LHCb Outer Tracker*, Master's thesis, Vrije Universiteit, Amsterdam, 2010, CERN-THESIS-2010-094.

R

[52] I. Mous, *The dependence of the signal strength on the applied voltage and gas mixture of the LHCb Outer Tracker detector*, Bachelor's thesis, Vrije Universiteit, Amsterdam, 2005, LHCb internal documentation, LHCb-2005-093.

[53] D. van Eijk, B. Storaci, N. Tuning, and A. Pellegrino, *OT ageing studies in situ*, LHCb-INT-2010-035.

[54] C. Grupen and B. Shwartz, *Particle Detectors*, Cambridge University Press, 2008.

[55] LHCb collaboration, R. Aaij *et al.*, *Search for the rare decays $B_s^0 \to \mu^+\mu^-$ and $B^0 \to \mu^+\mu^-$*, Phys. Lett. **B699** (2011) 330, arXiv:1103.2465.

[56] LHCb collaboration, R. Aaij *et al.*, *Measurement of the $B_s^0 \to \mu^+\mu^-$ branching fraction and search for $B^0 \to \mu^+\mu^-$ decays at the LHCb experiment*, Phys. Rev. Lett. **111** (2013) 101805, arXiv:1307.5024.

[57] CMS Collaboration, S. Chatrchyan *et al.*, *Measurement of the $B_s^0 \to \mu^+\mu^-$ branching fraction and search for $B^0 \to \mu^+\mu^-$ with the CMS Experiment*, Phys. Rev. Lett. **111** (2013) 101804, arXiv:1307.5025.

[58] J. Bracínk, M. Cacciari, M. Corradi, and G. Grindhammer, *Heavy quark fragmentation*, arXiv:hep-ph/0601013, Proceedings (Part B) of the workshop HERA and the LHC.

[59] B. Melé and P. Nason, *The fragmentation function for heavy quarks in QCD*, Nucl. Phys. **B361** (1990) 626.

[60] Y. L. Dokshitzer, *Calculation of the Structure Functions for Deep Inelastic Scattering and e^+e^- Annihilation by Perturbation Theory in Quantum Chromodynamics.*, Sov. Phys. JETP **46** (1977) 641.

[61] V. Gribov and L. Lipatov, *Deep inelastic ep scattering in perturbation theory*, Sov. J. Nucl. Phys. **15** (1972) 438.

[62] G. Altarelli and G. Parisi, *Asymptotic Freedom in Parton Language*, Nucl. Phys. **B126** (1977) 298.

[63] S. Catani, F. Krauss, R. Kuhn, and B. Webber, *QCD matrix elements + parton showers*, JHEP **0111** (2001) 063, arXiv:hep-ph/0109231.

[64] G. Marchesini and B. Webber, *Simulation of QCD jets including soft gluon interference*, Nucl. Phys. **B238** (1984) 1.

[65] B. Andersson, G. Gustafson, G. Ingelman, and T. Sjöstrand, *Parton Fragmentation and String Dynamics*, Phys. Rept. **97** (1983) 31.

[66] T. Sjöstrand, S. Mrenna, and P. Skands, *PYTHIA 6.4 physics and manual*, JHEP **05** (2006) 026, arXiv:hep-ph/0603175.

[67] T. Sjöstrand, S. Mrenna, and P. Skands, *A brief introduction to PYTHIA 8.1*, Comput. Phys. Commun. **178** (2008) 852, arXiv:0710.3820.

[68] T. Sjöstrand, *PYTHIA 5.7 and JETSET 7.4: Physics and manual*, arXiv:hep-ph/9508391.

[69] B. Andersson and G. Gustafson and T. Sjöstrand, *A model for baryon production in quark and gluon jets*, Nucl. Phys. **B197** (1982) 45.

[70] B. Andersson and G. Gustafson and G. Ingelman and T. Sjöstrand, *Baryon production in lepton-nucleon scattering and diquark fragmentation*, Z. Ph. C. **13** (1982) 306.

[71] P. Skands, *Introduction to QCD*, arXiv:1207.2389.

[72] TPC/Two Gamma Collaboration, H. Aihara *et al.*, *Baryon production in e^+e^- annihilation at $\sqrt{s} = 29$ GeV: clusters, diquarks, popcorn?*, Phys. Rev. Lett. **55** (1985) 1047.

[73] B. Andersson, G. Gustafson, and T. Sjöstrand, *Baryon production in jet fragmentation and Υ-decay*, Phys. Scr. **32** (1985) 574.

[74] M. Bowler, *e^+e^- Production of Heavy Quarks in the String Model*, Z. Phys. **C11** (1981) 169.

[75] C. Peterson, D. Schlatter, I. Schmitt, and P. M. Zerwas, *Scaling violations in inclusive e^+e^- annihilation spectra*, Phys. Rev. **D27** (1983) 105.

[76] V. Gribov and L. Lipatov, *Deep inelastic electron scattering in perturbation theory*, Phys. Lett. **B37** (1971) 78.

[77] V. Gribov and L. Lipatov, *e^+e^- pair annihilation and deep inelastic ep scattering in perturbation theory*, Sov. J. Nucl. Phys. **15** (1972) 675.

[78] V. Kartvelishvili, A. Likhoded, and V. Petrov, *On the fragmentation functions of heavy quarks into hadrons*, Phys. Lett. **B78** (1978) 615.

[79] P. D. B. Collins and T. P. Spiller, *The fragmentation of heavy quarks*, J. Phys. **G11** (1985) 1289.

[80] ALEPH Collaboration, A. Heister *et al.*, *Study of the fragmentation of b quarks into B mesons at the Z peak*, Phys. Lett. **B512** (2001) 30, arXiv:hep-ex/0106051.

[81] OPAL Collaboration, G. Abbiendi *et al.*, *Inclusive analysis of the b quark fragmentation function in Z decays at LEP*, Eur. Phys. J. **C29** (2003) 463, arXiv:hep-ex/0210031.

[82] SLD Collaboration, K. Abe *et al.*, *Measurement of the b quark fragmentation function in Z^0 decays*, Phys. Rev. **D65** (2002) 092006, arXiv:hep-ex/0202031.

[83] DELPHI Collaboration, J. Abdallah *et al.*, *A study of the b-quark fragmentation function with the DELPHI detector at LEP I and an averaged distribution obtained at the Z Pole*, Eur. Phys. J. **C71** (2011) 1557, arXiv:1102.4748.

[84] Particle Data Group, K. Olive *et al.*, *Review of Particle Physics*, Chin. Phys. **C38** (2014) 090001.

[85] R. Barate et al., *A measurement of the semileptonic branching ratio $\mathcal{B}$(b-baryon $\to$ $\mathrm{p}l\bar{\nu}X$) and a study of inclusive $\pi^{\pm}, \mathrm{K}^{\pm}, (\mathrm{p}, \bar{\mathrm{p}})$ production in Z decays*, Eur. Phys. J. **C5** (1998) 205.

[86] DELPHI Collaboration, P. Abreu *et al.*, *Lifetime and production rate of beauty baryons from Z decays*, Zeitschrift fur Physik C Particles and Fields **68** (1995) .

[87] ALEPH Collaboration, R. Barate et al., *Measurement of the b baryon lifetime and branching fractions in Z decays*, Eur. Phys. J. **C2** (1998) 197.

[88] ALEPH Collaboration, D. Buskulic *et al.*, *Strange b baryon production and lifetime in Z decays*, Phys. Lett. **B384** (1996) 449.

[89] DELPHI Collaboration, J. Abdallah *et al.*, *Production of Ξ_c^0 and Ξ_b in Z decays and lifetime measurement of Ξ_b*, Eur. Phys. J. **C44** (2005) 299, arXiv:hep-ex/0510023.

[90] DELPHI Collaboration, P. Abreu *et al.*, *Evidence for B_s^0 meson production in Z^0 decays*, Phys. Lett. **B289** (1992) 199.

R

[91] OPAL Collaboration, P. Acton *et al.*, *Evidence for the existence of the strange b-flavoured meson B_s^0 in Z^0 decays*, Phys. Lett. **B295** (1992) 357.

[92] ALEPH Collaboration, D. Buskulic *et al.*, *Measurement of the B_s^0 lifetime and production rate with $D_s^- l^+$ combinations in Z decays*, Phys. Lett. **B361** (1995) 221.

[93] DELPHI Collaboration, J. Abdallah *et al.*, *A Measurement of the branching fractions of the b-quark into charged and neutral b-hadrons*, Phys. Lett. **B576** (2003) 29, arXiv:hep-ex/0311005.

[94] CDF Collaboration, T. Affolder *et al.*, *Measurement of b quark fragmentation fractions in $p\bar{p}$ collisions at $\sqrt{s} = 1.8$ TeV*, Phys. Rev. Lett. **84** (2000) 1663, arXiv:hep-ex/9909011.

[95] CDF collaboration, T. Aaltonen *et al.*, *Measurement of ratios of fragmentation fractions for bottom hadrons in $p\bar{p}$ collisions at $\sqrt{s} = 1.96$-TeV*, Phys. Rev. **D77** (2008) 072003, arXiv:0801.4375.

[96] CDF collaboration, T. Aaltonen *et al.*, *First measurement of the ratio of branching fractions $B(\Lambda_b^0 \to \Lambda_c^+ \mu^- \bar{\nu}_\mu)/B(\Lambda_b^0 \to \Lambda_c^+ \pi^-)$*, Phys. Rev. **D79** (2009) 032001, arXiv:0810.3213.

[97] LHCb collaboration, R. Aaij *et al.*, *Measurement of b hadron production fractions in 7 TeV pp collisions*, Phys. Rev. **D85** (2012) 032008, arXiv:1111.2357.

[98] Heavy Flavor Averaging Group, Y. Amhis *et al.*, *Averages of b-hadron, c-hadron, and τ-lepton properties as of early 2012*, arXiv:1207.1158, updated results and plots available at: http://www.slac.stanford.edu/xorg/hfag/.

[99] LHCb collaboration, R. Aaij *et al.*, *Determination of f_s/f_d for 7 TeV pp collisions and measurement of the $B^0 \to D^- K^+$ branching fraction*, Phys. Rev. Lett. **107** (2011) 211801, arXiv:1106.4435.

[100] LHCb collaboration, R. Aaij *et al.*, *Measurement of the B^0–$\overline{B}^0$ oscillation frequency Δm_d with the decays $B^0 \to D^- \pi^+$ and $B^0 \to J/\psi K^{*0}$*, Phys. Lett. **B719** (2013) 318, arXiv:1210.6750.

[101] J. Charles *et al.*, *Current status of the Standard Model CKM fit and constraints on $\Delta F = 2$ New Physics*, Phys. Rev. **D91** (2015) 073007, arXiv:hep-ph/1501.05013.

[102] LHCb collaboration, R. Aaij *et al.*, *Measurement of CP asymmetry in $B_s^0 \to D_s^\mp K^\pm$ decays*, JHEP **11** (2014) 060, arXiv:1407.6127.

[103] R. Fleischer, *New strategies to obtain insights into CP violation through $B_s \to D_s^\pm K^\mp, D_s^{*\pm} K^\mp$, ... and $B_d \to D^\pm \pi^\mp, D^{*\pm} \pi^\mp$, ... decays*, Nucl. Phys. **B671** (2003) 459, arXiv:hep-ph/0304027.

[104] LHCb collaboration, R. Aaij *et al.*, *A measurement of the CKM angle γ from a combination of $B^\pm \to Dh^\pm$ analyses*, Phys. Lett. **B726** (2013) 151, arXiv:1305.2050.

[105] J. Brod, A. Lenz, G. Tetlalmatzi-Xolocotzi, and M. Wiebusch, *New physics effects in tree-level decays*, arXiv:1412.1446.

[106] LHCb collaboration, R. Aaij *et al.*, *Measurement of the $\overline{B}^0$–B^0 and $\overline{B}_s^0$–B_s^0 production asymmetries in pp collisions at $\sqrt{s} = 7$ TeV*, Phys. Lett. **B739** (2014) 218, arXiv:1408.0275.

[107] R. Fleischer and R. Knegjens, *Effective Lifetimes of B_s Decays and their Constraints on the B_s^0-$\bar{B}_s^0$ Mixing Parameters*, Eur. Phys. J. **C71** (2011) 1789, arXiv:1109.5115.

[108] LHCb collaboration, R. Aaij *et al.*, *Measurement of the $\overline{B}_s^0$ meson lifetime in $D_s^+\pi^-$ decays*, Phys. Rev. Lett. **113** (2014) 172001, arXiv:1407.5873.

[109] K. Hartkorn and H.-G. Moser, *A new method of measuring $\frac{\Delta\Gamma}{\Gamma}$ in the $B_s^0 - \bar{B}_s^0$ system*, Eur. Phys. J. **C8** (1999) 381.

[110] LHCb collaboration, R. Aaij *et al.*, *Measurements of the branching fractions of the decays $B_s^0 \to D_s^{\mp}K^{\pm}$ and $B_s^0 \to D_s^-\pi^+$*, JHEP **06** (2012) 115, arXiv:1204.1237.

[111] R. Fleischer, N. Serra, and N. Tuning, *A New Strategy for B_s Branching Ratio Measurements and the Search for New Physics in $B_s^0 \to \mu^+\mu^-$*, Phys. Rev. **D82** (2010) 034038, arXiv:1004.3982.

[112] R. P. Feynman and M. Gell-Mann, *Theory of the Fermi Interaction*, Phys. Rev. **109** (1958) 193.

[113] G. Buchalla, A. J. Buras, and M. E. Lautenbacher, *Weak decays beyond leading logarithms*, Rev. Mod. Phys. **68** (1996) 1125, arXiv:hep-ph/9512380.

[114] R. Fleischer, *Flavour Physics and CP Violation: Expecting the LHC*, arXiv:0802.2882, lectures given at 4th CERN-CLAF School of High-Energy Physics.

[115] D. Fakirov and B. Stech, *F- and D-decays*, Nucl. Phys. **B133** (1978) 315.

[116] N. Cabibbo and L. Maiani, *Two-body decays of charmed mesons*, Phys. Lett. **B73** (1978) 418.

[117] M. Wirbel, B. Stech, and M. Bauer, *Exclusive Semileptonic Decays of Heavy Mesons*, Z. Phys. **C29** (1985) 637.

[118] M. Bauer, B. Stech, and M. Wirbel, *Exclusive Nonleptonic Decays of D, D_s, and B Mesons*, Z. Phys. **C34** (1987) 103.

[119] M. Neubert, V. Rieckert, B. Stech, and Q. Xu, *Exclusive weak decays of b-mesons*, Adv. Ser. Direct. High Energy Phys. **10** (1992) 286.

[120] A. J. Buras, *QCD factors a_1 and a_2 beyond leading logarithms versus factorization in nonleptonic heavy meson decays*, Nucl. Phys. **B434** (1995) 606, arXiv:hep-ph/9409309.

[121] M. Beneke, G. Buchalla, M. Neubert, and C. T. Sachrajda, *QCD factorization for exclusive, nonleptonic B meson decays: General arguments and the case of heavy light final states*, Nucl. Phys. **B591** (2000) 313, arXiv:hep-ph/0006124.

[122] A. Khodjamirian, *Quantum chromodynamics and hadrons: An Elementary Introduction*, arXiv:hep-ph/0403145, lectures given at ESHEP 2003.

[123] J. L. Rosner and S. Stone, *Decay Constants of Charged Pseudoscalar Mesons*, arXiv:0802.1043.

[124] A. X. El-Khadra, *Quark Flavor Physics Review*, PoS **LATTICE2013** (2014) 001, arXiv:1403.5252.

[125] S. Aoki *et al.*, *Review of lattice results concerning low-energy particle physics*, Eur. Phys. J. **C74** (2014) 2890, arXiv:1310.8555, updated results and plots available at: http://itpwiki.unibe.ch/flag/index.php/Review_of_lattice_results_concerning_low_energy_particle_physics.

[126] C. W. Bauer, D. Pirjol, and I. W. Stewart, *A Proof of factorization for $B \to D\pi$*, Phys. Rev. Lett. **87** (2001) 201806, arXiv:hep-ph/0107002.

[127] A.J. Buras and J.-M. Gérard and R. Rückl, *1/N expansion for exclusive and inclusive charm decays*, Nucl. Phys. **B268** (1986) 16.

[128] J. D. Bjorken, *Topics in B Physics*, Nucl. Phys. Proc. Suppl. **11** (1989) 325.

[129] D. Bortoletto and S. Stone, *A Factorization test using $\overline{B}^0 \to D^{*+}\pi^-$ and an estimate of f_{D_s} using $B \to DD_s^-$*, Phys. Rev. Lett. **65** (1990) 2951.

[130] J. L. Rosner, *Determination of pseudoscalar-charmed-meson decay constants from b-meson decays*, Phys. Rev. **D42** (1990) 3732.

[131] M. Neubert and B. Stech, *Nonleptonic weak decays of B mesons*, Adv. Ser. Direct. High Energy Phys. **15** (1998) 294, arXiv:hep-ph/9705292.

[132] I. Caprini, L. Lellouch, and M. Neubert, *Dispersive bounds on the shape of $\overline{B} \to D^{(*)}l\bar{\nu}$ form-factors*, Nucl. Phys. **B530** (1998) 153, arXiv:hep-ph/9712417.

[133] Particle Data Group, K. Nakamura *et al.*, *Review of Particle Physics*, J. Phys. **G37** (2010) 075021.

[134] R. Fleischer, N. Serra, and N. Tuning, *Tests of Factorization and SU(3) Relations in B Decays into Heavy-Light Final States*, Phys. Rev. **D83** (2011) 014017, arXiv:1012.2784.

[135] BaBar Collaboration, B. Aubert *et al.*, *Study of the decay $\overline{B}^0 \to D^{*+}\omega\pi^-$*, Phys. Rev. **D74** (2006) 012001, arXiv:hep-ex/0604009.

[136] CLEO Collaboration, S. Csorna *et al.*, *Measurements of the branching fractions and helicity amplitudes in $B \to D^*\rho$ decays*, Phys. Rev. **D67** (2003) 112002, arXiv:hep-ex/0301028.

[137] LHCb collaboration, R. Aaij *et al.*, *Measurement of J/ψ production in pp collisions at $\sqrt{s} = 7$ TeV*, Eur. Phys. J. **C71** (2011) 1645, arXiv:1103.0423.

[138] Heavy Flavor Averaging Group (HFAG), Y. Amhis *et al.*, *Averages of b-hadron, c-hadron, and τ-lepton properties as of summer 2014*, arXiv:1412.7515.

[139] BaBar Collaboration, B. Aubert *et al.*, *Branching fraction measurement of $\overline{B}^0 \to D^{(*)+}\pi^-$, $B^- \to D^{(*)0}\pi^-$ and isospin analysis of $\overline{B} \to D^{(*)}\pi$ decays*, Phys. Rev. **D75** (2007) 031101, arXiv:hep-ex/0610027.

[140] CLEO, S. Ahmed *et al.*, *Measurement of $BR(B^- \to D^0\pi^-)$ and $BR(\overline{B}^0 \to D^+\pi^-)$ and isospin analysis of $B \to D\pi$ decays*, Phys. Rev. **D66** (2002) 031101, arXiv:hep-ex/0206030.

[141] Belle Collaboration, Y.-T. Duh *et al.*, *Measurements of branching fractions and direct CP asymmetries for $B \to K\pi$, $B \to \pi\pi$ and $B \to KK$ decays*, Phys. Rev. **D87** (2013) 031103, arXiv:1210.1348.

[142] BaBar Collaboration, B. Aubert *et al.*, *Improved Measurements of the Branching Fractions for $B^0 \to \pi^+\pi^-$ and $B^0 \to K^+\pi^-$, and a Search for $B^0 \to K^+K^-$*, Phys. Rev. **D75** (2007) 012008, arXiv:hep-ex/0608003.

[143] Belle Collaboration, R. Louvot *et al.*, *Measurement of the Decay $B_s^0 \to D_s^-\pi^+$ and Evidence for $B_s^0 \to D_s^\pm K^\mp$ in e^+e^- Annihilation at $\sqrt{s} \approx 10.87$ GeV*, Phys. Rev. Lett. **102** (2009) 021801, arXiv:0809.2526.

[144] CDF Collaboration, A. Abulencia *et al.*, *Measurement of the Ratios of Branching Fractions* $BR(B_s^0 \to D_s^- \pi^+ \pi^+ \pi^-)/BR(B^0 \to D^- \pi^+ \pi^+ \pi^-)$ *and* $BR(B_s^0 \to D_s^- \pi^+)/BR(B^0 \to D^- \pi^+)$, Phys. Rev. Lett. **98** (2007) 061802, arXiv:hep-ex/0610045.

[145] Belle Collaboration, K. Abe *et al.*, *Observation of Cabibbo suppressed* $B \to D^{(*)} K^-$ *decays at Belle*, Phys. Rev. Lett. **87** (2001) 111801, arXiv:hep-ex/0104051.

[146] K. De Bruyn *et al.*, *Branching Ratio Measurements of* B_s *Decays*, Phys. Rev. **D86** (2012) 014027, arXiv:1204.1735.

[147] LHCb collaboration, R. Aaij *et al.*, *Measurement of CP violation and the* B_s^0 *meson decay width difference with* $B_s^0 \to J/\psi K^+ K^-$ *and* $B_s^0 \to J/\psi \pi^+ \pi^-$ *decays*, Phys. Rev. **D87** (2013) 112010, arXiv:1304.2600.

[148] N. Isgur and M. B. Wise, *Weak transition form factors between heavy mesons*, Phys. Lett. **B237** (1990) 527.

[149] Belle Collaboration, K. Abe *et al.*, *Measurement of* $B(\overline{B}^0 \to D^+ l^- \bar{\nu})$ *and determination of* $|V_{cb}|$, Phys. Lett. **B526** (2002) 258, arXiv:hep-ex/0111082.

[150] BaBar Collaboration, B. Aubert *et al.*, *Measurements of the Semileptonic Decays* $\overline{B} \to Dl\bar{\nu}$ *and* $\overline{B} \to D^* l\bar{\nu}$ *Using a Global Fit to* $DXl\bar{\nu}$ *Final States*, Phys. Rev. **D79** (2009) 012002, arXiv:0809.0828.

[151] BaBar Collaboration, B. Aubert *et al.*, *Measurement of* $|V_{cb}|$ *and the Form-Factor Slope in* $\overline{B} \to Dl^- \bar{\nu}$ *Decays in Events Tagged by a Fully Reconstructed* B *Meson*, Phys. Rev. Lett. **104** (2010) 011802, arXiv:0904.4063.

[152] CLEO, J. E. Bartelt *et al.*, *Measurement of the* $B \to Dl\nu$ *branching fractions and form-factor*, Phys. Rev. Lett. **82** (1999) 3746, arXiv:hep-ex/9811042.

[153] D. Buskulic *et al.*, *Measurements of* $|V_{cb}|$*, form factors and branching fractions in the decays* $\overline{B}^0 \to D^{*+} l^- \bar{\nu}_l$ *and* $\overline{B}^0 \to D^+ l^- \bar{\nu}_l$, Phys. Lett. **B395** (1997) 373.

[154] J. A. Bailey *et al.*, $B_s \to D_s/B \to D$ *Semileptonic Form-Factor Ratios and Their Application to* $BR(B_s^0 \to \mu^+ \mu^-)$, Phys. Rev. **D85** (2012) 114502, arXiv:1202.6346.

[155] J. F. Kamenik and F. Mescia, $B \to D\tau\nu$ *Branching Ratios: Opportunity for Lattice QCD and Hadron Colliders*, Phys. Rev. **D78** (2008) 014003, arXiv:0802.3790.

[156] P. Blasi, P. Colangelo, G. Nardulli, and N. Paver, *Phenomenology of* B_s *decays*, Phys. Rev. **D49** (1994) 238, arXiv:hep-ph/9307290.

[157] Particle Data Group, J. Beringer *et al.*, *Review of particle physics*, Phys. Rev. **D86** (2012) 010001.

[158] W. Detmold, C. Lehner, and S. Meinel, $\Lambda_b \to p\ell^- \bar{\nu}_\ell$ *and* $\Lambda_b \to \Lambda_c \ell^- \bar{\nu}_\ell$ *form factors from lattice QCD with relativistic heavy quarks*, arXiv:hep-lat/1503.01421.

[159] V. E. Lyubovitskij, M. A. Ivanov, J. Korner, and A. Rusetsky, *Exclusive nonleptonic decays of heavy baryons in a relativistic quark model*, arXiv:hep-ph/9710523, Published in: Rostock 1997, Progress in heavy quark physics.

[160] I. Bigi, T. Mannel, and N. Uraltsev, *Semileptonic width ratios among beauty hadrons*, JHEP **1109** (2011) 012, arXiv:1105.4574.

R

[161] I. I. Bigi, M. A. Shifman, N. Uraltsev, and A. I. Vainshtein, *QCD predictions for lepton spectra in inclusive heavy flavor decays*, Phys. Rev. Lett. **71** (1993) 496, arXiv:hep-ph/9304225.

[162] A. V. Manohar and M. B. Wise, *Inclusive semileptonic B and polarized Λ_b decays from QCD*, Phys. Rev. **D49** (1994) 1310, arXiv:hep-ph/9308246.

[163] A. J. Buras, *Flavor physics and CP violation*, arXiv:hep-ph/0505175, lectures given at ESHEP 2004.

[164] LHCb collaboration, R. Aaij *et al.*, *Measurement of the fragmentation fraction ratio f_s/f_d and its dependence on B meson kinematics*, JHEP **04** (2013) 001, arXiv:1301.5286.

[165] LHCb collaboration, R. Aaij *et al.*, *Study of the kinematic dependences of Λ_b^0 production in pp collisions and a measurement of the $\Lambda_b^0 \to \Lambda_c^+\pi^-$ branching fraction*, JHEP **08** (2014) 143, arXiv:1405.6842.

[166] L. Breiman, J. H. Friedman, R. A. Olshen, and C. J. Stone, *Classification and regression trees*, Wadsworth international group, Belmont, California, USA, 1984.

[167] M. Pivk and F. R. Le Diberder, *sPlot: a statistical tool to unfold data distributions*, Nucl. Instrum. Meth. **A555** (2005) 356, arXiv:physics/0402083.

[168] M. Adinolfi *et al.*, *Performance of the LHCb RICH detector at the LHC*, Eur. Phys. J. **C73** (2013) 2431, arXiv:1211.6759.

[169] T. Skwarnicki, *A study of the radiative cascade transitions between the Upsilon-prime and Upsilon resonances*, PhD thesis, Institute of Nuclear Physics, Krakow, 1986, DESY-F31-86-02.

[170] K. S. Cranmer, *Kernel estimation in high-energy physics*, Comput. Phys. Commun. **136** (2001) 198, arXiv:hep-ex/0011057.

[171] S. Okubo, *ϕ-meson and unitary symmetry model*, Phys. Lett. **5** (1963) 165.

[172] G. Zweig, *An SU(3) model for strong interaction symmetry and its breaking. Version 2*, in *Developments in the quark theory of hadrons. Vol 1.* (D. Lichtenberg and S. P. Rosen, eds.), pp. 22–101. 1964.

[173] J. Iizuka, *A systematics and phenomenology of meson family*, Prog. Theor. Phys. Supplement **37** (1966) 21.

[174] LHCb collaboration, R. Aaij *et al.*, *Prompt charm production in pp collisions at $\sqrt{s} = 7$ TeV*, Nucl. Phys. **B871** (2013) 1, arXiv:1302.2864.

[175] K. De Bruyn *et al.*, *Exploring $B_s \to D_s^{(*)\pm}K^{\mp}$ Decays in the Presence of a Sizable Width Difference $\Delta\Gamma_s$*, Nucl. Phys. **B868** (2013) 351, arXiv:1208.6463.

[176] R. Fleischer and R. Knegjens, *In Pursuit of New Physics with $B_s^0 \to K^+K^-$*, Eur. Phys. J. **C71** (2011) 1532, arXiv:1011.1096.

[177] BaBar Collaboration, B. Aubert *et al.*, *Measurement of time-dependent CP asymmetries in $B^0 \to D^{(*)\pm}\pi^{\mp}$ and $B^0 \to D^{\pm}\rho^{\mp}$ decays*, Phys. Rev. **D73** (2006) 111101, arXiv:hep-ex/0602049.

[178] Belle Collaboration, F. Ronga *et al.*, *Measurements of CP violation in $B^0 \to D^{*-}\pi^+$ and $B^0 \to D^-\pi^+$ decays*, Phys. Rev. **D73** (2006) 092003, arXiv:hep-ex/0604013.

[179] CDF Collaboration, T. Aaltonen *et al.*, *First observation of $\overline{B}^0_s \to D^\pm_s K^\mp$ and measurement of the ratio of branching fractions $B(\overline{B}^0_s \to D^\pm_s K^\mp)/B(\overline{B}^0_s \to D^+_s \pi^-)$*, Phys. Rev. Lett. **103** (2009) 191802, arXiv:0809.0080.

[180] LHCb collaboration, R. Aaij *et al.*, *Determination of the branching fractions of $B^0_s \to D^\mp_s K^\pm$ and $B^0 \to D^-_s K^+$*, JHEP **02** (2015) 029, arXiv:1412.7654.

[181] A. Martin Sanchez, P. Robbe, and M.-H. Schune, *Performances of the LHCb L0 Calorimeter Trigger*, LHCb-PUB-2011-026.

[182] LHCb internal communication.

[183] A. V. Berezhnoy and A. K. Likhoded, *The relative yields of heavy hadrons as function of transverse momentum at LHC experiments*, arXiv:1309.1979.

[184] R. Barlow, *Asymmetric systematic errors*, arXiv:physics/0306138v1.

[185] R. Barlow, *Asymmetric statistical errors*, arXiv:physics/0306120v1.

[186] LHCb Collaboration, , *Updated average f_s/f_d b-hadron production fraction ratio for 7 TeV pp collisions*, LHCb-CONF-2013-011.

[187] Heavy Flavor Averaging Group (HFAG), Y. Amhis *et al.*, *Averages of b-hadron, c-hadron, and τ-lepton properties as of summer 2014*, arXiv:1412.7515.

[188] C. Bobeth *et al.*, *$B_{s,d} \to l^+ l^-$ in the Standard Model with Reduced Theoretical Uncertainty*, Phys. Rev. Lett. **112** (2014) 101801, arXiv:1311.0903.

[189] CMS and LHCb collaborations, V. Khachatryan *et al.*, *Observation of the rare $B^0_s \to \mu^+\mu^-$ decay from the combined analysis of CMS and LHCb data*, Nature **522** (2015) 68, arXiv:1411.4413.

[190] K. De Bruyn *et al.*, *Probing New Physics via the $B^0_s \to \mu^+\mu^-$ Effective Lifetime*, Phys. Rev. Lett. **109** (2012) 041801, arXiv:1204.1737.

[191] LHCb collaboration, R. Aaij *et al.*, *Measurement of $\sigma(pp \to b\bar{b}X)$ at $\sqrt{s} = 7$ TeV in the forward region*, Phys. Lett. **B694** (2010) 209, arXiv:1009.2731.

[192] LHCb collaboration, R. Aaij *et al.*, *Precision luminosity measurements at LHCb*, JINST **9** (2014) P12005, arXiv:1410.0149.

[193] CDF Collaboration, F. Abe *et al.*, *Measurement of b quark fragmentation fractions in the production of strange and light B mesons in $p\bar{p}$ collisions at $\sqrt{s} = 1.8$TeV*, Phys. Rev. **D60** (1999) 092005.

[194] LHCb Collaboration, I. Bediaga *et al.*, *Framework TDR for the LHCb upgrade: technical design report*, LHCb-TDR-12.

[195] A. J. Buras, *Relations between $\Delta M_{(s,d)}$ and $B_{(s,d)} \to \mu\bar{\mu}$ in models with minimal flavor violation*, Phys. Lett. **B566** (2003) 115, arXiv:hep-ph/0303060.

[196] F. Dettori, private communication.

[197] N. Tuning, private communication.

[198] LHCb collaboration, R. Aaij *et al.*, *Study of beauty hadron decays into pairs of charm hadrons*, Phys. Rev. Lett. **112** (2014) 202001, arXiv:1403.3606.

[199] LHCb collaboration, R. Aaij *et al.*, *Study of the productions of Λ_b and $\bar{B}^0$ hadrons in pp collisions and first measurement of the $\Lambda_b \to J/\psi p K^-$ branching fraction*, arXiv:1509.00292, submitted to Chin.Phys.C.

R

[200] LHCb collaboration, R. Aaij *et al.*, *Evidence for pentaquark-charmonium states in $\Lambda_b^0 \to J/\psi p K^-$ decays*, Phys. Rev. Lett. **115** (2015) 07201, arXiv:1507.0341.

[201] BaBar Collaboration, J. Lees *et al.*, *Branching fraction and form-factor shape measurements of exclusive charmless semileptonic B decays, and determination of $|V_{ub}|$*, Phys. Rev. **D86** (2012) 092004, arXiv:1208.1253.

[202] BaBar Collaboration, P. del Amo Sanchez *et al.*, *Study of $B \to \pi\ell\nu$ and $B \to \rho\ell\nu$ Decays and Determination of $|V_{ub}|$*, Phys. Rev. **D83** (2011) 032007, arXiv:1005.3288.

[203] Belle Collaboration, H. Ha *et al.*, *Measurement of the decay $B^0 \to \pi^-\ell^+\nu$ and determination of $|V_{ub}|$*, Phys. Rev. **D83** (2011) 071101, arXiv:1012.0090.

[204] Belle Collaboration, A. Sibidanov *et al.*, *Study of Exclusive $B \to X_u\ell\nu$ Decays and Extraction of $|V_{ub}|$ using Full Reconstruction Tagging at the Belle Experiment*, Phys. Rev. **D88** (2013) 032005, arXiv:1306.2781.

[205] LHCb collaboration, R. Aaij *et al.*, *Determination of the quark coupling strength $|V_{ub}|$ using baryonic decays*, Nature Physics **11** (2015) 743, arXiv:1504.0156.

[206] Belle Collaboration, S. Esen *et al.*, *Precise measurement of the branching fractions for $B_s \to D_s^{(*)+} D_s^{(*)-}$ and first measurement of the $D_s^{*+} D_s^{*-}$ polarization using e^+e^- collisions*, Phys. Rev. **D87** (2013) 031101, arXiv:1208.0323.

[207] Belle Collaboration, A. Drutskoy *et al.*, *Measurement of inclusive D_s, D^0 and J/ψ rates and determination of the $B_s^{(*)}\overline{B}_s^{(*)}$ production fraction in $b\bar{b}$ events at the $\Upsilon(5S)$ resonance*, Phys. Rev. Lett. **98** (2007) 052001, arXiv:hep-ex/0608015.

[208] CLEO, G. Huang *et al.*, *Measurement of $B(\Upsilon(5S) \to B_s^{(*)}\overline{B}_s^{(*)})$ Using ϕ Mesons*, Phys. Rev. **D75** (2007) 012002, arXiv:hep-ex/0610035.

[209] R. Aaij *et al.*, *The LHCb Trigger and its Performance in 2011*, JINST **8** (2013) P04022, arXiv:1211.3055.

[210] LHCb Collaboration, R. Antunes-Nobrega *et al.*, *LHCb trigger system: Technical Design Report*, LHCb-TDR-10.

[211] A. Puig, *The LHCb trigger in 2011 and 2012*, LHCb-PUB-2014-046.

[212] H. Dijkstra, N. Tuning, and N. Brook, *Some Remarks on Systematic Effects of the Trigger and Event Generator Studies*, LHCb-2003-157. LHCb internal documentation.

[213] V. V. Gligorov and M. Williams, *Efficient, reliable and fast high-level triggering using a bonsai boosted decision tree*, JINST **8** (2013) P02013.

Summary

The Standard Model (SM) of particle physics describes all known elementary particles and their interactions. Despite its tremendous success, some problems remain not understood. The abundance of matter over anti-matter is still an open question. Also the nature of so-called dark matter, invisible matter that can only be detected through its gravitational force, is yet to be discovered. New Physics (NP) models have been proposed to answer these (and more) open questions. These models are usually extensions of the already existing SM that assume the existence of yet unknown particles and forces.

The ATLAS and CMS experiments at the Large Hadron Collider (LHC) are designed to directly search for such new particles predicted by NP models. The LHCb experiment, however, is designed to measure observables for which there are SM predictions. New particles can modify these observables. Therefore, precision measurements can reveal hints of NP.

The experimental apparatus forms an integral part in the search for NP. I contributed to the control of the Outer Tracker subdetector system and monitored its performance using dedicated scans. In addition, I measured in detail the relative b-hadron production rates. This is needed to measure *any* B_s^0 or Λ_b^0 branching fraction at the LHC. Many B_s^0 branching fractions are precisely predicted in the SM, and can thus reveal signs of NP. In this thesis, I measured four world best branching fractions.

Ageing of the LHCb Outer Tracker

The LHCb detector operates in the unprecedented high radiation environment of the LHC. Especially the Outer Tracker (OT) subdetector system, consisting of gaseous straw tubes, is prone to radiation damage, a phenomenon referred to as ageing. The OT is responsible for the detection of tracks of charged particles and provides indispensable information for reconstruction of particle decays.

The monitoring of the ageing of the OT is performed using dedicated scans, "amplifier threshold scans", which are taken at regular intervals during normal proton-proton collisions. Therefore, the scans are at the expense of valuable physics data. Charged particles crossing the OT ionise the gas. Hits are measured when the collected charge supersedes a certain threshold setting. The hit efficiency is measured as a function of this threshold setting, and the threshold setting at half the optimal efficiency is determined. A shift of the half-efficiency point to a lower value (compared to a previous scan) is an indicator of ageing. A total of 15 scans have been recorded during the Run I running period. Taking advantage

of a hardware failure in the high voltage system of the OT, the method was validated: the half-efficiency point shifted by exactly the right amount as expected due to the lower gas amplification. Comparisons of the scans to the reference scan taken at the start of Run I, reveal no sign of ageing.

Alternative scanning methods are designed to monitor ageing in the case when no proton-proton interacting beam is present. Instead, the detector surface is irradiated with a dedicated ^{90}Sr source and the detector response (i.e. the current) to this radiation is measured. Based on observations in the lab, radiation damage is expected upstream of the area of highest radiation, with respect to the gas flow. Therefore, the scans are aimed at detecting a specific pattern in measured current, rather than measuring the absolute hit efficiency. The observed gain variations are uniform throughout the entire module within $\pm 5\%$ indicating no ageing. In addition, irradiation tests are performed during which a small part of the detector surface is irradiated with a ^{90}Sr source over a period of 475 hours. No ageing has been observed in the irradiated area.

Fragmentation fractions and branching fractions

The prime example of a branching fraction measurement sensitive to NP is the measurement of $\mathcal{B}(B_s^0 \to \mu^+\mu^-)$. This decay is heavily suppressed within the SM, but can be enhanced due to additional particles present in NP models. In order to measure any B_s^0 branching fraction at LHCb, knowledge is needed about the B_s^0 production rate. Alternatively, knowledge of the relative rates of B_s^0 and B^0 meson production, combined with the precisely known B^0-meson branching fractions measured at the B-factories, provides sufficient information to determine $\mathcal{B}(B_s^0 \to \mu^+\mu^-)$ at the LHC.

The production of b hadrons is difficult to calculate within QCD and needs to be measured experimentally. In proton-proton collisions, $b\bar{b}$-quark pairs are produced. A b quark hadronises to a B^+, B^0, B_s^0 meson or a b baryon, with the fractions f_u, f_d, f_s and f_{baryon}, respectively. These fractions were measured experimentally by the LEP experiments and CDF. However, a priori these fractions can depend on the centre-of-mass energy and the kinematics of the b hadron. Therefore they cannot straightforwardly be used at the LHC. Moveover, for a precise measurement of $\mathcal{B}(B_s^0 \to \mu^+\mu^-)$ a more precise measurement of B_s^0 production is needed than currently available.

The relative production rates of b hadrons are measured in this thesis using hadronic decays. The relative production of B_s^0 and B^0 mesons is denoted with f_s/f_d. The branching fractions of the decays $\overline{B}_s^0 \to D_s^+(\to K^-K^+\pi^+)\pi^-$ and $\overline{B}^0 \to D^+(\to \pi^+\pi^+K^-)K^-$ are theoretically related. This relation, combined with the measured yields of these decay in the LHCb dataset, allows for a measurement of f_s/f_d.

Interesting b-hadron decays need to be filtered from the wealth of data collected by the LHCb experiment. The b-hadron decays discussed in this work are of the b-to-c type: the b hadron first decays to a bachelor hadron and a charm hadron with finite lifetime, which then further decays into three final state particles. Due to their long lifetime and large boost, b hadrons typically fly a few mm in the detector before they decay. The momentum and spatial resolution of the LHCb detector allow to precisely reconstruct the primary vertex and the b and c-hadron decay vertices. The particle identification subdetectors allow to

identify the species of the different particles in the final state. The lifetime of the b and c hadron, their decay vertex quality and their reconstructed masses, as well as the particle identification performance, provide tools to select the signal decay while omitting a large fraction of the background. The background surviving the selection is modelled based on simulated events, and the signal yield is then extracted from a fit to the invariant mass distribution.

The ratio of fragmentation fractions, f_s/f_d, is measured in the 1 fb^{-1} dataset collected by the LHCb experiment in 2011 at $\sqrt{s} = 7$ TeV to be,

$$f_s/f_d = 0.238 \pm 0.004 \pm 0.015 \pm 0.021\,, \tag{1}$$

where the first uncertainty is statistical, the second systematic and the third from the theoretical relation between the branching fractions of $\overline{B}{}^0_s \to D^+_s\pi^-$ and $\overline{B}{}^0 \to D^+K^-$ decays. This measurement is combined with a independent measurement of f_s/f_d using semileptonic decays by LHCb, corrected for the difference between experimental and theoretical branching fractions, and taking into account the latest values of the b-hadron lifetimes and c-hadron branching fractions, to yield

$$f_s/f_d = 0.260 \pm 0.018\,. \tag{2}$$

The dependence of the ratio of fragmentation fractions f_s/f_d on the b-hadron kinematics has been evaluated using the hadronic decays $\overline{B}{}^0_s \to D^+_s\pi^-$ and $\overline{B}{}^0 \to D^+\pi^-$, where the more abundant decay $\overline{B}{}^0 \to D^+\pi^-$ is used instead of the Cabibbo-suppressed $\overline{B}{}^0 \to D^+K^-$ decay mode. The data is divided in bins of b-hadron transverse momentum and pseudorapidity and the efficiency corrected yield ratios are determined in each kinematic bin. From these the dependencies of f_s/f_d on the transverse momentum and pseudorapidity of the b hadron are determined. These measurements are of great importance to the determination of $\mathcal{B}(B^0_s \to \mu^+\mu^-)$ by the CMS experiment, which operates in a different pseudorapidity and transverse momentum region. The central value of f_s/f_d measured by the LHCb experiment therefore needs to be corrected for any dependency on these variables before use by CMS. The measured dependencies are shown in Figs. S1a–S1b. The ratio of f_s/f_d is observed to decrease with increasing transverse momentum of the b hadron. The ratio of f_s/f_d does not show a significant dependence on the pseudorapidity of the b hadron.

Recently Λ^0_b baryons gained a wider interest. The study of its production and decays can offer complementary information to that obtained from the study of b mesons. While significant progress has been made in the understanding of the production and decay properties of b mesons, knowledge of b baryons is limited. The relative production rates of Λ^0_b baryons and B^0 mesons are measured in this thesis using the hadronic decays $\Lambda^0_b \to \Lambda^+_c(\to pK^-\pi^+)\pi^-$ and $\overline{B}{}^0 \to D^+(\to \pi^+\pi^+K^-)\pi^-$. As no theoretical information is available which relates the branching ratios of these two decays, it is not possible to measure the central value of $f_{\Lambda^0_b}/f_d$. Therefore, only the dependence of $f_{\Lambda^0_b}/f_d$ on the b-hadron transverse momentum and pseudorapidity is measured. A previous LHCb measurement of $f_{\Lambda^0_b}/f_d$, using semileptonic decays for which a theoretical relation between branching fraction can be calculated, is used to determine the absolute scale of the measurement.

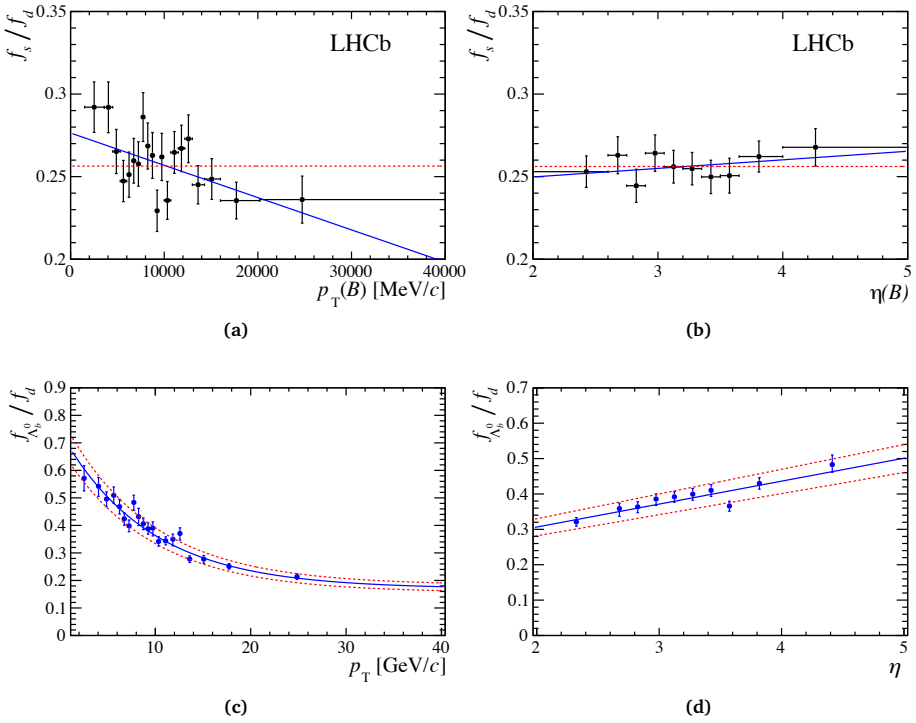

Fig. S1 · Kinematic dependencies of relative b-hadron production rates: a) f_s/f_d, $p_{\rm T}$ dependence; b) f_s/f_d, η dependence; c) $f_{\Lambda_b^0}/f_d$, $p_{\rm T}$ dependence; d) $f_{\Lambda_b^0}/f_d$, η dependence.

The observed dependencies (Figs. S1c–S1d) show a decrease of $f_{\Lambda_b^0}/f_d$ with transverse momentum of the b hadron which is best described by an exponential function, and a linear increase of $f_{\Lambda_b^0}/f_d$ with pseudorapidity. In addition, this method allows for the extraction of $\mathcal{B}(\Lambda_b^0 \to \Lambda_c^+\pi^-)$, independent of $\mathcal{B}(\Lambda_c^+ \to pK^-\pi^+)$, leading to the most precise Λ_b^0 branching fraction measurement to date:

$$\mathcal{B}(\Lambda_b^0 \to \Lambda_c^+\pi^-) = (4.30 \pm 0.03 \pm 0.12 \pm 0.26 \pm 0.21) \times 10^{-3}\,, \tag{3}$$

where the first uncertainty is statistical, the second systematic, the third results form the semileptonic measurement of $f_{\Lambda_b^0}/f_d$, and the fourth is from the knowledge of $\mathcal{B}(\overline{B}^0 \to D^+\pi^-)$.

The decay $\overline{B}_s^0 \to D_s^\pm K^\mp$ provides a sensitive probe to the CKM angle γ. The branching fraction of this decay was previously measured by the LHCb Collaboration in a subset of the currently available data. Its value relative to $\mathcal{B}(\overline{B}_s^0 \to D_s^+\pi^-)$ was found to be below the theoretical limit. To either confirm or strengthen this discrepancy, the measurement is repeated using the full LHCb dataset recorded in 2011 and 2012 at a centre-

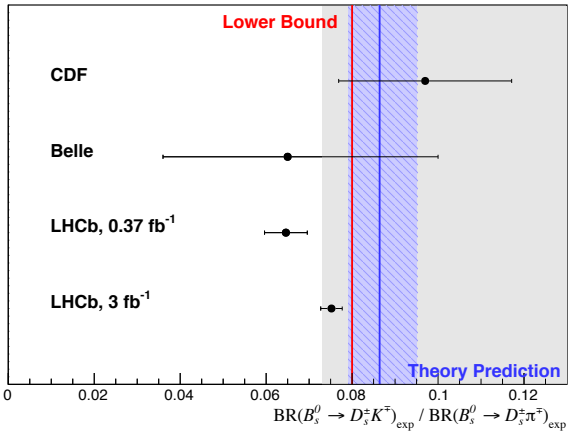

Fig. S2 · Measured values of $\mathcal{B}(\overline{B}{}^0_s \to D^\pm_s K^\mp)/\mathcal{B}(\overline{B}{}^0_s \to D^+_s \pi^-)$ by different experiments. The theoretical lower limit on this quantity is indicated with the red line. The grey area is the allowed region, including the uncertainty on the lower limit. The theoretical prediction and its uncertainty are indicated in blue.

of-mass energy of $\sqrt{s} = 7$ TeV and $\sqrt{s} = 8$ TeV, respectively. Due to the similarity of this decay with the hadronic decays used in the determination of f_s/f_d and $f_{\Lambda^0_b}/f_d$, the same selection strategy can be used. The signal yields of $\overline{B}{}^0_s \to D^\pm_s K^\mp$ and $\overline{B}{}^0_s \to D^+_s \pi^-$ decays are obtained from a fit to the respective invariant mass distributions. From these yields, the relative branching fractions are extracted to yield

$$\frac{\mathcal{B}(\overline{B}{}^0_s \to D^\pm_s K^\mp)}{\mathcal{B}(\overline{B}{}^0_s \to D^+_s \pi^-)} = 0.0752 \pm 0.0015 \pm 0.0019\,, \tag{4}$$

where the first uncertainty is statistical and the second is systematic. The measured value is in agreement with the lower limit on this quantity, as shown in Fig S2.

Samenvatting

Het begrijpen van het universum en de fundamentele wetten der natuurkunde die daaraan ten grondslag liggen, is iets wat mensen uit alle tijden bezig heeft gehouden. Wanneer we inzoomen op de kleinste afstanden, zien we moleculen die bestaan uit atomen en atomen die op hun beurt weer bestaan uit protonen, neutronen en elektronen. Als we nog verder inzoomen zien we dat protonen en neutronen bestaan uit quarks. Quarks zijn, net als elektronen, elementaire deeltjes die niet verder gedeeld kunnen worden. Het Standaard Model der materie (SM) beschrijft alle elementaire deeltjes en hun interacties (Fig. S1a) en ligt aan de basis van de deeltjesfysica.

Het SM is opgezet in de jaren '60 en '70 en sindsdien veelvuldig getest. Alle elementaire deeltjes die in het SM worden voorspeld zijn gevonden, met als meest recente ontdekking het Higgsdeeltje in 2012. Hoewel het SM een accurate beschrijving biedt van elementaire deeltjes en hun interacties, blijven er een aantal fundamentele vragen onbeantwoord. Er wordt aangenomen dat vlak na de oerknal het universum uit gelijke hoeveelheden materie en anti-materie bestond. Recente metingen wijzen uit dat het huidige universum voornamelijk uit materie bestaat. De studie van verschillen tussen materie en anti-materie is essentieel om deze *asymmetrie* te begrijpen. Een andere open vraag richt zich op *donkere materie*. Dit is materie waarvan de gravitationele aantrekkingskracht zichtbaar is, en verder niks. Het SM kent geen deeltje met de eigenschappen van donkere materie. Verschillende uitbreidingen van het SM zijn voorgesteld die dit type deeltje toevoegen.

Om fundamentele vragen over de allerkleinste deeltjes te beantwoorden, is het grootste natuurkundelaboratorium ter wereld gebouwd. Op CERN worden in de Large Hadron Collider (LHC) protonen versneld tot vrijwel de lichtsnelheid. De LHC is een circulaire protonenversneller van 27 km lang en is 100 m onder de grond gebouwd (Fig. S1b). Op vier plekken worden de protonen met elkaar in botsing gebracht. Op deze vier plekken zijn detectoren gebouwd, die de deeltjes kunnen waarnemen die ontstaan in de botsingen.

Voor mijn onderzoek gebruik ik data verzameld met behulp van de LHCb-detector. In proton-proton botsingen ontstaat ioniserende straling die de LHCb-detector kan beschadigen, een proces dat wordt aangeduid met *veroudering*. Met name het detectoronderdeel dat wordt gebruikt voor het reconstrueren van de sporen van geladen deeltjes die ontstaan in proton-proton botsingen, de *Outer Tracker*, is gevoelig voor het optreden van veroudering. Daarom is het van groot belang het functioneren van de Outer Tracker in de gaten te houden. Hiervoor heb ik regelmatig scans uitgevoerd, waarbij ik de efficiëntie voor het meten van een spoor van een deeltje heb bepaald. Een vermindering van de efficiëntie kan duiden op

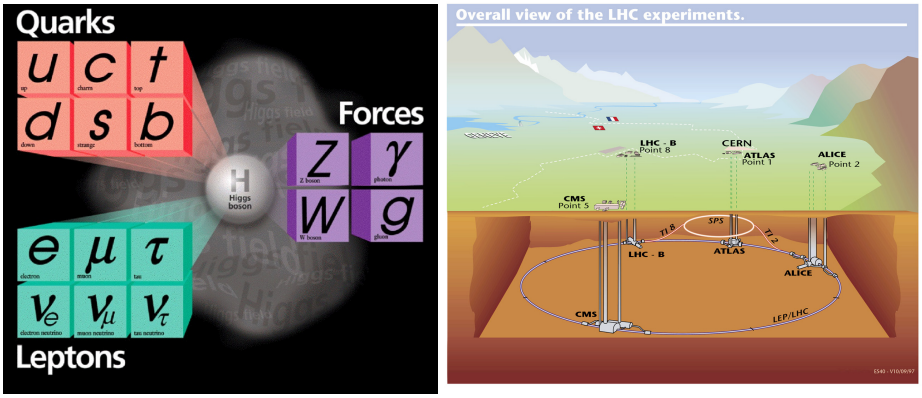

(a) (b)

Fig. S1 · a) Grafische representatie van het standaard model. b) De LHC is gebouwd in een 27 km lange tunnel ongeveer 100 m onder de grond. Op vier plekken worden protonen in botsing gebracht.

S

veroudering. De resultaten van de verschillende scans zijn samengevat in Fig. S2a, waar elk datapunt het resultaat is van één scan. Een positieve waarde van de meting betekent geen veroudering. Met de scans hebben we aangetoond dat het functioneren van de Outer Tracker gelukkig niet is verslechterd door veroudering. Dit resultaat wordt bevestigd door aanvullende scans die ik heb uitgevoerd in perioden dat er geen proton-proton botsingen zijn. Het Outer Tracker-oppervlakte hebben we bestraald met een radioactieve bron waarna we hebben gemeten of er signaalverlies is opgetreden op de plek van bestraling (Fig. S2b). Er zijn geen aanwijzingen voor stralingsschade gevonden.

De LHCb-detector is speciaal ontworpen voor de studie van b-hadronen. Deze deeltjes worden veelvuldig geproduceerd in proton-proton botsingen, ongeveer 100 000 keer per seconde. b-Hadronen zijn samengestelde deeltjes die bestaan uit verschillende quarks. Er zijn twee typen b-hadronen: een b-quark gecombineerd met een antiquark is een meson, en een b-quark gecombineerd met twee andere quarks is een baryon. Middels het verval van b-hadronen kunnen de parameters van het SM precies gemeten worden. Uitbreidingen van het SM, zogenaamde *Nieuwe Fysica* modellen, introduceren nieuwe deeltjes die leiden tot afwijkingen van de SM-voorspellingen.

Het b-hadron is een instabiel deeltje en zal snel vervallen naar andere deeltjes. De vertakkingsverhouding geeft aan hoe vaak een bepaald b-hadron naar een bepaalde eindtoestand vervalt. Nieuwe Fysica kan de vertakkingsverhouding van bepaalde b-hadron vervallen beïnvloeden. Door de gemeten, experimentele, vertakkingsverhouding te vergelijken met de theoretische waarde gebaseerd op het SM, kunnen nieuwe deeltjes worden ontdekt.

Een studie van B_s^0-mesonen kan inzicht bieden in fundamentele vraagstukken. Een B_s^0-meson is een deeltje dat bestaat uit een $\bar{b}$-antiquark en een s-quark. Het verval van een B_s^0-meson naar twee muonen, geschreven als $B_s^0 \to \mu^+\mu^-$, is zeer zeldzaam in het

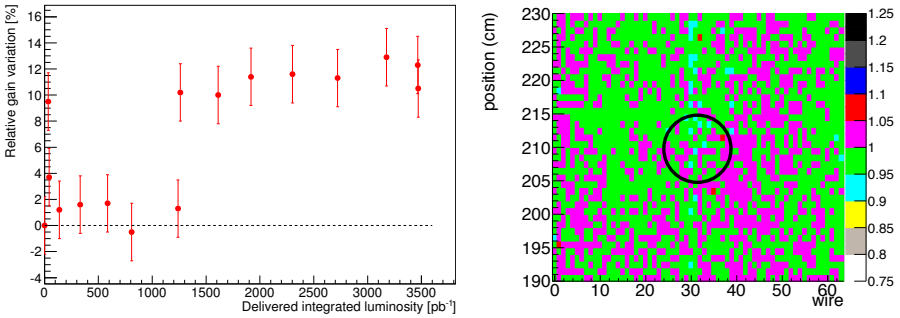

(a) (b)

Fig. S2 · a) Resultaten van de scans van de Outer Tracker. Op de horizontale as staat de "delivered integrated luminosity", een maat voor de hoeveelheid verzamelde data. De verticale as is een maat voor de relatieve efficiëntie van de detector op het moment van de scan ten opzichte van een eerder genomen referentiescan. Een waarde boven 0 betekent geen veroudering. b) Een scan van het oppervlakte van een gedeelte van de Outer Tracker. Het gebied aangegeven met de cirkel is bestraald met een radioactieve bron. Er is geen veroudering opgetreden.

SM en komt bijna niet voor. Als dit verval toch (veel) gemeten zou worden in de LHCb-dataset, dan is dit een sterke aanwijzing voor het bestaan van Nieuwe Fysica. Echter, om te bepalen hoe vaak dit verval voorkomt, is het vereist te weten hoeveel B_s^0-mesonen er worden geproduceerd in proton-proton botsingen bij de LHC. Dit is moeilijk om theoretisch te voorspellen en moet daarom experimenteel worden gemeten.

De relatieve productie van verschillende b-hadronen is het onderwerp van mijn proefschrift. Om te meten wat de vertakkingsverhouding van het verval $B_s^0 \to \mu^+\mu^-$ is, is het noodzakelijk om te bepalen hoeveel B_s^0-mesonen er worden gemaakt. Omgekeerd, als bekend is wat de vertakkingsverhouding van een bepaald B_s^0-meson verval is, kun je dit verval gebruiken om te meten hoeveel B_s^0-mesonen er gemaakt worden. Van dit principe heb ik gebruikgemaakt om de relatieve productie fracties van B_s^0- en B^0-mesonen (aangeduid met f_s/f_d) te meten. Een B^0-meson bestaat uit een $\bar{b}$-antiquark en een d-quark. Voor deze meting heb ik het B_s^0-meson verval naar een D_s-meson en een pion, (geschreven als $B_s^0 \to D_s^-\pi^+$) en het verval van een B^0-meson naar een D-meson en een kaon (geschreven als $B^0 \to D^-K^+$) gebruikt. De vertakkingsverhoudingen van deze vervallen zijn theoretisch nauwkeurig te bepalen en dit gegeven is gebruikt in de meting van f_s/f_d.

In de dataset verzameld met de LHCb-detector in 2011, heb ik het aantal $B_s^0 \to D_s^-\pi^+$ en $B^0 \to D^-K^+$ vervallen gemeten. Ik heb een selectie ontworpen waarmee ik een groot deel van de achtergrond verwijder, terwijl de efficiëntie voor het signaal hoog is. Het aantal signaal*events* heb ik daarna bepaald aan de hand van een fit aan de invariante massadistributie, zoals in Fig. S3. Hiervoor is het essentieel om de vorm van de invariante massadistributie van zowel het signaal als de verschillende contributies van de achtergrond

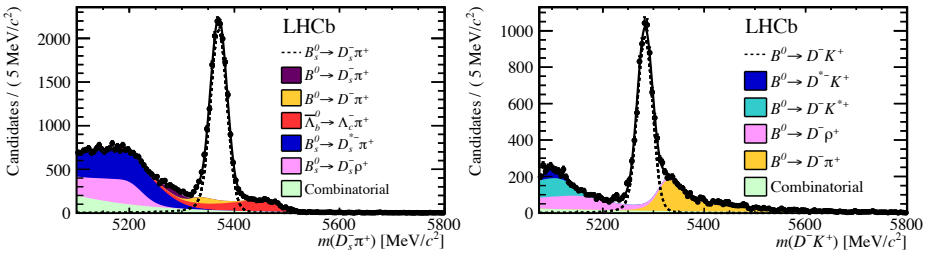

Fig. S3 · Invariante massadistributie gemeten in data van de LHCb-detector. De zwarte stippen zijn de datapunten en de lijn is de fit waarmee het aantal signaalevents is bepaald. Het signaal is aangeven met de stippellijn, en de verschillende typen achtergrond met de kleuren. Events reconstrueert als a) $B_s^0 \to D_s^- \pi^+$, en als b) $B^0 \to D^- K^+$.

correct te beschrijven. Nadat ik het gemeten aantal events heb gecorrigeerd voor de efficiëntie van mijn selectie, is het oorspronkelijke aantal signaalevents in de LHCb-dataset bekend. Gebruikmakend van het gemeten aantal $B_s^0 \to D_s^- \pi^+$ en $B^0 \to D^- K^+$ vervallen in de data, en de theoretische voorspelling van de vertakkingsverhoudingen van deze vervallen, heb ik bepaald wat de waarde van f_s/f_d is. Ik heb gemeten dat er 4.2 keer zoveel B^0-mesonen als B_s^0-mesonen worden geproduceerd in proton-proton botsingen bij de LHC. Omdat de vertakkingsverhoudingen van B^0-mesonverval precies zijn gemeten bij eerdere experimenten, kan nu de vertakkingsverhouding van B_s^0-meson verval worden gemeten door het aantal events van het B^0- en B_s^0-meson verval in de data te vergelijken. Dit gegeven is gebruikt om de vertakkingsverhouding van het $B_s^0 \to \mu^+\mu^-$ te bepalen. De gevonden waarde is in overeenstemming met de voorspelling in het SM.

Niet alleen het LHCb-experiment heeft de vertakkingsverhouding van het verval $B_s^0 \to \mu^+\mu^-$ gemeten. Ook een ander LHC-experiment, het CMS-experiment, heeft dit gemeten. Het ontwerp van het CMS-experiment is zodanig dat het minder geschikt is om f_s/f_d te meten. Daarom wordt de waarde van f_s/f_d gemeten door LHCb (uit mijn proefschrift) gebruikt. In tegenstelling tot de LHCb-detector, welke b-hadron verval alleen in de voorwaartse richting meet, meet het CMS-experiment in alle richtingen vanaf het punt waar de protonen met elkaar in botsing komen. De parameter die aangeeft hoe voorwaarts een proces is, is *pseudo-rapiditeit*: de hoek tussen een deeltje en de richting van de protonbundel. A priori hoeft de relatieve productie van b-hadronen niet hetzelfde te zijn in de voorwaartse richting en in het gebied waar de CMS-detector meet. Daarnaast, kan het zijn dat door verschillen in selectie de deeltjes bij de CMS-detector een andere (gemiddelde) *transversale impuls* hebben dan bij de LHCb-detector. Het is daarom van belang om te bepalen hoe f_s/f_d afhangt van de pseudo-rapiditeit en het transversale impuls. Dit heb ik gemeten met de vervallen $B_s^0 \to D_s^- \pi^+$ en $B^0 \to D^- \pi^+$. Het resultaat van deze meting wordt getoond Fig. S4. Hoe groter de transversale impuls van het b-meson, hoe minder B_s^0-mesonen er worden geproduceerd per B^0-meson. Het aantal B_s^0-mesonen per B^0-meson

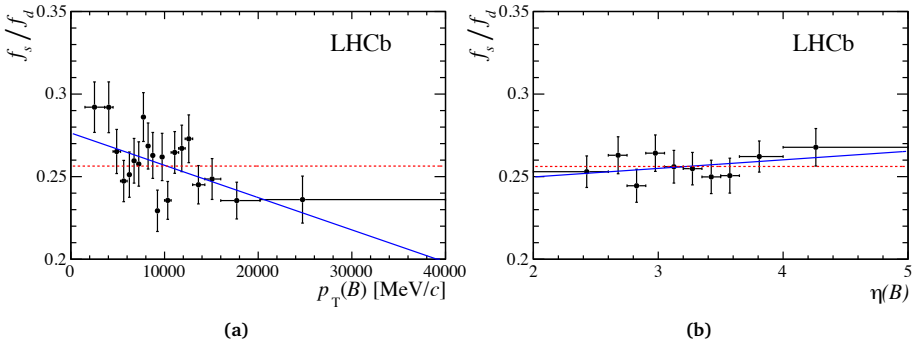

Fig. S4 · De relatieve productie van B_s^0- en B^0-mesonen. De afhankelijkheid van f_s/f_d van a) de transversale impuls en b) de pseudo-rapiditeit van het b-meson.

lijkt iets toe te nemen bij hogere pseudo-rapiditeit (voorwaartser), echter de toename is niet significant.

Naast b-mesonen kunnen ook b-baryonen worden gebruikt om het SM te testen. Het b-baryon is een complex deeltje (het bestaat uit drie quarks, terwijl een meson uit twee quarks bestaat) en theoretische voorspellingen over deze deeltjes zijn daarom moeilijker te maken dan voor mesonen. Desalnietemin worden er ook metingen gedaan aan b-baryonen. Bijvoorbeeld het Λ_b^0 baryon (bestaande uit de drie quarks u, d en b) is gebruikt om een meting te doen die verband heeft met verschillen tussen materie en anti-materie. Het is daarom van belang meer inzicht te krijgen in Λ_b^0 productie. Ik heb de relatieve productie van Λ_b^0-baryonen en B^0-mesonen gemeten met de vervallen $\Lambda_b^0 \to \Lambda_c^+\pi^-$ en $B^0 \to D^-\pi^+$, aangeduid met $f_{\Lambda_b^0}/f_d$. De afgehankelijkheid van $f_{\Lambda_b^0}/f_d$ van het transversale impuls en de peudo-rapiditeit wordt getoond in Fig. S5. Hoe groter de transversale impuls van het b-hadron, hoe minder Λ_b^0-baryonen er worden geproduceerd per B^0-meson. Tevens neemt de productie van het aantal Λ_b^0-baryonen per B^0-meson toe in de voorwaartse richting.

De vertakkingsverhouding van het verval van een B_s^0-meson naar een D_s-meson en een kaon, $B_s^0 \to D_s^\pm K^\mp$, is gemeten door de LHCb-Collaboratie met een subset van de nu beschikbare data. De gemeten waarde voor de vertakkingsverhouding is onder de theoretische limiet. Om deze discrepantie te bevestigen of te verwerpen, heb ik deze meting herhaald met de totale LHCb-dataset beschikbaar uit 2011 en 2012, welke tien keer zo groot is als de eerder gebruikte subset. Het aantal $B_s^0 \to D_s^\pm K^\mp$ vervallen in de LHCb-dataset heb ik gemeten door de invariante massadistributie te bestuderen (Fig. S6a). De relatieve productie van B_s^0- en B^0-mesonen, f_s/f_d, is nodig om het aantal events te vertalen naar een vertakkingsverhouding. In Fig. S6b wordt getoond dat de waarde die ik heb gemeten in overeenstemming is met de theoretische limiet.

De metingen in mijn proefschrift dragen bij aan de kennis van het SM. Kennis van de relatieve productie van b-hadronen is een vereiste voor alle metingen van vertakkingsver-

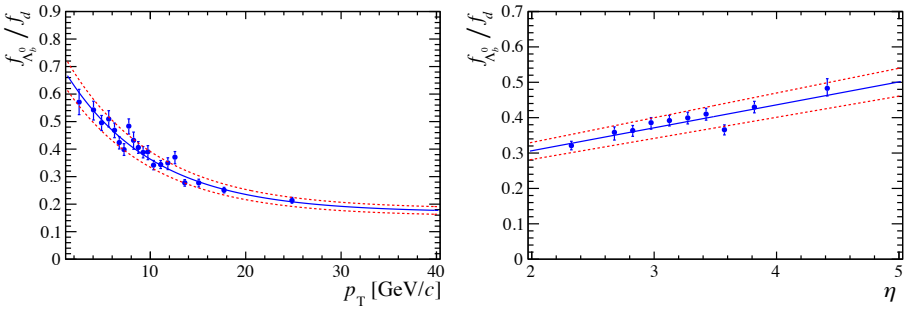

(a) (b)

Fig. S5 · De relatieve productie van Λ_b^0- en B^0-hadronen. De afhankelijkheid van $f_{\Lambda_b^0}/f_d$ van a) de transversale impuls en b) de pseudo-rapiditeit van het b-meson.

houdingen van B_s^0-mesonen en Λ_b^0-baryonen. Omdat nieuwe deeltjes uit Nieuwe Fysica modellen sommige vertakkingsverhoudingen kunnen veranderen, is het precies meten van vertakkingsverhoudingen een goede manier om naar aanwijzingen van Nieuwe Fysica te zoeken. Het belangrijkste voorbeeld is de vertakkingsverhouding van het verval $B_s^0 \to \mu^+\mu^-$. Met behulp van de relatieve productie van B_s^0 en B^0 mesonen gemeten in mijn proefschrift, is bepaald dat deze overeenkomt met de SM voorspelling. Tevens heb ik gemeten dat de vertakkingsverhouding van het verval $B_s^0 \to D_s^{\pm}K^{\mp}$ in overeenstemming is met de theoretische ondergrens. De metingen in mijn proefschrift hebben tot dusver niet geleid tot waarnemingen die wijzen op Nieuwe Fysica.

S

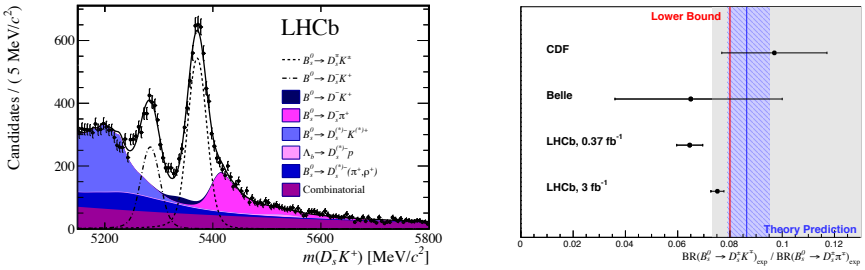

(a) **(b)**

Fig. S6 · a) Invariante massadistributie gemeten in data van de LHCb-detector. De zwarte stippen zijn de datapunten en de lijn is de fit waarmee het aantal signaalevents is bepaald. Het $B_s^0 \to D_s^\pm K^\mp$ signaal is aangeven met de stippellijn, en de verschillende typen achtergrond met de kleuren. b) De verschillende metingen van de relatieve vertakkingsverhoudingen van $B_s^0 \to D_s^\pm K^\mp$ en $B_s^0 \to D_s^- \pi^+$ vervallen zijn aangeven met de stippen en de horizontale bar duidt de onzekerheid op de meting aan. De meting met de subset van de LHCb-data is aangeven met "LHCb (0.37 fb^{-1})" en de meting beschreven in dit proefschrift met "LHCb (3 fb^{-1})". De theoretische ondergrens is aangegeven in rood/grijs en de theoretische voorspelling in blauw. De nieuwe meting is in overeenstemming met de theoretische ondergrens.

Dankwoord

Dit proefschrift had niet tot stand kunnen komen zonder de hulp van vele anderen. Deze laatste bladzijdes wil ik daarom richten aan hen die mij de afgelopen jaren hebben gemotiveerd en gesteund, aan hen die hun kennis en expertise met mij hebben gedeeld en aan hen met wie ik veel heb gelachen.

Niels, dankjewel voor je goede begeleiding. Onze discussies heb ik als zeer motiverend ervaren en vormden een bron van inspiratie. Ik heb altijd het gevoel gehad dat we als twee gelijken konden discussiëren, in plaats van als één begeleider, en één student. Je hebt veel meer met mij gedeeld dan alleen je kennis van de fysica: van jou heb ik geleerd om recht op het doel af te gaan en de details later in de vullen. Een vaardigheid die ik voordat ik aan dit avontuur begon zeker niet bezat, omdat ik graag alles tot in de puntjes uitpluis alvorens ik aan de volgende stap begin. Het spijt me dat je mij soms als streng hebt ervaren, als je, in drukke tijden, koffie wilde drinken terwijl ik net jouw aandacht te pakken had. Ik hoop dat je volgende student minder streng voor je is!

Marcel, speciaal voor jou: Merci veur 't creëren vaan 'n plezante werkomgeving. De LHCb gróp op Nikhef is neet wie e febrik boe zoe vääl meugelek fysica weurt bedreve. 't Is e plek boe ste gere veer jaore doorbringk, e plek boe nuie vrundsjappe oontstoon en boe ouch vääl ruimte is veur plezeer. Iech dink dat d'ch, es grópsleier, e groet deil vaan de credits heivaan touwkump. Op miene ierste bfys oetje in 't prachtege Limburg, gong 't wel evekes mis en iech kin 't neet laote om d'ch dao toch evenkes aon te rappelere: diech lees 'n euverziech zien vaan wie succesvol Limburgers zien in de fysica, en daan in 't bezunder in euze gróp. Tot miene groete verbazing stoont iech dao neet bij. Dit bleek te zien umtot iech in Mestreech aon de verkierde kant vaan de Maos geboren bin. Gelökkeg heet dat noets euze samenwerking in de weeg gestoan. Veural in de lèste maonde höbbe veer vääl samengewerkt en 't preufsjrif hat neet bestande in zien huidige vörm zoonder diene weerdevolle input. (Met dank aan Joost.)

Concerning supervision, I should also mention Barbara and Daan. Barbara, thank you for your guidance throughout the first year of my PhD. Your trust and dedication enabled me to make a flying start with the physics analysis. I think it was an adventure for both of us: for me as a fresh PhD student, and also for you in a new role supervising a PhD student. I think we did great! Daan, jij hebt me op weg geholpen met het werk voor de Outer Tracker. Dankjewel voor je gezelligheid en geduld.

I would also like to mention some people at CERN who were always happy to answer my questions. It was a pleasure to work with you. Manuel, I'm very impressed with your

programming skills and I'm grateful for all the times you helped me out with technical issues. Also, all the tasty dinners and fine whisky tastings are very much appreciated! Vava, thank you for the confidence you showed in me when you asked me to review an other analysis. Moritz, who sadly passed away recently. I think he was an inspiration to all young PhD students. I'm very grateful for having known Moritz and cherish the memories of every time we worked together.

Next, I would like to thank Laurence and Indrek, with whom I had the opportunity to work together on two different occasions. I always valued your opinions and I think we formed a good team! Jacco en Lennaert, jullie hebben mij de kans gegeven om in de rol van begeleider te stappen. Ik vond het heel leuk om met jullie samen te werken.

This brings me to the people at Nikhef. Roel, Veerle, Jeroen, Pieter, Rosemarie, Lucie, Panos, Vasilis, Elise, Suzanne, Rolf, Ingrid, Siim, Koen, Mick, Laurent, Elena, Maarten, thank you for the fruitful discussions on physics, for the gezelligheid, and for everything that makes Nikhef such a great place. A special thanks to a few people. Serena, mijn kantoorgenootje in het eerste jaar. Fijn dat er ook af en toe ruimte was voor "girl talk" in deze mannenwereld! Maurizio, thank you for offering me a place to stay when I moved to CERN. I really enjoyed all the laughing, singing and of course the Italian dinners. I still have the gigantic jar of salt you gave me four years ago. I'm afraid my pasta is still Dutch-unsalty! Suvayu, my office mate in the last year of the PhD and good friend, thank you for your support, the laughs and the late-night Indian dinners. You were always ready to help me, even though you were very busy yourself.

Ed en Pieter, jullie verdienen hier ook een plekje. Dank jullie wel voor jullie adequate handelen en het meedenken in moeilijke situaties.

I would like to thank my manuscript committee for their careful reading: Olaf, Robert, Antonio, Gerhard, Stan and Marcel. Thanks to those who helped improving the quality of the thesis, by proofreading some chapters. Merel, dankjewel voor het ontwerpen van de cover. Reuters en Novum Nieuws, bedankt voor het ter beschikking stellen van het beeldmateriaal voor de cover.

My time at CERN was really wonderful, thanks to some of the fantastic people I met. Duc, Kristof, you were always in for adventure; William, you introduced me to climbing high mountains; Robert, thank you for giving me timely fatherly advise; and Eva, my always cheerful housemate. Geert-Jan, Joern, dank jullie wel voor jullie geduld op de skipiste. Paul, thank you being new to skiing/snowboarding too!

Deze vier jaar had ik niet volgehouden zonder de steun van mijn vrienden. Floor, Marije, Katherine, Marieke, Annemarie, bedankt voor het even ergens anders aan denken, het lachen, de gezellige avonden en de vele weekendtripjes. Jullie zijn van onschatbare waarde!

Papa en mama, ik weet dat jullie altijd in mij geloven. Ook de rest van mijn familie wil ik bedanken voor alle steun die we, vooral dit laatste moeilijke jaar, aan elkaar hebben gehad.

Lieve Leendertjan, dankjewel dat je er altijd voor me bent. Dankjewel voor al het plezier dat we samen hebben en dat ik me bij jou thuis kan voelen. Dankjewel dat ik ook met je mag delen als het allemaal tegenzit. Jouw liefde en steun betekenen alles voor me.

D